Guiding Light by and beyond the Total Internal Reflection Mechanism

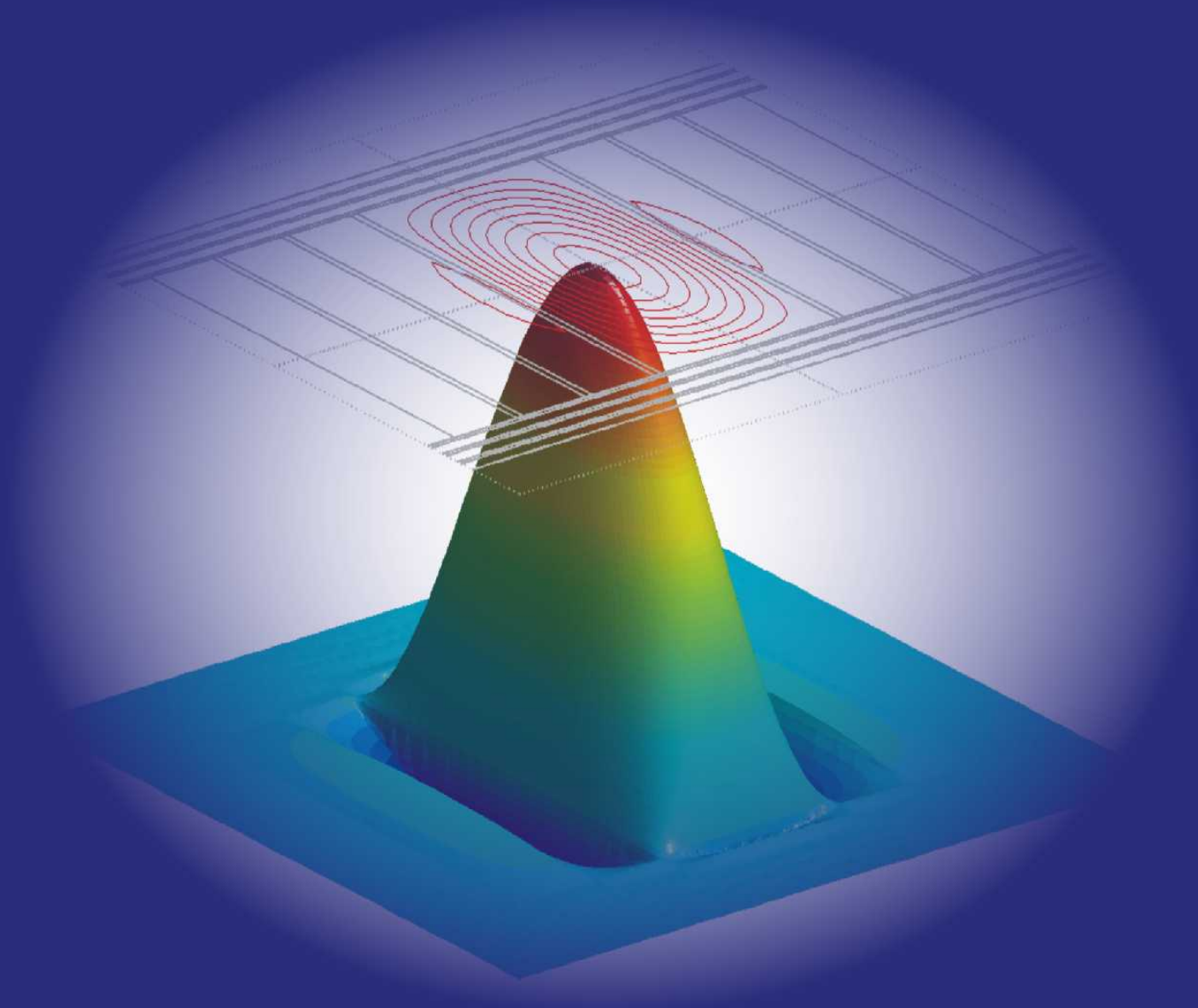

Henri P. Uranus

GUIDING LIGHT BY AND BEYOND THE TOTAL INTERNAL REFLECTION MECHANISM

Henri P. Uranus

The research presented in this dissertation was carried out at the Integrated Optical MicroSystems (IOMS) group and the Applied Analysis and Mathematical Physics (AAMP) group, Faculty of Electrical Engineering, Mathematics, and Computer Science and MESA+ Research Institute, University of Twente, P.O. Box 217, 7500 AE Enschede, The Netherlands.

This research was supported by the STW Technology Foundation (project TWI.4813), applied science division of NWO and technology program of the Ministry of Economic Affairs, The Netherlands.

Front cover : An ultra low loss air-core integrated optical waveguide.
The computed Re(H_y) field profile of the leaky q-TE_{00} mode of a waveguide composed of silicon-compatible materials, with 10μm×10μm air core, as discussed in Chapter 9. With only 3 periods of bilayers at every side of the cladding, the confinement loss of this mode is as low as 0.04 dB/cm at λ=1.55μm, which to the best of the author's knowledge, is 40 times (on a dB scale) lower than what have ever been reported before in the literature for air-core integrated optical waveguides.

Back cover : The air-core silica-air Bragg fiber.
The computed Re(H_y) field profile of the leaky HE_{12}^{a}-like mode of the air-core silica-air Bragg fiber discussed in Chapter 8. The eccentricity of the field profile indicates the vectorial character (polarization effect) of the mode. The small spots at the cladding indicate the onset of the anti-crossing with cladding-resonance mode.

ISBN 90-365-2158-0

GUIDING LIGHT BY AND BEYOND THE TOTAL INTERNAL REFLECTION MECHANISM

DISSERTATION

to obtain
the doctor's degree at the University of Twente,
on the authority of the rector magnificus,
prof. dr. W.H.M. Zijm,
on account of the decision of the graduation committee,
to be publicly defended
on Thursday 14 April 2005 at 15.00

by

Henri Putra Uranus
born on 2 December 1963
in Pontianak, Indonesia

Dit proefschrift is goedgekeurd door de promotor
Prof. Dr. E. van Groesen

En de assistent-promotor
Dr. H.J.W.M. Hoekstra

This dissertation is dedicated to
my wife Tris, and
our children Hanna and Hans

Abstract

Photonics plays an important role in modern technologies, e.g. in telecommunications and sensing systems. Waveguiding structures with micro- and nano-meter scale features are the basic building blocks of photonic circuits. Large varieties of structures have been used by scientists and engineers. These range from the conventional planar and channel waveguides, which work on the basis of the total-internal-reflection (TIR) mechanism, to the more advanced structures that utilize the anti-resonance-reflection, leaky-defect-resonance, and photonic-band-gap principles to (quasi-)confine and control the light. More and more complicated structures are emerging along with the development of both theory and fabrication technologies, leading to the improvement of existing applications and enabling access to many new application areas. As the fabrication of these devices usually involves costly facilities and time-consuming procedures, modeling tools are indispensable to explore new ideas, characterize and design the devices before their realization, as well as to understand the experimental results.

This thesis reports a series of techniques the author has developed to model various waveguiding structures, including the conventional planar and channel waveguides working by, and the advanced structures working beyond the TIR mechanism. Hence, this thesis contains both the methods and their applications to model and study the standard guided-wave and the advanced leaky-wave structures. The methods include mode solvers based on finite difference method (FDM) and finite element method (FEM), furnished with transparent boundary conditions (TBCs) for both guided and leaky modes. Based on the developed techniques, structures as simple as planar waveguides up to as complicated as photonic crystal fibers (PCFs) can be modeled rigorously.

For structures with 1-D cross-section, both FDM and FEM mode solvers have been developed. For the FDM, a special discretization scheme that takes into account both the permittivity gradients and discontinuities at interfaces between different graded-index anisotropic materials of planar structures, has been developed and applied to structures with complicated index profiles like the titanium-indiffused proton-exchanged $LiNbO_3$ waveguides. For the FEM, either the one based on the variational or Galerkin approaches, simple high-order schemes capable to give 4^{th}- or

6^{th}-order accuracy in effective indices have been developed for guided and leaky modes computation. Using the FEM mode solver; the properties of the anti-resonance reflecting optical waveguides (ARROWs), especially the anti-crossing phenomenon observed in the dispersion curves were studied. Together with the perturbation method, the FEM mode solver was also used to study the effect of a high-index medium in the proximity of a waveguiding structure. An interesting phenomenon on evolution of modes from guided to leaky and back to guided again as one varies the refractive index of the high-index medium was observed.

For structures with 2-D cross-section, a FEM scheme based on the Galerkin principle has been developed to solve the full vectorial wave-equation with a TBC that enables the computation of both guided and leaky modes in a relatively small computational domain. Using the mode solver, we investigate what happens when one varies the gap thickness of a Si_3N_4 strip waveguide with a DAST (4'-dimethylamino-*N*-methyl-4-stilbazolium tosylate) overlay. We observed in particular the evolution of modes from guided to leaky and back to guided again, from q-TM_{00} to q-TE_{10} and back to q-TM_{00} again, and from q-TE_{11} to q-TE_{10}. The vectorial leaky mode solver is well capable to handle complicated structure cross-section. It is suitable to rigorously study PCFs, including those that utilize the index-guiding mechanism as well as those that use the band-gap-guiding mechanism. Dispersion properties and confinement losses were investigated for a variety of PCFs, among others PCFs with circular or non-circular holes in the cladding, and with solid or air core. Another part of the study concerns the single-modeness of a commercial endlessly single-mode PCF. Based on the leaky mode picture, a criterion was proposed to locate its single mode operation regime. Additionally, hollow-core integrated optical waveguides were studied. A strategy, by considering the material composition of the anti-resonant bilayers to reduce the leakage loss, is reported. Low-loss hollow-core integrated optical waveguides designed based on that strategy, using silicon-compatible materials were proposed.

Acknowledgements

This thesis is a result of three and half years of research at IOMS group in the Department of Electrical Engineering and AAMP group in the Department of Applied Mathematics, University of Twente. Within this period, I have met many nice people and enjoyed beneficial interactions with them. I would like to take this opportunity to thank those people for supports, discussions, guidance, friendship, and sincere help.

Firstly, I would like to thank my supervisor Hugo Hoekstra for his guidance on my research. He is always willing to stop his own work for a while and answer my questions whenever I knock his door, even *zonder afspraak*. I have learned a lot from his extensive knowledge on the theory of optical waveguides. I also would like to thank him for giving me freedom to choose my topics of interest and for his patience in reading and giving many constructive comments on my manuscripts. I also would like to thank my promoter Brenny van Groesen for giving me opportunity to work in his STW project and for his patience in reading and commenting many draft of my manuscripts.

Furthermore, I would like to acknowledge the financial support from the STW Technology Foundation to the TWI.4813 project, where my research is part of it. I also would like to thank the EPAM-KNAW project that financed my short visit to University of Twente prior to the start of my Ph.D work, which gave me opportunity to make contact with people from IOMS and AAMP group. I would like to thank my promotion committee: Aziz Rahman, Paul Lambeck, Paul Urbach, Erik Fledderus, Jos van der Tol, and Manfred Hammer, for reviewing my thesis manuscript and giving many constructive remarks. I also would like to thank the users committee of my research project (most of them are within my promotion committee), especially Hans Blok, for their interest and many useful discussions during the project meetings.

I am also benefiting from the fruitful discussions in the informal (bi)weekly ‘optics meeting’. I would like to express my gratitude to all members of that meeting, especially to Manfred Hammer, Remco Stoffer, and Hugo Hoekstra for many interesting questions raised within that meeting, which help me to see the hidden aspects of my work.

My work at IOMS and AAMP groups has become interesting and enjoyable through interaction with many people. I enjoy both the scientific (IOMS group talk and

AAMP Seminar on Math. Phys.) and social activities (IOMS year-end party, IOMS summer *gezellig* bicycle trip, IOMS *borrel*, MPCM year-end dinner and walk) in both groups. I would like to thank my so-many office-mates: Joris van Lith, Geert Altena, Sami Musa, Iwan Heeskamp, Alex Iskandar, Douwe Geuzebroek, Arne Leinse, Muralidharan Balakrishnan, and Marcel Hoekman from IOMS; and Edi Cahyono, Timco Visser, Davit Harutyunyan, Pablo Tassi, Monika Polner, and Jaqueline Nicolau from AAMP/NACM for sharing the office room. Special thanks are addressed to Alfred Driessen for showing me several nice places in the nearby German cities, and Herman for giving me a half-hour-introduction to the group theory. My thanks also go to Gamar Hussein, Cazimir Bostan, Freddy Tan, David Marpaung, Didit Yudistira, Husin Alatas, Hardian Suprapto, Robert Taniman, Sena Sopaheluwakan, and Gan Shuyi, for many interesting conversations on life and technical topics; Agus Suryanto (with whom I also share the same research project) and Kiran Hiremath for answering many of my stupid questions on mathematics, and Davit Harutyunyan for discussions on FEM. I also would like to thank Anton Hollink and Henk van Wolferen for their prompt help on technical problems with the computer and copier machine, Rita ter Weele-Stokkers for helpful administrative supports, and Carla Hassink for dealing with all formalities.

My thanks also go to several people from overseas. I would like to thank Nader Issa from University of Sidney, Australia, who is always ready to play with his FDM-ABC code to calculate modes of PCF, whenever I need comparison and verification of my computational results. I also would like to thank Salah Obayya from Brunel University, UK, for sharing the way he implemented line integration, which gives me confidence on the way I implemented similar things. Additionally, I would like to thank Pak Tjia from ITB, Indonesia, for advices and encouragements.

My research work has been made possible by many blessings I receive in my personal life. I would like to praise and thank the Almighty Father for His love, blessing, and guidance to my life; without which I am nothing. I also would like to thank my beloved family: my wife Tris and our children Hanna and Hans, for their love, patience, and understanding. Their willingness to accompany me during this last one and half year of my stay in The Netherlands has been a great encouragement for me. Finally, I also would like to thank many people, whose kindness and friendship have made the stay of me and my family in The Netherlands more enjoyable. Ci Iing and Henk, Tante Lena and Oom Julius, and Mbak Yati and Oom Proost, thank you for your kindness. My thanks also go to many of Indonesian students from PPI-Enschede and KKI-Almelo for their friendship.

Henri P. Uranus Enschede, February 2005

Contents

Chapter 1

Introduction

A general perspective of this thesis will be presented. Then, structures that "guide" light without employing the total internal reflection mechanism will be introduced. Finally, the organization of the thesis will be outlined.

Introduction

This introductory chapter is aimed to give a general perspective on the work presented in this thesis. Additionally, an introduction to the "unusual" structures being modeled in substantial parts of this thesis will be given. Finally, the organization of this thesis will be outlined.

1.1. General perspective

Photonics plays an increasingly important role in modern technologies, e.g. in telecommunications and sensing systems, which have great impact on modern society. By just making a long-distance phone call or accessing the high-speed internet, one has made use of the availability of the advanced telecommunication infrastructure, where photonic technologies are intensively employed. Besides, in a much smaller scale and impact, photonics is also utilized in other application areas like instrumentation, environmental monitoring, and medical sensing.

Optical waveguiding structures are the basic building blocks of a photonic system. The most widespread optical waveguide is the optical fiber, which provides the huge bandwidth required to carry all the information between tele-/data-communication centres; which may be located within just the same building or disperse in different distant continents. At the end of the fiber, devices that can switch, modulate, split, combine, multiplex, and demultiplex optical signals, built on a compact chip, are required to perform all kinds of functionalities. Within this so-called integrated optical chip [1], optical waveguides together with other tiny photonic components are configured to form circuits that manipulate light.

Traditionally, these waveguiding structures, either fibers or integrated optical waveguides, rely on the total-internal-reflection principles. However, more advanced structures, which utilize the anti-resonance-reflection, the leaky-defect-resonance (more popularly known also as the modified-total-internal-reflection; see our comments in subsection 1.3.1.3), and the photonic-band-gap principles to (quasi-)confine and control the light have emerged. The classical single- and multi-mode fibers have recently got their new young brother, the so-called photonic crystal fiber [2-7] that opens up a huge number of new applications such as supercontinuum light generation, dispersion engineering, delivery of high-energy short-pulses, light-gas/liquid/particle interactions, etc. The unique benefits offered by this new class of optical fibers are so realistic, that factories [8-10] have been set-up to produce them commercially. Similar concepts have also been demonstrated for integrated optics [11]

since a long time ago, but might take longer time before air-hole-based structures [12-13] can be used in practical applications. These advanced waveguiding structures usually incorporate micrometer-scale features of high index-contrast. Additionally, they used to bring along leaky behavior induced by the high-index background material and the finite number of scattering features that form the cladding. As the fabrication of these structures usually involves costly facilities and time-consuming procedures, modeling tools are indispensable in research and development related to them. Modeling tools are required to explore, verify, and refine new ideas; characterize and design the structures/devices before their realization; as well as to interpret the results coming out of measurements.

This thesis deals with numerical methods and their applications in modeling various kinds of optical waveguiding structures. These include guided- and leaky-wave structures composed of either isotropic or anisotropic materials. Mainly, longitudinally invariant structures with 1-D and 2-D cross-sectional geometry will be considered. These structures can be a combination of step- and graded-index planar waveguides, up to structures with complicated 2-D cross-section employing many micrometer-scale features. The methods used to tackle these problems are the finite element method (FEM) and finite difference method (FDM). These methods have been chosen as they can handle the complicated index profiles and cross-section geometrical shape, and are applicable for both fiber- and integrated-optical structures. As the implementation of the FEM for higher order of accuracy and complicated cross-sectional shape is more transparent than the FDM, most schemes developed within this thesis will focus on the first method, while the latter one will only be used in one chapter, dealing with planar structures. Since for these methods, the efficiency, accuracy, and capability to deal with guided- and leaky-waves depend on how the fields at the computational boundaries are treated, special attention has been consistently paid to the transparent boundary conditions (TBC). Also, anisotropic materials of diagonal permittivity tensor have been considered within all schemes developed in this work as they are widely used in integrated optics and the efforts spend on handling these materials are almost comparable with those of isotropic materials.

The work presented within this thesis was carried out within the framework of Project TWI.4813 (“Efficient numerical schemes and nonlinear aspects beyond the SVEA”) supported by the Stichting Technische Wetenschappen (STW Technology Foundation). Another part of this project, carried out by another Ph.D. student, has been reported elsewhere [14]. The work reported in this thesis was executed partly (80%) in the Integrated Optical MicroSystems (IOMS) group of Dept. of Electrical Engineering and partly (20%) in the Applied Analysis and Mathematical Physics (AAMP) group of Dept. of Applied Mathematics of University of Twente.

1.2. Modes of optical waveguides

Modes of optical waveguides can be classified by the value of their effective indices (n_{eff}) as illustrated in Fig. 1.1 and Table 1.1 for a planar waveguide, where for leaky modes we have assumed no light inflow from substrate/cladding into the waveguide. For simplicity reason, we illustrate the modes using a 2-D picture (where we assume ∂_y=0) and consider an open system of step-index 3-layer symmetric structure with symmetry plane located at x=0. The refractive index of core and substrate/cladding media are n_f and n_{ext}, respectively, which are assumed to be real and isotropic, with $n_f > n_{ext}$. In principle, an asymmetric structure can also be treated in a similar way.

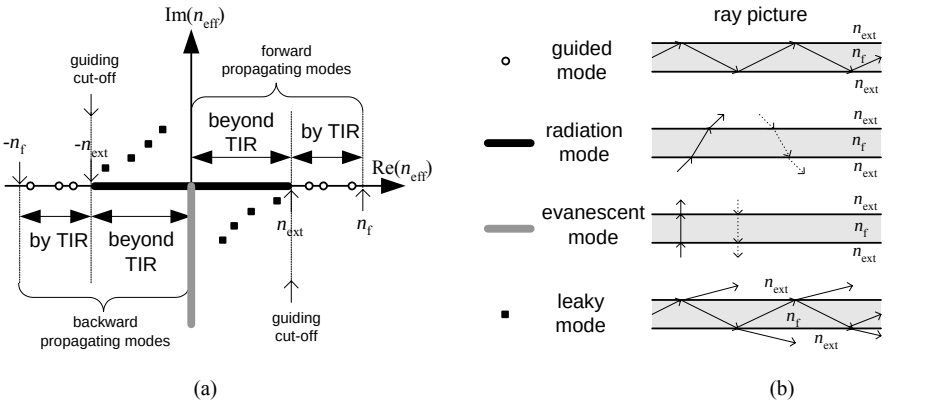

Figure 1.1. *Illustration on the modes of a step-index 3-layer symmetric planar waveguide by (a). the location of their effective indices in the complex plane and (b). ray picture.*

Table 1.1. *The properties of forward propagating modes in a step-index 3-layer planar waveguide.*

Mode	n_{eff}=Re(n_{eff})+jIm(n_{eff})	$k_{t,ext}$	Outward field dependence in substrate/cladding $\varphi_{0,ext}(\lvert x\rvert)$	Forward field dependence in z-direction exp(-$jk_0n_{eff}z$)
Guided	real, n_{ext}<Re(n_{eff})<n_f	imaginary	decaying	oscillatory
Radiation	real, 0<Re(n_{eff})<n_{ext}	real	oscillatory	oscillatory
Evanescent	imaginary, Im(n_{eff})<0	real	oscillatory	decaying
Leaky	complex, 0<Re(n_{eff})<n_{ext} Im(n_{eff})<0	complex	oscillatory with growing envelope	oscillatory with decaying envelope

For time-harmonic solution with exp($j\omega t$) time dependence, for forward (z+) propagating modes (which will be considered in the rest of this section), within layer i, we can have field solution ansatz of the wave-equation as follows.

$$\varphi_i = \varphi_{0,i}(x)\exp\left[\, j\left(\omega t - k_0 n_{eff}\, z\right)\right] \tag{1.1}$$

with

$$\varphi_{0,i}(x) = \varphi_{1,i}\exp\left(jk_{t,i}x\right) + \varphi_{2,i}\exp\left(-jk_{t,i}x\right) \tag{1.2}$$

where $k_{t,i}$ denotes the transverse wave-number, while $\varphi_{1,i}$ and $\varphi_{2,i}$ are constants governed by the continuity condition at interfaces and field at x=+∞ and -∞. As for leaky modes we assume no light inflow from outermost layers, while for guided modes we consider only the decaying solutions, in these outermost layers, one of $\varphi_{1,ext}$ and $\varphi_{2,ext}$ is zero for these two types of modes. In a homogeneous outermost layer, the transverse wavenumber in that region is

$$k_{t,ext} = k_0\sqrt{n_{ext}^2 - n_{eff}^2} \tag{1.3}$$

Note that, only solution with one sign of the square root is required, as solution with the other sign has been included by writing φ_0 into two terms with different sign in their exponent term in eq. (1.2).

1.2.1. Guided modes

If the value of n_{eff} is real and located between n_{ext} and n_f, we will have lossless propagation with light being confined within the core layer. The field in the substrate/cladding will have an exponentially decaying profile since $k_{t,ext}$ is imaginary and one of φ_1 and φ_2 is zero due to no field at x=+∞ and -∞ assumption. These modes are called guided modes, which in ray picture can be considered to be governed by the total internal reflection (TIR) principle. These modes are discrete as only those that fulfill the transverse resonant conditions can produce constructive interference, and are hence localized within the core.

1.2.2. Radiation and evanescent modes

Beyond the TIR, we will have a continuum of radiation modes, which has real-valued n_{eff} smaller than n_{ext}. In the ray picture, they can be considered as rays coming from outside of the core, which can't contribute to the guided mode, but will partly pass through the core and partly be reflected. These modes will have real-valued $k_{t,ext}$, hence will have an oscillatory profile in the substrate/cladding region. A special kind of radiation modes with a ray direction perpendicular to the waveguide material-interface planes is called the evanescent mode [1], as its field profile in the z-direction will be evanescently decaying. This mode will have an imaginary-valued effective index. Guided, radiation, and evanescent modes form a complete orthogonal set, based on which an arbitrary field profile can be decomposed [15].

1.2.3. Leaky modes

Leaky modes are the discrete complex solutions of the wave equation beyond cut-off, beyond the TIR operation region [15]. For forward propagating modes, the real part of their effective index [Re(n_{eff})] will be positive, while the imaginary part [Im(n_{eff})] will be negative, indicating the presence of loss. This so-called confinement or leakage loss should be interpreted as the leakage of energy outward from the core layer. As consequence, this value will lead to $k_{t,ext}$ which can only be located within the 1st and 3rd quadrants in the complex plane as can be seen by inspecting eq. (1.3). This will lead to an oscillatory field profile [due to the Re($k_{t,ext}$)] but with growing envelope [due to the Im($k_{t,ext}$) with the same sign as the Re($k_{t,ext}$)] in the substrate/cladding region, if no light inflow from the x=+∞ and -∞ is assumed. This growing envelope makes these modes to be unnormalizable, and hence they are often considered to be unphysical [15]. Nevertheless, these modes can be used to explain the working principles of prism coupling and various unconventional waveguiding structures, which will be introduced in the next section. As these modes should fulfill a transverse resonance condition, they are discrete.

1.3. "Guiding" light beyond the total internal reflection mechanism

This subsection introduces the advanced structures that use different mechanism than the traditional guided-wave structures to "guide"[1] light. Instead of exploiting the TIR principle, they use the anti-resonant reflection, the leaky defect-resonance, or the photonic bandgap mechanism to (quasi-)guide light. Although in their practical forms, structures based on these working principles exhibit inherent confinement losses, they are particularly interesting as they offer several unique properties unattainable by traditional structures. In integrated optics, they can be fabricated using low-cost, widely available semiconductor wafers as substrates together with the well-developed processing technologies available for them. For the fiber, they enable the use of only a single solid material, but opens up a larger degree of freedoms in designing, since the properties of the waveguides can be controlled by the size, shape, orientation, and arrangement of the microstructural air holes. Most of the structures exhibit unusual dispersion properties, which can be utilized for specific applications. They also enable the quasi-guiding of light in an air or liquid core, which opens up various new applications regarding very localized light-gas, light-liquid, or even light-particle interactions, both using fiber- or chip-based structures. In this thesis, structures based on these working principles will be considered as leaky-waves structures, hence they

[1] The quotation mark is used to denote that the structures being considered here do not work in the guided-mode regime but in the leaky mode regime. Hence, the term *quasi-guiding* is more appropriate than *guiding* light.

can be modeled using the leaky mode solver developed within the framework of this project.

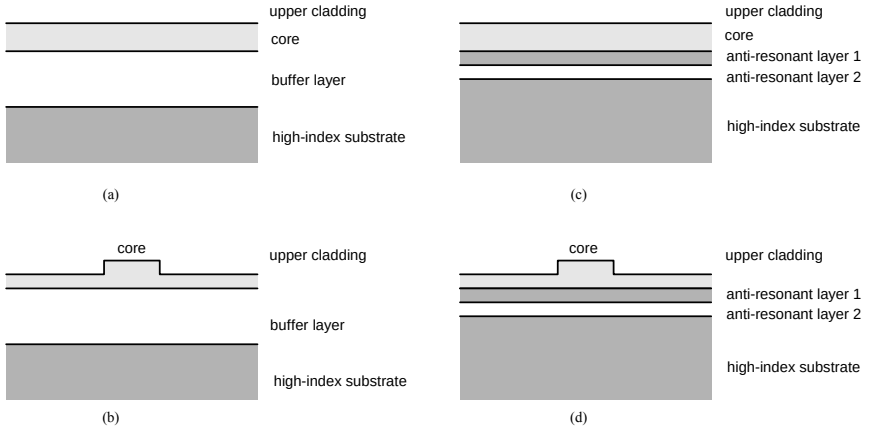

Figure 1.2. *(a). A planar and (b). a rib buffered leaky waveguide, where a low-index buffer layer suppresses the leakage into the high-index substrate. (c). A planar and (d) a rib ARROW where cladding layers operating in anti-resonant condition suppress the leakage of light from the waveguiding structure into the substrate.*

1.3.1. Solid-core waveguides

1.3.1.1. Buffered leaky waveguides

Optical waveguides made on a semiconductor substrate are widely used. They gain advantages from the wide availability of such substrates. Besides, they also share the well-developed processing technologies being used also by other disciplines, like the well-established microelectronics industry. Among others, are the waveguides made on the low-cost silicon substrate. Unfortunately, the refractive index of this substrate is high, while materials which are compatible with this substrate and suitable for guiding light, like silicon oxynitride, silicon nitride, or silica, have lower refractive index. One way to deal with this circumstance is by putting another lower refractive index material between the waveguiding structures and the high-index substrate as shown in Fig. 1.2.a-b. This so-called buffer layer acts as a buffer that isolates the light in the waveguiding structures from the substrate. These structures are apparently leaky, as the light prefers to travel into the high-index substrate. However, as already well known, if this layer is thick enough, the confinement loss of the structure can be small enough to allow functional integrated optical circuits to be built based on this approach [16]. For thick buffer-layer case, a guided-mode (or TIR-based) approximate analysis can be used to design this kind of structures by simply neglecting the existence of the

substrate. In Chapter 6, we will do a rigorous leaky-mode analysis of these structures and validate that approach, while figuring out the relationship between the thickness of the buffer layer, the refractive index of the high-index substrate, and the losses. Additionally, we also interpret various interesting phenomena found for this kind of structures using perturbation method.

1.3.1.2. ARROWs

A more advanced way to reduce the leakage of energy from the waveguiding structures into the high-index substrate is proposed by Duguay *et al.* [11] by putting a high and a low refractive index cladding layers of correct thicknesses between the waveguiding structures and the high-index substrate as illustrated in Fig. 1.2.c-d. These cladding layers behave as Fabry-Perot (anti-)resonators operating in the anti-resonant condition, hence exhibiting a very high reflection for the mode of interest, and suppressing the energy leakage into the high index substrate. Based on the way they quasi-guide light, these structures are called the *a*nti-*r*esonant *r*eflecting *o*ptical *w*aveguides (ARROWs). The thicknesses of the cladding layers are designed such that the corresponding layers lay in the anti-resonant condition for a transverse wavenumber as follows.

$$2k_{t,i}d_i = 2\pi\left(M + \tfrac{1}{2}\right) \tag{1.4}$$

where $k_{t,i}$ and d_i denote the transverse wavenumber and the thickness of cladding layer i, while M=0,1,2,… denotes the order of the anti-resonance. It is clear that in the design, this anti-resonant condition is associated with one mode (usually the fundamental TE mode) of interest only through the transverse wavenumber. For other higher order modes, these cladding layers are expected to operate not in the anti-resonant condition, hence exhibiting low reflection and consequently, high confinement loss. However, some higher order modes may still operate in the anti-resonant condition in one of the layers but might be not in the other one; hence, their overall anti-resonant condition is not optimal, leading to higher loss than the fundamental mode. Therefore, there is loss discrimination between modes, which allows the ARROW to be regarded as effectively single-moded if the difference of losses between the mode of interest and the higher order modes are large enough.

ARROWs have been widely used for various applications including sensors [17], splitters [18], spot-size converters [19], etc. Analytical approximate formulae for calculating the thickness of the anti-resonant layers and the losses of the fundamental mode [11, 20] are available and have been widely used. Besides, rigorous techniques to model ARROW are also available in the literature [21-22]. In this thesis, we will treat ARROWs as leaky structures, and use the developed numerical method to model and study them rigorously, including the anti-crossing phenomenon observed in their dispersion curves. Surprisingly, the concept of ARROWs, which is relatively simple, can be used to understand part of phenomena appears in the photonic bandgap fibers

[23]. In addition to solid core ARROWs, recently hollow-core ARROWs have also been proposed. These structures will be introduced in section 1.3.2.

1.3.1.3. High-index-core photonic crystal fibers

Photonic crystal fibers (PCFs) are fibers with a cladding composed of microstructural inclusions running parallel with the propagation axis. In general, the microstructural features are voids (air holes), but in principle, either solid [24] or liquid [25] microstructural features can also be realized. Fig. 1.3 illustrates some possible PCF structures. Since the idea originated from the use of 2-D photonic crystal to confine light within the core [2], they are popularly referred to as photonic crystal fibers. Unfortunately, later on the community realized, that not all of them work on the basis of the photonic band-gap principles. However, since the name was already widely used, people still keep the same name and add new names to distinguish specific classes of these fibers. Several alternate names have also been given by different research groups to these fibers; e.g. holey fibers, microstructured optical fibers, or crystal fibers. Despite of the existence of these diversity of names, in this thesis we will use the term *high-index-core PCF* to denote the fiber working on the basis of the leaky defect resonance[2] principles (Fig. 1.3.a-c) and *photonic bandgap fiber* (PBF) to denote the one based on the photonic bandgap principles (Fig. 1.3.d-f). One specific type of the PBF, which uses coaxial Bragg reflectors in the cladding will be called as *Bragg fiber* (Fig. 1.3.f). Meanwhile, the term *PCF* will be used as a universal name to denote all of them. We chose to use these terms as they are widely used by the community [3-5]. In general, high-index-core PCFs have a solid core, and PBFs have a hollow-core; but in principle, it is also possible to make a PBF with solid core or a leaky-defect-resonance PCF with a non-solid core.

Since the fabrication of the first PCF was demonstrated [2], they have attracted many scientific and commercial interest. Since they allow the use of only a single solid material, they relieve the engineer from the restriction caused by thermal/mechanical incompatibility of different solid materials. However, they allow a new way to engineer the fiber through their geometrical parameters; where the size, shape, orientation, position, and arrangement of the microstructural features are manipulated to tailor their properties. This way of engineering apparently offers more degrees of freedom to the designer. Many new properties unattainable through ordinary fibers can be obtained by this class of fibers. These include fibers with single-mode property over a wide wavelength range [26] while still offering a large mode field

[2]Although they are widely used in the literature, in this thesis we will avoid to use the terms *modified total internal reflection* or *index-guiding* to denote this quasi-guiding mechanism, as these terms lead to the notion of lossless guided modes. Instead, we will call this mechanism a *defect resonance,* which will be discussed in more detail in the next page.

diameter [27], zero-dispersion wavelength down to the visible wavelength [28], ultra-flat and ultra-low dispersion [29] or highly negative-dispersion [30] at long-wavelength telecommunication window, fibers with relatively high [31] or low [27] non-linearity, fibers with high birefringence but low temperature-sensitivity [32], etc.

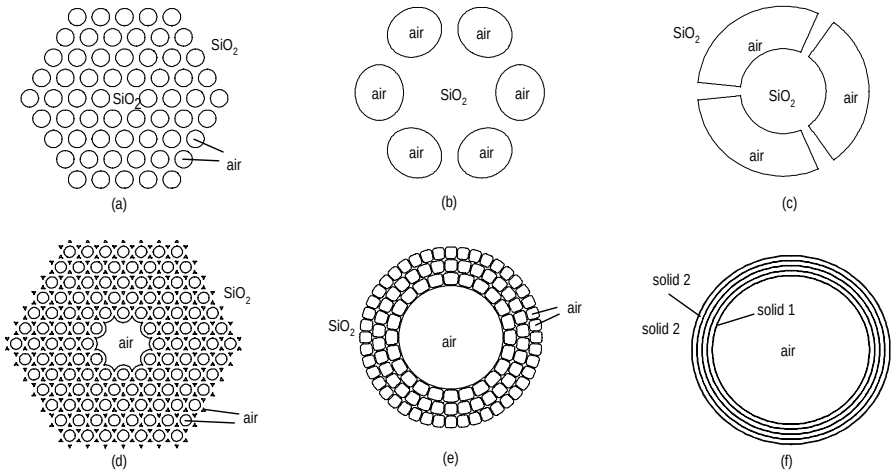

Figure 1.3. *Examples of cross-section of photonic crystal fibers with (a). high-index core with circular, (b). elliptical, and (c). annular-sector-shaped holes in the cladding; the photonic bandgap fibers with (d). circular and interstitial, (e). annular-sector-shaped holes in the cladding, and (f). the Bragg fiber.*

The simple model that is widely used to explain the light "guiding" mechanism in the high-index-core PCF is the so-called modified total internal reflection or the index-guiding model [3-5]. In this model, the presence of holes will lower the effective refractive index of the holey cladding, hence leads to an equivalent structure with a high-index core surrounded by a low-index cladding, which will guide light losslessly in a similar way as the ordinary fiber. However, the practical PCFs usually have limited size of holey cladding section, surrounded by a large section of uniform high-index outer cladding. Apparently, this situation will lead to a leaky structure. Therefore, in this thesis we will prevent to use the term modified total internal reflection or index-guiding, since they will lead to the notion of lossless guided modes. Instead, we will refer their quasi-guiding mechanism to the resonance mechanism. Within this picture, we can consider the holey section of the cladding together with the core as a kind of defect in the background of a uniform high-index outer cladding, hence can be simply considered as a resonance center, within which the light will be quasi-trapped. Therefore, we can simply call this quasi-guiding mechanism as a defect resonance, which is basically the same principle as the one that governs the truly guided-wave structures. In the PCF, since there is no TIR (which

would need a lower cladding than core index) and no perfect photonic bandgap (which would need a periodic structure extending to infinity) to prevent the leakage of light from the resonant center, we will also observe the presence of leakage or confinement loss. This quasi-guiding mechanism can be applied to understand both the high-index-core PCF and the PBF. In the light of this notion, it is very intuitive to understand the existence of the ordinary-fiber-like core modes, cladding- and core-cladding modes [33], and also the so-called surface modes [34] in the PBF. In this thesis the PCFs, regardless of either they utilized the bandgap effect or not, are handled as leaky-wave structures, and solved rigorously by the leaky-mode solver developed in the framework of this project. Hence, both the dispersion and confinement loss properties can be investigated.

1.3.2. Hollow-core waveguides

During recent years, the interest in (quasi-)guiding light in hollow-core structures is growing. Initially, their development was driven by the fact that glasses (or other solid materials suitable for making the fiber) available at that moment, are not transparent in some wavelength range, especially in the UV and mid/far IR regions. Besides, the emergence of high power lasers for industrial and medical applications requires a waveguide with a high damage threshold for power delivery applications. These requirements lead to the development of the hollow fiber [35-36], which is a fiber with a hollow core and reflective coating(s) at the inner wall. Thereafter, along with the development of the concept of guiding light with the photonic bandgap cladding [37], hollow-core fibers with more complicated cladding structures are developed [38-39]. Recently, similar concepts were also proposed for integrated optics by utilizing the ARROW and photonic-bandgap principles [13, 40-41]. Nowadays, the potential applications of hollow-core waveguides are not limited on exploiting the high-damage threshold of the hollow waveguides only, but also on the high linearity, low loss, and low dispersion of air. Besides, the possibility to fill the hole with gas, liquid, or even particles opens up new applications in the field of light-matter interactions.

1.3.2.1. Hollow-core photonic bandgap fibers

Basically, there are 2 groups of hollow-core fibers that utilize the photonic bandgap concept, which are the Bragg fibers and the holey-cladding PBFs. The Bragg fibers are as shown in Fig. 1.3.f. They incorporate 1-D periodic concentric layers of alternating high and low refractive indices which form a Bragg reflector as cladding [37]. For wavelengths located within the bandgap of this 1-D photonic crystal, modes within the core can't pass through the cladding, and hence are being trapped within the low-index core, which can be just a hollow core. A special type of Bragg fiber that uses an omni-directional reflector as cladding is known as the omni-guide fiber [42]. Besides having

the ability to guide light within the air core, the Bragg fibers are interesting since they exhibit lowest loss for TE_{01} mode [43], which is not the fundamental mode of the fiber. This property, which arises from the fact that TE reflection is higher than TM in thin film optics, makes this kind of fiber particularly interesting since the TE (and also TM) modes in fibers are non-degenerate modes. By exploiting the Brewster angle phenomenon, it is possible to design fibers, which are not only single-mode, but also single-(non-degenerate-)polarization, hence suitable to overcome the polarization mode dispersion (PMD) issues in high-speed fiber optic communications.

The holey-cladding PBFs are fibers with a cladding composed of transverse periodic structure in such a way that modes located within the bandgap of this 2-D photonic crystal can't pass through, hence will be trapped within the core (as the defect), which can be just an air core. Fig. 1.3.d-f depicts some examples of these fibers. The first hollow-core guidance by the 2-D photonic bandgap effect was demonstrated by Cregan *et al.* [38]. After that, various cladding structures have been proposed. Those, which exhibit promising results, are mostly with air holes of non-circular shapes in order to achieve the high air-filling fraction which is required to open a wide bandgap [44] in one hand and less surface modes in the other hand. Recently, an air core PBF with air holes in the cladding arranged in a circular arrangement has been demonstrated [45]. This fiber can be viewed as a marriage between the holey cladding PBF and the Bragg fiber.

As most part of the light is concentrated within the hollow core, the effect of the material loss in these structures is small. Hence, these fibers are expected to be able to surpass the lowest-loss limit of the ordinary fiber [3]. However, it is not easy to achieve low structural loss, which is mainly dominated by the scattering due to the fabrication imperfection and the existence of the highly leaky surface modes, which anti-cross with the core modes [46] and introduce extra loss for some wavelength regions, even in the bandgap. Meanwhile, various interesting applications have been demonstrated for these types of fibers, e.g. guiding particles through the air core [47], gas absorption spectroscopy [48], high power [49] and short pulses [50] delivery, gas nonlinear optics [51], etc.

In their practical forms, these fibers have a limited size of the periodic cladding structures. Most of them incorporate a large portion of uniform high index outer cladding in order to get good mechanical strength and size compatibility with the ordinary fiber. Hence, these fibers can also be considered as leaky structures. In this thesis, we will apply the leaky mode solver to study one of hollow-core fibers.

1.3.2.2. Hollow-core integrated optical waveguides

Although quasi-guiding light in low-index core has been employed in integrated optics since a long time ago (see section 1.3.1.1 and 1.3.1.2), the use of hollow core for integrated optics is still in its infancy at this moment. Some possible cross-sections for such structures are illustrated in Fig. 1.4. In general, these structures consist of a hollow core with reflective layer(s) at the inner wall. The reflective coating itself can be simply a metallic coating, or can also consist of dielectric layers, which are designed to give high reflection for the mode of interest (usually the fundamental mode), such that the power of this mode is trapped within the core. To get the expected high reflection, the ARROW principles and the omni-directional Bragg reflectors are used to design the layers.

In 2001, Miura *et al.*, demonstrated a hollow-core waveguiding in a metal coated groove made on a GaAs wafer [52]. Later on, the same group also demonstrated a hollow-core slab waveguide with other optical component(s) such as grating integrated on it [53]. Recently, more and more efforts have been put into air core channel integrated optical structures. Yin *et al.* employed a sacrificial layer to demonstrate hollow-core light guidance on a Si wafer as in Fig. 1.4.c. [13]. Campopiano *et al.* combined a large hollow-core waveguide with a microfluidic system to construct a liquid refractometric sensor [40].

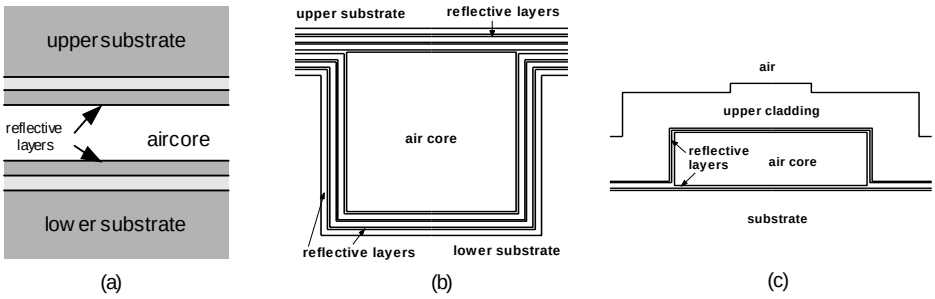

Figure 1.4. *Examples of cross-section of hollow-core integrated optical waveguides: (a). slab hollow-core waveguide, (b). channel hollow-core waveguide made by wafer bonding, and (c). by the employment of a sacrificial layer. The reflective layer(s) can be metallic or dielectric layers that apply anti-resonant or omni-directional reflection principles.*

Up to now, there are mainly 2 fabrication methods being used to realize these structures, i.e. the wafer bonding techniques and the use of a sacrificial layer. Due to the limitation of the fabrication technologies, the realized structures are usually not as complicated as the PBF. In general, the devices realized by some authors [13, 40]

exhibit rather high confinement loss and are hence usable for simple functionality only. However, once the advancement of the fabrication technologies enables the realization of more complicated structures, and low loss structures can be realized, we believe that this kind of structures would be very interesting, as they allow the integration of various functionalities into a compact chip.

1.4. Outline of the thesis

The organization of this thesis is illustrated schematically in Fig. 1.5. Chapter 1 and 2 are not shown in the diagram due to their introductory character. Chapter 1 gives a general perspective on the work and introduces the concept of quasi-guiding light in leaky structures being analyzed in substantial parts of this thesis. Chapter 2 introduces the basics of modal-based modeling of optical waveguides. The diagram clearly shows that this thesis starts with a study of planar problems and ends with focusing on structures with a 2-D cross-section. All considered structures are composed of either isotropic or anisotropic materials with diagonal permittivity tensor. In Chapter 3 and 4, we consider only guided-mode problems, while starting from Chapter 5, leaky-mode problems will also be considered. Within all schemes, special attention has been paid to the boundary conditions.

Chapter 3 describes a FDM scheme that takes into account both the smooth index gradient and the sharp index discontinuity in planar structures, hence it is suitable for the analysis of anisotropic planar waveguides with complicated refractive index profiles, like titanium-indiffused proton-exchange (TIPE) $LiNbO_3$ waveguides [54].

In Chapter 4, we describe a variational FEM scheme with TBCs on the basis of decaying basis functions adopted from the WKB method for the exterior domain, hence it is able to handle structures with graded-index inhomogeneous exterior domain. For a homogeneous exterior domain, it will give the same result as infinite elements by using the exact decaying basis functions for the exterior domain. Within the interior, by using Richardson-like extrapolation, the scheme was extended into a high-order scheme. We also combine the scheme with a semivectorial effective index method (EIM) and analyze indiffused channel waveguides made by using uniaxial crystals.

In Chapter 5, we introduce a high-order Galerkin FEM scheme that can handle both guided and leaky modes. Using this method, we also study an anti-resonant reflecting optical waveguide (ARROW).

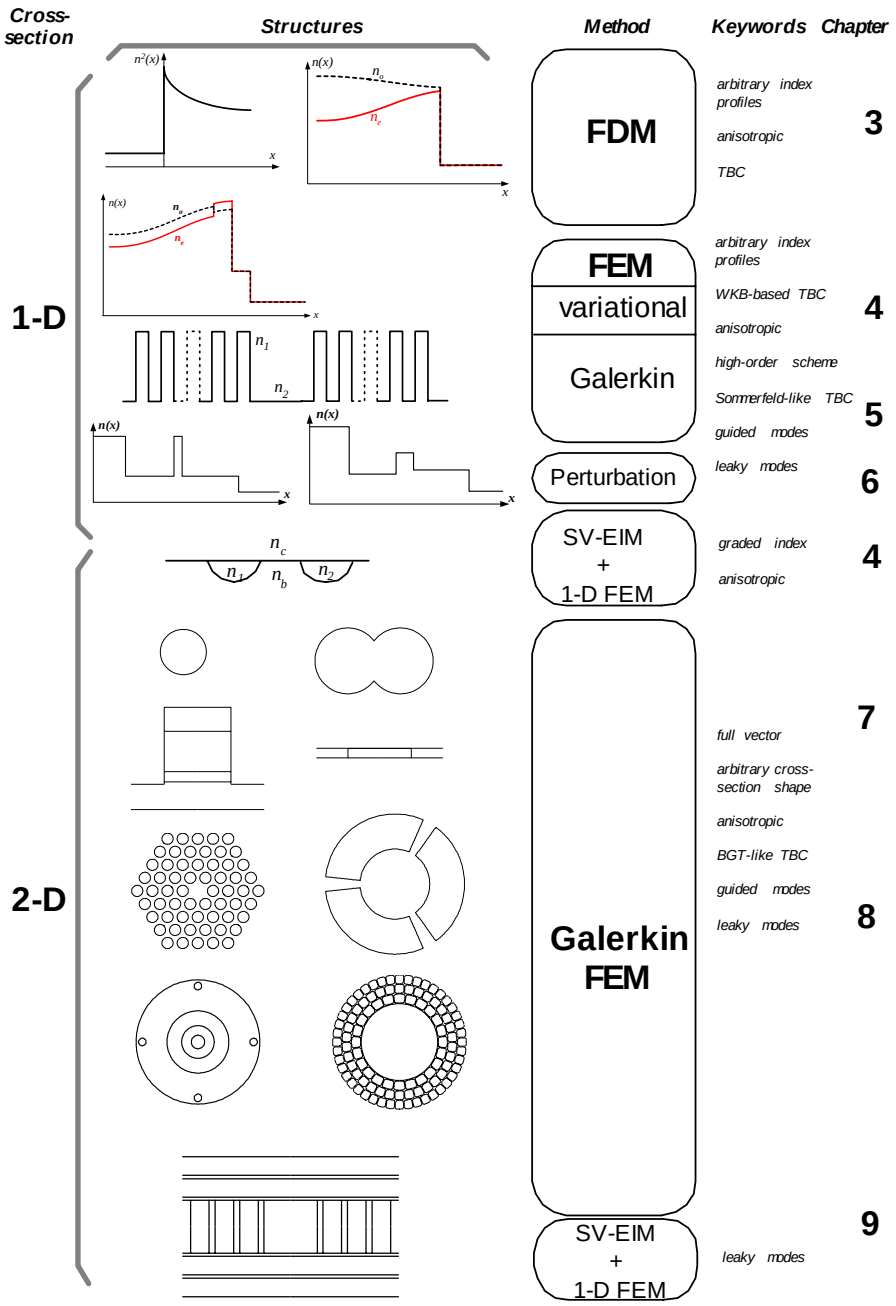

Figure 1.5. *Outline of the thesis: a diagram that shows the topics and related structures being considered within the chapters.*

Chapter 6 demonstrates the application of FEM scheme developed in Chapter 5 to rigorously study the leaky buffered waveguide. Additionally, approximate analytical expressions are derived using perturbation method and used to give some

insights about interesting phenomena regarding on the effect of buffer layer, refractive index of the high-index substrate/cladding, and degree of mode confinement to both the propagation constant and confinement loss.

Chapter 7 reports the formulation of a Galerkin FEM scheme furnished with TBCs that can calculate both guided and leaky modes of anisotropic structures with 2-D cross-section. The applications of the scheme to calculate modes of fiber and integrated optical waveguides will also be demonstrated. Chapter 8 deals with the application of the scheme for rigorous modeling of the photonic crystal fibers.

Chapter 9 reports the strategy of considering cladding anti-resonant bilayer material composition to pursue low-loss hollow-core integrated optical waveguides. The one dimensional Galerkin FEM leaky mode solver discussed in Chapter 5, together with a semivectorial EIM is used in the optimization of the bilayer thicknesses, while the vectorial FEM leaky mode solver discussed in Chapter 7 is used to verify the results.

This thesis ends with Summary and Outlook. Discussion on topics, which might be interested only for limited number of reader, are put in the appendixes.

References

1. T. Tamir *ed.*, *Guided-wave optoelectronics*, Springer Verlag, Berlin, 1990.
2. J.C. Knight *et al.*, "All-silica single-mode optical fiber with photonic crystal cladding," **Opt. Lett**., Vol. 21, No. 19, pp. 1547-1549, 1996.
3. P. Russell, "Photonic crystal fibers," **Science**, Vol. 299, No. 5605, pp. 358-362, 2003.
4. J.C. Knight, "Photonic crystal fibres," **Nature**, Vol. 424, No. 6950, pp. 847-851, 2003.
5. A. Bjarklev, J. Broeng, and A.S. Bjarklev, *Photonic Crystal Fibres*, Kluwer Academic Pub., Dordrecht, 2003.
6. B.J. Eggleton *et al.*, "Microstructured optical fiber devices," **Opt. Express**, Vol. 9, No. 13, pp. 698-713, 2001.
7. T.M. Monro and D.J. Richardson, "Holey optical fibres: fundamental properties and device applications," **C.R. Physique**, Vol. 4, No. 1, pp. 175-186, 2003.
8. http://www.blazephotonics.com
9. http://www.crystal-fibre.com
10. http://www.omni-guide.com

11. M.A. Duguay, Y. Kokubun, and T.L. Koch, "Antiresonant reflecting optical waveguides in SiO_2-Si multilayer structures," **Appl. Phys. Lett.**, Vol. 49, No. 1, pp. 13-15, 1986.

12. J. Moosburger *et al.*, "Nanofabrication of high quality photonic crystals for integrated optics circuits," **Nanotechnology**, Vol. 13, No. 3, pp. 341-345, 2002.

13. D. Yin *et al*., "Integrated ARROW waveguides with hollow cores," **Opt. Express**, Vol. 12, No. 12, pp. 2710-2715, 2004.

14. A. Suryanto, *Optical waves in inhomogeneous Kerr media beyond paraxial approximation*, thesis Univ. Twente, Twente Univ. Press, Enschede, 2003.

15. D. Marcuse, *Theory of dielectric optical waveguides*, Academic Press, New York, 1974.

16. R.M. de Ridder *et al.*, "Silicon oxynitride planar waveguiding structures for application in optical communication," **J. Sel. Topics in Quantum Electron.** Vol. 4, No. 6, pp. 930-937, 1998.

17. K. Benaissa and A. Nathan, "Silicon anti-resonant reflecting optical waveguides for sensor applications," **Sensors and Actuators A**, Vol. 65, No. 1, pp. 34-44, 1998.

18. J.M. Heaton *et al.*, "Novel 1-to-N way integrated optical beam splitters using symmetric mode mixing in GaAs/AlGaAs multimode waveguides," **Appl. Phys. Lett.**, Vol. 61, No. 15, pp. 1754-1756, 1992.

19. M. Galarza *et al.*, "1.55μm InP-InGaAsP Fabry-Perot lasers with integrated spot size converters using antiresonant reflecting optical waveguides," **Photonics Technol. Lett.**, Vol. 14, No. 8, pp. 1043-1045, 2002.

20. T. Baba and Y. Kokubun, "Dispersion and radiation loss characteristics of antiresonant reflecting optical waveguides - numerical results and analytical expressions," **J. Quantum Electron.** Vol. 28, No. 7, pp. 1689-1700, 1992.

21. W.P. Huang *et al.*, "The modal characteristics of ARROW structures," **J. Lightwave Technol.**, Vol. 10, No. 8, pp. 1015-1022, 1992.

22. C. Chen *et al.*, "Efficient and accurate numerical analysis of multilayer planar waveguides in lossy anisotropic media," **Opt. Express**, Vol. 7, No. 8, pp. 260-272, 2000.

23. N.M. Litchinitser *et al.*, "Application of ARROW model for designing tunable photonic devices," **Opt. Express**, Vol. 12, No. 8, pp. 1540-1550, 2004.

24. P.S. Westbrook *et al.*, "Cladding-mode resonances in hybrid polymer-silica microstructured optical fiber gratings," **Photonics Technol. Lett.**, Vol. 12, No. 5, pp. 495-497, 2000.

25. T.T. Larsen *et al.*, "Optical devices based on liquid crystal photonic bandgap fibres," **Opt. Express**, Vol. 11, No. 20, pp. 2589-2596, 2003.

26. T.A. Birks, J.C. Knight, and P. St. J. Russell, "Endlessly single-mode photonic crystal fiber," **Opt. Lett.**, Vol. 22, No. 13, pp. 961-963, 1997.

27. J.C. Knight *et al.*, "Large mode area photonic crystal fibre," **Electron. Lett.**, Vol. 34, No. 13, pp. 1347-1348, 1998.

28. J.C. Knight *et al.*, "Anomalous dispersion in photonic crystal fiber," **Photonics Technol. Lett.**, Vol. 12, No. 7, pp. 807-809, 2000.

29. W.H. Reeves *et al.*, "Demonstration of ultra-flattened dispersion in photonic crystal fibers," **Opt. Express**, Vol. 10, No. 14, pp. 609-613, 2002.

30. T.A. Birks *et al.*, "Dispersion compensation using single-material fibers," **Photonics Technol. Lett.**, Vol. 11, No. 6, pp. 674-676, 1999.

31. K.M. Kiang *et al.*, "Extruded singlemode non-silica glass holey optical fibres," **Electron. Lett.**, Vol. 38, No. 12, pp. 546-547, 2002.

32. A. Michie *et al.*, "Temperature independent highly birefringent photonic crystal fibre," **Opt. Express**, Vol. 12, No. 21, pp. 5160-5165, 2004.

33. H.P. Uranus, H.J.W.M. Hoekstra, and E. van Groesen, "Modes of an endlessly single-mode photonic crystal fiber: a finite element investigation," **Proc. Annual Symposium IEEE LEOS Benelux Chapter**, Ghent, 2-3 Dec. 2004.

34. J.A. West *et al.*, "Surface modes in air-core photonic band-gap fibers," **Opt. Express**, Vol. 12, No. 8, pp. 1485-1496, 2004.

35. J.A. Harrington, "A review of IR transmitting hollow waveguides," **Fiber and Integrated Optics**, Vol. 19, No. 3, pp. 211-227, 2000.

36. H. Jelinkova *et al.*, "Hollow waveguide delivery systems for laser technological application," **Prog. Quantum Electron.**, Vol. 28, pp. 145-164, 2004.

37. P. Yeh, A. Yariv, and E. Marom, "Theory of Bragg fiber," **J. Opt. Soc. Am.**, Vol. 68, No. 9, pp. 1196-1201, 1978.

38. R.F. Cregan *et al.*, "Single-mode photonic band gap guidance of light in air," **Scienc**e, Vol. 285, No. 5433, pp. 1537-1539, 1999.

39. Y. Fink *et al.*, "Guiding optical light in air using an all-dielectric structure," **J. Lightwave Technol.**, Vol. 17, No. 11, pp. 2039-2041, 1999.

40. S. Campopiano *et al.*, "Microfluidic sensor based on integrated optical hollow waveguides," **Opt. Lett.**, Vol. 29, No. 16, pp. 1894-1896, 2004.

41. Y. Yi *et al.,* "On-chip Si-based Bragg cladding waveguide with high index contrast bilayers," **Opt. Express**, Vol. 12, No. 20, pp. 4775-4780, 2004.

42. S.G. Johnson *et al.*, "Low-loss asymptotically single-mode propagation in large-core OmniGuide fibers," **Opt. Express**, Vol. 9, No. 13, pp. 748-779, 2001.

43. I.M. Bassett and A. Argyros, "Elimination of polarization degeneracy in round waveguides," **Opt. Express**, Vol. 10, No. 23, pp. 1342-1346, 2002.

44. N.A. Mortensen and M.D. Nielsen, "Modeling of realistic cladding structures for air-core photonic bandgap fibers," **Opt. Lett.**, Vol. 29, No. 4, pp. 349-351, 2004.

45. G. Vienne *et al.*, "First demonstration of air-silica Bragg fiber," post deadline paper PDP25, Optical Fiber Conf. 2004, Los Angeles, 22-27 Feb. 2004.

46. K. Saitoh, N.A. Mortensen, and M. Koshiba, "Air-core photonic band-gap fibers: the impact of surface modes," **Opt. Express**, Vol. 12, No. 3, pp. 394-400, 2004.

47. F. Benabid, J.C. Knight, and P. St. J. Russell, "Particle levitation and guidance in hollow-core photonic crystal fiber," **Opt. Express**, Vol. 10, No. 21, pp. 1195-1203, 2002.

48. T. Ritari *et al.*, "Gas sensing using air-guiding photonic bandgap fibers," **Opt. Express**, Vol. 12, No. 17, pp. 4080-4087, 2004.

49. B. Temelkuran *et al.*, "Wavelength-scalable hollow optical fibres with large photonic bandgaps for CO_2 laser transmission," **Nature**, Vol. 420, No. 6916, pp. 650-653, 2002.

50. G. Humbert *et al.*, "Hollow core photonic crystal fibers for beam delivery," **Opt. Express**, Vol. 12, No. 8, pp. 1477-1484, 2004.

51. F. Benabid *et al.*, "Stimulated Raman scattering in hydrogen-filled hollow-core photonic crystal fiber," **Science**, Vol. 298, No. 5592, pp. 399-402, 2002.

52. T. Miura *et al.*, "Hollow optical waveguide for temperature-insensitive photonic integrated circuits," **Jpn. J. Appl. Phys.**, Vol. 40, No. 7A, pp. L688-L690, 2001.

53. Y. Sakurai and F. Koyama, "Tunable hollow waveguide distributed Bragg reflectors with variable air core," **Opt. Express**, Vol. 12, No. 13, pp. 2851-2856, 2004.

54. M. de Micheli *et al.*, "Fabrication and characterization of titanium indiffused proton exchanged (TIPE) waveguides in lithium niobate," **Opt. Commun.**, Vol. 42, No. 2, pp. 101-103, 1982.

Chapter 2

Introduction to the modal analysis of optical waveguides

An introduction to the modal-based modeling of optical waveguides will be presented. Starting with Maxwell's equation, the governing equations will be introduced for vectorial, semivectorial, and scalar approaches. Then, a brief introduction to the finite difference, finite element, and effective index mode solver will be presented.

Introduction to the modal analysis of optical waveguides

This chapter is prepared as a brief introduction for reader who is not familiar with modal analysis of optical waveguides. It outlines the basic principles of the numerical methods for modal analysis, which will be treated in more details in the following chapters.

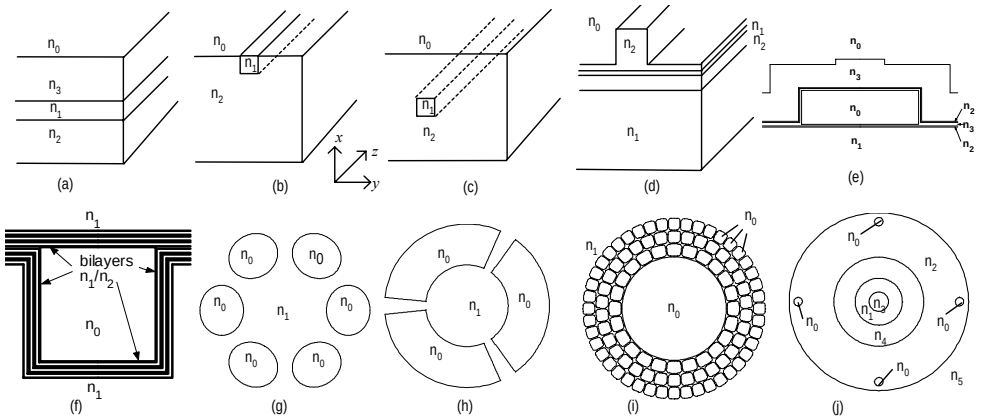

Figure 2.1. *Examples of various longitudinally-invariant optical waveguides: integrated-optic-based (a-f) and fiber-based (g-j). (a). Planar, (b). surface channel, (c). embedded channel, (d). rib anti-resonant waveguide, (e). & (f). hollow-core integrated optical waveguides, (g). & (h). solid-core photonic crystal fibers, (i). hollow-core photonic bandgap, fiber, and (j). hole-assisted multiring fiber. Typically:* $n_0=1$, $n_1>n_2>n_3>n_4>n_5>1$.

Many numerical techniques have been employed to analyze photonic devices [1]. For general structures with an inhomogeneous refractive index distribution in 2 (and sometimes 3) dimensional directions including the light propagation direction, modeling techniques like beam propagation method (BPM) [2], finite difference time domain (FDTD) [3], finite element method [4], bi- and quadri-directional eigenmode propagation method (BEP/QuEP) [5-6], and method of lines (MoL) [7] are widely used. Some of them, like BEP/QuEP and MoL use the modal solutions of longitudinally invariant structures, in one order lower in dimensionality, as the basis for solving the longitudinally variant structure. Besides, perturbative analytical methods also often use modal solutions of simplified structures as the basis for approximating the solution of more complicated structure. Therefore, the most fundamental information required in designing photonic devices, is the information on the modes that can propagate along a given longitudinally invariant structure. Some

examples of such structures are given in Fig. 2.1. This information includes the propagation constants and the shape of the modal fields. Based on that, additional information can be derived, e.g. overlap integrals (if the waveguide is excited with a given input field), coupling coefficients (for coupled structures), dispersion (a measure on how pulses will broaden as they travel in the waveguide), losses, etc. Hence, accurate and efficient calculation of modal solutions of longitudinally invariant structures is indispensable for many modeling activities. Mode solvers are tools being used to address the computation of modes. There are many techniques being employed for modal solving [8]. However, this chapter only introduces methods, which are used within this thesis. Firstly, Maxwell's equations are used to derive the governing equations for the waveguiding problem. Then, the finite difference, finite element, and effective index mode solvers will be introduced.

2.1. The governing equations

The analysis of optical waveguides starts with Maxwell's equations. By assuming, that the device is composed of source-free materials, these are given by

$$\nabla \times \vec{H} = \bar{\bar{\varepsilon}} \partial_t \vec{E} \tag{2.1}$$

$$\nabla \times \vec{E} = -\partial_t \vec{B} = -\bar{\bar{\mu}} \partial_t \vec{H} \tag{2.2}$$

$$\nabla \cdot \vec{D} = \nabla \cdot \bar{\bar{\varepsilon}} \vec{E} = 0 \tag{2.3}$$

$$\nabla \cdot \vec{B} = \nabla \cdot \bar{\bar{\mu}} \vec{H} = 0 \tag{2.4}$$

with $\vec{H}$ and $\vec{E}$ denoting the magnetic and electric field vectors, respectively; while $\bar{\bar{\mu}} = \mu_0 \bar{\bar{\mu}}_r$ and $\bar{\bar{\varepsilon}} = \varepsilon_0 \bar{\bar{\varepsilon}}_r$ the magnetic permeability and dielectric permittivity tensor, respectively, and $\partial_\eta \equiv \dfrac{\partial}{\partial \eta}$. For non-magnetic materials, most commonly used in integrated and fiber optical waveguides, $\bar{\bar{\mu}}_r$ is just an identity matrix, hence $\bar{\bar{\mu}}$ can be considered as a scalar constant μ_0. Within this thesis, we will consider only this class of materials. The relative dielectric permittivity tensor is related to the refractive indices of the materials. In a Cartesian coordinate system, for an anisotropic but non-magnetic material, $\bar{\bar{\varepsilon}}_r$ can be expressed as

$$\bar{\bar{\varepsilon}}_r = \begin{bmatrix} n_{xx}^2 & n_{xy}^2 & n_{xz}^2 \\ n_{yx}^2 & n_{yy}^2 & n_{yz}^2 \\ n_{zx}^2 & n_{zy}^2 & n_{zz}^2 \end{bmatrix} \tag{2.5}$$

which is normally a function of the spatial coordinates. If the axes of the waveguide coordinate system coincide with the principal axes of the material, all off-diagonal entries in eq. (2.5) will be 0, leading to a so-called anisotropic material with a diagonal permittivity tensor, a material which will be considered within most parts of this thesis. For isotropic materials, where the diagonal elements have the same value, $\bar{\bar{\varepsilon}}_r$ is just a scalar, n^2. If the material has optical non-linearity, this quantity is also a function of the

electric field itself. For lossless materials, this quantity is real, while for lossy materials, it has a complex value.

By using Maxwell's equations (2.1)-(2.4) for the time harmonic case (with exp[$j\omega t$] time dependence), we will get

$$\nabla \times \nabla \times \vec{E} = k_0^2 \overline{\overline{\varepsilon}}_r \vec{E} \tag{2.6a}$$

or

$$\nabla^2 \vec{E} + k_0^2 \overline{\overline{\varepsilon}}_r \vec{E} = \nabla\left(\nabla \cdot \vec{E}\right) \tag{2.6b}$$

and

$$\nabla \times \overline{\overline{\varepsilon}}_r^{-1} \nabla \times \vec{H} = k_0^2 \vec{H} \tag{2.7}$$

which are the full vectorial wave-equations for general waveguiding problems, where $k_0 = \frac{\omega}{c} = \frac{2\pi}{\lambda}$ denotes the free space wave-number, with λ the free space wavelength. For structures composed of isotropic materials, these equations can be simplified to

$$\nabla^2 \vec{E} + k_0^2 n^2 \vec{E} = -\nabla\left(\vec{E} \cdot \frac{\nabla n^2}{n^2}\right) \tag{2.8}$$

and

$$\nabla^2 \vec{H} + k_0^2 n^2 \vec{H} = -\frac{\nabla n^2}{n^2} \times \left(\nabla \times \vec{H}\right) \tag{2.9}$$

The right hand terms will make these equations to be coupled partial differential equations (p.d.e.), meaning that all components of the (vectorial) fields depend on the others.

For longitudinally invariant structures, i.e. structures for which the refractive index is only a function of the transverse coordinates *x* and *y*, one may look for modal field solutions of forward propagating modes in the form of

$$\vec{E}(x, y, z, t) = \vec{E}_t(x, y) e^{-j\beta z} e^{j\omega t} \tag{2.10a}$$

and

$$\vec{H}(x, y, z, t) = \vec{H}_t(x, y) e^{-j\beta z} e^{j\omega t} \tag{2.10b}$$

where the *z*-dependence of the field is defined by the propagation constant $\beta \equiv k_0 n_{eff}$. The quantity n_{eff} is called the effective refractive index or modal index, or simply the effective index. For lossy and leaky waveguides, where attenuation exists due to the material being employed and the nature of the structure, respectively, the propagation constant becomes complex, whereby its imaginary part is a measure for the loss and the real part for the phase velocity. Substituting ansatz (2.10) into (2.8) and (2.9), results in the vectorial wave equations for waveguides with 2-D cross sectional geometry as follows

$$\nabla_t^2 \vec{E}_t + k_0^2 n^2 \vec{E}_t - \beta^2 \vec{E}_t = -\nabla_t \left(\vec{E}_t \cdot \frac{\nabla_t n^2}{n^2}\right) \tag{2.11a}$$

and

$$\nabla_t^2 \vec{H}_t + k_0^2 n^2 \vec{H}_t - \beta^2 \vec{H}_t = -\frac{1}{n^2}\begin{bmatrix} \left(\partial_y n^2\right)\left(\partial_x H_y - \partial_y H_x\right) \\ -\left(\partial_x n^2\right)\left(\partial_x H_y - \partial_y H_x\right) \end{bmatrix} \tag{2.11b}$$

with $\nabla_t^2 \equiv \partial_{xx} + \partial_{yy}$, $\nabla_t \equiv \left[\partial_x, \partial_y\right]^T$, $\vec{E}_t = \left[E_x, E_y\right]^T$, $\vec{H}_t = \left[H_x, H_y\right]^T$, and $\partial_{\eta\eta} \equiv \dfrac{\partial^2}{\partial \eta^2}$. For a structure with a very small index gradient in one direction (say, the y direction), e.g. a channel waveguide with very low lateral index contrast (Fig. 2.1.b with $n_1 \approx n_2$) the gradient of the refractive index for that direction can sometimes be neglected, which leads to a semivectorial wave equation for respective structure as follows

$$\partial_x\left[\frac{1}{n^2}\partial_x\left(n^2 E_x\right)\right] + \partial_{yy}E_x + k_0^2 n^2 E_x - \beta^2 E_x = 0 \tag{2.12a}$$

for quasi-TM modes, and

$$\partial_{xx}H_x + \partial_{yy}H_x + k_0^2 n^2 H_x - \beta^2 H_x = 0 \tag{2.12b}$$

for quasi-TE modes. Another semivectorial formulation can also be obtained by assuming that the electric field propagating in the waveguide is linearly polarized and parallel to only one of the transverse coordinate [9], which will give the same equation as (2.12a) for quasi-TM modes and

$$\partial_{xx}E_y + \partial_y\left[\frac{1}{n^2}\partial_y\left(n^2 E_y\right)\right] + k_0^2 n^2 E_y - \beta^2 E_y = 0 \tag{2.12c}$$

for quasi-TE modes. The latter semivectorial approach can also be applied to the H-field, which leads to

$$\partial_x\left[\frac{1}{n^2}\partial_x H_y\right] + \frac{1}{n^2}\partial_{yy}H_y + k_0^2 H_y - \frac{\beta^2}{n^2}H_y = 0 \tag{2.12d}$$

for quasi-TM modes, and

$$\frac{1}{n^2}\partial_{xx}H_x + \partial_y\left[\frac{1}{n^2}\partial_y H_x\right] + k_0^2 H_x - \frac{\beta^2}{n^2}H_x = 0 \tag{2.12e}$$

for quasi-TE modes. It is obvious from these expressions, that the semivectorial wave equation is not a coupled p.d.e. anymore, hence it can easier be solved. For structures with very small index contrast in both transverse directions, the whole gradient of the refractive index term can sometimes be neglected, leading to a scalar wave equation as follows

$$\partial_{xx}\varphi + \partial_{yy}\varphi + k_0^2 n^2 \varphi - \beta^2 \varphi = 0 \tag{2.13}$$

where φ represents any one of E_x, E_y, E_z, H_x, H_y, or H_z.

For planar structures (Fig. 2.1.a), since the refractive index is only a function of x, the components of the vectorial wave equations become uncoupled if it is assumed that there is no y-dependence of the field solutions, hence the wave equations can be expressed in a scalar form as

$$d_{xx}E_y + k_0^2 n^2 E_y - \beta^2 E_y = 0 \tag{2.14}$$

for TE-modes, and

$$d_x\left(\frac{1}{n^2} d_x H_y\right) + k_0^2 H_y - \beta^2 \frac{1}{n^2} H_y = 0 \tag{2.15}$$

for TM-modes, with $d_x \equiv \frac{d}{dx}$ and $d_{xx} \equiv \frac{d^2}{dx^2}$.

2.2. Introduction to methods for modal analysis

In mode-solving analysis, the values of β or n_{eff} and the corresponding electric or magnetic fields are to be determined by solving the governing wave-equation, which is practically an eigenvalue problem. One way to solve it numerically, is by translating the p.d.e./o.d.e. into a system of algebraic equations through discretizations, hence the problem becomes a matrix eigenvalue problem with β^2 or $n_{\text{eff}}{}^2$ as the eigenvalue and the corresponding modal field as the eigenvector. The numerical methods developed within this work are based on this approach. In this subsection, we will briefly introduce these numerical methods, i.e. finite difference method (FDM) and finite element method (FEM), which will be used in other chapters of this thesis. For simplicity, we will initially consider structures with 1-D cross-section to illustrate the methods. Later on, we will also briefly show the extension into 2-D cross sectional problem by using the FEM and the effective index method. Methods, which are not employed within this thesis, and methods which are already well-known (like the transfer matrix method) will not be treated in this section.

2.2.1. Finite difference method

The FDM is based on approximating the differential operator acting on the field function within the governing p.d.e or o.d.e. by the difference operator acting on the value of that field function at a finite number of points known as nodal or grid points. The process involves restricting the area of interest into a finite-sized domain, referred to as the computational domain, subdividing the computational domain into many nodes, expressing the field value (and their derivatives) at each node as an expansion of the field values (and their derivatives) at other nodes, and derives the difference operators from there. This discretization is illustrated in Fig. 2.2 for a simple waveguiding problem.

Suppose the field function $\varphi(x)$ is as shown in Fig. 2.2.a. Defining the computational domain Ω and discretizing it will lead to Fig. 2.2.b. If the field and its derivatives are assumed to be continuous, it is possible to use Taylor's expansion to express field at particular grid points j-1 and j+1 as an expansion of the field (and their derivatives) at their neighbor grid point j as follows.

$$\varphi_{j-1} = \varphi_j - \Delta x \;\; d_x\varphi_j + \frac{\Delta x^2}{2!} d_{xx}\varphi_j - \frac{\Delta x^3}{3!} d_{xxx}\varphi_j + \frac{\Delta x^4}{4!} d_{xxxx}\varphi_j + \ldots \tag{2.16}$$

$$\varphi_{j+1} = \varphi_j + \Delta x \;\; d_x\varphi_j + \frac{\Delta x^2}{2!} d_{xx}\varphi_j + \frac{\Delta x^3}{3!} d_{xxx}\varphi_j + \frac{\Delta x^4}{4!} d_{xxxx}\varphi_j + \ldots \tag{2.17}$$

where $\varphi_j \equiv \varphi\left(x_j\right)$. From eq. (2.16) and (2.17) we obtain

$$d_x\varphi_j = \frac{\varphi_{j+1} - \varphi_{j-1}}{2\Delta x} + O\left(\Delta x^2\right) \tag{2.18}$$

$$d_{xx}\varphi_j = \frac{\varphi_{j-1} - 2\varphi_j + \varphi_{j+1}}{\Delta x^2} + O\left(\Delta x^2\right) \tag{2.19}$$

Hence, $d_x\varphi_j$, the first derivative operator acting on the (continuous) field at grid point j can be approximated by a difference operator $\hat{d}_x\varphi_j \equiv \frac{\varphi_{j+1} - \varphi_{j-1}}{2\Delta x}$. Similarly, $d_{xx}\varphi_j$ can be approximated by $\hat{d}_{xx}\varphi_j \equiv \frac{\varphi_{j-1} - 2\varphi_j + \varphi_{j+1}}{\Delta x^2}$. The term $O\left(\Delta x^2\right)$ in eqs. (2.18) and (2.19) indicates that there is an error induced by the truncation of the series expansion, which depends quadratically on the discretization size or mesh size Δx. By reducing the mesh size, we will reduce this error and hence get a higher accuracy. It is also possible to use more terms in the Taylor's expansion and take more grid points in the neighborhood of the node to obtain a higher order scheme, which also leads to higher accuracy for the same mesh size. It may be clear, that the expansions (2.16) and (2.17) could only be carried out if the field and its derivatives which taken into account are continuous in the neighborhood of those grid points. At refractive index discontinuities, this condition does not hold anymore; hence, corrections should be made onto the finite difference (FD) formulae at grid points in the neighborhood of the interfaces. It is also clear that modification to the FD formulae are also needed to be carried out for the grid points located at the computational boundaries as the field value(s) in one (or more) neighboring grid point(s) is (are) not defined.

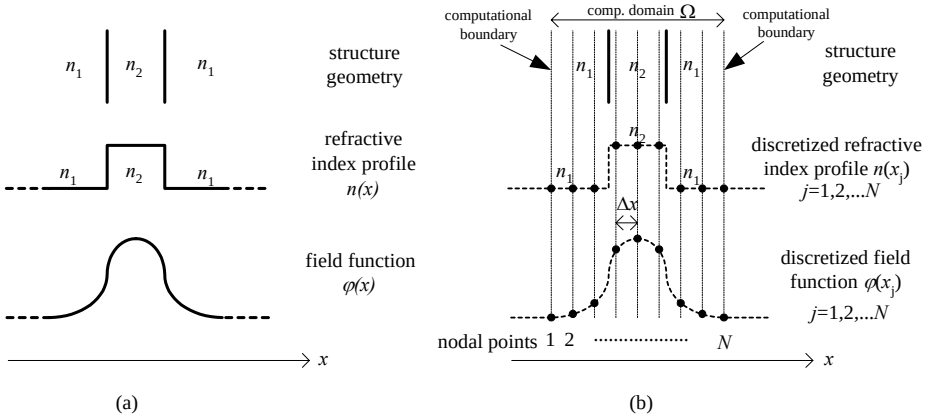

Figure 2.2. *Illustration on the discretization in FDM.*

Applying the FD approximation onto the modal field equation [e.g. eq. (2.14)] discussed in the previous section, leads to a matrix eigenvalue equation $\left(\mathbf{A}-\beta^2\mathbf{I}\right)\{\varphi\}=\mathbf{0}$ where $\mathbf{I}$ is the identity matrix, $\{\varphi\}$ is a column vector representing the fields at the grid points, while $\mathbf{A}$ is a matrix coming out from the difference equation and the discretization of the second term in eq. (2.14). Since one grid point is only related to its two neighbors for the 2nd-order FD formula for the 1-D problem, the matrix $\mathbf{A}$ will be a sparse tridiagonal matrix. For the 2-D problem, if a regular rectangular mesh is used, the matrix $\mathbf{A}$ can be as simple as a matrix with non-zero entries at only five diagonals, if a simple 5-point stencil is employed. Hence, the advantages of FDM are its relatively simple formulation and nice matrix structure, which can be solved easily. However, the necessity to incorporate interface corrections makes it rather intricate for higher order extension. The use of a regular rectangular mesh is somehow inconvenient for 2-D structures with a complicated cross-sectional geometry. A semi-irregular triangular mesh [10] has also been proposed for FDM, but at the expense of loosing its ease of formulation and nice matrix structure. A highly accurate FDM scheme [11] has also been proposed, but its formulation involves the computation of analytic Bessel function, and such accuracy is attained only for step-index waveguides with no more than horizontal and vertical interfaces, which fit well to the rectangular mesh. However, since the FDM is generally cheaper than FEM, it is still an interesting choice for large problems.

2.2.2. Finite element method

The FEM is based on approximating the function, which is the exact solution of the governing p.d.e./o.d.e. by an approximate function, which is obtained through an equivalent functional in a discretized domain. In the variational (Rayleigh-Ritz) FEM, the solution is approximated by the extremum function of a functional. The Euler-Lagrange equation (i.e. a differential equation derived from the stationary condition $\delta F=0$) of that functional (F) corresponds to the governing p.d.e./o.d.e. For example, for modal field equation (2.14), the corresponding functional is

$$F=\frac{1}{2}\int_{\Omega}\left[-\left(d_x\varphi\right)^2+\left(k_0^2n^2-\beta^2\right)\varphi^2\right]dx+b.t. \tag{2.20}$$

where *b.t.* denotes the boundary term, and φ has been used to replace E_y for simplicity. The function is then approximated by interpolation in terms of the basis functions (normally polynomials) within each discretized subdomain, which is also known as the element.

For example, as illustrated in Fig. 2.3., using the first order polynomial (linear) basis functions

$$N_1 = 1 - \frac{x}{\Delta x} \tag{2.21.a}$$

and

$$N_2 = \frac{x}{\Delta x} \tag{2.21.b}$$

where x is the local coordinate within the corresponding element, the subscript is the local node number, and Δx is the mesh size, the approximation within each element is

$$\varphi_e(x) \approx \tilde{\varphi}_e(x) = \sum_{i=1}^{2} N_{i,e}\varphi_{i,e} \tag{2.22}$$

where the subscript e has been added to denote the element number e. The basis functions N_1 and N_2 are also known as the shape functions. Note that the interpolation coefficients or the unknown parameters $\varphi_{i,e}$ are the values of the field at the corresponding nodal points. By plugging in the approximation (2.22) into (2.20) for the discretized domain, composed of a finite number of elements, we will get an approximate discretized functional $\tilde{F}$, for which the extremum function can be found by

$$\nabla\tilde{F} = \left[\frac{\partial\tilde{F}}{\partial\varphi_1}, \ldots, \frac{\partial\tilde{F}}{\partial\varphi_N}\right]^T = [0, \ldots, 0]^T \tag{2.23}$$

where the subscripts denote global node number. Equation (2.23) produces a matrix generalized eigenvalue equation of the form

$$\left(\mathbf{A} - \beta^2\mathbf{B}\right)\{\varphi\} = \mathbf{0} \tag{2.24}$$

with the eigenvalue corresponding to the propagation constant of the modes and the eigenvector $\{\varphi\}$, a column vector representing the discretized extremum function of the discretized functional as the approximation to the modal field function of the corresponding mode at the nodal points. Approximate modal field value at every point within the computational domain can then be obtained through the interpolation (2.22).

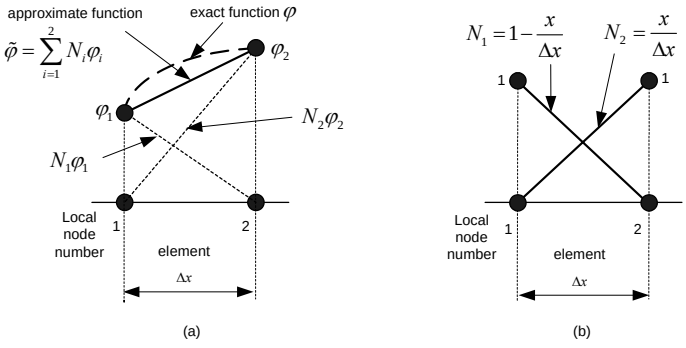

Figure 2.3. *Illustration on (a). approximating the exact function with interpolation in terms of (b). shape functions in FEM. Linear shape functions are employed in this illustration. For notational simplicity, local coordinate and node number have been used.*

Another finite element approach is the Galerkin FEM, which is based on the weighted residual method. In this method, the solution is obtained by seeking for approximate function that produces the least weighted residual of the p.d.e./o.d.e. over the whole domain Ω as follows.

$$R = \int_{\Omega} w\left(\mathcal{D}\tilde{\varphi} - \mathcal{D}\varphi\right) d\Omega = 0 \tag{2.25}$$

where R, w, $\mathcal{D}$, φ, and $\tilde{\varphi}$ denoting the weighted residual, the weight function, the operator of the governing p.d.e./o.d.e., the exact field function, and the approximate field function, respectively. For the modal field equation (2.14) this weighted residual can be written as

$$\int_{\Omega} w\left(d_{xx}\tilde{\varphi} + k_0^2 n^2 \tilde{\varphi} - \beta^2 \tilde{\varphi}\right) dx = 0 \tag{2.26.a}$$

which can further be written in a weak form as

$$\int_{\Omega} \left[-\left(d_x w\right)\left(d_x \tilde{\varphi}\right) + k_0^2 n^2 w\tilde{\varphi} - \beta^2 w\tilde{\varphi} \right] dx + w d_x \tilde{\varphi}\Big|_{\partial\Omega 1}^{\partial\Omega 2} = 0 \tag{2.26.b}$$

where, again the approximate electric field function $\tilde{E}_y$ has been replaced by $\tilde{\varphi}$ for notational simplicity. In this equation $\partial\Omega$ denotes the computational boundary. In Galerkin FEM, which is a variant of the weighted residual method, within each element, the exact function is approximated by interpolation in terms of the shape functions as in eq. (2.22), while the basis functions have been taken as the weight function. Plugging these into the weak formulation leads to a matrix generalized eigenvalue equation as in (2.24). For the same problem, Galerkin FEM will lead to the same matrices as the variational FEM. However, the Galerkin FEM can handle problems with non-self-adjoint operators, for which the variational formulation is not applicable, since it is not possible to construct corresponding functional for such problems.

It can be shown, that the error induced by the approximation in FEM depends on the size of the mesh and the order of the polynomial basis functions. Finer mesh or higher order basis functions will produce a smaller error.

For waveguides with 2-D cross-sectional geometry, meshes with 2-D elements have to be employed. Among others, the most common one is the unstructured triangular element, where elements in the shape of triangles of different sizes and orientations are arranged to fit the structure as in Fig. 2.4.a. As has been discussed in section 2.1, for these kinds of waveguides, the governing wave-equations are in general coupled p.d.e., which can be reduced to the uncoupled semivectorial or scalar equations only for very special cases. To deal with this, we can use basis functions, which are already vectorial basis functions in the so-called edge-element approach [12], or use the vectorial unknown parameters with still scalar polynomial

basis functions in the so-called nodal-based element. For simplicity reason, we have chosen the latter approach. For a formulation based on the transverse components of the magnetic field (H_x and H_y), using the second order polynomial (quadratic) basis functions, as will be done within this thesis, the discretization and basis functions are illustrated in Fig. 2.4. In this figure, $L_{m,nD}$ denotes the linear basis function m for n dimensional element, while $N_{m,nD}$ denotes the quadratic basis function m for n dimensional element, with m denoting the local node number. Using this element, we need 6 nodal points for each triangular element and a vectorial unknown consists of 2 vector elements for each nodal point. Since the formulation uses magnetic fields, we can take advantage from the continuity of the magnetic field at interfaces between non-magnetic materials, hence we only require basis functions that preserve the continuity of the function at the nodal points. Nodal-based element with this requirement is called Lagrange element. More advanced element like the isoparametric triangular element with a mix of nodal and edge basis functions [13] also exists in the literature. This element can be used for either H- or E-field formulation (hence more handy to tackle structures with non-linear materials) and handle curved interfaces in a better way, but in general it will lead to more unknowns, hence will produce a larger matrix size than the ordinary triangular nodal-based element. However, this type of element is beyond the scope of this thesis.

As explained earlier, the FEM can handle the vectorial wave-equation transparently, hence it is suitable for a waveguiding structure with high index-contrast. Besides, the elements can also easily fit to tilted and curved interfaces, leading to a straightforward treatment of realistic geometry of material discontinuities and transparent way to handle interface conditions. We can also apply finer meshes within areas which need that (e.g. if the field changes rapidly or the microstructure gets finer) in order to efficiently reduce the error. Hence, the FEM is very suitable for handling structures with a complicated geometry. As will be shown in Chapter 7, by properly handling the field at the computational boundaries, we can also deal with leaky modes. These entire features suit the requirements for modeling of advanced structures which quasi-guide light beyond the total internal reflection principles through the existence of many micrometer scale features as discussed in section 1.2. However, in general FEM is more expensive than FDM, as the irregular character of the mesh leads to the worse matrix structure (but still sparse). Also, the FEM matrix usually has more entries than FDM due to the larger number of neighboring elements induced by the mesh unstructureness. Additionally, the eigenvalue equation resulting from FEM is the generalized one. Nevertheless, the capability of FEM to handle complicated structures compensates this expense.

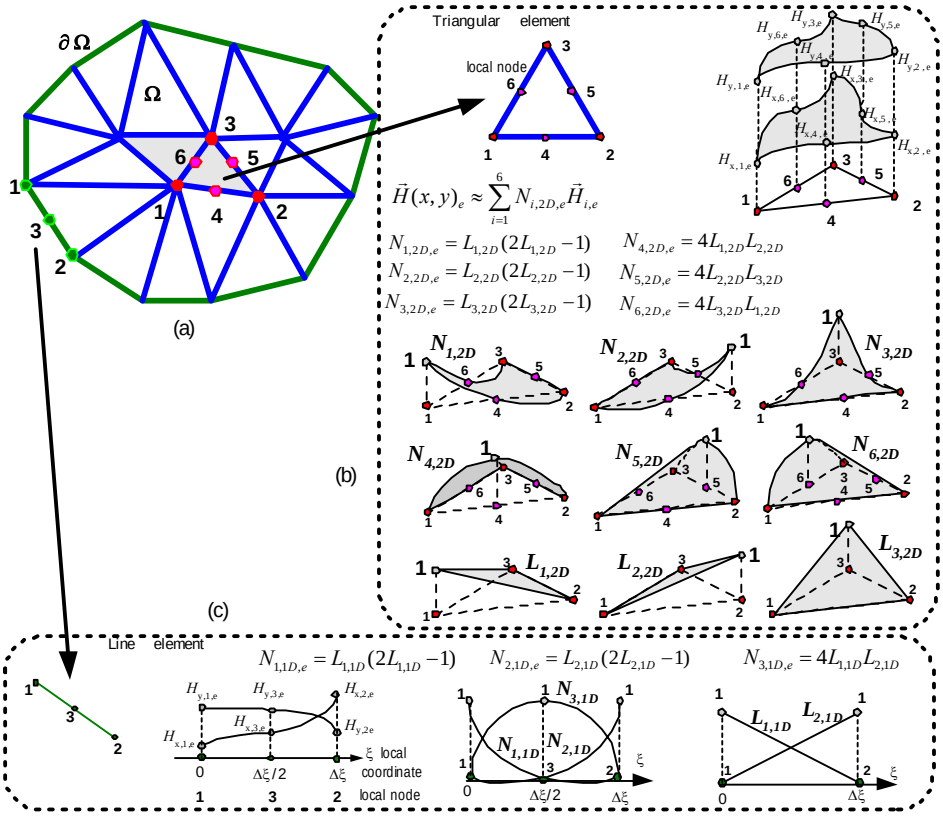

Figure 2.4. *Illustration on (a). a discretization in a structure with 2-D cross-section, which uses nodal-based (b). triangular element and (c). line element with quadratic basis functions. All node numbers in the picture are the local node numbers.*

2.2.3. Effective index method

Structures with 2-D cross-section are governed by 2-D p.d.e with an index profile and field solutions that are function of both transversal coordinates x and y. However, solving this type of equation is not always easy. Effective index method (EIM) [14] is an approximate way to deal with this equation by solving one-order lower dimensional problems successively.

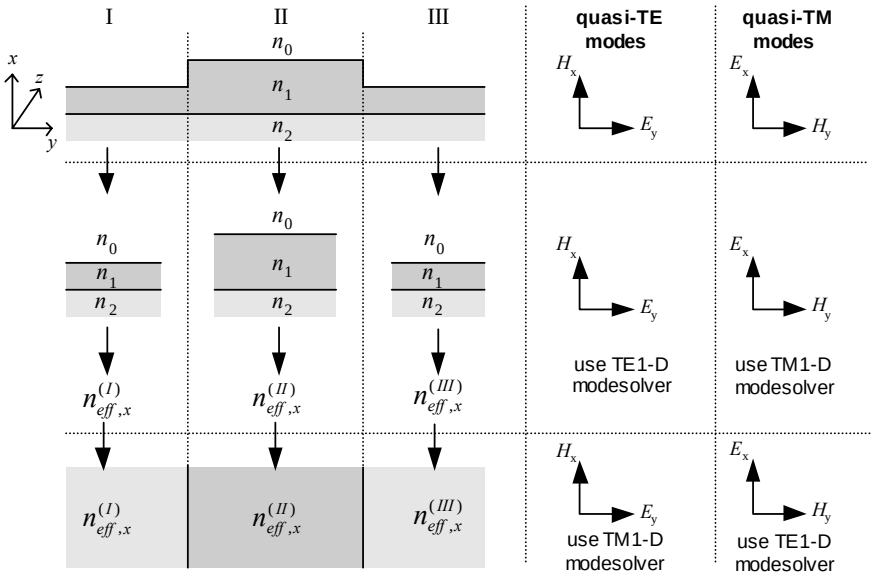

Figure 2.5. *Illustration of the semivectorial effective index method.*

The wave-equations that can be handled by the EIM are the scalar and the semivectorial wave-equations. Here, we will illustrate the use of the semivectorial (SV-) EIM for solving semivectorial wave-equation (2.12a) for quasi-TM modes for a rib structure as shown in Fig. 2.5. In order to be able to split eq. (2.12a) into two equations of reduced dimensionality, we assume that the modal field can be expressed in

$$E_x(x,y) = X(x,y)Y(y) \tag{2.27a}$$

with

$$\partial_y X \approx 0 \tag{2.27b}$$

Hence, eq. (2.12a) can be approximated by

$$\frac{1}{X}\partial_x\left[\frac{1}{n^2}\partial_x\left(n^2X\right)\right] + k_0^2 n^2 + \frac{1}{Y}\partial_{yy}Y - \beta^2 = 0 \tag{2.28}$$

For each constant $y=y_i$, we will have an x-dependent substructure, for which we can define constant $\beta_x^2(y_i) \equiv k_0^2 n_{eff,x}^2(y_i)$ which makes up the first-two terms in eq. (2.28) as follows.

$$\frac{1}{X(x,y_i)}d_x\left[\frac{1}{n^2(x,y_i)}d_x\left(n^2(x,y_i)X(x,y_i)\right)\right] + k_0^2 n^2(x,y_i) - \beta_x^2(y_i) = 0 \tag{2.29}$$

This equation can be further written as

$$d_x\left[\frac{1}{n^2(x,y_i)}d_x P(x,y_i)\right] + \left[k_0^2 - \frac{\beta_x^2(y_i)}{n^2(x,y_i)}\right]P(x,y_i) = 0 \tag{2.30a}$$

with

$$P(x, y_i) = n^2(x, y_i) X(x, y_i) \tag{2.30b}$$

Eq. (2.30a) has the same form of eq. (2.15). Besides, P also has the same interface continuity conditions as H_y for each x-dependent substructure. Hence eq. (2.30) can be solved for each $y=y_i$ using a 1-D TM mode solver to get $\beta_x^2(y)$. Then eq. (2.28) can be written as

$$d_{yy} Y(y) + \left[\beta_x^2(y) - \beta^2\right] Y(y) = 0 \tag{2.31}$$

which has the form of eq. (2.14) with corresponding interface continuity conditions. Hence, eq. (2.31) can be solved for a y-dependent equivalent structure using a 1-D TE mode solver to get the final β.

We can also use the SV-EIM to solve eq. (2.12c) approximately for quasi-TE modes, which results in solving the x-dependent substructures using 1-D TE mode solver and then use their results to form a y-dependent equivalent structure, which will be solved using a 1-D TM mode solver as illustrated in Fig. 2.5. However, the mathematical picture of this sequence is not as transparent as the quasi-TM case.

Generally, the EIM has limited accuracy and can be applied only for specific structure cross sections like rib waveguides and diffused surface channel waveguides, for which assumption like eq. (2.27) can be made. However, for rectangular waveguides, it has been reported that the EIM actually solves an equivalent structure with some error in the corner segments [14]. Hence, for this kind of structures, accuracy can be increased through perturbative correction and combination of 2 different substructuring sequences [15]. EIM for circular coordinate has also been reported for scalar analysis of photonic crystal fibers with circularly distributed holes [16], which is applicable only for cases with small air filling fraction. However, thanks to its efficiency, EIM is a useful tool for quick observation of modes, which is a frequent activity in designing photonic waveguide. Also, due to its ability to reduce dimensionality, it is useful to study trends in complicated 3-D structures, for which rigorous calculation is very expensive.

References

1. R. Scarmozzino et al., "Numerical techniques for modeling guided-wave photonic devices," **J. Sel. Topics in Quantum Electron.**, Vol. 6, No. 1, pp. 150-162, 2000.
2. H.J.W.M. Hoekstra, "Theory and numerical strategies of BPMs: on beam propagation methods for modeling of integrated optics," **Opt. Quantum Electron.**, Vol. 29, No. 2, pp. 157-171, 1997.
3. A. Taflove and S.C. Hagness, *Computational Electrodynamics: The Finite Difference Time Domain Method*, 2nd ed., Artech House, Boston, MA, 2000.

4. F. Schmidt, "Computation of discrete transparent boundary conditions for the 2D Helmholtz equation," **Opt. Quantum Electron.**, Vol. 30, No. 5-6, pp. 427-441, 1998.
5. G. Sztefka and H.P. Nolting, "Bidirectional eigenmode propagation for large refractive index steps," **Photonics Technol. Lett.**, Vol. 5, No. 5, pp. 554-557, 1993.
6. M. Hammer, "Quadridirectional eigenmode expansion scheme for 2-D modeling of wave propagation in integrated optics," **Opt. Commun.**, Vol. 235, No. 4-6, pp. 285-303, 2004.
7. J. Gerdes and R. Pregla, "Beam-propagation algorithm based on the method of lines," **J. Opt. Soc. Am. B**, Vol. 8, No. 2, pp. 389-394, 1991.
8. C. Vassallo, "Mode solvers, 1993-1995 optical mode solvers," **Opt. Quantum Electron.**, Vol. 29, No. 2, pp. 95-114, 1997.
9. H. Noro and T. Nakayama, "A new approach to scalar and semivector mode analysis of optical waveguides," **J. Lightwave Technol.**, Vol. 14, No. 6, pp. 1546-1556, 1996.
10. G.R. Hadley, "Numerical simulation of waveguides of arbitrary cross-section," **Int. J. Electron. Commun. (AEU)**, Vol. 58, No. 2, pp. 86-92, 2004.
11. G.R. Hadley, "High-accuracy finite difference equations for dielectric waveguide analysis I: uniform regions and dielectric interfaces," **J. Lightwave Technol.**, Vol. 20, No. 7, 1210-1218, 2002.
12. J.F. Lee, D.K. Sun, and Z.J. Cendes, "Full-wave analysis of dielectric waveguides using tangential vector finite elements," **Trans. Microwave Theory and Tech.**, Vol. MTT-39, No. 8, pp. 1262-1271, 1991.
13. M. Koshiba and Y. Tsuji, "Curvilinear hybrid edge/nodal elements with triangular shape for guided-wave problems," **J. Lightwave Technol.**, Vol. 18, No. 5, pp. 737-743, 2000.
14. K.S. Chiang, "Effective-index analysis of optical waveguides," **Proc. SPIE**, Vol. 2399, pp. 2-12, 1995.
15. K.S. Chiang, "Analysis of the effective-index method for vector modes of rectangular-core dielectric waveguides," **Trans. Microwave Theory and Tech.**, Vol. 44, No. 5, pp. 692-700, 1996.
16. V. Rastogi and K.S. Chiang, "Holey optical fiber with circularly distributed holes analyzed by the radial effective-index method," **Opt. Lett.**, Vol. 28, No. 24, pp. 2449-2451, 2003.

Chapter 3

Finite difference scheme for anisotropic planar waveguides with arbitrary index profiles

A finite difference scheme with a uniform mesh for planar waveguides with arbitrary refractive index profiles that takes full account of any smooth index variation and index discontinuity is derived for TE and TM-polarized waves. Discretizations that lead to a second-order error in the effective indices are given for TE and TM polarizations. At the computational boundaries, transparent boundary conditions are used. The scheme was implemented for anisotropic waveguides with a diagonal permittivity tensor and examined by using samples with various refractive index profiles, ranging from simple step- and graded-index up to complicated refractive index profile structures composed of either isotropic or anisotropic materials. For simple cases where the results of other methods are available in the literature, the proposed scheme shows a very good agreement.

This chapter is adapted from:
H.P. Uranus, H.J.W.M. Hoekstra, and E. van Groesen, "Finite difference scheme for planar waveguides with arbitrary index profiles and its implementation for anisotropic waveguides with a diagonal permittivity tensor," **Opt. Quantum Electron.**, Vol. 35, No. 4, pp. 407-427, 2003.

Finite difference scheme for anisotropic planar waveguides with arbitrary index profiles

3.1. Introduction

Some fabrication technologies of optical waveguides may lead to devices with complicated refractive index profiles [1-3]. These profiles can be combinations of one or more graded-index and uniform-index regions with index discontinuities at their interfaces. Efficient and accurate computation techniques for structures with arbitrary index profiles are thus important for the design and characterization of such devices. Since an exact solution for structures with complicated index profiles is not always available, numerical methods are indispensable.

The finite difference (FD) method is a popular tool for waveguide analysis. In this method, accuracy is not only determined by the discretization scheme used in the continuous index region, but also by the discretization at grid points around the index discontinuities and computational boundaries [4]. Various schemes for improvement of finite difference discretization at the vicinity of index discontinuities have been proposed [5-10]. So far, all of these schemes consider only discontinuities of step-index waveguides.

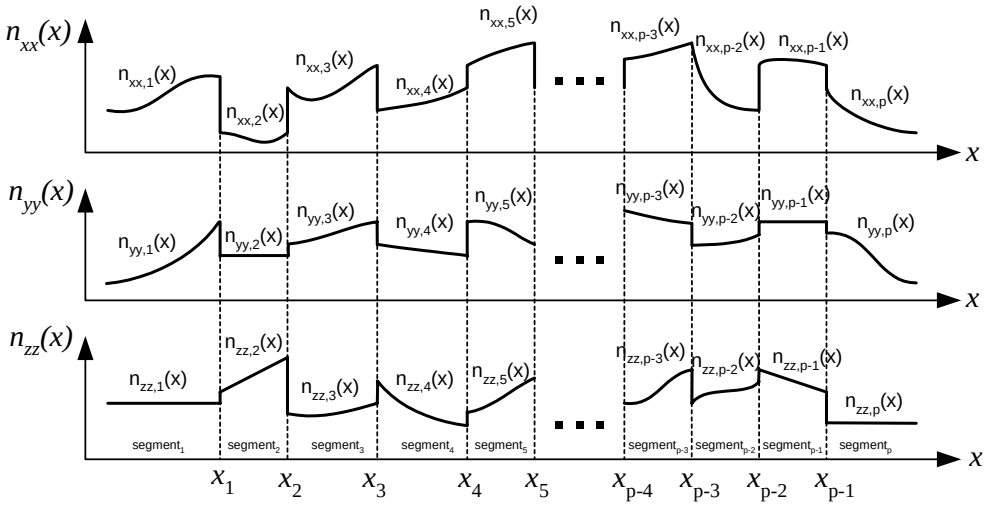

Figure 3.1. *General arbitrary refractive index profiles.*

In this chapter, we propose a finite difference scheme that takes full account of the gradient of the refractive indices in the vicinity of index discontinuities of anisotropic media with diagonal permittivity tensor, hence suitable to analyze structures of complicated arbitrary index profiles as depicted in Fig. 3.1. A uniform mesh size has been incorporated and index discontinuities can be located anywhere between two adjacent grid points.

This chapter is organized as follows. After a short description of the type of structures for which the scheme is applicable in section 3.2, interface continuity conditions that take full account of both the index continuity and discontinuity around interfaces are presented in section 3.3. Based on these interface continuity conditions, the discretization scheme is derived and completed with simple transparent boundary condition. Finally, in section 3.4, results of calculation with the proposed scheme for several samples are presented and compared with the results of other methods.

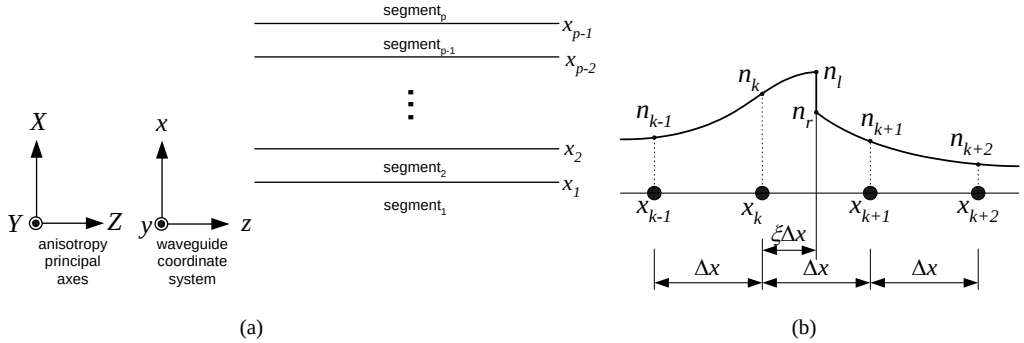

Figure 3.2. *(a). The structure and its coordinate system, and (b). possible refractive index profile at the vicinity of interface between two segments.*

3.2. Backgrounds

3.2.1. Anisotropic waveguides with diagonal permittivity tensor

For anisotropic but non-magnetic planar waveguides, where the principal axes of the anisotropy are parallel to the Cartesian coordinate system of the waveguide, as shown in Fig. 3.2.a, the permittivity tensor can be expressed in a diagonal form as follows.

$$\bar{\bar{\varepsilon}} = \varepsilon_0 \begin{bmatrix} n_{xx}^2 & 0 & 0 \\ 0 & n_{yy}^2 & 0 \\ 0 & 0 & n_{zz}^2 \end{bmatrix} \tag{3.1}$$

with ε_0 is the free space permittivity; and n_{xx}, n_{yy}, and n_{zz} are the refractive indices associated with electric field polarized in direction parallel to the x, y, and z axes of the

coordinate system, respectively. By taking the *z*-axis as the propagation direction and assuming that the waveguide is composed of source-free and lossless material with refractive index changes only in the *x* direction, it is possible to have uncoupled TE- and TM-polarized waves with corresponding scalar Helmholtz's equations

$$\left(d_{xx} + k_0^2 n_{yy}^2(x) - \beta^2\right) E_y(x) = 0 \tag{3.2}$$

and

$$\left[d_{xx} + n_{zz}^2(x)\left(d_x \frac{1}{n_{zz}^2(x)}\right) d_x + k_0^2 n_{zz}^2(x) - \beta^2 \frac{n_{zz}^2(x)}{n_{xx}^2(x)}\right] H_y(x) = 0 \tag{3.3}$$

respectively.

3.2.2. Arbitrary refractive index profiles

A structure showing all the features that can be modeled in this work is as shown in Fig. 3.1, where the discontinuities in the refractive indices determine the division into several segments. Within each segment, the refractive indices and their derivatives up to the second-order are assumed continuous. At interfaces between segments, there can be a discontinuity of the refractive indices or their derivatives. For segment *i* located between x_{i-1} and x_i, either the relative permittivity or refractive index profiles can be written with an arbitrary normalized function *f* or *g*, following the commonly used notation, like

$$n_{\eta,i}^2(x) = n_{0;\eta,i}^2 + \tilde{\Delta}_{\eta,i} f_{\eta,i}(x) \qquad \text{for} \qquad x_{i-1} < x \le x_i \tag{3.4}$$

or

$$n_{\eta,i}(x) = n_{0;\eta,i} + \Delta_{\eta,i} g_{\eta,i}(x) \qquad \text{for} \qquad x_{i-1} < x \le x_i \tag{3.5}$$

where $\tilde{\Delta}$ and Δ denote the constants that determine the increase of relative permittivity and refractive index from their asymptotical value n_0^2 and n_0, respectively; while subscript η denotes the direction of polarization, which could be *x*, *y*, or *z*.

3.3. Description of the scheme

We will first derive the continuity conditions of the field and its derivatives at an interface between two segments. Based on these conditions, the discretization scheme will be derived.

3.3.1. Interface continuity conditions

We will use a uniform mesh with a step size Δx. It is assumed that the interface between two adjacent segments is located between x_k and x_{k+1} at $\xi\Delta x$ away from x_k as illustrated in Fig. 3.2.b. It is also assumed that there is no other interface between x_{k-1} and x_{k+2}.

By using Maxwell's equations we can get relations between the field and its derivatives up to the 3rd-order derivatives at the left and right hand side of the interface. Writing E_y as φ with subscripts l and r denoting the left hand side (lhs) and right hand side (rhs) of the interface, respectively; for TE polarization, where the field is parallel to the interface, the results are

$$\varphi_l = \varphi_r \tag{3.6}$$

$$d_x\varphi_l = d_x\varphi_r \tag{3.7}$$

$$d_{xx}\varphi_l = d_{xx}\varphi_r + k_0^2\left(n_{yy_r}^2 - n_{yy_l}^2\right)\varphi_r \tag{3.8a}$$

$$d_{xx}\varphi_r = d_{xx}\varphi_l + k_0^2\left(n_{yy_l}^2 - n_{yy_r}^2\right)\varphi_l \tag{3.8b}$$

$$d_{xxx}\varphi_l = d_{xxx}\varphi_r + k_0^2\left(n_{yy_r}^2 - n_{yy_l}^2\right)d_x\varphi_r + k_0^2\left[\left(d_x n_{yy}^2\right)_r - \left(d_x n_{yy}^2\right)_l\right]\varphi_r \tag{3.9a}$$

$$d_{xxx}\varphi_r = d_{xxx}\varphi_l + k_0^2\left(n_{yy_l}^2 - n_{yy_r}^2\right)d_x\varphi_l + k_0^2\left[\left(d_x n_{yy}^2\right)_l - \left(d_x n_{yy}^2\right)_r\right]\varphi_l \tag{3.9b}$$

In the same way, we can get the interface conditions for TM polarization; with φ denoting H_y as follows.

$$\varphi_l = \varphi_r \tag{3.10}$$

$$d_x\varphi_l = \frac{n_{zz_l}^2}{n_{zz_r}^2}d_x\varphi_r \tag{3.11a}$$

$$d_x\varphi_r = \frac{n_{zz_r}^2}{n_{zz_l}^2}d_x\varphi_l \tag{3.11b}$$

$$d_{xx}\varphi_l = c_1 d_{xx}\varphi_r + c_2 d_x\varphi_r + c_3\varphi_r \tag{3.12a}$$

$$d_{xx}\varphi_r = \hat{c}_1 d_{xx}\varphi_l + \hat{c}_2 d_x\varphi_l + \hat{c}_3\varphi_l \tag{3.12b}$$

$$d_{xxx}\varphi_l = c_4 d_{xxx}\varphi_r + c_5 d_{xx}\varphi_r + c_6 d_x\varphi_r + c_7\varphi_r \tag{3.13a}$$

$$d_{xxx}\varphi_r = \hat{c}_4 d_{xxx}\varphi_l + \hat{c}_5 d_{xx}\varphi_l + \hat{c}_6 d_x\varphi_l + \hat{c}_7\varphi_l \tag{3.13b}$$

with

$$c_1 = \frac{n_{xx_r}^2}{n_{zz_r}^2}\frac{n_{zz_l}^2}{n_{xx_l}^2} \tag{3.14a}$$

$$c_2 = \left[n_{xx_r}^2\left(d_x\frac{1}{n_{zz}^2}\right)_r - n_{xx_l}^2\frac{n_{zz_l}^2}{n_{zz_r}^2}\left(d_x\frac{1}{n_{zz}^2}\right)_l\right]\frac{n_{zz_l}^2}{n_{xx_l}^2} \tag{3.14b}$$

$$c_3 = k_0^2\left(n_{xx_r}^2 - n_{xx_l}^2\right)\frac{n_{zz_l}^2}{n_{xx_l}^2} \tag{3.14c}$$

$$c_4 = \frac{n_{zz_l}^4}{n_{zz_r}^4}\frac{n_{xx_r}^2}{n_{xx_l}^2} \tag{3.14d}$$

$$\begin{aligned} c_5 = \Big\{ & n_{zz_l}^2 n_{xx_l}^2\left(d_x n_{xx}^2\right)_r - n_{zz_r}^2 n_{xx_r}^2\left(d_x n_{xx}^2\right)_l \\ & + 2n_{zz_l}^2 n_{zz_r}^2 n_{xx_l}^2 n_{xx_r}^2\left[\left(d_x\frac{1}{n_{zz}^2}\right)_r - \left(d_x\frac{1}{n_{zz}^2}\right)_l\right]\Big\}\frac{n_{zz_l}^2}{n_{zz_r}^4 n_{xx_l}^4} \end{aligned} \tag{3.14e}$$

$$c_6 = \frac{n_{zz_l}^2}{n_{xx_l}^2}\left(d_x \frac{1}{n_{zz}^2}\right)_r \left[\frac{n_{zz_l}^2}{n_{zz_r}^2}\left(d_x n_{xx}^2\right)_r - \frac{n_{xx_r}^2}{n_{xx_l}^2}\left(d_x n_{xx}^2\right)_l\right]$$
$$+2n_{zz_l}^4\left(d_x \frac{1}{n_{zz}^2}\right)_l \left[\frac{n_{zz_l}^2}{n_{zz_r}^2}\left(d_x \frac{1}{n_{zz}^2}\right)_l - \frac{n_{xx_r}^2}{n_{xx_l}^2}\left(d_x \frac{1}{n_{zz}^2}\right)_r\right]$$
$$+\frac{n_{zz_l}^4}{n_{zz_r}^2}\left[\frac{n_{xx_r}^2}{n_{xx_l}^2}\left(d_{xx} \frac{1}{n_{zz}^2}\right)_r - \left(d_{xx} \frac{1}{n_{zz}^2}\right)_l\right] + k_0^2 \frac{n_{zz_l}^4}{n_{zz_r}^2}\left(\frac{n_{xx_r}^2}{n_{xx_l}^2} - 1\right) \quad (3.14f)$$

$$c_7 = \frac{k_0^2 n_{zz_l}^2}{n_{zz_r}^2 n_{xx_l}^4}\Big[\; n_{zz_l}^2 n_{xx_l}^2 \left(d_x n_{xx}^2\right)_r - n_{zz_r}^2 n_{xx_r}^2 \left(d_x n_{xx}^2\right)_l$$
$$+2n_{zz_r}^2 n_{xx_l}^2 n_{zz_l}^2 \left(d_x \frac{1}{n_{zz}^2}\right)_l \left(n_{xx_l}^2 - n_{xx_r}^2\right)\Big] \quad (3.14g)$$

Here and also later in eqs. (3.21), (3.23), and (3.24), the hat (^) symbol denotes the simultaneous interchange of ξ and $1\text{-}\xi$ and subscripts l and r.

3.3.2. Discretization in a continuous refractive index region

It is obvious from eqs. (3.6)-(3.13) and also from the wave equations that within each segment where the refractive indices and their derivatives up to second order are continuous, the field and derivatives up to third order are also continuous for both TE and TM polarization. Hence, the well-known central difference formula can be used to discretize second- and first-order derivatives of the fields. For TE polarization the discretized Helmholtz's equation for a grid point i not adjacent to the interface becomes

$$\varphi_{i-1} - 2\varphi_i + \varphi_{i+1} + k_0^2 \Delta x^2 n_{yy_i}^2 \varphi_i - k_0^2 \Delta x^2 n_{eff}^2 \varphi_i = 0 \quad (3.15)$$

which will give second-order accuracy. For TM, it turns out to be

$$\varphi_{i-1} - 2\varphi_i + \varphi_{i+1} + \frac{n_{zz_i}^2}{2}\left(d_x \frac{1}{n_{zz}^2}\right)_i \Delta x\left(\varphi_{i+1} - \varphi_{i-1}\right) + k_0^2 \Delta x^2 n_{zz_i}^2 \varphi_i - k_0^2 \Delta x^2 \frac{n_{zz_i}^2}{n_{xx_i}^2} n_{eff}^2 \varphi_i = 0 \quad (3.16)$$

Since the refractive index profiles are known beforehand, it is possible to use exact value of $d_x\left(1/n_{zz}^2\right)$ into eq. (3.16). But it is also possible to use a 2nd-order accurate central difference approximation for this term, which still gives 2nd-order accuracy to the discretization of Helmholtz's equation at the corresponding grid point.

3.3.3. Discretization around index discontinuities

For grid points that are adjacent to the interface between segments, 2nd and 3rd-order derivatives of the field for TE polarization are not continuous anymore. For TM polarization, the discontinuity starts from the 1st-order derivatives. Hence, corrections should be made to the FD formulae for these grid points.

By using a Taylor's expansion, we can express field at x_{k+1} i.e. φ_{k+1} in terms of field and it derivatives at the rhs of the interface. For TE polarization, using the continuity conditions (3.6)-(3.9) we can then express φ_{k+1} in terms of field and its derivatives at the lhs of the interface. Since the field at the lhs of the interface can also be expressed as an expansion of φ_k and its derivatives, we finally can express φ_{k+1} in terms of φ_k. This successive operation gives

$$\varphi_{k+1} = \left(1 + c_8\Delta x^2 + c_9\Delta x^3\right)\varphi_k + \left(\Delta x + c_{10}\Delta x^3\right)d_x\varphi_k + \frac{\Delta x^2}{2}d_{xx}\varphi_k + \frac{\Delta x^3}{6}d_{xxx}\varphi_k + O\left(\Delta x^4\right) \tag{3.17}$$

with

$$c_8 = \frac{\left(1-\xi\right)^2}{2}k_0^2\left(n_{yy_l}^2 - n_{yy_r}^2\right) \tag{3.18a}$$

$$c_9 = \frac{\left(1-\xi\right)^3}{6}k_0^2\left[\left(d_x n_{yy}^2\right)_l - \left(d_x n_{yy}^2\right)_r\right] \tag{3.18b}$$

$$c_{10} = \frac{\left(2\xi+1\right)\left(\xi-1\right)^2}{6}k_0^2\left(n_{yy_l}^2 - n_{yy_r}^2\right) \tag{3.18c}$$

By using eq. (3.17) and a Taylor's expansion of φ_{k-1} in terms of φ_k and its derivatives, and use a 1st-order accurate forward difference to approximate $d_x\varphi_k$ (also using a successive procedure as above) we can get rid of $d_x\varphi_k$ and $d_{xxx}\varphi_k$, and obtain a 2nd-order-accurate interface-corrected FD formulae for 2nd-order derivative of field at a grid point just left of the interface as follows

$$d_{xx}\varphi_k = \frac{\varphi_{k-1} - \left(2 + c_{11}\Delta x^2 + c_9\Delta x^3\right)\varphi_k + \left(1 - c_{10}\Delta x^2\right)\varphi_{k+1}}{\Delta x^2} + O\left(\Delta x^2\right) \tag{3.19}$$

with

$$c_{11} = c_8 - c_{10} \tag{3.20}$$

Derivatives of refractive index terms within the expression for c_9 can be evaluated either using their exact values or the 1st-order forward and backward difference approximation. In the same way, we can also get interface-corrected FD formulae for 2nd-order derivative of the field at the grid point just after the interface as

$$d_{xx}\varphi_{k+1} = \frac{\left(1 - \hat{c}_{10}\Delta x^2\right)\varphi_k - \left(2 + \hat{c}_{11}\Delta x^2 - \hat{c}_9\Delta x^3\right)\varphi_{k+1} + \varphi_{k+2}}{\Delta x^2} + O\left(\Delta x^2\right) \tag{3.21}$$

The same procedures can be repeated for TM polarization. But, due to its more complicated interface continuity conditions, by using just 3 grid points, we are not able to get 2nd-order accuracy for the discretization around interfaces. By neglecting more higher order terms during the successive Taylor's expansion process, we can aim at 1st-order FD formulae as follows

$$d_x\varphi_k = \frac{\varphi_{k+1} - \varphi_{k-1}}{(1+c_{12})\Delta x} + O(\Delta x) \tag{3.22a}$$

$$d_{xx}\varphi_k = \frac{(c_{12} + c_{13}\Delta x)\varphi_{k-1} - (1 + c_{12} + c_{14}\Delta x^2)\varphi_k + (1 - c_{13}\Delta x)\varphi_{k+1}}{c_{15}\Delta x^2} + O(\Delta x) \tag{3.22b}$$

$$d_x\varphi_{k+1} = \frac{\varphi_{k+2} - \varphi_k}{(1+\hat{c}_{12})\Delta x} + O(\Delta x) \tag{3.23a}$$

$$d_{xx}\varphi_{k+1} = \frac{(1+\hat{c}_{13}\Delta x)\varphi_k - (1 + \hat{c}_{12} + \hat{c}_{14}\Delta x^2)\varphi_{k+1} + (\hat{c}_{12} - \hat{c}_{13}\Delta x)\varphi_{k+2}}{\hat{c}_{15}\Delta x^2} + O(\Delta x) \tag{3.23b}$$

with

$$c_{12} = \xi + (1-\xi)\frac{n_{zz_r}^2}{n_{zz_l}^2} \tag{3.24a}$$

$$c_{13} = \frac{(1-\xi)^2 \hat{c}_2}{2(1+c_{12})} \tag{3.24b}$$

$$c_{14} = \frac{(1-\xi)^2 \hat{c}_3}{2} \tag{3.24c}$$

$$c_{15} = c_{16} + \frac{c_{12}}{2} \tag{3.24d}$$

$$c_{16} = \frac{\xi^2}{2} + \xi(1-\xi)\frac{n_{zz_r}^2}{n_{zz_l}^2} + \frac{(1-\xi)^2}{2}\hat{c}_1 \tag{3.24e}$$

Although the discretization at the interface is only 1st-order accurate, the above scheme will still give 2nd-order overall accuracy [8] in the effective indices, if the number of grid points is much larger than the number of interfaces. A perturbation analysis of this will be given in Appendix 1. In order to achieve 2nd-order accuracy for discretization at grid point *k* and *k+1*, we need to use eq. (3.3) and incorporate fields at grid points *k+2* and *k-1*. By doing so, we get 2nd-order accurate, 4-point interface-corrected discretization of first- and second-order derivatives at grid points just before and after the interface. However, due to the lengthy expressions, we decided not to present this here, but elsewhere [11].

3.3.4. Discretization at the computational domain boundaries

In this chapter, we are interested in guided modes of the structure; hence, at the computational boundaries we can use the fact that guided mode fields are exponentially decaying. In this way, we can express fields at ghost points as function of fields at boundary points. The exponential decay rates follow from analytical solutions of the guided modes in the substrate and cover.

By assuming that the refractive index gradient at the boundaries is already negligible, the field at ghost points *0* and *N+1* can be approximated by

$$\varphi_0 = \varphi_1 \exp\left(-k_0 \sqrt{n_{eff}^2 - n_{yy_0}^2}\,\Delta x\right) \tag{3.25a}$$

and

$$\varphi_{N+1} = \varphi_N \exp\left(-k_0 \sqrt{n_{eff}^2 - n_{yy_{N+1}}^2}\,\Delta x\right) \tag{3.25b}$$

for TE polarization, and

$$\varphi_0 = \varphi_1 \exp\left(-k_0 \frac{n_{zz_0}}{n_{xx_0}} \sqrt{n_{eff}^2 - n_{xx_0}^2}\,\Delta x\right) \tag{3.26a}$$

and

$$\varphi_{N+1} = \varphi_N \exp\left(-k_0 \frac{n_{zz_{N+1}}}{n_{xx_{N+1}}} \sqrt{n_{eff}^2 - n_{xx_{N+1}}^2}\,\Delta x\right) \tag{3.26b}$$

for TM polarization. It should be noted that expressions (3.25)-(3.26) are not correct for structures with graded index substrate or cover, but as will be shown later, these expressions are reasonable approximations as long as the computational boundaries are positioned at points where the gradients of the refractive indices are negligible. For better results, these equations should be replaced by expressions adapted from the exact analytic solution of fields at the corresponding region of the structure. The same changes should also be done if we want to analyze fields that are not decaying, e.g. when we want to analyze leaky modes.

3.3.5. Eigenvalue searching

Since the effective index values are used in the implementation of the boundary conditions, the eigenvalue problem differs from the standard linear matrix eigenvalue problem. In this work, instead of solving non-linear matrix eigenvalue problem, we solve the dispersion relation det(**M**)=0 by using the bisection root-searching algorithm, with **M** denotes the matrix of the discretized Helmholtz's equations.

3.4. Results and discussions

Several samples are used to test the proposed scheme. The index profiles of the samples range from a simple step-index, a combination of one graded- and one step-index segment, up to more complicated structures, either based on isotropic or anisotropic materials. All the results for TM-polarization presented in this paper were calculated using the scheme that is 2nd-order accurate in the continuous index region and 1st-order accurate at interfaces.

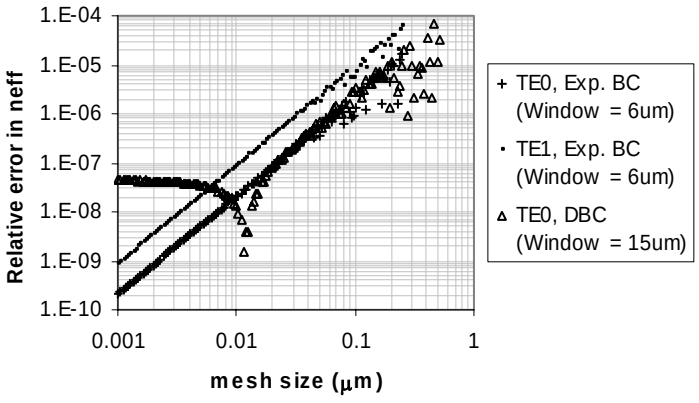

(a)

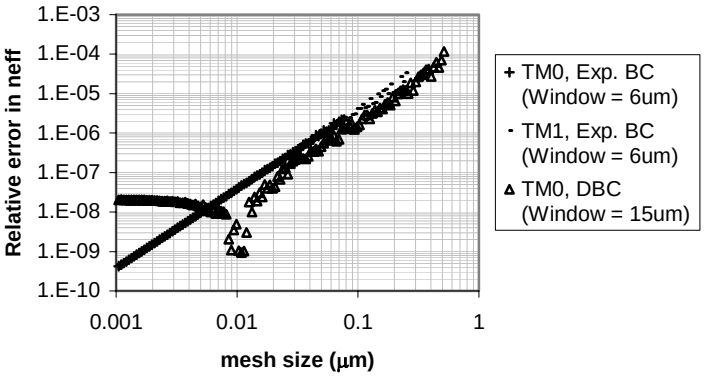

(b)

Figure 3.3. *Relative error in the calculated effective indices for a 3-layer step-index isotropic waveguide of thickness 5μm: (a). TE polarization and (b). TM polarization.*

3.4.1. Step-index isotropic waveguide sample

An isotropic 3-layer structure with a refractive index of the substrate n_s=1.5, guiding film n_f=1.52, air cladding n_c=1, and the film thickness 5μm was analyzed for a vacuum wavelength λ=1.55μm. The effective indices were compared to their exact values obtained using the transfer matrix method (TMM) [12, 13] and the results are depicted in Fig. 3.3. It is obvious from the results that the scheme is 2nd-order accurate for both TE and TM, as expected. For large mesh size, the errors fluctuate due to the fluctuation of truncation errors in the discretization around interfaces, which depends on the interface relative position ($T = O\left(f(\xi)\Delta x^2 \right)$). As the grid size is refined, the

sensitivity of this error to changes in interface position ($dT/d\xi$) becomes smaller. It is obvious from these results, that the implemented boundary condition (denoted as *Exp. BC*) is much better than the simple homogeneous Dirichlet boundary condition (denoted as *DBC*) that uses perfect electric conductor (for TE) or perfect magnetic conductor (for TM) at boundaries, even when we take a much larger window for the *DBC*. This is due to the long evanescent tail for such an asymmetric structure for modes near to cut off, which requires a very large window in order to reduce the effect of the Dirichlet boundary condition.

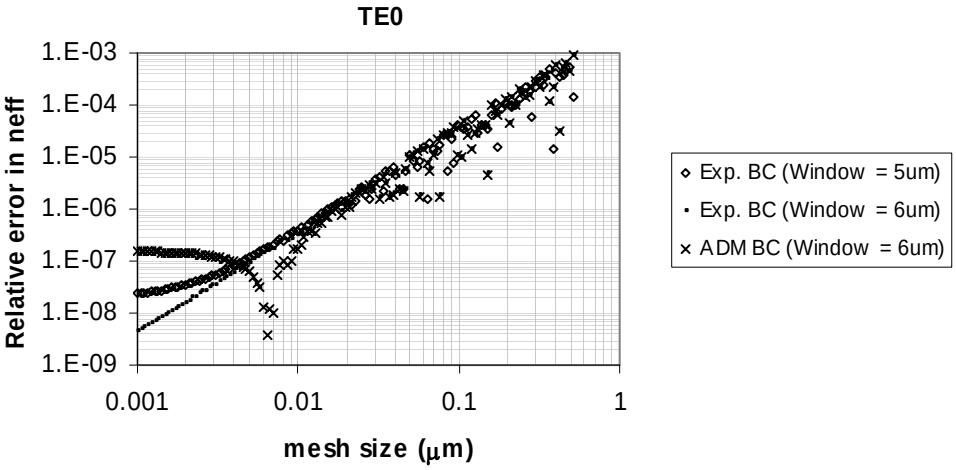

Figure 3.4. *Relative error in the calculated effective index for the isotropic waveguide with an exponential relative permittivity profile.*

3.4.2. Graded-index isotropic waveguide sample

For graded index isotropic waveguide sample, we take a waveguide with exponential relative permittivity profile as follows

$$n^2(x) = n_s^2 + 2n_s\bar{\Delta}\exp\left(-\frac{|x|}{d}\right) \qquad \text{for } x \le 0 \qquad (3.27a)$$

$$n^2(x) = n_c^2 \qquad \text{for } x > 0 \qquad (3.27b)$$

with d denotes the effective depth of the exponential profile. The exact values of its effective indices for TE polarization were calculated using the exact dispersion relation [14]. The results of the present FD scheme for n_s=2.177, n_c=1, $\bar{\Delta}$=0.043, and $V = k_0 d\sqrt{2n_s\bar{\Delta}} = 4$ are shown in Fig. 3.4 for various boundary conditions. The computation was carried out for λ=1μm and a computational window size of only 3.4 and 4 times the effective depth of the exponential permittivity profile. Since the

waveguide is asymmetric which will lead to longer evanescent tail into the substrate than the cover, the computation was carried out in an asymmetric grid distribution way, where 90% of the grid points are put into the substrate and only 10% within the cover region.

Table 3.1. *Calculated normalized propagation constants for the isotropic waveguide with an exponential relative permittivity profile.*

	$b=\frac{n_{eff}^2-n_s^2}{2n_s\bar{\Delta}}$							
Mode	Exact [14]	Present FD scheme (W=10μm, 98 grids)	Present FD scheme (W=10μm, 962 grids)	Variational CE [16]	Variational EHG [17]	WKB [16]	MAF [18]	FEM [19] (800 grids)
TE_0	0.321179	0.32134	0.32119	0.3155	0.313	0.2992	0.32116	0.318
TE_1	0.053972	0.05421	0.05398	-	-	-	-	-

As shown in Fig. 3.4, for small computational window size where the gradient of the refractive index at one side of the boundaries is still significant, the results with exponential boundary condition (*Exp. BC*) are not 2nd-order anymore for small grid sizes, because for this exponential index substrate, the field at ghost point 0 is not correctly represented by eq. (3.25), but should be expressed in Bessel's functions [14]. Hence, for small grid sizes, the boundary error becomes more dominant than the interior discretization error. However, this boundary condition still gives better results than the 4-point asymmetric discretization boundary condition (*ADM BC*) [15]. Table 3.1 shows the normalized propagation constants calculated by the present FD scheme, and other published methods, i.e. variational method using cosine-exponential trial function [16], variational method using evanescent-Hermite-Gaussian trial function [17], WKB [16], modified Airy function [18], and finite element method [19]. In this table, W denotes the computational window size. As can be seen from the table, the results of present scheme agree nicely with the exact values. The results of present FD scheme with a small number of grid points are already more accurate than the FEM results with a much larger number of grid points. This improvement, we believe is to be attributed to the boundary conditions and the asymmetric grid distribution scheme that enable us to carry out our computation in a relatively small window.

Additionally, we also compare the results of the proposed FD scheme with a method which is based on invariant imbedding and transverse impedance concept [20] for waveguide with cosinusoidal relative permittivity transition as depicted in Fig. 3.5.a. For waveguide with n_s^2=1.5, n_f^2=1.53, n_c^2=1.0, d=4μm, and w/d=0.2, the dispersion curves of both methods are depicted in Fig. 3.5.b., which shows the agreement of the n_{eff} values of better than 3 digits. For the transverse impedance

method results, we have taken the data from Fig. 5 of the paper of Kuester and Chang, and adjust the quantity of the vertical axis from $n_{eff} - 1.225$ (in their figure) into $n_{eff} - n_s = n_{eff} - \sqrt{1.5}$ (in our figure).

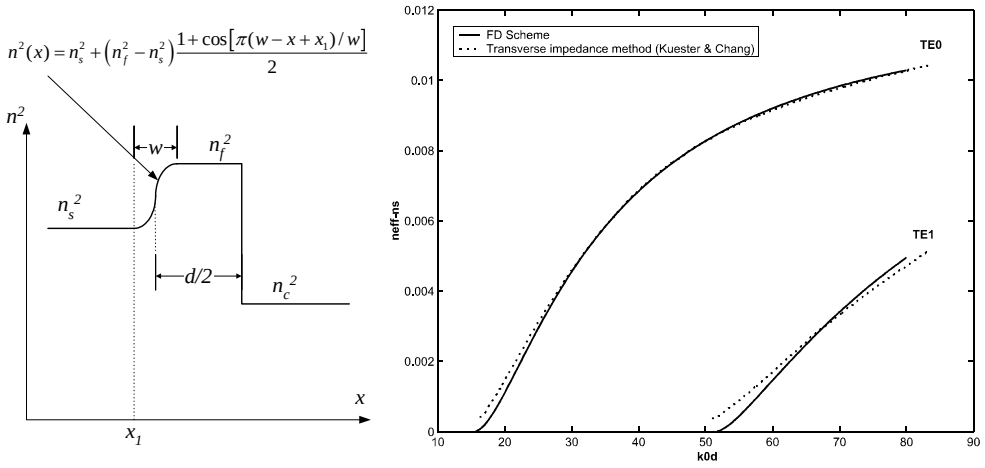

(a) (b)

Figure 3.5. *Asymmetric waveguide with cosinusoidal transition: (a). relative permittivity profile, and (b). calculated dispersion curves by present FD scheme and the transverse impedance method.*

3.4.3. Step-index anisotropic waveguide sample

For step index anisotropic samples, we take a 4-layer step-index waveguide composed of anisotropic SiO_xN_y film deposited onto isotropic SiO_2 substrate, covered with anisotropic calix[4]arene and an air cladding [21]. For light with wavelength of 957.44 nm the refractive index of the substrate and air cover are 1.4526 and 1.0, respectively. The refractive index of the SiON and calyx[4]arene are n_{xx}=1.6721, n_{yy}=n_{zz}=1.6738 and n_{xx}=1.5630, n_{yy}=n_{zz}=1.5622, respectively. The thickness of SiON and calyx[4]arene layers are 591 nm and 600 nm, respectively. The calculated results for TM polarization using a computational window of 5μm with mesh size of 3.9 nm are presented in Table 3.2 along with results of TMM and another FD scheme. In this table $n_{xx,f}$ denotes n_{xx} at the guiding film. This table clearly shows the agreement of the results of present scheme with those of other methods.

Table 3.2. *Calculation results for anisotropic step-index waveguide*

Mode	$b=\frac{n_{eff}^2-n_s^2}{n_{xx,f}^2-n_s^2}$		
	TMM [13]	Present FD scheme (W=5μm, Δx=3.9nm)	FD BPM [21] (Δx=3.9nm)
TM0	0.671163	0.671157	0.671158
TM1	0.100810	0.100816	-

3.4.4. Graded-index anisotropic waveguide sample

The scheme is also used to evaluate an anisotropic graded-index waveguide. The considered sample is an annealed proton-exchanged (APE) X-cut Y-propagating $LiNbO_3$ waveguide with crystal axes that coincide with the waveguide axes. The refractive indices are assumed to follow

$$n_o(x) = n_{os} + \Delta_o \exp\left(-\frac{x^2}{d^2}\right) \qquad \text{for } x \le 0 \qquad (3.28a)$$

$$n_e(x) = n_{es} + \Delta_e \exp\left(-\frac{x^2}{d^2}\right) \qquad \text{for } x \le 0 \qquad (3.28b)$$

$$n(x) = n_c \qquad \text{for } x > 0 \qquad (3.28c)$$

where n_o and n_e denote the ordinary and extraordinary refractive index of $LiNbO_3$, respectively. Since the proton exchange process will increase the extraordinary index and decrease the ordinary index, one could expect refractive index profiles with positive Δ_e and negative Δ_o as depicted in Fig. 3.6. In this sample, within the substrate we will have $n_{xx}(x)=n_{zz}(x)=n_o(x)$ and $n_{yy}(x)=n_e(x)$. For this kind of structure, only TE-polarized waves can be guided. The calculated results for λ=0.6328μm, n_{os}=2.286, n_{es}=2.2, Δ_e=0.01, Δ_o=-0.004, n_c=1.0, and d=5μm are shown along with published data and the results of TMM in Table 3.3. Since the profile is expressed in refractive index instead of relative permittivity, it is more convenient to use an approximated formula for the normalized propagation constants in the table. Here Δ_x and Δ_y denote the maximum index increase for n_{xx} and n_{yy}, respectively; while $n_{xx,s}$ and $n_{yy,s}$ denote the asymptotic n_{xx} and n_{yy} of the substrate, respectively. For the TMM calculation we have used 2000 layers with uniform thickness to staircase-approximate up to $3d$ depth into the graded index region. It should be noted, that our samples are different from the Ti-indiffused sample analyzed by Katsriku *et al.* [19], but for the TE analysis they are computationally identical, since computation for this polarization only need n_{yy} and we have chosen the same index profile parameters for this index profile. Our FD results are obtained using 500 grid points with 90% of the points located within the graded-index region and by using a computational domain width of 25 μm. As seen from the table, the results of the FD scheme are in good agreement with the published data and the results of TMM.

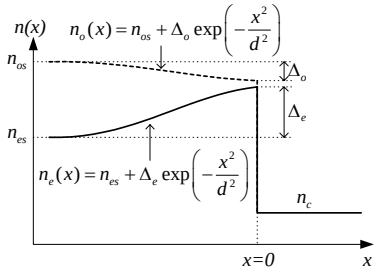

Figure 3.6. *Anisotropic index profile of the APE-$LiNbO_3$ sample.*

For TM-polarization we take a Z-cut Y-propagating $LiNbO_3$ sample with the same index profile parameter as the previous one, but in this case within the sample we will have $n_{xx}(x)=n_e(x)$ and $n_{yy}(x)=n_{zz}(x)=n_o(x)$. As shown in Fig. 3.6, in this case we will have different index profiles for n_{xx} (Gaussian with positive Δ) and n_{zz} (Gaussian with negative Δ) that are fully taken into account in present scheme. The computation results are also shown in Table 3.3, where present scheme exhibits nice agreement with the results of the TMM.

Table 3.3. *Calculation results for the APE- $LiNbO_3$ waveguide.*

Sample	Modes	$b_{TE} = \frac{n_{eff} - n_{yy,s}}{\Delta_y}$ $\quad b_{TM} = \frac{n_{eff} - n_{xx,s}}{\Delta_x}$		
		Present FD Scheme (W=25μm, 500 grids)	FEM [19]	TMM [13] (2000 layers staircase approximation for graded index region)
X-cut Y-prop. APE-$LiNbO_3$	TE_0	0.7363	0.7360	0.7362
	TE_1	0.4277	0.4270	0.4274
	TE_2	0.1854	0.1840	0.1851
	TE_3	0.0286	0.0280	0.0284
Z-cut Y-prop. APE-$LiNbO_3$	TM_0	0.7394	-	0.7393
	TM_1	0.4376	-	0.4374
	TM_2	0.1990	-	0.1988
	TM_3	0.0392	-	0.0390

3.4.5. Samples with complicated index profiles

To demonstrate the applicability of the scheme for structures with complicated refractive index profiles, we take a Ti-indiffused proton-exchanged (TIPE) $LiNbO_3$ waveguide with SiO_2 buffer and air cover [1, 22]. To be more realistic, we have preserved the index gradient caused by Ti-indiffusion and the decrease in ordinary

index within the proton-exchanged region. With these assumptions we could expect a truncated half Gaussian index profile in Ti-indiffused only (TI) region, and a combination of half Gaussian and step index profile within the Ti-indiffused and proton-exchanged (TI+PE) region as depicted in Fig. 3.7. The index profile of this structure can be expressed as

$$n_o(x) = n_{os} + \Delta_{TI_o} \exp\left[-\frac{(x_2 - x)^2}{d_{TI}^2}\right] \quad \text{for } x \le x_1 \quad (3.29a)$$

$$n_o(x) = n_{os} + \Delta_{PE_o} + \Delta_{TI_o} \exp\left[-\frac{(x_2 - x)^2}{d_{TI}^2}\right] \quad \text{for } x_1 < x \le x_2 \quad (3.29b)$$

$$n_o(x) = n_b \quad \text{for } x_2 < x \le x_3 \quad (3.29c)$$

$$n_o(x) = n_c \quad \text{for } x > x_3 \quad (3.29d)$$

for the ordinary index, and

$$n_e(x) = n_{es} + \Delta_{TI_e} \exp\left[-\frac{(x_2 - x)^2}{d_{TI}^2}\right] \quad \text{for } x \le x_1 \quad (3.30a)$$

$$n_e(x) = n_{es} + \Delta_{PE_e} + \Delta_{TI_e} \exp\left[-\frac{(x_2 - x)^2}{d_{TI}^2}\right] \quad \text{for } x_1 < x \le x_2 \quad (3.30b)$$

$$n_e(x) = n_b \quad \text{for } x_2 < x \le x_3 \quad (3.30c)$$

$$n_e(x) = n_c \quad \text{for } x > x_3 \quad (3.30d)$$

for the extra-ordinary index. For an X-cut Y-propagating substrate, we will have $n_{xx}(x)=n_{zz}(x)=n_o(x)$ and $n_{yy}(x)=n_e(x)$.

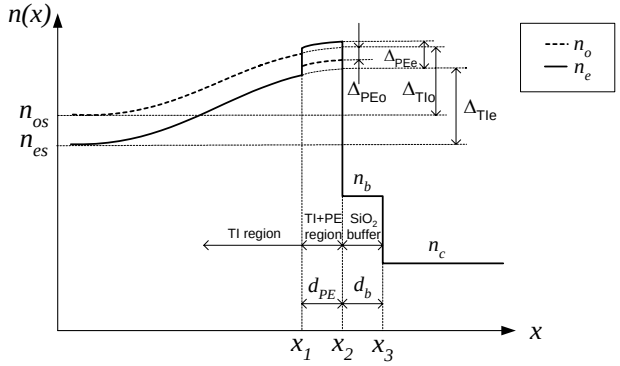

Figure 3.7. *Refractive index profile of TIPE sample.*

The calculated result for n_{es}=2.2, n_{os}=2.286, n_b=1.45, n_c=1.0, Δ_{TIe}=0.014, Δ_{TIo}=0.009, Δ_{PEe}=0.11, Δ_{PEo}=-0.04, d_{TI} =3μm, d_{PE} =x_2-x_1=1μm, d_b= x_3-x_2=1μm, and vacuum wavelength λ=0.6328μm are presented in Table 3.4 along with the results of TMM. It should be noted from Fig. 3.7, that for the X-cut Y-propagating substrate, the value of Δ_y and Δ_x being used in Table 3.4 are Δ_e=Δ_{TIe}+Δ_{PEe} and Δ_o=max(Δ_{TIo}+Δ_{PEo},

$\Delta_{TIo}\exp(-d_{PE}^2/d_{TI}^2)$), respectively. For TMM calculation, we have used 2000 and 1000 layers with uniform thickness to staircase-approximate the gradient index within TI and TI+PE regions, respectively. This approximation is taken into TI region up to $3d_{TI}$ depth. As can be seen from the table, this structure supports different number of modes for the two polarizations due to the different index contrast between ordinary and extra-ordinary index. The table also shows that the results of present scheme agree nicely with the results of TMM.

Table 3.4. *Calculation results for TIPE sample.*

Modes	$b_{TE}=\frac{n_{eff}-n_{yy,s}}{\Delta_y}$ $\quad b_{TM}=\frac{n_{eff}-n_{xx,s}}{\Delta_x}$	
	Present FD scheme (W=15μm, Δx=0.01μm)	TMM [13] (2000 layers at TI region, 1000 layers at TI+PE region)
TE0	0.87510	0.87507
TE1	0.51915	0.51900
TE2	0.05688	0.05681
TE3	0.01794	0.01786
TM0	0.40744	0.40745
TM1	0.02127	0.02127

3.5. Conclusions

A finite difference scheme for planar waveguides composed of segments with different index profile functions was derived for both TE and TM polarizations by taking into account the gradient of the refractive indices and the effect of index discontinuities which lead to 2^{nd}-order accuracy in the calculated effective indices. Beside the interface correction, discretizations at boundaries are also being taken into account by using the exponentially decaying nature of guided fields. The scheme was implemented for anisotropic waveguide with diagonal permittivity tensor and examined by using samples with index profiles of increasing complexity. The results show good agreement with results obtained by other methods.

Acknowledgements

We would like to thank Dr. K.A. Remley and Prof. A. Weisshaar from Oregon State Univ. for providing their impedance boundary method of moments results for verification during the development of this work, and Prof. E.F. Kuester from Univ. Colorado at Boulder for providing information on the transverse impedance method.

References

1. M. de Micheli, "Nonlinear effects in TIPE-$LiNbO_3$ waveguides for optical communications," **J. Opt. Commun.**, Vol. 4, pp. 25-31, 1983.
2. P.L. Auger and S.I. Najafi, "Potassium- and silver-double-ion-exchanged slab glass waveguides: characterization and modeling," **Appl. Optics**, Vol. 33, No. 16, pp. 3333-3337, 1994.
3. Y.N. Korkishko, V.A. Fedorov, and O.Y. Feoktistova, "$LiNbO_3$ optical waveguide fabrication by high-temperature proton exchange," **J. Lightwave Technol.**, Vol. 18, No. 4, pp. 562-568, 2000.
4. C. Vassallo, "Interest of improved three-point formulas for finite-difference modeling of optical devices," **J. Opt. Soc. Am. A.**, Vol. 14, No. 12, pp. 3273-3284, 1997.
5. C. Vassallo, "Improvement of finite-difference methods for step-index optical waveguides," **IEE Proc. J. Optoelectronics**, Vol. 139, No. 2, pp. 137-142, 1992.
6. H.J.W.M. Hoekstra, G.J.M. Krijnen, and P.V. Lambeck, "Efficient interface conditions for the finite-difference beam propagation method," **J. Lightwave Technol.**, Vol. 10, No. 10, pp. 1352-1355, 1992.
7. J. Yamauchi *et al.*, "Modified finite-difference formula for the analysis of semivectorial modes in step-index optical waveguides," **Photonics Technol. Lett.**, Vol. 9, No. 7, pp. 961-963, 1997.
8. R. Stoffer and H.J.W.M. Hoekstra, "Efficient interface conditions based on a 5-point finite difference operator," **Opt. Quantum Electron.**, Vol. 30, No. 5-6, pp. 375-383, 1998.
9. Y.P. Chiou, Y.C. Chiang, and H.C. Chang, "Improved three-point formulas considering the interface conditions in the finite-difference analysis of step-index optical devices," **J. Lightwave Technol.**, Vol. 18, No. 2, pp. 243-251, 2000.
10. H.A. Jamid and M.N. Akram, "A new higher order finite-difference approximation scheme for the method of lines," **J. Lightwave Technol.**, Vol. 19, No. 3, pp. 398-404, 2001.
11. H.P. Uranus, H.J.W.M. Hoekstra, and E. van Groesen, "Second-order finite difference discretization for TM polarization of anisotropic planar waveguides with arbitrary index profiles," Internal Technical Report, IOMS and AAMP, Univ. Twente, 2002.
12. J. Chilwell and I. Hodgkinson, "Thin-films field-transfer matrix theory of planar multilayer waveguides and reflection from prism-loaded waveguides," **J. Opt. Soc. Am. A**, Vol. 1, No. 7, pp. 742-753, 1984.
13. http://www.math.utwente.nl/~uranushp/freesoft.htm.
14. E.M. Conwell, "Modes in optical waveguides formed by diffusion," **Appl. Phys. Lett.**, Vol. 23, No. 6, pp. 328-329, 1973.

15. W.W. Lui, K. Yokoyama, and W.P. Huang, "Asymmetric discretization of wave equation as boundary condition in modal analysis," **J. Sel. Topics on Quantum Electron**., Vol. 2, No. 2, pp. 174-180, 1996.

16. P.K. Mishra and A. Sharma, "Analysis of single mode inhomogeneous planar waveguides," **J. Lightwave Technol.**, Vol. LT-4, No. 2, pp. 204-212, 1986.

17. A. Sharma and P. Bindal, "Analysis of diffused planar and channel waveguides," **J. Quantum Electron.**, Vol. 29, No. 1, pp. 150-153, 1993.

18. I.C. Goyal, R. Jindal, and A.K. Ghatak, "Planar optical waveguides with arbitrary index profile: an accurate method of analysis," **J. Lightwave Technol.**, Vol. 15, No. 11, pp. 2179-2182, 1997.

19. F.A. Katsriku, B.M.A. Rahman, and K.T.V. Grattan, "Finite element analysis of diffused anisotropic optical waveguides," **J. Lightwave Technol.**, Vol. 14, No. 5, pp. 780-786, 1996.

20. E.F. Kuester and D.C. Chang, "Propagation, attenuation, and dispersion characteristics of inhomogeneous dielectric slab waveguides," **Microwave Theory and Tech.**, Vol. MTT-23, No. 1, pp. 98-106, 1975.

21. H.J.W.M. Hoekstra *et al.*, "Beam-propagation method for second-harmonic generation in waveguides with birefringent materials," **J. Opt. Soc. Am. B**, Vol. 14, No. 7, pp. 1823-1830, 1997.

22. K.A. Remley and A. Weisshaar, "Impedance boundary method of moments with extended boundary conditions," **J. Lightwave Technol.**, Vol. 13, No. 12, pp. 2372-2377, 1995.

Chapter 4

High-order variational finite element mode solver for anisotropic planar waveguides

A variational finite element scheme that gives 4^{th}-order accuracy by using only linear basis functions within the computational domain is reported for the mode solving of anisotropic planar waveguides with a diagonal permittivity tensor. A quasi-uniform mesh is used to get rid of the necessity to incorporate interface corrections and higher-order basis functions, while Richardson-like extrapolation is used to obtain 4^{th}-order accuracy. The scheme was derived for both TE and TM mode analysis and completed with infinite elements as transparent boundary conditions. For structures with a graded-index exterior domain, the boundary conditions employ basis functions adopted from the WKB method. Together with the effective index method, the application of the scheme for semivectorial analysis of indiffused channel waveguides made in a uniaxial crystal will be demonstrated.

This chapter is adapted from:
H.P. Uranus, H.J.W.M. Hoekstra, and E. van Groesen, "Fourth-order variational mode solving for anisotropic planar structures," **J. Nonlinear Opt. Phys. and Materials**, Vol. 12, No. 2, pp. 247-261, 2003.
H.P. Uranus, H.J.W.M. Hoekstra, and E. van Groesen, "Analysis of integrated optical waveguides," **J. Indonesian Math. Soc. (MIHMI)**, Vol. 8, No. 4, pp. 49-62, 2002.

High-order variational finite element mode solver for anisotropic planar waveguides

4.1. Introduction

Materials that exhibit anisotropy are widely used in realizing integrated optical devices. Among others are ferro-electric crystals like $LiNbO_3$, $LiTaO_3$, KDP, KTP, etc. which have large electro-optic coefficients [1], amorphous materials like silicon oxynitride (SiO_xN_y) which can be fabricated using silicon-compatible technologies and has a relatively wide refractive index range [2], and poled-polymers with their prospect for the realization of cheap devices [3]. Hence, waveguiding analysis of structures with optical anisotropy is important for the design and characterization of such devices.

Accuracy is one of the main issues in numerical and approximate methods for optical waveguide analysis. High accuracy is generally preferable, but this feature is usually achieved at the expense of the efficiency, i.e. the computational time and memory requirements. Additionally, it used to introduce more complexity in the method. A variational finite element (FE) scheme with 4^{th}-order accuracy for transverse discretization of isotropic structure by using Richardson-like extrapolation has been proposed by Stoffer *et al.* [4] for BPM. In this scheme, linear basis functions are used for regions of uniform index while cubic basis functions are needed around index discontinuities.

In this chapter, we describe a scheme almost similar to Stoffer's scheme, but instead of using higher-order basis functions at the interfaces, quasi-uniform meshes are employed in order to retain the 4^{th}-order accuracy and extend the scheme also for analyzing modes of anisotropic structures. The scheme does not need complicated interface correction, hence it is simple and requires only modest computational effort. The scheme is completed with infinite elements as the transparent boundary conditions (TBC) that are exact for homogeneous exterior domains and presented for both TE- and TM-polarized guided-mode analysis of anisotropic planar structures with diagonal permittivity tensor. For structures with anisotropic graded-index (inhomogeneous) exterior domain, approximate boundary conditions by using basis functions adopted from the Wentzel-Kramers-Brillouin (WKB) method is also proposed. Although we only present the scheme for 4^{th}-order accuracy (in the interior domain), in principle it can be extended to 6^{th}-, 8^{th}-, or even higher-order accuracy with the same simplicity. Additionally, we introduce a simple extrapolation scheme by using two consecutive calculation results to further refine the results. We also combine the FE scheme with

the effective index method (EIM), and apply the hybrid method for semivectorial analysis of indiffused channel waveguides made in uniaxial crystals.

This chapter is organized as follows. After a variational formalism for the problem and its implementation using 1-D finite elements are described, a simple upgrade to a higher order scheme by using Richardson-like extrapolation is presented. Afterward, the application of infinite elements for the TBC, the additional extrapolation scheme to enhance the accuracy, and the semivectorial EIM for channel waveguides with uniaxial materials will be discussed. The scheme is finally illustrated by using samples composed of either isotropic or anisotropic materials. The results confirm the expected order of accuracy, the effectiveness of the boundary conditions and the additional extrapolation.

4.2. Description of the method

4.2.1. Variational finite element method

In this chapter we consider waveguides, which are composed of non-magnetic, source-free, and lossless materials with the anisotropy principal axes parallel to the axes of the Cartesian coordinate of the structure. We assumed that the *z*-axis is the propagation direction. In general, we consider planar structures with refractive indices vary only in the *x* direction. Additionally, by incorporating the EIM, we also consider channel structures with refractive indices vary in both *x* and *y* directions, which can be approximated by successive planar structures. For the *x*-variant planar system, it is possible to have uncoupled TE- and TM-polarized waves with corresponding scalar Helmholtz's equations

$$\left[d_{xx} + k_0^2 \left(n_{yy}^2(x) - n_{eff}^2 \right) \right] E_y(x) = 0 \qquad \text{for TE} \qquad (4.1)$$

and

$$\left[d_x \left(\frac{1}{n_{zz}^2(x)} d_x \right) + k_0^2 \left(1 - \frac{n_{eff}^2}{n_{xx}^2(x)} \right) \right] H_y(x) = 0 \qquad \text{for TM,} \qquad (4.2)$$

while the *y*-variant planar structures follow similarly.

The following functionals

$$F = \frac{1}{2} \int_{-\infty}^{\infty} \left[-\left(d_x E_y(x) \right)^2 + k_0^2 \left[n_{yy}^2(x) - n_{eff}^2 \right] E_y^2(x) \right] dx \qquad (4.3)$$

and

$$F = \frac{1}{2} \int_{-\infty}^{\infty} \left[-\frac{1}{n_{zz}^2(x)} \left(d_x H_y(x) \right)^2 + k_0^2 \left(1 - \frac{n_{eff}^2}{n_{xx}^2(x)} \right) H_y^2(x) \right] dx \qquad (4.4)$$

can be associated with differential equations (4.1) and (4.2), respectively. Since the Euler-Lagrange equations of the functionals correspond to the original wave equations, the solutions of the latter equations can be approximated by extremization of the functionals. The functions are approximated using interpolation of polynomial basis functions and the functionals are discretized in a finite number of elements within the computational domain, while outside the computational domain, infinite elements (elements that extend to + or - infinity) are used. The extremization of the discretized functionals are then carried out by finding the combination of the interpolation coefficients where the gradient of the discretized functional is zero as in eq. (2.23).

For element *j*, located between node *j* and *j+1*, not located at the computational boundary, and has no interface within it, by expressing the function as interpolation of linear basis functions as illustrated in Fig. 2.3, we obtain

$$\frac{\partial \tilde{F}}{\partial \varphi_j} = c_{1,j}\varphi_{j-1} + c_{2,j}\varphi_j + c_{3,j}\varphi_{j+1} - n_{eff}^2\left(c_{4,j}\varphi_{j-1} + c_{5,j}\varphi_j + c_{6,j}\varphi_{j+1}\right) \tag{4.5}$$

for TE-polarized waves, and

$$\frac{\partial \tilde{F}}{\partial \varphi_j} = c_{7,j}\varphi_{j-1} + c_{8,j}\varphi_j + c_{9,j}\varphi_{j+1} - n_{eff}^2\left(c_{10,j}\varphi_{j-1} + c_{11,j}\varphi_j + c_{12,j}\varphi_{j+1}\right) \tag{4.6}$$

for TM-polarized waves, with

$$c_{1,j} = \frac{1}{\Delta x_{j-1}} + \frac{1}{6}k_0^2 n^2_{yy,j-\frac{1}{2}}\Delta x_{j-1} \tag{4.7a}$$

$$c_{2,j} = -\left(\frac{1}{\Delta x_{j-1}} + \frac{1}{\Delta x_j}\right) + \frac{1}{3}k_0^2\left(n^2_{yy,j-\frac{1}{2}}\Delta x_{j-1} + n^2_{yy,j+\frac{1}{2}}\Delta x_j\right) \tag{4.7b}$$

$$c_{3,j} = \frac{1}{\Delta x_j} + \frac{1}{6}k_0^2 n^2_{yy,j+\frac{1}{2}}\Delta x_j \tag{4.7c}$$

$$c_{4,j} = \frac{1}{6}k_0^2\Delta x_{j-1} \tag{4.7d}$$

$$c_{5,j} = \frac{1}{3}k_0^2\left(\Delta x_{j-1} + \Delta x_j\right) \tag{4.7e}$$

$$c_{6,j} = \frac{1}{6}k_0^2\Delta x_j \tag{4.7f}$$

$$c_{7,j} = \frac{1}{n^2_{zz,j-\frac{1}{2}}\Delta x_{j-1}} + \frac{1}{6}k_0^2\Delta x_{j-1} \tag{4.7g}$$

$$c_{8,j} = -\left(\frac{1}{n^2_{zz,j-\frac{1}{2}}\Delta x_{j-1}} + \frac{1}{n^2_{zz,j+\frac{1}{2}}\Delta x_j}\right) + \frac{1}{3}k_0^2\left(\Delta x_{j-1} + \Delta x_j\right) \tag{4.7h}$$

$$c_{9,j} = \frac{1}{n^2_{zz,j+\frac{1}{2}}\Delta x_j} + \frac{1}{6}k_0^2\Delta x_j \tag{4.7i}$$

$$c_{10,j} = k_0^2 \frac{\Delta x_{j-1}}{6n^2_{xx,j-\frac{1}{2}}} \tag{4.7j}$$

$$c_{11,j} = \frac{1}{3} k_0^2 \left(\frac{\Delta x_{j-1}}{n^2_{xx,j-\frac{1}{2}}} + \frac{\Delta x_j}{n^2_{xx,j+\frac{1}{2}}} \right) \tag{4.7k}$$

$$c_{12,j} = k_0^2 \frac{\Delta x_j}{6n^2_{xx,j+\frac{1}{2}}} \tag{4.7l}$$

where for convenience, φ_j has been used to denote the value of the function at node j, which is $E_{y,j}$ for TE or $H_{y,j}$ for TM, while $\tilde{F}$ and Δx denote the discretized functional and mesh size, respectively. In eq. (4.7), we have approximated the relative permittivity within each element by taking their mid-point value as shown in Fig. 4.1. Equation (2.23) can then be written as a matrix generalized eigenvalue equation

$$\nabla \tilde{F} = \left(\mathbf{A} - n_{eff}^2 \mathbf{B} \right) \{\varphi\} = \{0\} \tag{4.8}$$

with **A** and **B** representing tridiagonal matrices with the non-zero elements of their j^{th} row consist of $c_{1,j}$ … $c_{3,j}$ for TE or $c_{7,j}$ … $c_{9,j}$ for TM; and $c_{4,j}$ … $c_{6,j}$ for TE or $c_{10,j}$ … $c_{12,j}$ for TM. Equation (4.8) can be solved for its eigenvalues (n_{eff}^2) and their corresponding eigenvectors $\{\varphi\}$, which are the approximate solutions of the corresponding Helmholtz's equation.

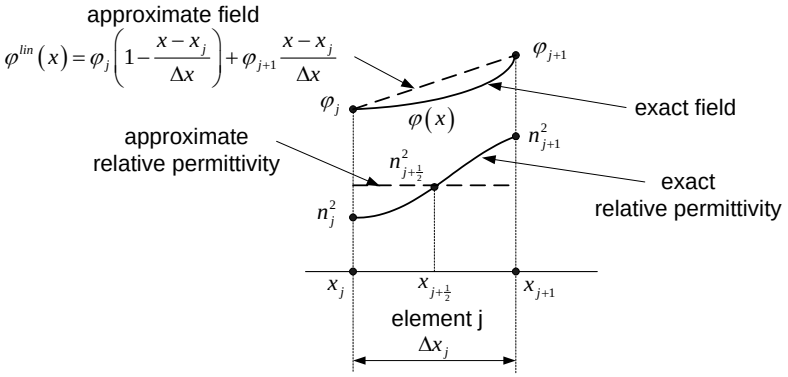

Figure 4.1. *Approximating the field function by interpolation using linear basis functions and the graded relative permittivity by their mid-point value within element j.*

The use of interpolation of linear basis functions to approximate the function and taking the mid-point values to approximate the structure (possibly graded) relative permittivity implies that only 3rd-order local error can be obtained for integration within the functional at element located between node j and $j+1$ as follows:

$$F_{j\div j+1} = \tilde{F}^{lin}_{j\div j+1} + \Delta x_j^3\, err(x_{j+\frac{1}{2}}) + O(\Delta x_j^5) \qquad (4.9)$$

which could be obtained by using Taylor's expansion around $x_{j+\frac{1}{2}}$. In eq. (4.9), $F_{j\div j+1}$ denotes the exact value of the functional between grid *j* and *j+1*, while $\tilde{F}^{lin}_{j\div j+1}$ the discretized functional using interpolation of linear basis functions. For the case of uniform mesh size, there will be $\Omega/\Delta x$ meshes within the computational domain Ω, which implies only 2nd-order global error of the results.

4.2.2. Richardson-like extrapolation and mesh-evenization scheme

To achieve 4th-order accuracy, we use Richardson-like extrapolation that combines integration results of different mesh sizes to eliminate the 3rd-order local error term in eq. (4.9). By taking $\Delta x_j = \Delta x_{j+1}$ and combine the integration results with the results of $2\Delta x_j$-sized mesh, we get rid of the 3rd-order error term for local integration interval between grid *j* and *j+2* as follows:

$$F_{j\div j+2} = \tfrac{4}{3}\tilde{F}^{lin}_{j\div j+2,\Delta x_j} - \tfrac{1}{3}\tilde{F}^{lin}_{j\div j+2,2\Delta x_j} + O(\Delta x_j^5) \qquad (4.10)$$

with $\tilde{F}^{lin}_{j\div j+2,\Delta x_j}$ denotes the integration of the discretized functional between node *j* and *j+2* using linear basis functions for normal-sized (Δx_j-sized) mesh and $\tilde{F}^{lin}_{j\div j+2,2\Delta x_j}$ for double-sized ($2\Delta x_j$-sized) mesh. In this way, matrices **A** and **B** will become penta-diagonal.

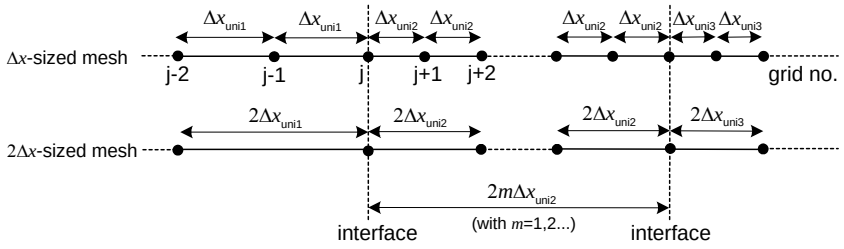

Figure 4.2. *Mesh-evenization scheme that gives quasi-uniform meshes.*

To keep the scheme simple, we use quasi-uniform meshes as depicted in Fig. 4.2, where meshes in a segment (i.e. substructure in-between two adjacent interfaces) are uniform, but meshes of different segments can be slightly different due to an evenization scheme. We term this meshing scheme as the mesh-evenization scheme. This scheme avoids the necessity of either incorporating complicated interface corrections or the use of higher-order basis functions at interfaces to retain the accuracy. Here, to get rid of the complicated interface corrections, we put the node exactly at the interface, hence the integration within each element will not cross the interface. To have the Richardson-like extrapolation to work correctly at interfaces, we have forced the number of normal-sized mesh within each segment to be an even

number. By this mesh-evenization scheme, none of the integration interval, either the normal- or double-sized interval will cross the interfaces, hence the same form of eq. (4.5)-(4.7) with proper mesh sizes will remain valid in this formulation and 4th-order-like accuracy can be achieved in a simple way. The scheme can also be extended to 6th-, 8th-, or even higher-order accuracy with the same simplicity.

4.2.3. Transparent boundary conditions

A simple TBC is implemented for guided-wave analysis within this scheme by using a 1-D version of infinite element techniques [5]. In this case, the element outside the computational domain is extended to -∞ at the left boundary and to +∞ at the right boundary as shown in Fig. 4.3, and a proper selection of basis function is made to ensure the convergence of the integration of the functional within the element. In this way eqs. (4.3) and (4.4) can be written as

$$F = \frac{1}{2}\int_{-\infty}^{x_1}\left[-\left(d_x\varphi\right)^2 + k_0^2\left(n_{yy,s}^2 - n_{eff}^2\right)\varphi^2\right]dx + \sum_{j=1}^{N-1}F_j + \frac{1}{2}\int_{x_N}^{+\infty}\left[-\left(d_x\varphi\right)^2 + k_0^2\left(n_{yy,c}^2 - n_{eff}^2\right)\varphi^2\right]dx \tag{4.11}$$

and

$$F = \frac{1}{2}\int_{-\infty}^{x_1}\left[-\frac{1}{n_{zz,s}^2}\left(d_x\varphi\right)^2 + k_0^2\left(1-\frac{n_{eff}^2}{n_{xx,s}^2}\right)\varphi^2\right]dx + \sum_{j=1}^{N-1}F_j + \frac{1}{2}\int_{x_N}^{+\infty}\left[-\frac{1}{n_{zz,c}^2}\left(d_x\varphi\right)^2 + k_0^2\left(1-\frac{n_{eff}^2}{n_{xx,c}^2}\right)\varphi^2\right]dx \tag{4.12}$$

for TE- and TM-polarized wave, respectively. In these equations, subscripts *s* and *c* denote the substrate and cover of the structure, respectively. It is assumed that the substrate is located at the left hand side (*lhs*) and the cover at the right hand side (*rhs*) of the structure.

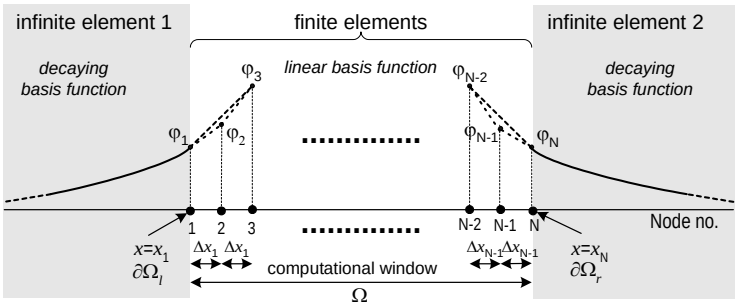

Figure 4.3 *Infinite elements as transparent boundary conditions for guided mode analysis.*

4.2.3.1. Infinite elements for a homogeneous exterior domain

For guided mode analysis of homogeneous exterior domain, we can use exponentially decaying basis function for the infinite element. For TE mode analysis, we use

$$\varphi_l(x) = \varphi_1 \exp\left[k_0\sqrt{n_{eff}^2 - n_{yy,s}^2}\,(x - x_1)\right] \tag{4.13a}$$

and

$$\varphi_r(x) = \varphi_N \exp\left[-k_0\sqrt{n_{eff}^2 - n_{yy,c}^2}\,(x - x_N)\right] \tag{4.13b}$$

while for TM mode analysis, we use

$$\varphi_l(x) = \varphi_1 \exp\left[k_0 \frac{n_{zz,s}}{n_{xx,s}}\sqrt{n_{eff}^2 - n_{xx,s}^2}\,(x - x_1)\right] \tag{4.14a}$$

and

$$\varphi_r(x) = \varphi_N \exp\left[-k_0 \frac{n_{zz,c}}{n_{xx,c}}\sqrt{n_{eff}^2 - n_{xx,c}^2}\,(x - x_N)\right] \tag{4.14b}$$

as basis functions within the infinite elements, where subscripts *l* and *r* denote the *lhs* and *rhs* infinite element, respectively. Since these functions are the exact solutions of guided waves for homogeneous exterior domains, the use of these exponential basis functions will lead to an exact TBC. As a result, the functionals can be written as

$$F = F_{\partial\Omega} + F_{\Omega} \tag{4.15a}$$

with

$$F_{\partial\Omega} = \varsigma\varphi d_x\varphi\Big|_{\partial\Omega_l}^{\partial\Omega_r} = \alpha_r\varphi_N^2 - \alpha_l\varphi_1^2 \tag{4.15b}$$

where $F_{\partial\Omega}$ and F_{Ω} denote the boundary terms contributed by the infinite elements and interior terms contributed by the finite elements, respectively. To get eq. (4.15b) we have used integration by parts, the fact that the fields vanish at $\pm\infty$, and eq. (4.1)-(4.2). For TE-polarized waves we will have

$$\varsigma = 1/2 \tag{4.16a}$$

$$\alpha_l = \frac{1}{2}k_0\sqrt{n_{eff}^2 - n_{yy,s}^2} \tag{4.16b}$$

and

$$\alpha_r = -\frac{1}{2}k_0\sqrt{n_{eff}^2 - n_{yy,c}^2} \tag{4.16c}$$

while for TM-polarized waves, they are

$$\varsigma = \frac{1}{2n_{zz,ext}^2} \qquad \text{with } ext=s,\ c \tag{4.17a}$$

$$\alpha_l = \frac{1}{2}k_0\frac{\sqrt{n_{eff}^2 - n_{xx,s}^2}}{n_{xx,s}n_{zz,s}} \tag{4.17b}$$

$$\alpha_r = -\frac{1}{2}k_0 \frac{\sqrt{n_{eff}^2 - n_{xx,c}^2}}{n_{xx,c} n_{zz,c}}. \tag{4.17c}$$

This implies that the $\frac{\partial \tilde{F}}{\partial \varphi_1}$ and $\frac{\partial \tilde{F}}{\partial \varphi_N}$ (the first and last rows in matrices **A** and **B**) differ from the other rows as follows

$$\frac{\partial \tilde{F}}{\partial \varphi_1} = c_{2,1}\varphi_1 + c_{3,1}\varphi_2 - n_{eff}^2 \left(c_{5,1}\varphi_1 + c_{6,1}\varphi_2 \right) \tag{4.18}$$

$$\frac{\partial \tilde{F}}{\partial \varphi_N} = c_{1,N}\varphi_{N-1} + c_{2,N}\varphi_N - n_{eff}^2 \left(c_{4,N}\varphi_{N-1} + c_{5,N}\varphi_N \right) \tag{4.19}$$

for TE, and

$$\frac{\partial \tilde{F}}{\partial \varphi_1} = c_{8,1}\varphi_1 + c_{9,1}\varphi_2 - n_{eff}^2 \left(c_{11,1}\varphi_1 + c_{12,1}\varphi_2 \right) \tag{4.20}$$

$$\frac{\partial \tilde{F}}{\partial \varphi_N} = c_{7,N}\varphi_{N-1} + c_{8,N}\varphi_N - n_{eff}^2 \left(c_{10,N}\varphi_{N-1} + c_{11,N}\varphi_N \right) \tag{4.21}$$

for TM, with

$$c_{2,1} = -\frac{1}{\Delta x_1} + \frac{1}{3}k_0^2 n^2_{yy,1\frac{1}{2}} \Delta x_1 - k_0 \sqrt{n_{eff}^2 - n_{yy,s}^2} \tag{4.22a}$$

$$c_{2,N} = -\frac{1}{\Delta x_{N-1}} + \frac{1}{3}k_0^2 n^2_{yy,N-\frac{1}{2}} \Delta x_{N-1} - k_0 \sqrt{n_{eff}^2 - n_{yy,c}^2} \tag{4.22b}$$

$$c_{5,1} = \frac{1}{3}k_0^2 \Delta x_1 \tag{4.22c}$$

$$c_{5,N} = \frac{1}{3}k_0^2 \Delta x_{N-1} \tag{4.22d}$$

$$c_{8,1} = -\frac{1}{n^2_{zz,1\frac{1}{2}} \Delta x_1} + \frac{1}{3}k_0^2 \Delta x_1 - k_0 \frac{\sqrt{n_{eff}^2 - n_{xx,s}^2}}{n_{xx,s} n_{zz,s}} \tag{4.22e}$$

$$c_{8,N} = -\frac{1}{n^2_{zz,N-\frac{1}{2}} \Delta x_{N-1}} + \frac{1}{3}k_0^2 \Delta x_{N-1} - k_0 \frac{\sqrt{n_{eff}^2 - n_{xx,c}^2}}{n_{xx,c} n_{zz,c}} \tag{4.22f}$$

$$c_{11,1} = \frac{1}{3}k_0^2 \frac{\Delta x_1}{n^2_{xx,1\frac{1}{2}}} \tag{4.22g}$$

$$c_{11,N} = \frac{1}{3}k_0^2 \frac{\Delta x_{N-1}}{n^2_{x,N-\frac{1}{2}}} \tag{4.22h}$$

while $c_{3,1}$, $c_{6,1}$, $c_{1,N}$, $c_{4,N}$, $c_{9,1}$, $c_{12,1}$, $c_{7,N}$, and $c_{10,N}$ remain the same as in eq. (4.7). The last terms of eq. (4.22a), (4.22b), (4.22e), and (4.22f) are attributed to the infinite elements.

4.2.3.2. Infinite elements for an inhomogeneous exterior domain

For graded-index exterior domain, we chose basis functions adopted from the *WKB* approximation [6], i.e.

$$\varphi_l(x) = \frac{A}{\gamma^{\frac{1}{2}}(x)} \exp\left[-\int_{x}^{x_{t,l}} \gamma(x)dx\right] \tag{4.23a}$$

for the *lhs* and

$$\varphi_r(x) = \frac{B}{\gamma^{\frac{1}{2}}(x)} \exp\left[-\int_{x_{t,r}}^{x} \gamma(x)dx\right] \tag{4.23b}$$

for the *rhs* infinite element, with with $x_{t,l}$ and $x_{t,r}$ denote the *lhs* and *rhs* turning points (i.e. the points where the field changes from oscillatory to decaying profile), respectively. In eq. (4.23), A and B are constants that depend on the turning points position, while

$$\gamma(x) = k_0\sqrt{n_{eff}^2 - n_{yy}^2(x)} \tag{4.24}$$

for TE-, and

$$\gamma(x) = k_0 \frac{n_{zz}(x)}{n_{xx}(x)}\sqrt{n_{eff}^2 - n_{xx}^2(x)} \tag{4.25}$$

for TM-polarized waves. The computational boundaries should be located beyond the turning points, i.e. at position where $n_{eff} > n_{yy}$ for TE and $n_{eff} > n_{xx}$ for TM. By substituting eq. (4.23) into the boundary terms of the functionals, we get

$$\alpha_l = \frac{1}{2}\left[\frac{d_x n_{yy}^2(x_1)}{4\left[n_{eff}^2 - n_{yy}^2(x_1)\right]} + k_0\sqrt{n_{eff}^2 - n_{yy}^2(x_1)}\right] \tag{4.26a}$$

and

$$\alpha_r = \frac{1}{2}\left[\frac{d_x n_{yy}^2(x_N)}{4\left[n_{eff}^2 - n_{yy}^2(x_N)\right]} - k_0\sqrt{n_{eff}^2 - n_{yy}^2(x_N)}\right] \tag{4.26b}$$

for TE, and

$$\alpha_l = \frac{n_{xx}^4(x_1)d_x n_{zz}^2(x_1) - n_{eff}^2\left[n_{xx}^2(x_1)d_x n_{zz}^2(x_1) - n_{zz}^2(x_1)d_x n_{xx}^2(x_1)\right]}{8n_{xx}^2(x_1)n_{zz}^4(x_1)\left[n_{eff}^2 - n_{xx}^2(x_1)\right]}$$
$$+\frac{1}{2}k_0\frac{\sqrt{n_{eff}^2 - n_{xx}^2(x_1)}}{n_{xx}(x_1)n_{zz}(x_1)} \tag{4.27a}$$

$$\alpha_r = \frac{n_{xx}^4(x_N)d_x n_{zz}^2(x_N) - n_{eff}^2\left[n_{xx}^2(x_N)d_x n_{zz}^2(x_N) - n_{zz}^2(x_N)d_x n_{xx}^2(x_N)\right]}{8n_{xx}^2(x_N)n_{zz}^4(x_N)\left[n_{eff}^2 - n_{xx}^2(x_N)\right]}$$
$$-\frac{1}{2}k_0\frac{\sqrt{n_{eff}^2 - n_{xx}^2(x_N)}}{n_{xx}(x_N)n_{zz}(x_N)} \tag{4.27b}$$

for TM. It is worth noting that if the exterior domain is homogeneous, eqs. (4.26) and (4.27) will reduce to (4.16) and (4.17), respectively. Hence, the WKB-based basis functions will also result in exact TBC for this particular case, while for the inhomogeneous exterior domain it is approximate.

The boundary conditions induce non-linearity to the generalized eigenvalue equation. In this chapter, we handle this situation by using bisection root searching algorithm to solve the dispersion relation $\det(\mathbf{A} - n_{eff}^2 \mathbf{B})=0$.

4.2.4. Additional extrapolation

As will be shown later, by a proper choice of the average mesh size and neglecting the higher order terms, the error profile of the results of the proposed scheme will follow

$$ord \simeq \frac{\log\left(Err_k / Err_l\right)}{\log\left(\Delta\bar{x}_k / \Delta\bar{x}_l\right)} \tag{4.28}$$

with *ord* denotes the order of accuracy (2 for scheme without and 4 for scheme with Richardson-like extrapolation), $\Delta\bar{x}_k$ and $\Delta\bar{x}_l$ the average mesh sizes for k^{th} and l^{th} computation, respectively, while Err_k and Err_l are the relative errors in the calculated effective indices of corresponding computations which can be expressed as

$$Err_\eta = \frac{\left| n_{eff,calc\_\eta} - n_{eff,ex} \right|}{n_{eff,ex}} \qquad \text{with } \eta = k, l \,. \tag{4.29}$$

In eq. (4.29), $n_{eff,calc\_k}$ and $n_{eff,calc\_l}$ denote the effective indices resulted from k^{th} and l^{th} computation, respectively, while $n_{eff,ex}$ denotes the exact effective index. This relation can be used to further refine the results by using calculated results taken from two different mesh sizes. By substituting eq. (4.29) into eq. (4.28), we arrive at

$$n_{eff,extrapolate} = \frac{\left(\frac{\Delta\bar{x}_k}{\Delta\bar{x}_l}\right)^{ord} n_{eff,calc\_l} - n_{eff,calc\_k}}{\left(\frac{\Delta\bar{x}_k}{\Delta\bar{x}_l}\right)^{ord} - 1} \tag{4.30}$$

In eq. (4.30) we have taken $sign\left(n_{eff,calc\_k} - n_{eff,ex}\right) = sign\left(n_{eff,calc\_l} - n_{eff,ex}\right)$, which comes from the systematic property of the error term in eq. (4.9) and (4.10).

Since a small fluctuation remains in the computational results induced by the quasi-uniform discretization scheme and the higher order error terms (see e.g. Fig. 4.4-4.6), better results could be achieved by using more calculated points and implementing data fitting techniques.

4.2.5. Semivectorial analysis of diffused channel waveguides in uniaxial crystal

In this section, we will show that the planar solver discussed earlier can be used for semivectorial analysis of indiffused channel waveguides made in uniaxial crystals. This is applicable for the case where the crystals are cut in a specific way, such that the electric field polarized in the direction normal to the surface of the substrate feels the extraordinary index (n_e), while the other two orthogonal fields experience the ordinary index (n_o). In this case, we incorporate the *EIM* to approximate the 2-D semivectorial wave equation with successive 1-D wave equations.

In this case, we make use of the slowly varying inhomogeneity (small $\partial_y n^2$) nature of the indiffused channel waveguides to reduce the vectorial wave equation into semivectorial formulation as in eq. (2.12). By doing so, and by taking $n_{xx}=n_e$ and $n_{yy}=n_{zz}=n_o$ for the specific cut of the crystals noted earlier, we get

$$\partial_x\left[\frac{1}{n_o^2}\partial_x\left(n_e^2E_x\right)\right]+\partial_{yy}E_x+k_0^2\left(n_e^2-n_{eff}^2\right)E_x=0 \qquad (4.31)$$

for quasi-TM waves. Following the same procedure as in section 2.2.3, the approximate solutions of this equation can be obtained by solving

$$d_x\left(\frac{1}{n_0^2}d_xP\right)+k_0^2\left(1-\frac{N_{eTM}^2}{n_e^2}\right)P=0 \qquad \text{for every } y \qquad (4.32a)$$

and

$$d_{yy}G+k_0^2(N_{eTM}^2(y)-n_{eff}^2)G=0 \qquad (4.32b)$$

successively, with

$$E_x=F(x,y)G(y) \qquad (4.33a)$$

and

$$P=n_e^2F\ . \qquad (4.33b)$$

Equations (4.32a) and (4.32b) can be solved by using 1-D TM and TE anisotropic mode solver discussed earlier, respectively.

In a similar way, for quasi-TE waves, we solve

$$\partial_{xx}H_x+\partial_{yy}H_x+k_0^2\left(n_0^2-n_{eff}^2\right)H_x=0 \qquad (4.34)$$

approximately by solving

$$d_{xx}R+k_0^2\left(n_o^2-N_{eTE}^2\right)R=0 \qquad \text{for every } y \qquad (4.35a)$$

and

$$d_{yy}S+k_0^2(N_{eTE}^2(y)-n_{eff}^2)S=0 \qquad (4.35b)$$

successively, with

$$H_x=R(x,y)S(y)\ . \qquad (4.36)$$

Both of eqs (4.35a) and (4.35b) can be solved using 1-D TE mode solver. It is worth noting that the sequence of applying the 1-D mode solver is different than the usual EIM [7] (see e.g. Fig. 2.5), as here we make use of the slowly varying lateral refractive indices, while the usual formulation of semivectorial EIM assumes linearly polarized fields to decouple the components of vectorial into semivectorial wave equation.

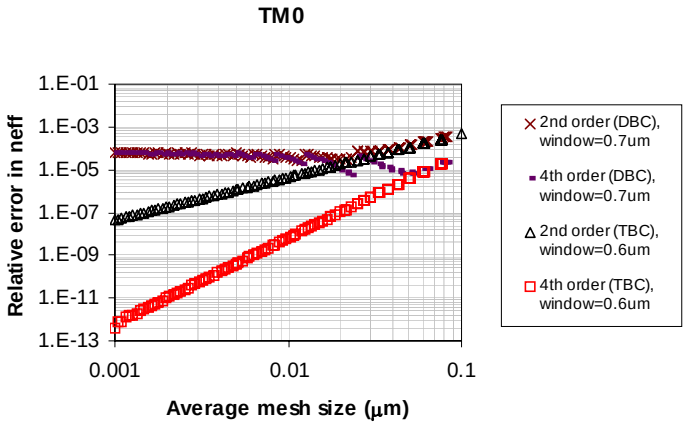

(a)

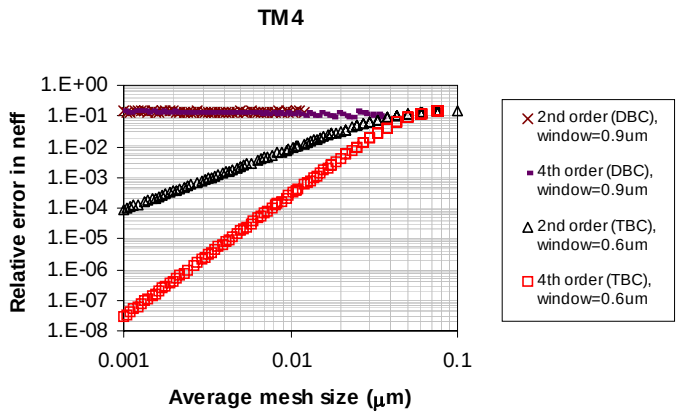

(b)

Figure 4.4. *Results of a 3-layer high-contrast isotropic waveguide. (a). TM_0 mode. (b). TM_4 mode.*

4.3. Numerical results

4.3.1. Isotropic waveguide

The first sample is a 3-layer isotropic structure with sub-wavelength film thickness and high index-contrast corresponding to an air-GaAs-air structure [8]. The refractive indices at λ=0.86μm for the substrate, film, and cover layers are n_s=1, n_f =3.6, and n_c=1, respectively, while the film thickness is 0.6 μm. The results for fundamental and highest order TM-polarized modes that were calculated using a computational window that has exactly the same size as the width of the guiding layer (only 0.6μm) for the proposed TBC are shown in Fig. 4.4. Here, the relative error in n_{eff} is as defined by eq. (4.29). The exact values of effective indices of this structure are calculated using transfer matrix method (TMM). Even with such a small computational window, the implemented TBC already gives nice results, while the DBC suffers from the error caused by the incorrect representation of the field at the computational boundary even when a larger computational window (0.7μm) is used. This superiority is more pronounced in the 4th- (highest-) order mode analysis. In this case, the DBC does not give any results unless the computational window is enlarged to 0.9μm, while the TBC gives good results starting from 0.6μm. Almost the same error profile was also obtained for TE polarization analysis. These results confirm the expected order of accuracy of the proposed scheme, which are 2nd-order for the scheme without and 4th-order for the scheme with Richardson-like extrapolation.

4.3.2. Anisotropic waveguide

As an anisotropic waveguide sample, we choose a 4-layer waveguide with isotropic substrate and cover and with 2 birefringent films [9]. The sample is composed of SiO_2 substrate with Silicon Oxynitride (SiO_xN_y) and calix[4]arene films on top of it and air as the covering layer. For light with a wavelength of 957.44 nm, the refractive indices of SiO_2, SiO_xN_y, calix[4]arene, and air are n_x=n_y=n_z=1.4526, n_x=1.6721 n_y=n_z=1.6738, n_x=1.5630 n_y=n_z=1.5622, and n_x=n_y=n_z=1, respectively. The thickness of the SiO_xN_y and calix[4]arene are 591 nm and 600 nm, respectively. There are 2 guided-modes for this structure, and the results for TE_0 and TM_0 modes are shown in Fig. 4.5. Again, the exact values of effective indices of this structure are calculated using the TMM [10] formulated for anisotropic media, and the calculation for the scheme with the TBC was carried out using a computational window of exactly the same size as the thickness of the guiding region. As shown in the figure, the order of the accuracy is as expected and the results of the scheme with TBC are much better than the one with DBC.

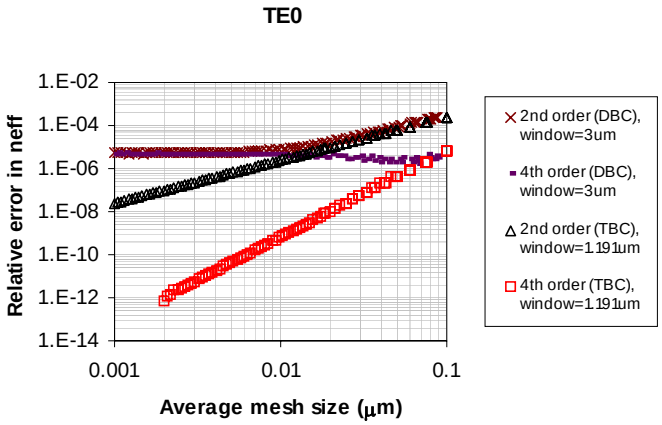

(a)

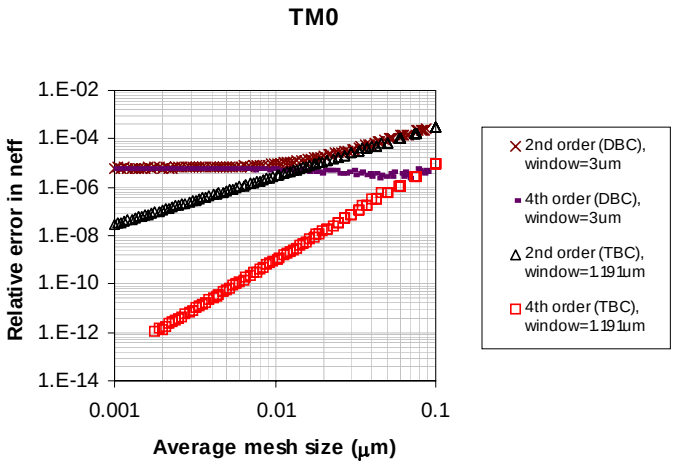

(b)

Figure 4.5. *The results for a 4-layer asymmetric waveguide with birefringent films. (a). TE_0 (b). TM_0.*

4.3.3. Effect of the computational window size

To further demonstrate the advantages of the TBC, we present calculations of the isotropic structure discussed earlier by using different window sizes. The results are depicted in Fig. 4.6. As can be seen from the results, the application of the TBC minimizes the error caused by incorrect representation of field values at the boundaries, which allows the computation to be carried out in a relatively small computational window, even as small as the thickness of the guiding region.

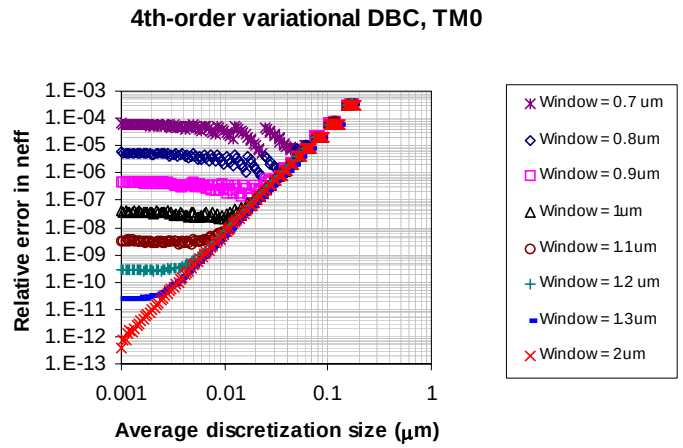

(a)

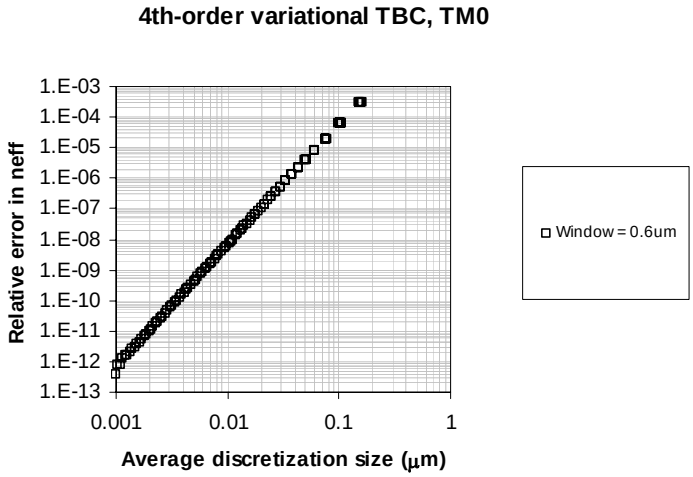

(b)

Figure 4.6. *The effect of window size for TM_0 analysis of the 3-layer isotropic waveguide. (a). 4^{th}-order scheme with DBC (b). 4^{th}-order scheme with TBC.*

4.3.4. Extrapolation results

As could be seen from the results of the scheme with TBC, for proper discretization size, the error profile follows eq. (4.28), hence we could use results from two consecutive calculations with different mesh sizes to further refine the results. For structures with an inhomogeneous exterior domain, since the boundary conditions

becomes approximate, this can only be carried out in the mesh- and window-size region where the total error is dominated by the interior discretization error (see e.g. Fig. 3.4). Table 4.1 and 4.2 show the extrapolated results for the 4-layer anisotropic structure discussed earlier by using 2^{nd}- and 4^{th}-order calculation results, respectively. The results are presented in terms of relative error in effective indices, which have been truncated to a few digits for clarity. All these results are obtained by computational window size of 1.191μm, which is just the thickness of the guiding region. These tables clearly show the refinement of the computational results by means of the simple extrapolation scheme.

Table 4.1. *Extrapolation using 2^{nd}-order results of the 4-layer anisotropic sample*

Mode	Before extrapolation				After extrapolation
	$\Delta\bar{x}_k$ (nm)	Err_k	$\Delta\bar{x}_l$ (nm)	Err_l	Err
TE0	100	2.45E-4	30	2.20E-5	3.83E-7
TE1		9.46E-4		8.61E-5	2.72E-6
TM0	30	2.57E-5	3	2.72E-7	3.33E-9
TM1		9.24E-5		9.78E-7	9.74E-9

Table 4.2. *Extrapolation using 4^{th}-order results of the 4-layer anisotropic sample*

Mode	Before extrapolation				After extrapolation
	$\Delta\bar{x}_k$ (nm)	Err_k	$\Delta\bar{x}_l$ (nm)	Err_l	Err
TE0	100	6.39E-6	30	5.26E-8	2.81E-9
TE1		1.01E-4		8.61E-7	7.30E-8
TM0	30	7.40E-8	3	8.28E-12	1.43E-13
TM1		9.58E-7		1.08E-10	2.88E-12

4.3.5. Ti-indiffused channel waveguide

We consider a multimode channel waveguide made by Ti-indiffusion into Z-cut Y-propagating $LiNbO_3$ crystal with index profiles

$$n_{o,e}(x,y) = ns_{o,e} + \Delta_{o,e} f_{o,e}(x) g_{o,e}(y) \qquad \text{for } x \le 0 \qquad (4.37a)$$

and

$$n_{o,e}(x,y) = n_c \qquad \text{for } x > 0 \qquad (4.37b)$$

with subscripts *o* and *e* denote the ordinary and extraordinary index, respectively, while *ns* denotes the bulk crystal refractive index, and *f(x)* and *g(y)* denote the normalized index profile functions. In this case, we take light vacuum wavelength λ=0.6328μm, ns_o=2.286, ns_e=2.2, n_c=1, and $\Delta_o=\Delta_e$=0.01. We assume exponential index profile in vertical (*x*) direction and Gaussian index profile in lateral (*y*) direction of the diffused channel, which reads as

$$f_{o,e}(x) = \exp\left(-\frac{|x|}{d_{x_{o,e}}}\right) \qquad (4.38a)$$

and

$$g_{o,e}(y) = \exp\left(-\frac{y^2}{d_{y_{o,e}}^2}\right) \tag{4.38b}$$

We take $d_{xo}=d_{xe}=6\mu m$ and $d_{yo}=d_{ye}=3\mu m$.

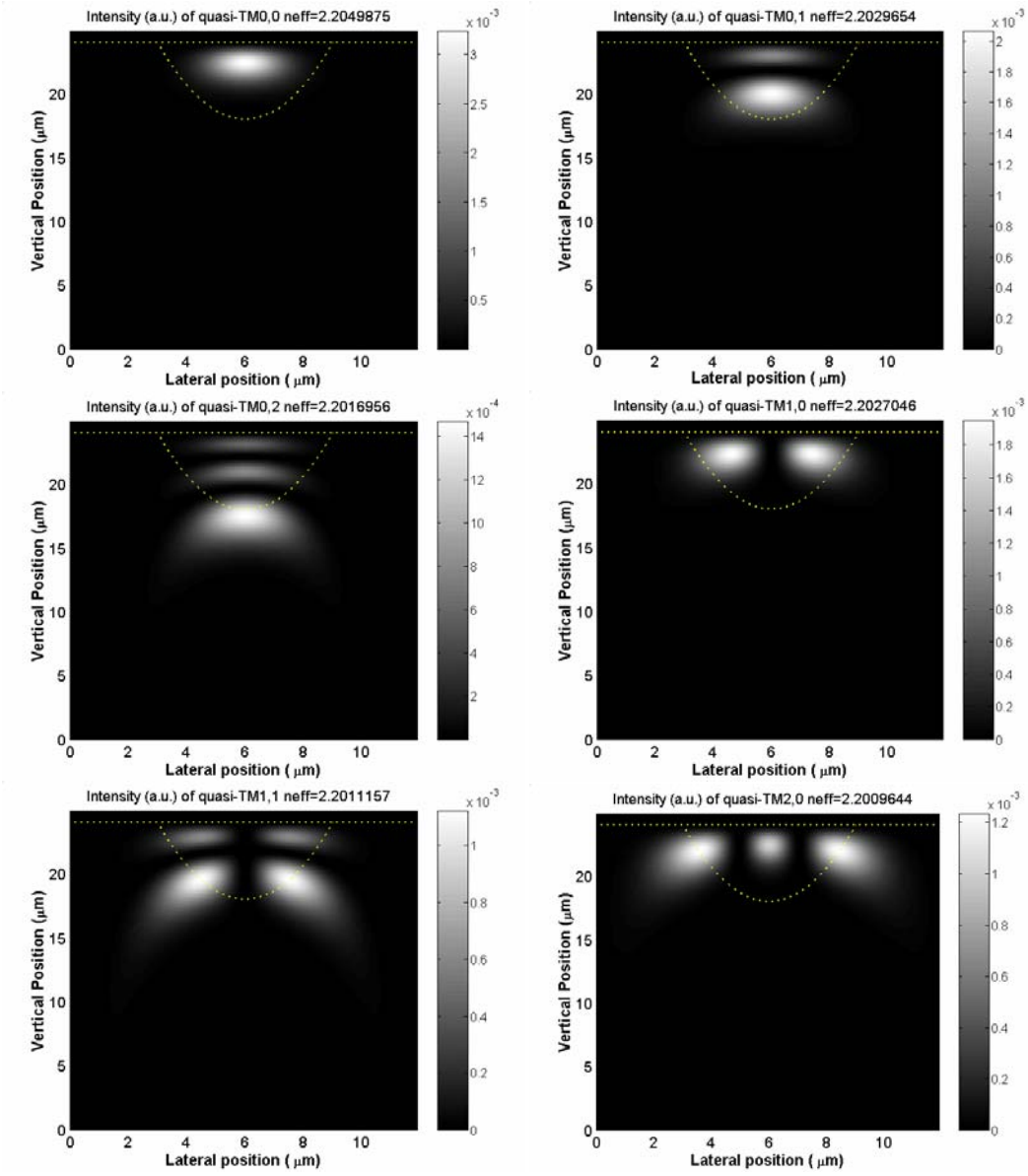

Figure 4.7. *Mode indices and corresponding intensity profile of several guided quasi-TM modes of Ti-indiffused $LiNbO_3$ channel waveguide.*

By using the hybrid EIM-FEM scheme as described in section 4.2.5, we can get the mode effective indices of guided modes and their corresponding field solutions. The computation was carried out by using a window width of 12μm, height of 25μm with only a 1μm thick air cladding inside the computational window, and initial (i.e. before mesh-evenization) lateral and vertical mesh sizes of 0.1μm. Some of the results are shown in Fig. 4.7 for quasi-TM modes. Almost similar intensity profiles were also obtained for quasi-TE modes, hence not shown here. As can be seen from these results, for higher order modes, the intensity is less confined and shifted toward the substrate. It is also shown that the effective indices of guided quasi-TM modes for this kind of crystal cut are bounded by the extraordinary index of the crystal, while for quasi-TE modes (not shown in the figure) by the ordinary index.

4.3.6. Directional-coupler-based polarization splitter

Here, we will demonstrate the use of the hybrid EIM-FEM scheme to analyze a polarization splitter on the basis of a directional coupler with Ti-indiffusion in one channel and annealed proton exchange (APE) process in the other channel in a Z-cut Y-propagating $LiNbO_3$ substrate as proposed by Maruyama *et al.* [11].

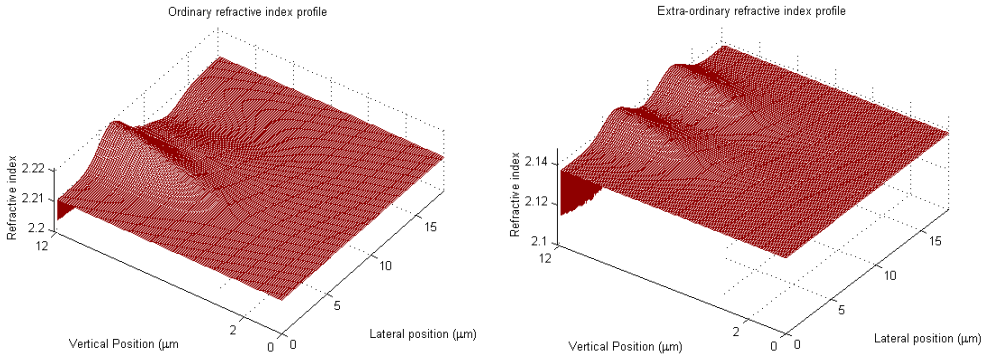

(a) (b)

Figure 4.8. *Refractive index profile of (a). ordinary index and (b). extraordinary index of Ti-indiffused to APE directional coupler.*

To simplify the analysis, we neglect the interaction between optical signals at the non-parallel waveguide regions of the directional coupler. Therefore, we only need to analyze a simplified structure with 2 parallel graded-index channel waveguides. For λ=1.55μm the bulk ordinary and extraordinary index of the crystal are ns_o=2.21122 and ns_e=2.1380646, respectively. We assume that both the lateral and vertical diffusion will give Gaussian index profiles for both kind of processes. For the Ti-indiffused channel we assume $\Delta_o=\Delta_e$=0.01, $d_{x,o}=d_{x,e}$=4μm, and $d_{y,0}=d_{y,e}$=2μm. For the APE channel we assume Δ_o=-0.004, Δ_e=0.01, $d_{x,o}=d_{x,e}$=4μm, and $d_{y,0}=d_{y,e}$=2μm. The

separation between the center of the two channels is 6.5μm. The refractive index profile of this structure is shown in Fig. 4.8 where we can see different refractive index profile for the two channels due to the effect of the two different processes.

The mode solving was carried out by using computational window width of 18.5μm, height of 12.2μm with just 0.2μm thick air cover inside the window, and initial lateral and vertical mesh size of 0.1μm. The result shows that there are two guided quasi-TM modes and only one guided quasi-TE mode. The n_{eff} of the quasi-TM_{00} is 2.13898 and quasi-TM_{10} is 2.13820, while that of quasi-TE_{00} mode is 2.211828. Therefore, we can calculate the coupling length for quasi-TM polarization waves using

$$L_c = \frac{\lambda}{2\left(n_{eff,TM00} - n_{eff,TM10}\right)} \tag{4.39}$$

which gives L_c=0.994mm. Hence, if we make the interaction length exactly the same as the coupling length ($L=L_c$), and launch light into the Ti-indiffused channel, then we will have the quasi-TM polarized light to be coupled into the APE channel, while the quasi-TE polarized waves still remain in the Ti-indiffused channel. This is basically a polarization splitter functionality as demonstrated experimentally by Maruyama *et al.* [11].

4.4. Conclusions

A simple variational finite element scheme for modal analysis of anisotropic planar waveguides with diagonal permittivity tensor is reported. The scheme uses a quasi-uniform mesh and Richardson-like extrapolation to achieve 4^{th}-order accuracy without any interface correction, using only simple linear basis functions within the computational domain. The scheme is furnished with infinite elements as the transparent boundary conditions, which is exact for structures with homogeneous exterior domain. For the inhomogeneous exterior domain case, by using basis functions adopted from the WKB method, approximate boundary conditions were formulated. Further refinement by extrapolating two consecutive computational results were also demonstrated. Together with the effective index method, the scheme was applied for semivectorial analysis of indiffused channel waveguides made on uniaxial crystal.

References

1. E.L. Wooten *et al.*, "A review of lithium niobate modulators for fiber-optic communications systems," **J. Sel. Topics in Quantum Electron.**, Vol. 6, No. 1, pp. 69-82, 2000.
2. K. Wörhoff, P.V. Lambeck, and A. Driessen, "Design, tolerance analysis, and fabrication of silicon oxynitride based planar optical waveguides for

communication devices," **J. Lightwave Technol.**, Vol. 17, No. 8, pp. 1401-1407, 1999.

3. M.C. Oh *et al.*, "Recent advances in electrooptic polymer modulators incorporating highly nonlinear chromophore," **J. Sel. Topics in Quantum Electron.**, Vol. 7, No. 5, pp. 826-835, 2001.
4. R. Stoffer *et al.*, "New true fourth-order accurate scalar beam propagation methods for both TE and TM polarization," **Opt. Quantum Electron.**, Vol. 31, No. 9-10, pp. 705-720, 1999.
5. M.J. McDougall and J.P. Webb, "Infinite elements for the analysis of open dielectric waveguides," **Trans. Microwave Theory and Tech.**, Vol. 37, No. 11, pp. 1724-1731, 1989.
6. F. Xiang and G.L. Yip, "A modified WKB method for the improved phase shift at a turning point," **J. Lightwave Technol.**, Vol. 12, No. 3, pp. 442-452, 1994.
7. C.R. Pollock, *Fundamentals of optoelectronics*, Richard D. Irwin Inc., Chicago, 1995.
8. H.A. Jamid, M.N. Akram, "A new higher order finite-difference approximation scheme for the method of lines," **J. Lightwave Technol.**, Vol. 19, No. 3, pp. 398-404, 2001.
9. H.J.W.M. Hoekstra *et al.*, "Beam-propagation method for second-harmonic generation in waveguides with birefringent materials," **J. Opt. Soc. Am. B**, Vol. 14, No. 7, pp. 1823-1830, 1997.
10. C.K. Chen *et al.*, "Efficient and accurate numerical analysis of multilayer planar optical waveguides in lossy anisotropic media," **Optics Express**, Vol. 7, No. 8, pp. 260-272, 2000.
11. H. Maruyama, M. Haruna, and H. Nishihara, "TE-TM mode splitter using directional coupling between heterogeneous waveguides in $LiNbO_3$," **J. Lightwave Technol.**, Vol. 13, No. 7, pp. 1550-1554, 1995.

Chapter 5

Simple high-order Galerkin finite element scheme for guided and leaky modes computation of anisotropic planar waveguides

A simple high-order Galerkin finite element scheme is formulated to compute both the guided and leaky modes of anisotropic planar waveguides with a diagonal permittivity tensor. Transparent boundary conditions derived from the Sommerfeld radiation conditions are used to model the fields at the computational boundaries. These conditions allow for radiation into high index cladding/substrate and decay into low index cladding/substrate, hence work for both guided and leaky modes. Richardson-like extrapolation is employed to achieve high-order accuracy by only using simple first-order-polynomial basis functions. Schemes up to 6^{th}-order accuracy in the effective index are demonstrated. The ability of the scheme to compute leaky and guided modes of various structures with isotropic and anisotropic materials, step and graded index profiles is demonstrated. Using the scheme, a detailed study on ARROW structures is presented.

This chapter is adapted from:
H.P. Uranus, H.J.W.M. Hoekstra, and E. van Groesen, "Simple high-order Galerkin finite element scheme for the investigation of both guided and leaky modes in anisotropic planar waveguides," **Opt. and Quantum Electronics**, Vol. 36, No. 1-3, pp. 239-257, 2004.
H.P. Uranus, H.J.W.M. Hoekstra, and E. van Groesen, "Modeling of quasi-guiding light within the lower refractive index core layer(s)," **J. Indonesian Math. Soc. (MIHMI)**, accepted 2005.

Simple high-order Galerkin finite element scheme for guided and leaky modes computation of anisotropic planar waveguides

5.1. Introduction

Optical waveguides that are made on a high-index substrate are particularly interesting. This class of waveguides includes structures made on a semiconductor wafer. Structures that are composed of silicon compounds grown on top of silicon substrate are not only benefiting from the low cost of silicon wafer, but also sharing the well developed technologies used by the microelectronics industries, and offering better prospect for integration between the optical and electronic circuits [1]. It has been shown that structures made of these materials have a wide range of available refractive indices [2]. Besides, arbitrary refractive index profiles can be made by precise computer control of the fabrication parameters as has been demonstrated by the realization of a rugate filter [3]. This feature gives more degrees of freedom in refractive index profile engineering, i.e. tailoring of the refractive index profiles to meet certain desired properties of the waveguide, like bandwidth [4], mode profiles [5], phase matching of modes of different wavelengths [6-7], etc. Hence, numerical investigations of this class of structure are important.

To analyze this kind of structures, computational methods that are able to solve leaky structures are needed. Among others, the finite element method (FEM) [8-10], the finite difference method (FDM) [11], the transverse matrix method (TMM) [12-13], the transverse resonance method (TRM) [14], the Wentzel-Kramers-Brillouin (WKB) method [15], and the imaginary distance (ID) BPM [16-17] with either perfectly matched layers (PML) or transparent boundary conditions (TBCs) have been used to solve such problem. Solvers that are originally made for 2-D cross-section problems are applicable to general structures, but might be too expensive for 1-D problem modeling tasks like those required in film deposition studies. Methods that can handle leaky planar structures with arbitrary index profile efficiently are needed for this kind of purpose. Since some materials exhibit birefringence [2], the method should be able to handle anisotropic dielectric permittivity. The TMM is known as an exact method for the step index planar case. However, the requirement of doing root searching in the complex plane makes this method to be not very easy to implement [18]. Simplification of the characteristic equation, for which it is sufficient to do root searching only along the real axis by assuming a certain phase relation in the outer interface, has been proposed for ARROW structures with small losses [19]. For

graded-index structures, TMM becomes too tedious, while its solution will not be exact any longer. For these structures, a staircase approximation to the graded index profile has to be performed, which leads to an accuracy of only 2nd-order, unless precautions like the extrapolation as we proposed in this chapter are taken.

In this chapter, we report a simple high-order 1-D Galerkin FEM scheme. By using TBCs derived from the Sommerfeld radiation conditions and allowing the transverse wave number to have complex value, the scheme allows light to leak into the high index substrate/cladding, and to decay into the low index substrate/cladding, and is hence able to compute both the guided and leaky modes. The inclusion of Richardson-like extrapolation and a simple mesh-adjustment scheme leads to higher order schemes by using only first-order-polynomial basis functions. The sparse non-linear matrix eigenvalue equation produced by the scheme can be solved using a simple iteration scheme. Hence, the scheme turns out to be very simple, easy to implement, but highly accurate. The method is suitable for leaky planar waveguides of arbitrary index profile with a diagonal permittivity tensor. Using the scheme, we also present detailed study on ARROW structures.

5.2. Description of the method

5.2.1. Finite element formulation

Here, we make the same assumption as in Section 4.2.1. Following the Galerkin procedure, doing partial integration to terms that contain second order derivatives, and using of the continuity of E_y, H_y, d_xE_y, and $(1/n_{zz}^2)d_xH_y$ across material interfaces, the weak formulation of wave equations (4.1) and (4.2) can be written as

$$w d_x\varphi\Big|_{\partial\Omega 1}^{\partial\Omega 2} + \int_{\Omega}\left[-\left(d_x w\right)\left(d_x\varphi\right) + k_0^2\left(n_{yy}^2 - n_{eff}^2\right)w\varphi\right]dx = 0 \tag{5.1}$$

for TE, and

$$\frac{1}{n_{zz}^2} w d_x\varphi\Big|_{\partial\Omega 1}^{\partial\Omega 2} + \int_{\Omega}\left[-\frac{1}{n_{zz}^2}\left(d_x w\right)\left(d_x\varphi\right) + k_0^2\left(1-\frac{n_{eff}^2}{n_{xx}^2}\right)w\varphi\right]dx = 0 \tag{5.2}$$

for TM polarization, with w, Ω, $\partial\Omega 1$, and $\partial\Omega 2$ denoting the weight function, computational interior domain, lower, and upper computational boundary, respectively. For notational simplicity, φ has been used to denote both the E_y in eq. (5.1) and H_y in eq. (5.2). By discretizing the interior domain Ω into N elements, eq. (5.1) and (5.2) can be written as

$$w d_x\varphi\Big|_{\partial\Omega 1}^{\partial\Omega 2} + \sum_{e=1}^{N}\int_{\Omega_e}\left[-\left(d_x w\right)\left(d_x\varphi\right) + k_0^2\left(n_{yy}^2 - n_{eff}^2\right)w\varphi\right]dx = 0 \tag{5.3}$$

and

$$\frac{1}{n_{zz}^2} w d_x \varphi \Big|_{\partial\Omega 1}^{\partial\Omega 2} + \sum_{e=1}^{N} \int_{\Omega_e} \left[-\frac{1}{n_{zz}^2} (d_x w)(d_x \varphi) + k_0^2 \left(1 - \frac{n_{eff}^2}{n_{xx}^2} \right) w\varphi \right] dx = 0 \tag{5.4}$$

respectively. Approximating the function φ in the interior domain by interpolation of first-order-polynomial basis functions, for each element e, we can write

$$\varphi_e \approx \tilde{\varphi}_e = \sum_{l=1}^{2} N_{l,e} \varphi_{l,e} = \begin{bmatrix} N_{1,e} & N_{2,e} \end{bmatrix} \begin{bmatrix} \varphi_{1,e} & \varphi_{2,e} \end{bmatrix}^T \tag{5.5}$$

with basis functions

$$N_{1,e} = 1 - \frac{x - x_{1,e}}{\Delta x_e} \tag{5.6a}$$

$$N_{2,e} = \frac{x - x_{1,e}}{\Delta x_e} \tag{5.6b}$$

and $\Delta x_e = x_{2,e} - x_{1,e}$ as the local mesh size. Subscripts 1 and 2 in eq. (5.5) and (5.6) denote the local node number within the element. By substituting (5.5) and (5.6) into (5.3) and (5.4), using the same basis functions as the weight functions, we can express the approximation to eq. (5.3) and (5.4) in matrix equations

$$\mathbf{C}^{\mathrm{TE}} \{\varphi\} + \left(\mathbf{A}^{\mathrm{TE}} - n_{eff}^2 \mathbf{B}^{\mathrm{TE}} \right) \{\varphi\} = \{\mathbf{0}\} \tag{5.7}$$

and

$$\mathbf{C}^{\mathrm{TM}} \{\varphi\} + \left(\mathbf{A}^{\mathrm{TM}} - n_{eff}^2 \mathbf{B}^{\mathrm{TM}} \right) \{\varphi\} = \{\mathbf{0}\} \tag{5.8}$$

respectively, where $\mathbf{A}^{\mathrm{TE}}$, $\mathbf{B}^{\mathrm{TE}}$, $\mathbf{A}^{\mathrm{TM}}$, and $\mathbf{B}^{\mathrm{TM}}$ are sparse tridiagonal matrices that result from the evaluation of the corresponding integral terms within eq. (5.3) and (5.4), while $\mathbf{C}^{\mathrm{TE}}$ and $\mathbf{C}^{\mathrm{TM}}$ are matrices associated with the boundary terms. Here

$$\{\varphi\} = [\varphi_1 ... \varphi_{N+1}]^T \tag{5.9}$$

where the subscript denotes the global node number, are column vectors representing the discretized y-component of the electric field for eq. (5.7) and magnetic field for eq. (5.8) at nodal points.

5.2.2. Boundary conditions

In order to handle both guided and leaky modes, the boundary conditions should allow light with either evanescently decaying or oscillatory outer transverse profile to transparently passes the computational boundary. To do this, we incorporate the Sommerfeld-like radiation conditions and allow the transverse wave number to have complex value.

By assuming the field to have a time dependence of $exp(i\omega t)$, we impose Sommerfeld-like radiation conditions at the computational boundaries for waves coming from within the computational domain interior as follows

$$(d_r + ik_r)\varphi(r) = 0 \tag{5.10}$$

with r denotes the length of $\vec{r}$, a position vector pointing outward, and k_r denotes the transverse wave number. Condition (5.10) gives following Dirichlet to Neumann (DtN) map at the computational boundaries

$$d_x\varphi = \hat{r} \bullet \hat{x}\, d_r\varphi = -ik_r \left(\hat{r} \bullet \hat{x}\right) \varphi \tag{5.11}$$

with the hat (^) symbol denotes unit vector. The transverse wavenumbers at the computational boundaries obtained from the wave equations (4.1) and (4.2) are $k_r = k_0 \sqrt{n_{yy}^2 - n_{eff}^2}\Big|_{\partial\Omega}$ for TE and $k_r = k_0 \frac{n_{zz}}{n_{xx}} \sqrt{n_{xx}^2 - n_{eff}^2}\Big|_{\partial\Omega}$ for TM, for structures with a homogeneous exterior domain. By using DtN (5.11), the non-zero entries of matrices $\mathbf{C}^{\mathrm{TE}}$ and $\mathbf{C}^{\mathrm{TM}}$ can be determined as follows.

$$c_{1,1}^{\mathrm{TE}} = -i\, k_r\big|_{\partial\Omega 1} = -ik_0 \sqrt{n_{yy}^2 - n_{eff}^2}\Big|_{\partial\Omega 1} \tag{5.12a}$$

$$c_{N+1,N+1}^{\mathrm{TE}} = -i\, k_r\big|_{\partial\Omega 2} = -ik_0 \sqrt{n_{yy}^2 - n_{eff}^2}\Big|_{\partial\Omega 2} \tag{5.12b}$$

$$c_{1,1}^{\mathrm{TM}} = -i \frac{1}{n_{zz}^2} k_r\Big|_{\partial\Omega 1} = -ik_0 \frac{\sqrt{n_{xx}^2 - n_{eff}^2}}{n_{xx} n_{zz}}\Big|_{\partial\Omega 1} \tag{5.12c}$$

$$c_{N+1,N+1}^{\mathrm{TM}} = -i \frac{1}{n_{zz}^2} k_r\Big|_{\partial\Omega 2} = -ik_0 \frac{\sqrt{n_{xx}^2 - n_{eff}^2}}{n_{xx} n_{zz}}\Big|_{\partial\Omega 2} \tag{5.12d}$$

Since the n_{eff}^2 as the eigenvalue of the matrix eigenvalue equations (5.7) and (5.8) also resides within matrix **C**, the matrix eigenvalue equations become non-linear. This kind of equations can be solved using linearization by simple iteration scheme, i.e. by using n_{eff}^2 from the previous iteration for evaluation of terms within matrix **C**. Hence, within each iteration, the problem can be solved using linear matrix eigenvalue solver. In this work, we have used ARPACK that implement implicitly restarted Arnoldi method as the eigenvalue solver. To be able to model both guided and leaky modes, the sign of the square root within eq. (5.12) should be correctly chosen at each iteration step to fulfill the physical conditions. At a boundary where the wave should leak-out (i.e. at high index substrate/cladding for the leaky mode case), the sign of the square root is chosen to give $\mathrm{Re}(k_r)>0$, which is associated to $\mathrm{Im}(n_{eff})<0$ for forward propagating leaky modes as has been explained in Section 1.2. At the boundary where the wave should decay, the sign of the square root is chosen to give $\mathrm{Im}(k_r)<0$.

5.2.3. High-order extension

By using the first-order-polynomial basis functions as described in section 5.2.1, the scheme will give 2nd-order accuracy in n_{eff}. As has been shown in previous chapter, 4th-order accuracy can be obtained by simply combining results of single- and double-sized mesh in evaluating the integral within FEM scheme using a Richardson-like

extrapolation. Below, we generalize the scheme to obtain even higher (4^{th}-, 6^{th}-, 8^{th}-, etc.) order accuracy while keeping the simplicity of the scheme described previously.

For element located between global nodal point *j* (at x_j) and *j+1* (at x_{j+1}), using Taylor's expansion around $x_{j+\frac{1}{2}}$, it can be shown that approximating the function with an interpolation of first-order-polynomial basis functions will produce errors of

$$F_{j\div j+1} = \tilde{F}^{lin}_{j\div j+1} + \Delta x_j^3 err_3\left(x_{j+\frac{1}{2}}\right) + \Delta x_j^5 err_5\left(x_{j+\frac{1}{2}}\right) + \Delta x_j^7 err_7\left(x_{j+\frac{1}{2}}\right) + \Delta x_j^9 err_9\left(x_{j+\frac{1}{2}}\right) + \ldots \quad (5.13)$$

where $F_{j\div j+1}$ and $\tilde{F}^{lin}_{j\div j+1}$ denote the exact and the linear-approximate value of the integral terms of eq. (5.3) and (5.4) within the element, respectively, while $err_k\left(x_{j+\frac{1}{2}}\right)$ is just a short form notation for the function related to the k^{th}-order error terms evaluated at $x_{j+\frac{1}{2}}$. After summation, for uniform meshes, the global error of approximating eq. (5.3) and (5.4) will be just 2^{nd}-order as follows.

$$F_{1\div N+1} = \tilde{F}^{lin}_{1\div N+1,\Delta x} + O\left(\Delta x^2\right) \quad (5.14)$$

with $F_{1\div N+1}$ and $\tilde{F}^{lin}_{1\div N+1,\Delta x}$ denoting the exact and approximate (using Δx-sized meshes) value for the integral over the whole interior domain. Hence, in order to get 4^{th}-order of accuracy, we should get rid of the 3^{rd}-order error term within each integration interval. Similarly, to get 6^{th}-order accuracy, we should eliminate the 3^{rd}- and 5^{th}-order error terms. In this chapter, we use Richardson-like extrapolation by combining integration results from meshes with different sizes to get high-order of accuracy while still using the simple first-order basis functions.

By using integration results from Δx-sized and $2\Delta x$-sized meshes, 4^{th}-order accuracy can be achieved by Richardson-like extrapolation as follows

$$F_{1\div N+1} = \tfrac{4}{3}\tilde{F}^{lin}_{1\div N+1,\Delta x} - \tfrac{1}{3}\tilde{F}^{lin}_{1\div N+1,2\Delta x} + \Delta x^5 \sum_{l=2,4,\ldots N}\left[-8err_5\left(x_l\right) + \tfrac{1}{3}\partial_{xx}err_3\left(x_l\right)\right] + h.o.t. \quad (5.15a)$$

$$F_{1\div N+1} = \tfrac{4}{3}\tilde{F}^{lin}_{1\div N+1,\Delta x} - \tfrac{1}{3}\tilde{F}^{lin}_{1\div N+1,2\Delta x} + O\left(\Delta x^4\right) \quad (5.15b)$$

In eq. (5.15a), the index *l* denotes the middle grid point of each group of 2 meshes of Δx size while $\partial_{xx}err_3\left(x_l\right) \equiv \partial_{xx}err_3\left(x\right)\big|_{x=x_l}$ and *h.o.t.* denotes the higher order terms. Since there will be $\Omega/\left(2\Delta x\right)$ number of these groups of meshes, the order of accuracy will be 4^{th}-order. Similarly, by using Δx-sized, $2\Delta x$-sized, and $4\Delta x$-sized meshes, 6^{th}-order accuracy can be achieved by

$$F_{1\div N+1} = \tfrac{64}{45}\tilde{F}^{lin}_{1\div N+1,\Delta x} - \tfrac{20}{45}\tilde{F}^{lin}_{1\div N+1,2\Delta x} + \tfrac{1}{45}\tilde{F}^{lin}_{1\div N+1,4\Delta x} + \Delta x^7 \sum_{l=3,7,\ldots,N-1}\left[256err_7\left(x_l\right) - \tfrac{32}{3}\partial_{xx}err_5\left(x_l\right) + \tfrac{14}{45}\partial_{xxxx}err_3\left(x_l\right)\right] + h.o.t. \quad (5.16a)$$

$$F_{1\div N+1} = \tfrac{64}{45}\tilde{F}^{lin}_{1\div N+1,\Delta x} - \tfrac{20}{45}\tilde{F}^{lin}_{1\div N+1,2\Delta x} + \tfrac{1}{45}\tilde{F}^{lin}_{1\div N+1,4\Delta x} + O\left(\Delta x^6\right) \quad (5.16b)$$

with index *l* denoting the middle grid point of each group of 4 meshes of Δx size. Using Δx-sized, $2\Delta x$-sized, $4\Delta x$-sized, and $8\Delta x$-sized meshes, 8^{th}-order accuracy can be obtained by

$$F_{1\div N+1} = \tfrac{4096}{2835}\tilde{F}^{lin}_{1\div N+1,\Delta x} - \tfrac{1344}{2835}\tilde{F}^{lin}_{1\div N+1,2\Delta x} + \tfrac{84}{2835}\tilde{F}^{lin}_{1\div N+1,4\Delta x} - \tfrac{1}{2835}\tilde{F}^{lin}_{1\div N+1,8\Delta x} + O\left(\Delta x^8\right) \qquad (5.17)$$

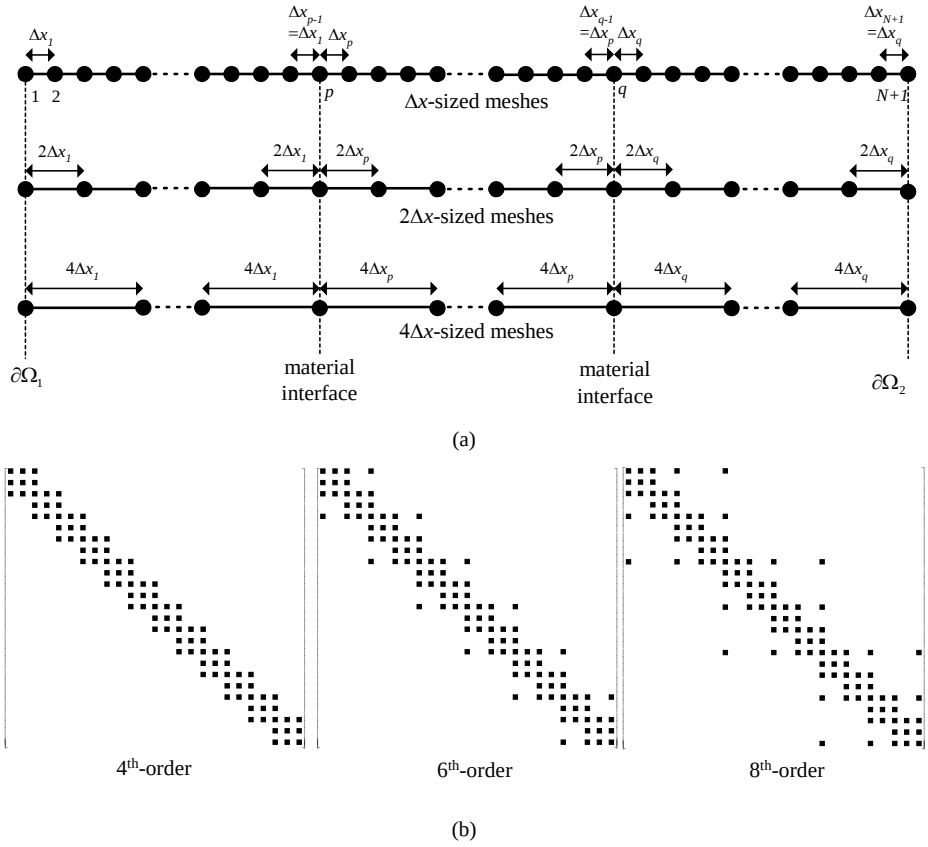

Figure 5.1. *Richardson-like extrapolation with mesh-adjustment scheme: (a). meshes for 6^{th}-order scheme, (b). matrix structure for 4^{th}-, 6^{th}-, and 8^{th}-order scheme (black dots denote the non-zero matrix entries).*

Since the integral terms will contribute only to matrices **A** and **B**, the final way of implementing the Richardson-like extrapolation is just a matter of multiplication of scalars with sparse matrices and addition/subtraction operation of sparse matrices before eigenvalue computation. Since the right hand side (*rhs*) of eq. (5.7) and (5.8) is just a null vector, the matrices can be scaled by multiplying them with the denominator occurring in eq. (5.15)-(5.17) to get more convenient integer coefficients for combining the matrices. Moreover, since the integrations only differ in their interval sizes, the same expressions for evaluation of matrix entries can be reused by just plugging in the proper mesh sizes. It should be noted here, that since iteration is

used to solve the non-linear matrix eigenvalue problem, the convergence depth will also limit the number of digits of accuracy. In the implementation, we have used convergence depth of 10^{-10} in n_{eff}^2, which is more than enough for most practical applications. Besides, the expected order of accuracy will only be effective if the mesh size is small enough to effectively exclude the effect of the higher order terms within eq. (5.13) for all mesh sizes being used in the extrapolation. Also, since the coefficients within the summation of eq. (5.16a) are larger than that of eq. (5.15a), the 6th-order scheme will only be more accurate than the 4th-order scheme if the mesh size is small enough to compensate the effect of these coefficients. The same thing holds for any higher order scheme compared to the lower order one. We are aware that this fact might limit the benefits of further higher order extension.

To let the Richardson-like extrapolation works properly, none of the integration intervals should cross material interfaces. Generalizing the mesh-evenization scheme that we reported in previous chapter, the number of Δx-sized meshes within each layer of the structure should be adjusted to be integer multiple of $2^{Ord/2-1}$ with *Ord* denoting the expected order of accuracy, and interfaces should coincide with nodal points. Figure 5.1 illustrates this simple and easy to implement mesh-adjustment scheme and their corresponding matrix structure. It should be noted that due to different mesh sizes between terms in eq. (5.15)-(5.17), the combined matrices will not be tridiagonal anymore, but of the form as shown in Fig. 5.1b.

5.3. Computational results

The ability of the scheme to compute guided modes will be demonstrated using a sample with an exponential permittivity profile, for which exact solutions are available. ARROW structures, either isotropic or anisotropic structures will be used as samples to demonstrate the ability to compute leaky modes. Finally, computational results for an anisotropic graded index buffered leaky waveguide, a Bragg, and a hollow waveguide will be presented.

5.3.1. Guided modes

As the first sample, we take a waveguide with the following relative permittivity profile:

$$n^2(x) = n_s^2 + 2n_s\Delta\exp\left(-|x|/d\right) \qquad \text{for } x \le 0 \qquad (5.18a)$$

$$n^2(x) = n_c^2 \qquad \text{for } x > 0 \qquad (5.18b)$$

where d denotes the effective depth of the exponential profile. The calculated normalized propagation constants using the present scheme as well as the exact values for n_s=2.177, n_c=1 (air), Δ=0.043, and $V \equiv k_0 d\sqrt{2n_s\Delta} = 4$, are presented in Table 5.1.

The computation is carried out for λ=1μm and a computational window of W=9μm with the upper computational boundary located exactly at the waveguide-air interface. The exact values of the effective indices for TE polarization were calculated using the exact dispersion relation given by Conwell [20]. As shown in the table, the results approach the exact values either by using finer mesh or higher order scheme for coarse mesh.

Table 5.1. *Computational results of structure with exponential permittivity profile.*

	$b=\left(n_{eff}^2-n_s^2\right)/\left(2n_s\Delta\right)$					
	Present scheme (W=9μm, 900 meshes)		Present scheme (W=9μm, 40 meshes)			Exact
	2nd-order	4th-order	2nd-order	4th-order	6th-order	
TE0	0.321176	0.321179	0.319757	0.321065	0.321134	0.321179
TE1	0.053969	0.053972	0.052618	0.053823	0.053942	0.053972
TM0	0.300843	0.300846	0.299536	0.300716	0.300794	-
TM1	0.046947	0.046950	0.045761	0.046807	0.046917	-

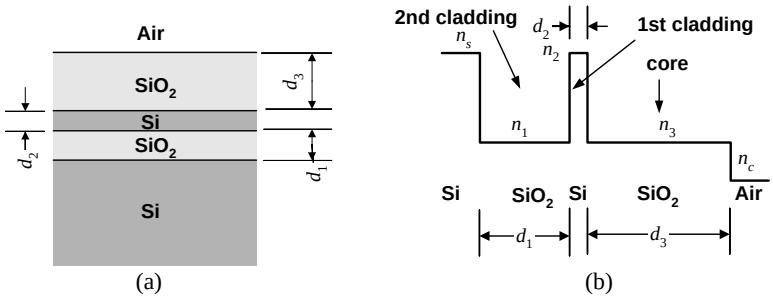

Figure 5.2. *The isotropic ARROW sample: (a). structure and (b). refractive index profile.*

5.3.2. Isotropic ARROW structure

As an isotropic ARROW structure, we take the same structure as the one calculated by Kubica *et al*. [12] and Liu *et al*. [19]. The structure is as shown in Fig. 5.2 with n_s=3.5, n_1=1.45, n_2=3.5, n_3=1.45, n_c=1, d_1=2.0985μm, d_2=0.1019μm, and d_3=4μm. The computation was carried out for a vacuum wavelength of 1.3μm. The calculated results for the first-two leaky TE and TM modes are given in Table 5.2 where subscripts L indicate that the modes are leaky modes. The table shows agreement between results of present scheme with the published data. The effective mesh size being used in the table is defined as

$$\Delta x_{eff} \equiv \left(\frac{1}{N} \sum_{j=1}^{N} \Delta x_j^{Ord} \right)^{1/Ord} \tag{5.19}$$

This definition is based on the expectation that the error within each element will be $O(\Delta x^{Ord})$ and the fact that the mesh sizes vary slightly due to the mesh-adjustment scheme. This structure will be studied in more detail in Section 5.4.

Table 5.2. *Computational results of the isotropic ARROW sample*

Mode	Present scheme (6th-order) (W=9.2μm Δx_{eff}=0.01μm)			TMM (Kubica *et al*. [12])		Simplified TMM (Liu *et al*. [19])	
	Re(n_{eff})	Im(n_{eff}) ($\times 10^{-3}$)	Att. (dB/cm)	Re(n_{eff})	Att. (dB/cm)	Re(n_{eff})	Att. (dB/cm)
$TE_{0,L}$	1.44170845	-0.00060491	0.253944	1.4417085	0.25	1.4417085	0.25
$TE_{1,L}$	1.41759871	-0.97220073	408.1377	1.4176	407	1.41798	270
$TM_{0,L}$	1.44130390	-0.12983415	54.50543	-	-	-	-
$TM_{1,L}$	1.42164054	-5.30958274	2229.006	-	-	-	-

5.3.3. Anisotropic ARROW structure

For the anisotropic ARROW sample, we take the same structure as the one studied by Chen *et al.* [13] using TMM. The structure is a 5-layer ARROW with isotropic substrate and cover, but with anisotropic inner layers. The refractive indices for layers counted sequentially from substrate to cover are n_s=3.85, n_{zz1}=1.46, n_{zz2}=2.3, n_{zz3}=1.46, n_c=1. For the anisotropic inner layers $n_{xxi}=n_{yyi}=1.03n_{zzi}$ for i=1,2,3. The vacuum wavelength λ is 0.6328μm. The thicknesses of the anisotropic layers are d_1=3.15λ, d_2=0.142λ, d_3=6.3λ. The calculated results for the first-five TE and TM leaky modes are given in Table 5.3 for the 4th- and 6th-order scheme using effective mesh size of 0.005μm, with upper computational boundary positioned at the surface of the structure (interface between layer 3 and air cover) while the lower one at 0.5 μm into the substrate. This mesh size has been chosen in order to represent the thin layer with a sufficient number of meshes. In addition to modes quasi-confined within the second cladding and the core of the ARROW structure, i.e. layer 1 and 3; our scheme also captures those leaky modes resonance within the first cladding, i.e. the thin anisotropic layer with second highest refractive indices. Although these modes ($TE_{0,L}$ and $TM_{0,L}$ in the table) resonance in the 1st cladding, their losses are very low, since their fields decay very fast in the 2nd cladding due to the large difference between their effective index and the refractive index of the 2nd cladding. For these modes, the structure behaves as a buffered leaky structure, while for other modes it works as an ARROW structure.

Table 5.3. *Computational results of the anisotropic ARROW structure.*

	Present scheme				TMM (Chen *et al*. [13])	
	4th-order		6th-order			
	Re(n_{eff})	Im(n_{eff}) ($\times 10^{-3}$)	Re(n_{eff})	Im(n_{eff}) ($\times 10^{-3}$)	Re(n_{eff})	Im(n_{eff}) ($\times 10^{-3}$)
$TE_{0,L}$	1.867833649	-0.000000000	1.867833876	-0.000000000	-	-
$TE_{1,L}$	1.501798936	-0.000050179	1.501798936	-0.000050179	1.501798936	-0.000050179
$TE_{2,L}$	1.495945498	-0.053815080	1.495945499	-0.053815130	1.495945499	-0.053815143
$TE_{3,L}$	1.495255343	-0.184243985	1.495255344	-0.184243812	1.495255344	-0.184243873
$TE_{4,L}$	1.485698163	-0.004051177	1.485698165	-0.004051177	1.485698165	-0.004051178
$TM_{0,L}$	1.632729635	-0.000000004	1.632729919	-0.000000004	-	-
$TM_{1,L}$	1.501625054	-0.002544521	1.501625054	-0.002544520	1.501625054	-0.002544521
$TM_{2,L}$	1.495287894	-0.576100220	1.495287895	-0.576101327	1.495287895	-0.576101022
$TM_{3,L}$	1.494855075	-1.189341232	1.494855077	-1.189338782	1.494855078	-1.189339701
$TM_{4,L}$	1.484121305	-0.197863266	1.484121307	-0.197863148	1.484121307	-0.197863211

5.3.4. Anisotropic graded-index buffered leaky waveguides

To demonstrate the ability of the scheme to model anisotropic leaky planar waveguide with arbitrary refractive index profile, we take a full Gaussian buffered leaky waveguide made by silicon oxynitride. The refractive index profile of the structure is given in Fig. 5.3. The refractive index of the silicon substrate is n_s=3.476, while the refractive index profile of the anisotropic graded index SiO_xN_y is

$$n_g = n_{lo} + \Delta \exp\left[-\left(x - x_0\right)^2 / d^2\right] \tag{5.20}$$

with $n_{lo,xx}=n_{lo,yy}=n_{lo,zz}$=1.45, Δ_{xx}=0.1, $\Delta_{yy}=\Delta_{zz}$=0.098, and d =0.5μm. The cladding of the structure is air with n_c =1. The position of the peak of the SiO_xN_y index profile from the waveguide-air interface is d_2 =2μm, while d_1 being varied from 2 to 8 μm. The computational results by taking a vacuum wavelength of λ=1.55μm, using computational window size of just d_1+d_2 with the computational boundaries put exactly at the SiO_xN_y – Si and SiO_xN_y – air interfaces and an effective mesh size of 0.05μm using 4th-order scheme are given in Table 5.4. In this table, $d_1=\infty$ denotes a simplified structure by neglecting the silicon substrate but calculated using finite computational domain width with the lower boundary put at 8μm from the peak of the Gaussian profile. It should be noted, that since our boundary conditions assume a homogeneous exterior domain while this simplified structure has inhomogeneous exterior domain, the error in representing the field at the boundary will also limit the accuracy. Also note that the losses decrease while the real part of the effective indices approaching the results of the simplified lossless structure as the thickness of the buffer d_1 is increased. Hence, the simplified lossless structure model can be used to approximate the leaky structure for thick enough buffer.

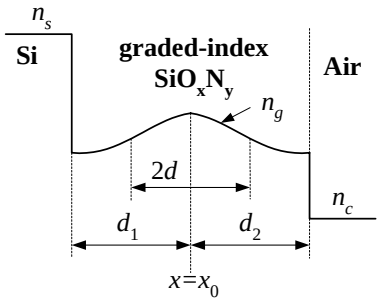

Figure 5.3. *Refractive index profile of a Gaussian SiO_xN_y buffered leaky structure.*

Table 5.4. *Computational results of the Gaussian SiO_xN_y leaky structure.*

d_1 (μm)	Polarization	Re(n_{eff})	Im(n_{eff}) ($\times 10^{-3}$)	α (dB/cm)
2	TE	1.4876498	-0.0984765	34.673298
	TM	1.4865629	-0.4558552	160.505289
4	TE	1.4880960	-0.0004157	0.146365
	TM	1.4867917	-0.0021471	0.755969
8	TE	1.4880980	-0.00000001	0.000003
	TM	1.4867929	-0.00000005	0.000018
∞	TE	1.4880980	0	0
	TM	1.4867929	0	0

5.3.5. Planar Bragg and hollow waveguides

We also apply the FE scheme to study planar Bragg [21] and hollow waveguides as depicted in Fig. 5.4. Here, the term hollow does not mean that the core is air or vacuum, but a medium with a lower refractive index than the cladding. We pick up a Bragg waveguide with similar parameters as the one analyzed by Litchinitser *et al.* [22] and take a hollow waveguide of comparable size. The 10-period Bragg gratings that act as claddings at each side of the Bragg waveguide, have a period of Λ=5μm with a refractive index of n_{hi}=1.8 and n_{lo}=1.4 and thickness of high index layer of d_{hi}=3.437μm. With a defect of missing 3 grating periods, the width of the low index core of the waveguide is $d_{core}=4\Lambda-d_{hi}$. The associated hollow waveguide has the same width of the low-index core with a homogeneous high-index cladding with refractive index n_{hi} at both sides.

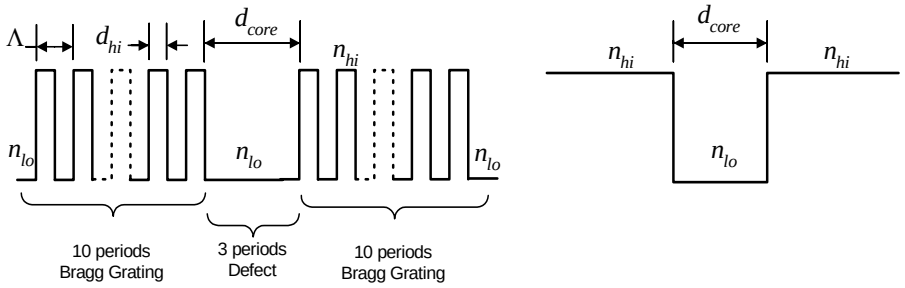

(a) (b)

Figure 5.4. *The refractive index profile of (a). the Bragg and (b). the hollow waveguide.*

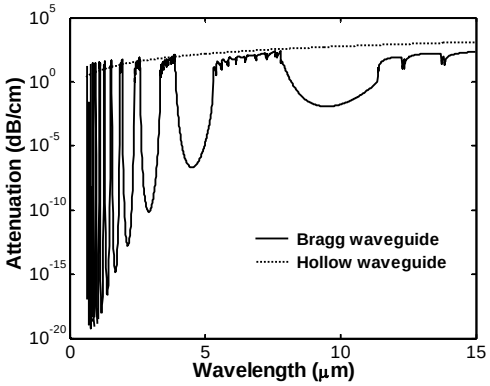

Figure 5.5. *Attenuation due to confinement loss of the Bragg and the hollow waveguide as function of wavelength for $TE_{0,L}$ mode.*

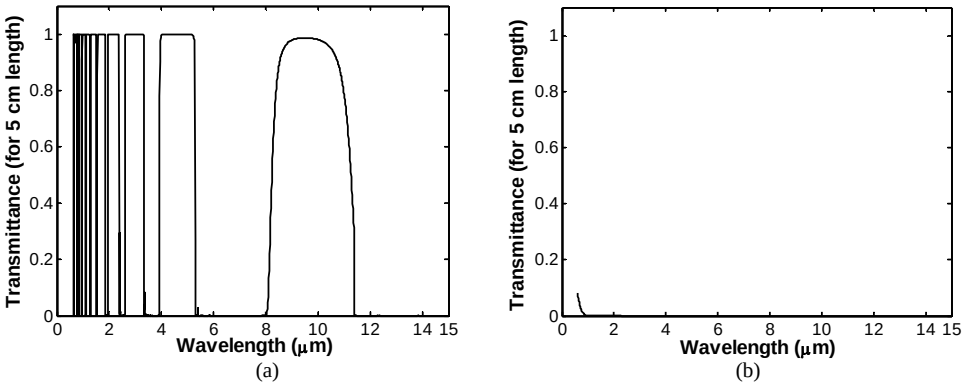

Figure 5.6. *The transmittance of $TE_{0,L}$ mode in (a). the Bragg and (b). the hollow waveguide with a length of 5 cm.*

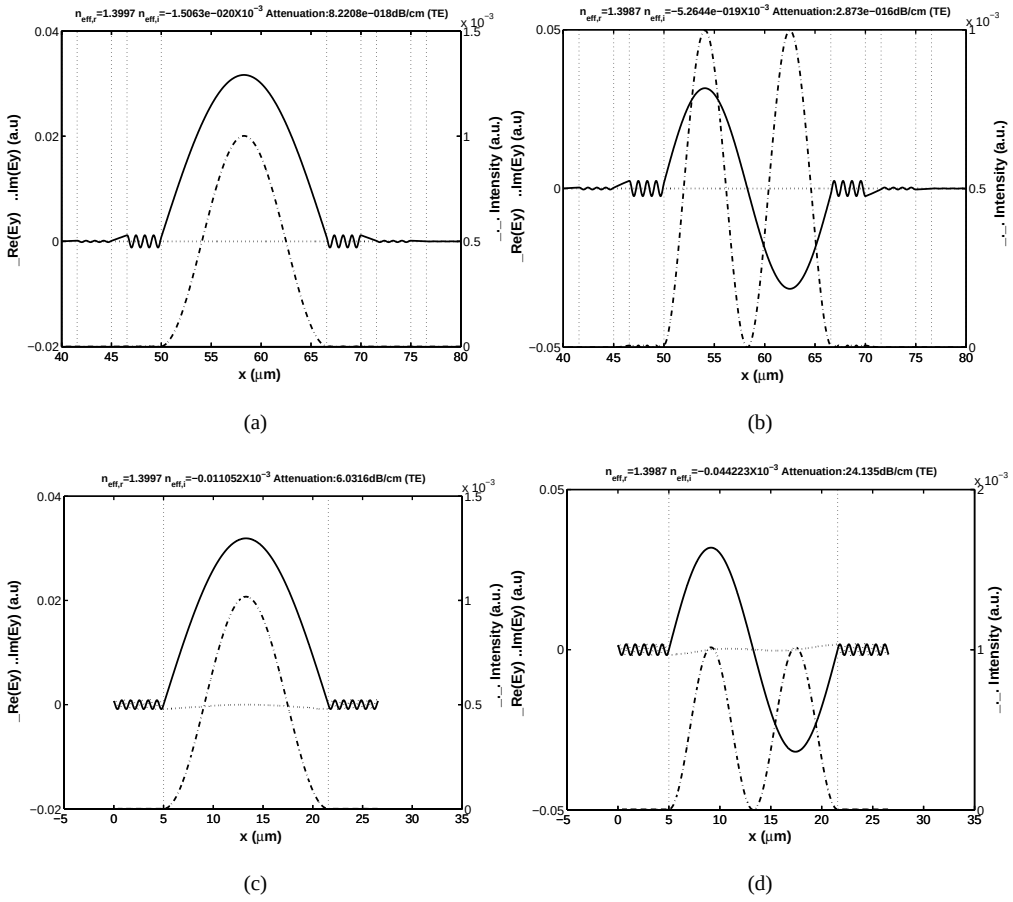

Figure 5.7. *The mode profiles of (a). $TE_{0,L}$, (b). $TE_{1,L}$ of the Bragg, and (c). $TE_{0,L}$ and (d). $TE_{1,L}$ of the hollow waveguide for λ=1μm. The plotting windows have been chosen equal to ease the comparison.*

The confinement loss and the associated transmittance curves for the fundamental TE mode of both waveguides for wavelengths spanning from 0.6 to 15 μm are given in Fig. 5.5 and 5.6, whereby we have neglected the material chromatic dispersion. The figures show that the leakage of power in the hollow waveguide steadily increases for increasing wavelength due to the decrease of the field confinement, while for the Bragg waveguide at certain wavelengths where the modal transverse wavenumber is near to the Bragg wavenumber of the grating, the grating helps to decrease the leakage. Fig. 5.6a is qualitatively similar to the results of BPM simulation given by Litchinitser *et al.* [22]. At some part of the curve, Litchinitser *et al.* got a lower transmittance, which we believe comes from the low overlap between the Gaussian excitation field used by them with the mode profile of the waveguide, especially to the wave-like tail of the mode profile. The mode profiles of the two-first TE modes of both structures at wavelength 1μm are given in Fig. 5.7. Mode profiles of

TM modes have similar features and hence are not shown here. The figure shows that the mode profiles and real part of the effective indices of the two structures are similar, but with much lower leakage loss of the Bragg waveguide. This similarity comes from the fact that they both comes from resonance resulted by almost similar resonance center, i.e. the core. Note that the field plotted in Fig. 5.7 and also elsewhere in this chapter has been adjusted by a phase factor such that the real part of the field be dominant. This phase factor is determined by the phase at nodal point where the complex field takes its largest magnitude.

5.4. Detailed study of ARROW structures

To study the properties of ARROW structures, we take the isotropic ARROW as in Section 5.3.2, and compare the calculated results of the full (original) structure (Fig. 5.8a) with two simplified structures (Fig. 5.8.b and Fig. 5.8.c). The structure parameters have the same values as in Section 5.3.2, unless when stated otherwise.

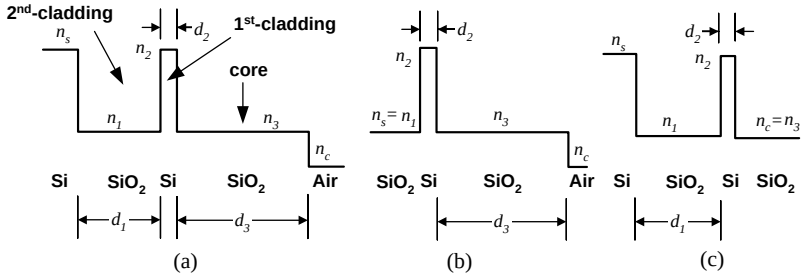

Figure 5.8. *Refractive index profile of the isotropic ARROW sample: (a). full structure, (b). simplified structure with $n_s=n_1$, and (c). $n_c=n_3$.*

Figure 5.9 and 5.10 present the real part of the n_{eff} for the first-ten leaky modes as a function of the thickness of 2nd cladding d_1 and core layer d_3, respectively. The solid line curves of Fig. 5.10a have also been presented by Kubica *et al.* [12] and agree well with these. The figures show unusual dispersion curves due to the anti-crossing between modes, which have a strong (dispersive) and a weak (non-dispersive) dependence on the variable of the horizontal axis of the curves. This phenomenon can be intuitively explained by comparing the dispersion curve plot of the full structure with the simplified structures as shown in Fig. 5.9a and 5.10a for TE polarization. Results for simplified structure with $n_s=n_1$ (Fig. 5.8b) and $n_c=n_3$ (Fig. 5.8c) are shown as crosses and circles, respectively. For clarity, only modes of the full structure were labeled in these figures, ordered by their Re(n_{eff}). The transitions between the dispersive and non-dispersive part of the full structure curves take place around the crossings between dispersion curves of the two simplified structures. For TM polarization, the anti-crossing effect is that strong so the relation between the curves of

the full and those of the simplified structures is more difficult to be recognized. Hence, for TM, we present only the plots for the full structure.

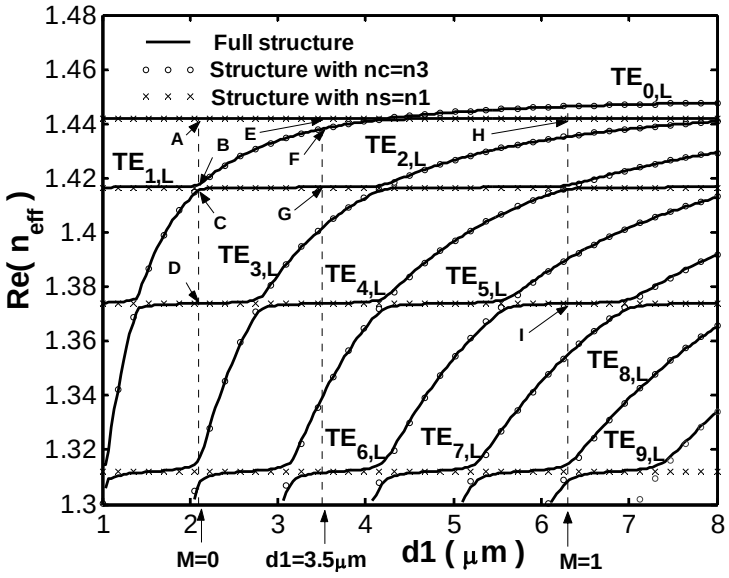

(a)

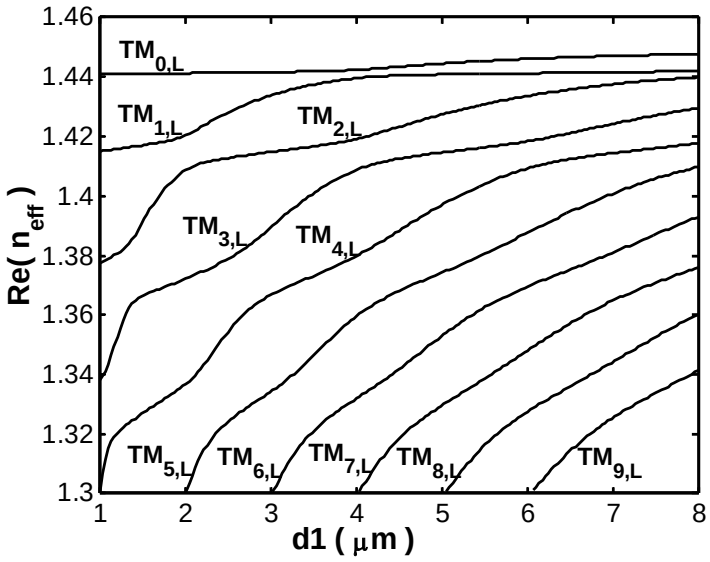

(b)

Figure 5.9. *Dispersion curves by varying d_1 of the isotropic ARROW structure: (a). TE (b). TM. Other parameters are as in Section 5.3.2.*

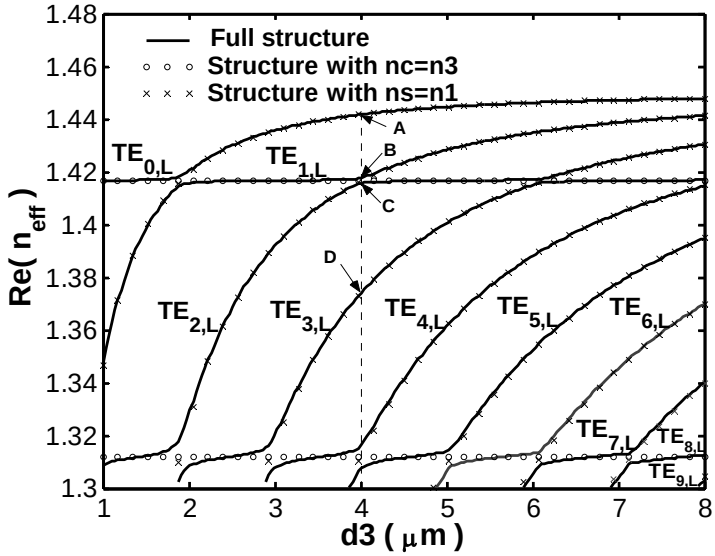

(a)

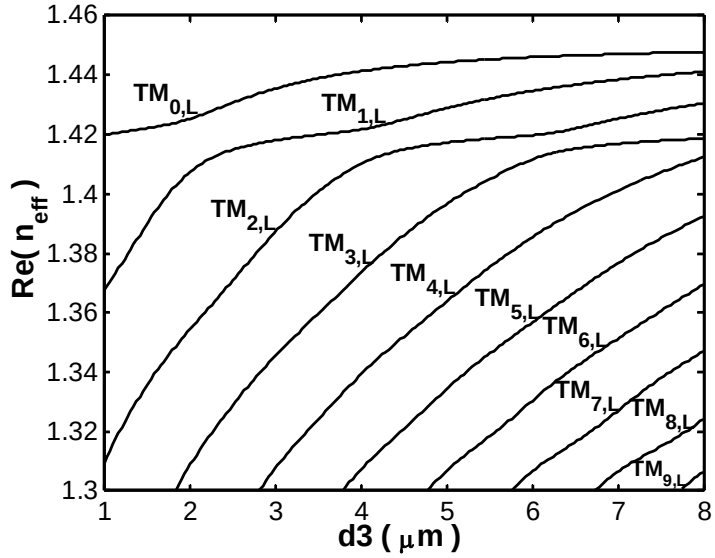

(b)

Figure 5.10. *Dispersion curves by varying d_3 of the isotropic ARROW structure: (a). TE (b). TM. Other parameters are as in Section 5.3.2.*

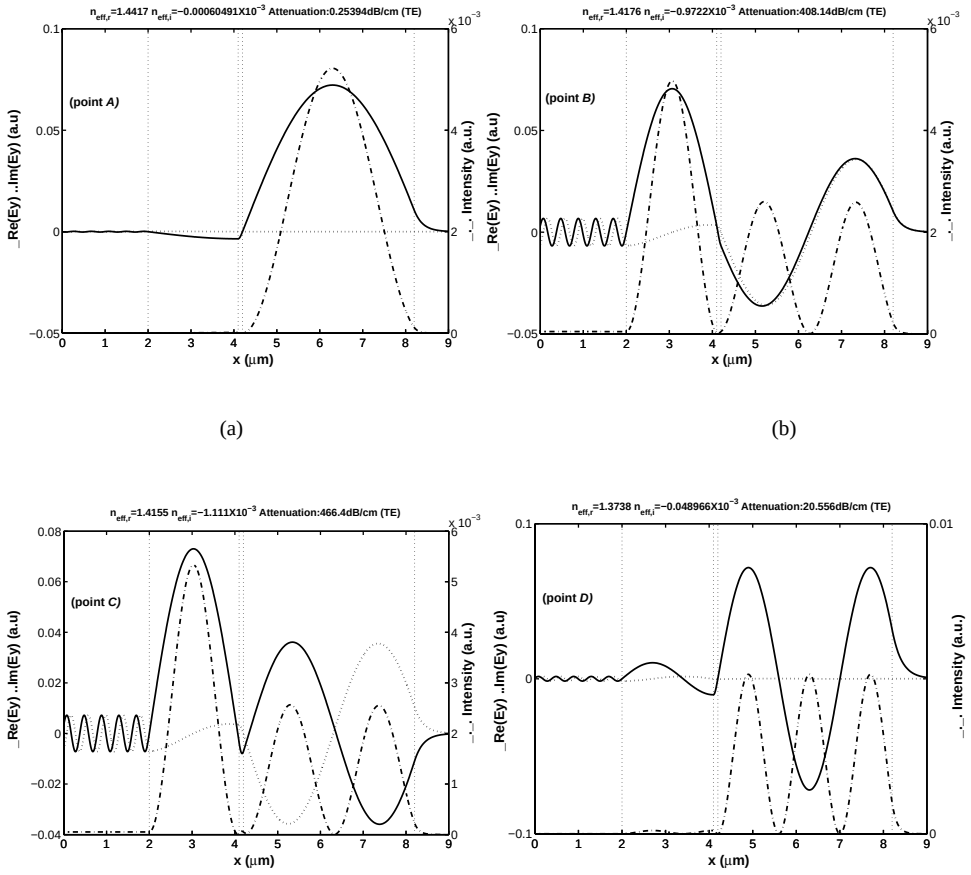

Figure 5.11. *Mode and intensity profiles of (a). $TE_{0,L}$, (b). $TE_{1,L}$, (c). $TE_{2,L}$, and (d). $TE_{3,L}$ modes of the full structure, which correspond to point A to D in the curves, respectively.*

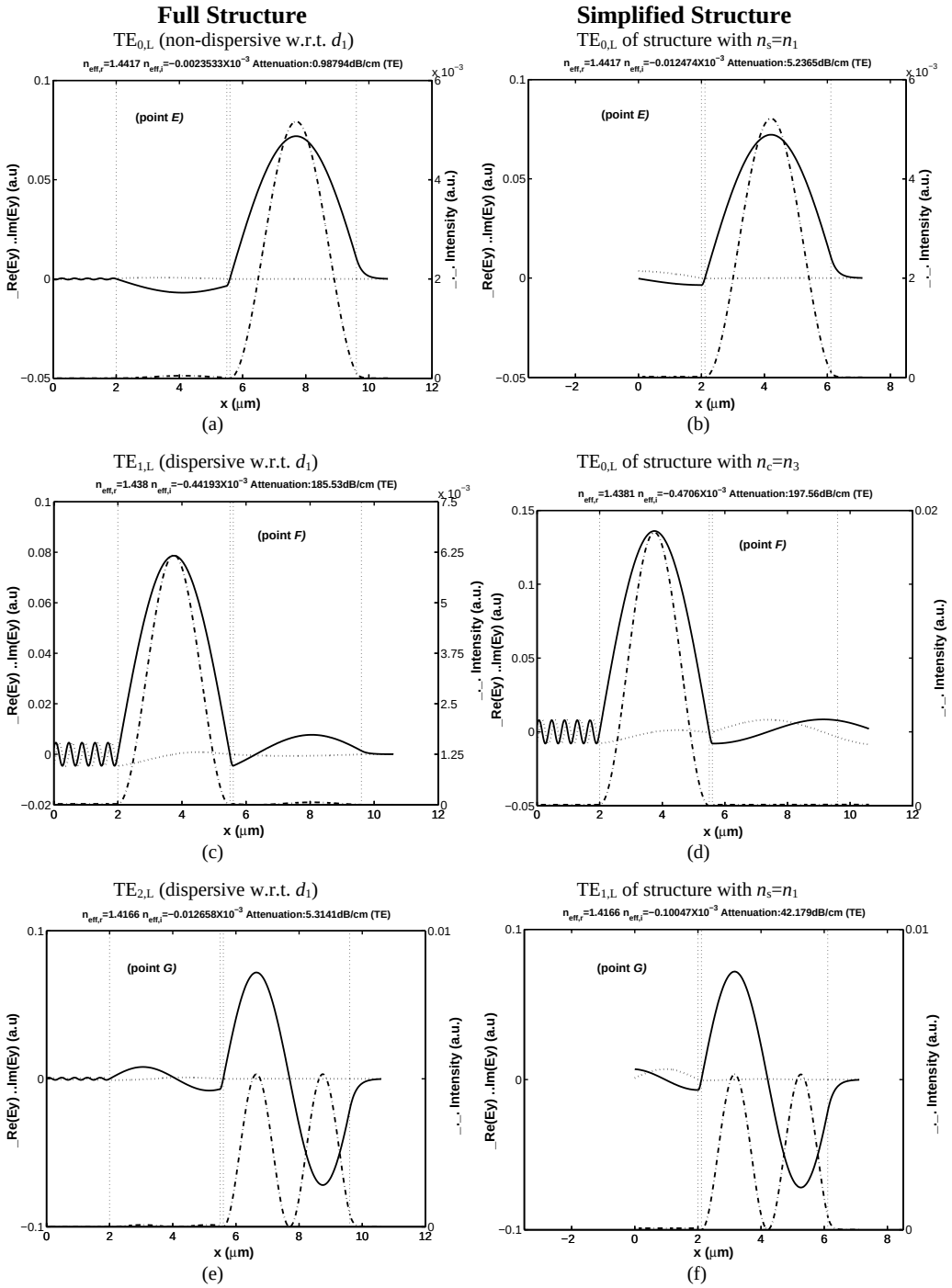

Figure 5.12. *Mode and intensity profiles of the full structure (left column) and the corresponding simplified structures (right column) for d_1=3.5μm. The figure at the 1st, 2nd, and 3rd row correspond to point E, F, and G in the curves, respectively.*

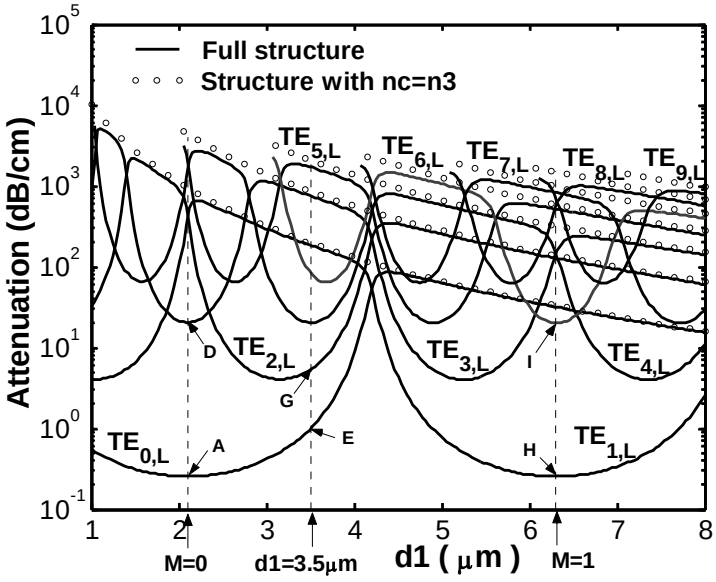

(a)

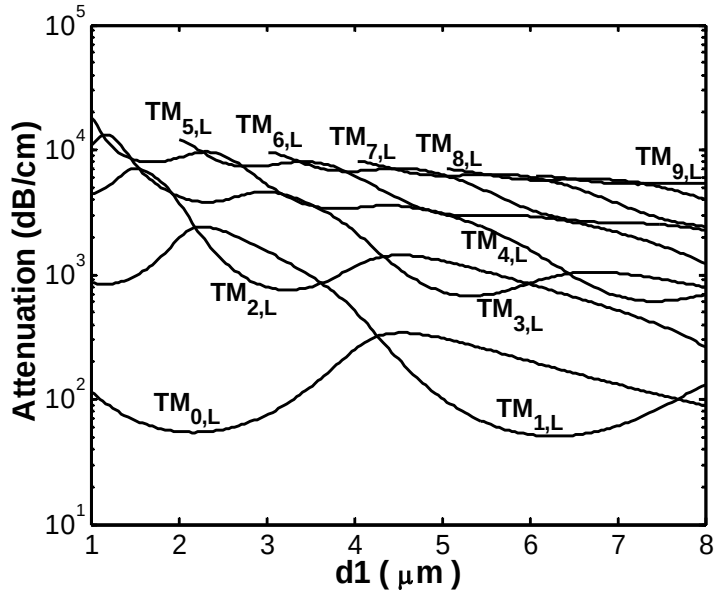

(b)

Figure 5.13. *Attenuation as function of d_1 of the isotropic ARROW sample: (a). TE (b). TM. Other parameters are as Section 5.3.2.*

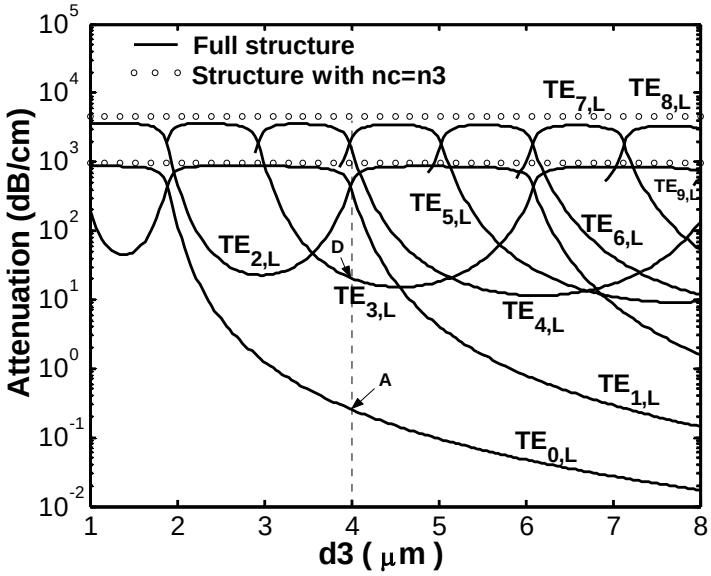

(a)

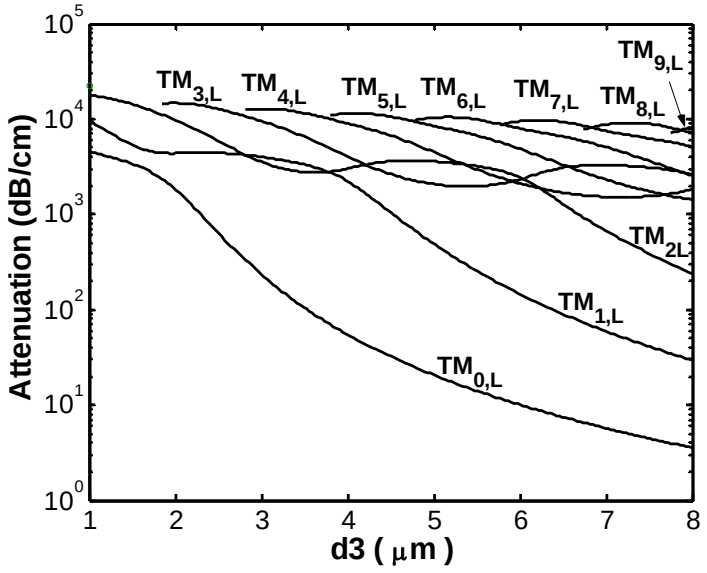

(b)

Figure 5.14. *Attenuation as function of d_3 of the isotropic ARROW sample: (a). TE (b). TM. Other parameters are as in Section 5.3.2.*

The core modes (i.e. modes which resonate in the core layer) should exhibit a weak dependence on the 2nd-cladding thickness (d_1), but strong dependence on the core thickness (d_3). Hence, they are located at the flat and curved parts of the curves in Fig. 5.9a and Fig. 5.10a, respectively. For 2nd-cladding-resonance modes (i.e. modes which

resonate in the 2nd-cladding layer), this is the other way around, hence situated at the curved and flat parts of the curves in Fig. 5.9a and Fig. 5.10a, respectively. If their effective indices are nearby each other, they become phase-matched, and hence strongly coupled, which shows up in the anti-crossing phenomenon. Hence, the unusual dispersion curves come from the anti-crossing between the core and the 2nd-cladding-resonance modes. This becomes clearer if we plot the field profiles related to point *A* to *G* in the curves. Fig. 5.11 shows the mode and intensity profiles of $TE_{0,L}$ to $TE_{3,L}$ of the full structure which correspond to points *A* to *D* in the curves, respectively. It is obvious that fields corresponding to points *A* and *D*, which are located far enough from the anti-crossing region and situated at the core-mode region of the curve, are strongly confined within the core layer and associated with the 0th- and 2nd-order core modes, respectively. Contrary, fields corresponding to points *B* and *C*, which are located at the anti-crossing region, correspond to a mix between 1st-order core and 0th-order 2nd-cladding-resonance mode. Fig. 5.12 compares the mode and intensity profiles of modes of the full structure (at the left column) with those of the simplified structures (at the right column) corresponding to points *E* to *G*, all far enough from the anti-crossing regions. The figure shows similarity between mode profiles of the full structure with those of the simplified structures at the same point. It is obvious that fields at point *E* and *G* corresponds to the 0th- and 1st-order core modes, respectively, while fields at point *F* associated with the 0th-order 2nd-cladding-resonance mode.

Modes of TM polarization are less confined than their TE counterpart. This means that more significant amount of power of the core modes will penetrate into the 2nd-cladding, and vice versa for the 2nd-cladding resonance modes. This leads to stronger coupling between core and 2nd-cladding resonance modes as shows up in the wider anti-crossing gap. That is why the relation between curves of the full and the simplified structures becomes more difficult to be recognized for TM modes.

Figure 5.13 and 5.14 show the attenuation of the first-ten modes of the ARROW as function of d_1 and d_3, respectively. Figure 5.13a and 5.14a show that the top of the attenuation curves corresponds to the attenuation curves of structure with $n_c=n_3$, i.e. those related to the 2nd-cladding resonance modes. Since their resonance center is located nearer to the high-index substrate, they are more leaky than the core modes.

The working principles of the ARROW can also be understood from Fig. 5.9-5.10 and 5.13-5.14. The structure as in Section 5.3.2 is designed with the 1st- and 2nd-cladding layer operate in 0th-order anti-resonant condition for the fundamental TE core mode. This corresponds to the vertical dashed line indicated by M=0 in the figures. For this condition, the loss of $TE_{0,L}$ (point *A*) is very low due to the high reflection of the cladding layers. For the 1st-order TE core mode, the 2nd-cladding layer operate in

resonance condition (since this mode is located at the anti-crossing region, i.e. point *B* and *C*), hence this mode is relatively leaky due to the low reflection of the 2nd-cladding layer. However, for the 2nd-order core mode (point *D*), the 2nd-cladding again operates in the anti-resonant condition, but the 1st-cladding does not, producing a confinement loss which is smaller than the 1st-order core mode, but greater than that of the fundamental core mode. This creates loss discrimination between modes, which is required for effectively single-mode operation. Besides, it is also possible to choose the thickness of the 2nd-cladding layer in order to let it operated in the 1st-order anti-resonant condition for the fundamental TE core mode, which is denoted by the vertical dashed line indicated by M=1 in the figures. For this setting, the confinement loss of the fundamental TE core mode is also very low (point *H*). However, the real part of its effective index is rather close to the 2nd-cladding-resonance mode, hence the performance of this structure might be rather sensitive to fabrication imperfections. It should be noted that for this setting, the fundamental TE core mode is not the lowest order mode, but the $TE_{1,L}$ due to the existence of a 2nd-cladding-resonance mode with $\mathrm{Re}(n_{\mathrm{eff}})$ of higher than the one of the core mode.

Fig. 5.14a also shows that beyond point *A*, we still can decrease the confinement loss of the fundamental TE core mode by enlarging the core size. Although for this condition, this mode is not optimally located at the anti-resonant region of the two cladding layers, the loss is lower due to the higher degree of confinement of the field within the core layer. However, the loss of higher order core modes also gets lower, resulting in a poorer single-modeness condition.

5.5. Conclusion

A simple high-order Galerkin finite element scheme is reported for the computation of both guided and leaky modes of anisotropic planar waveguides with a diagonal permittivity tensor. Transparent boundary conditions based on the Sommerfeld radiation conditions are used to model the field at the computational boundaries, both at the one where the wave should leak and at the one where the wave should decay. Richardson-like extrapolation and mesh adjustment scheme are used to extend the order of the scheme while still keep its simplicity. The scheme was demonstrated using various guided- and leaky-wave structures. Using the scheme, we also performed a detailed study on ARROW structures.

References

1. H. Wong, “Recent developments in silicon optoelectronics devices,” **Microelectronics Reliability**, Vol. 42, No. 3, pp. 317-326, 2002.

2. K. Wörhoff *et al.*, "Plasma enhanced chemical vapor deposition silicon oxynitride optimized for application in integrated optics," **Sensors and Actuators A**, Vol. 74, No. 1-3, pp. 9-12, 1999.

3. S. Lim, S. Shih, and J.F. Wager, "Design and fabrication of a double bandstop rugate filter grown by plasma-enhanced chemical vapor deposition," **Thin Solid Films**, Vol. 277, No. 1-2, pp. 144-146, 1996.

4. T. Ishigure *et al.*, "Accurate refractive index profiling in a graded-index plastic optical fiber exceeding gigabit transmission rates," **J. Lightwave Technol.**, Vol. 20, No. 8, pp. 1449-1456, 2002.

5. C. Thompson and B.L. Weiss, "Modal characteristics of graded multilayer optical waveguides," **J. Lightwave Technol.**, Vol. 14, No. 5, pp. 894-900, 1996.

6. M. de Micheli, "Nonlinear effects in TIPE-LiNbO3 waveguides for optical communications," **J. Opt. Commun.**, Vol. 4, pp. 25-31, 1983.

7. J.C.G. de Sande, G. Leo, and G. Assanto, "Phase-matching engineering in birefringent AlGaAs waveguides for difference frequency generation," **J. Lightwave Technol.**, Vol. 20, No. 4, pp. 651-660, 2002.

8. J.C. Grant, J.C. Beal, and N.J.P. Frenette, "Solving certain leaky wavrguides with lossless, simply bounded finite element modeling," **Photonics Technol. Lett.**, Vol. 2, No. 12, pp. 890-892, 1990.

9. H.E. Hernandez-Figueroa *et al.*, "Vectorial finite-element modeling of 2D leaky waveguides," **Trans. Magnetics**, Vol. 31, No. 3, pp. 1710-1713, 1995.

10. G. Tartarini, "Efficient beta-formulation for the FEM analysis of leaky modes in general anisotropic channel waveguides," **Opt. Quantum Electron.**, Vol. 32, No. 6-8, pp. 719-734, 2000.

11. W.P. Huang *et al.*, "The perfectly matched layer boundary condition for modal analysis of optical waveguides: leaky mode calculation," **Photonics Technol. Lett.**, Vol. 8, No. 5, pp. 652-654, 1996.

12. J. Kubica, D.Uttamchandani, and B. Culshaw, "Modal propagation within ARROW waveguides," **Optics Commun.**, Vol. 78, No. 2, pp. 133-136, 1990.

13. C. Chen *et al.*, "Efficient and accurate numerical analysis of multilayer planar optical waveguides in lossy anisotropic media," **Optics Express**, Vol 7, No. 8, pp. 260-272, 2000.

14. W.P. Huang *et al.*, "The modal characteristics of ARROW structures," **J. Lightwave Technol.**, Vol. 10, No. 8, pp. 1015-1022, 1992.

15. A.K. Ghatak, "Leaky modes in optical waveguides," **Opt. Quantum Electron.**, Vol. 17, pp. 311-321, 1985.

16. Y. Tsuji and M. Koshiba, "Guided-mode and leaky-mode analysis by imaginary distance beam propagation method based on finite element scheme," **J. Lightwave Technol.**, Vol. 18, No. 4, pp. 618-623, 2000.

17. S.S.A. Obayya *et al.*, "Full vectorial finite-element-based imaginary distance beam propagation solution of complex modes in optical waveguides," **J. Lightwave Technol.**, Vol. 20, No. 6, pp. 1054-1060, 2002.

18. J. Petracek and K. Singh, "Determination of leaky modes in planar multilayer waveguides," **Photonics Technol. Lett.**, Vol. 14, No. 6, pp. 810-812, 2002.

19. B. Liu, A. Shakouri, and J.E. Bowers, "Characteristic equations for different ARROW structures," **Opt. Quantum Electron.**, Vol. 31, No. 12, pp. 1267-1276, 1999.

20. E.M. Conwell, "Modes in optical waveguides formed by diffusion," **Appl. Phys. Lett.**, Vol. 23, No. 6, pp. 328-329, 1973.

21. P. Yeh and A. Yariv, "Bragg reflection waveguides", **Optics Commun.**, Vol. 19, No. 3, pp. 427-430, 1976.

22. N.M. Litchinitser *et al.*, "Antiresonant reflecting photonic crystal optical waveguides", **Optics Lett.**, Vol. 27, No. 18, pp. 1592-1594, 2002.

Chapter 6

Finite element and perturbative study of buffered leaky planar waveguides

The effects of the existence of a high-index medium in the proximity of the planar waveguiding structures that makes up buffered leaky waveguides are studied using the finite element method (FEM) leaky mode solver and a perturbation method. Various aspects of the effects are obtained through FEM computations, while the interpretations of the observed phenomena are carried out through the approximate analytical expressions derived using the perturbation method. The effect of the buffer layer thickness, the high-index-medium refractive index, and the quasi-confinement of the modal field are investigated. A two-parameter formula is used as a convenient way to characterize those effects on the leakage loss. The results show that the perturbation due to the high-index-medium does not always lead to an increase in the real part of the effective index, but can also decrease this quantity as well. Similarly, the leakage loss of a TE-polarized mode is not always lower than TM-polarized mode of the same order. It is found that as the refractive index of the high-index medium goes to infinity, a leaky-wave structure evolves into a guided-wave structure.

This chapter is adapted from:
H.P. Uranus, H.J.W.M. Hoekstra, and E. van Groesen, "Finite element and perturbative study of buffered leaky planar waveguides," (submitted for publication).

Finite element and perturbative study of buffered leaky planar waveguides

6.1. Introduction

Optical waveguides made on semiconductor substrates are widely used, benefiting from the wide availability of such substrates. In addition, the fabrication of these waveguides shares the well-developed processing technologies used also by other disciplines, such as microelectronics and micro-electromechanical-systems (MEMS). Waveguides made on a low-cost silicon substrate are examples of such structures. Unfortunately, the refractive index of this substrate is high, while materials, which are compatible with this substrate and often used for making up waveguides, such as silicon oxynitride, silicon nitride, or silica, have lower refractive indices. One way to deal with this is by placing another material with a lower refractive index between the waveguiding structure and the high-index substrate. This so-called buffer layer isolates the light in the waveguiding structure from the substrate. Various functional integrated optical circuits [1] can be made using this approach, including those that exploit the specific properties of these structures like waveguide polarizers [2]. Besides waveguides made on high-index substrates, the existence of a high-index component in the proximity of an ordinary waveguide also creates a buffered leaky waveguiding structure. Such situations occur in case of a prism-loaded waveguide [3], a waveguide tuned by high-index material overlaid on top of it (see e.g. Section 7.3.4), or an optical MEMS movement sensor [4]. In the last three cases, either air or index-matching oil can be regarded as the buffer layer. Fig. 6.1 shows some examples of buffered leaky planar structures.

Such structures are generally leaky, as they used to possess structure-induced loss, known as leakage loss, even when composed of lossless materials. If the buffer layer is sufficiently thick, a simplified lossless structure by neglecting the existence of the high-index medium can be used as a good approximation to the complete leaky structure.

However, the knowledge about the effect of the high-index medium in the proximity of the waveguiding structure is indispensable. For waveguides made on silicon substrate, for example, the buffer layer is usually made either through thermal oxidation of the silicon wafer or deposition of a SiO_2 layer. Since the thickness of this oxide layer is related to the duration of the oxidation or deposition process, knowledge about how this thickness will affect the waveguiding and loss properties of the structure is important so as to be able to choose a just sufficient thickness of that layer

in order to reduce the machine occupation time and related costs. In addition, an oxide layer that is too thick could bring mechanical problems such as wafer-bowing or layer-cracking. For the prism-loaded waveguide, the high-index-overlaid waveguide, the MEMS movement sensor, and the waveguide polarizer, knowledge about the high-index-medium proximity effect is essential, since it forms the basis of the working principle behind the structures.

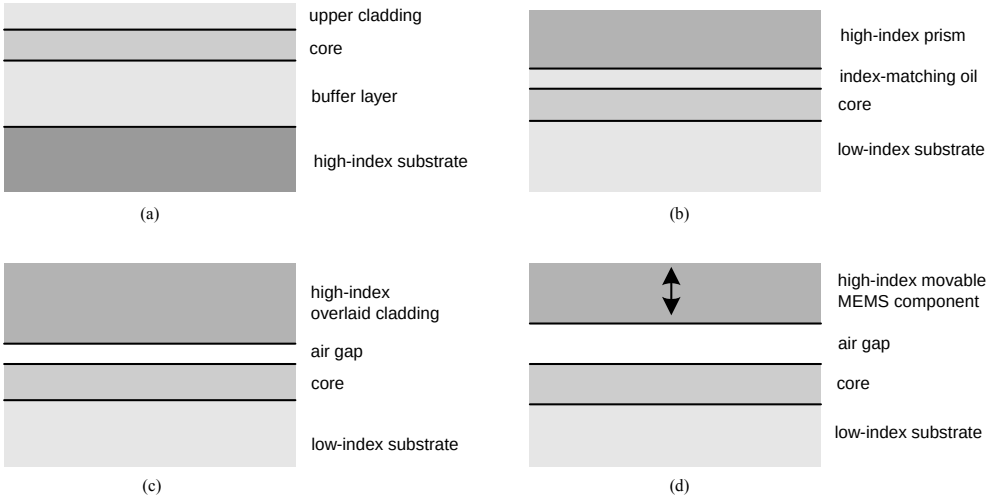

Figure 6.1. *Examples of buffered leaky planar waveguides: (a). a waveguide made on a high-index substrate, (b). a prism-loaded waveguide, (c). a high-index-overlaid waveguide, and (d). an optical MEMS movement sensor.*

Although many mode solvers [5-9] can calculate the leaky modes of such structures, so far only few efforts have been put into the comprehensive study of the effect of the high-index medium in the proximity of a waveguiding structure. Lu *et al.* [8] derived analytical dispersion equations for a 4-layer buffered leaky waveguide, solved it numerically, and used that to study the effect of the buffer and upper-cladding thicknesses on the leakage loss and the real part of the effective indices. In this chapter, the leaky mode solver based on Galerkin finite element method (FEM) reported in the previous chapter is used to study rigorously the effect of the high-index medium proximity to the waveguiding structures. Approximate analytical expressions of that effect are obtained by a perturbation method, and used to interpret phenomena, which are observed numerically.

6.2. Description of the methods used in the study

In this chapter, we consider planar waveguides composed of lossless dielectric materials whereby a high-index medium constitutes one of their semi-infinite

outermost cladding/substrate. Without that high-index medium, the structures are lossless guided-wave structures.

6.2.1. FEM leaky mode solver

By using the Galerkin FEM scheme furnished with Sommerfeld-like transparent boundary conditions, we can compute the guided and leaky modes of such structures. Through the mode indices and field profiles, we can study the effect of the high-index medium to the waveguides. The detailed explanation of the FEM scheme has been given in the previous chapter, and so will not be repeated here.

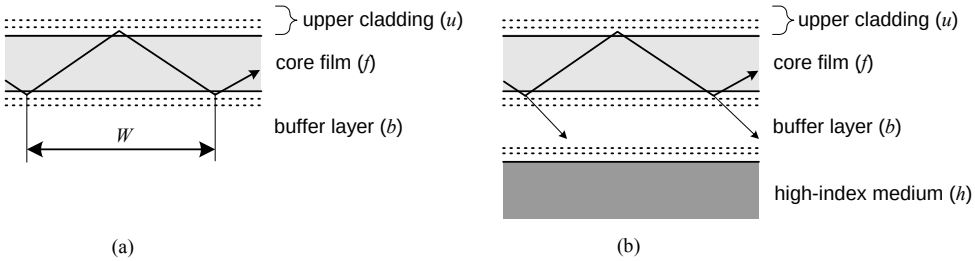

Figure 6.2. *(a). The unperturbed and (b). the perturbed structure.*

6.2.2. Perturbation method

To obtain more insights into the effect of the existence of a high-index medium in the proximity of a lossless waveguiding structure, we use a perturbation method [10] to derive approximate analytical expressions of that effect. Here, we consider the lossless multilayer structure without the high-index medium as the unperturbed structure and the complete structure as the perturbed structure. As shown in Fig. 6.2, it is possible to have a multilayer-coated high-index medium, which might be the case for the high-index-overlaid waveguides or the optical MEMS movement sensor.

Modes of the unperturbed structure fulfill the transverse resonance condition

$$\psi_0 = -2k_{t,0}d_f + \theta_{f,u} + \theta_{f,b} + 2\pi m = 0\,, \tag{6.1}$$

with $k_{t,0}$, d_f, $\theta_{f,u}$, and $\theta_{f,b}$ denoting the transverse wavenumber of the unperturbed structure, the thickness of the core film, the (real-valued) phase shift due to total internal reflection of light going from the core film to the upper cladding, and to the buffer, respectively, while m=0,1,… denoting the mode order. Similarly, the modes of the perturbed structure fulfill the transverse resonance condition

$$\psi - \theta_{f,b} + \theta_{f,h} + j\gamma = 0\,, \tag{6.2a}$$

with

$$\psi = -2k_{t,p}d_f + \theta_{f,u} + \theta_{f,b} + 2\pi m = \psi_0 + \delta\psi \,, \tag{6.2b}$$

where $k_{t,p}$, $\theta_{f,h}$, and γ denote the transverse wavenumber of the perturbed structure, the real and imaginary part of the phase shift due to partial reflection of light going from the core film to the high-index medium, respectively. Here, Ψ depends on the perturbed effective index (through $k_{t,p}$) and the parameters of the unperturbed structure, hence can be expressed as Ψ_0 with a small perturbation $\delta\Psi$. We assume that the effective index experiences a small perturbation expressed by

$$n_{eff} = n_{eff,0} + \delta n_{eff} \,, \tag{6.3}$$

with n_{eff}, $n_{eff,0}$, and δn_{eff} denoting the effective index of the perturbed structure, the effective index of the unperturbed structure, and the effective index perturbation, respectively. Using Taylor's expansion around $n_{eff,0}$ we arrive at

$$\delta\psi \approx \frac{\partial\psi}{\partial n_{eff}}\delta n_{eff} \,. \tag{6.4}$$

Using $\dfrac{\partial\psi}{\partial\beta} = W$ (see reference [3]) with the propagation constant defined as $\beta \equiv k_0 n_{eff}$ and W denoting the length of one zig-zag path along propagation direction including the Goos-Hänchen shift (GHS), we can further rewrite eq. (6.4) as

$$\delta\psi \approx k_0 W \delta n_{eff} \,. \tag{6.5}$$

Susbtituting eq. (6.5) into eq. (6.2) and using eq. (6.1) leads to

$$\delta n_{eff} \approx j\frac{1}{k_0 W}\ln\left(\frac{r_{f,h}}{r_{f,b}}\right), \tag{6.6}$$

where $r_{f,h} = \exp\left[\, j\left(\theta_{f,h} + j\gamma\right)\right]$ and $r_{f,b} = \exp\left[\, j\theta_{f,b}\,\right]$ are the reflection coefficients of light going from the core film to the high-index medium and the buffer layer, respectively. Using the multilayer thin film reflection and transmission formula [11], we can further rewrite eq. (6.6) as

$$\delta n_{eff} \approx 2r_{b,h}\sin\left(\theta_{f,b}\right)\exp\left(-a_b\right)\Big/\left(k_0 W\right), \tag{6.7a}$$

with

$$a_b = 2k_0 d_b\sqrt{n_{eff,0}^2 - n_b^2} \,, \tag{6.7b}$$

where $r_{b,h}$, d_b, and n_b denote the reflection coefficient of light going from the buffer layer to the high-index medium, the thickness, and the refractive index of the buffer layer, respectively. Equation (6.7) is an approximate analytical expression for the effect of the high-index medium in the proximity of the waveguide to the mode effective index. It is worth noting that $r_{b,h}$ is the only complex quantity in eq. (6.7) which will change the real-valued $n_{eff,0}$ into complex-valued n_{eff}. From the imaginary part of eq. (6.7a), we can obtain an approximate analytical expression of the attenuation constant (in dB per unit length) due to the high-index medium as

$$\alpha \approx -40\log(e)\,\mathrm{Im}\left(r_{b,h}\right)\sin\left(\theta_{f,b}\right)\exp\left(-a_b\right)\Big/W \,. \tag{6.8}$$

In connection with the numerical simulation results to be presented in the next section, we will rewrite α as a two-parameter formula

$$\alpha = c_1 10^{c_2 d_b}, \tag{6.9}$$

where c_2 characterizes the sensitivity of the attenuation to the buffer layer thickness (i.e. $\frac{\partial \alpha}{\partial d_b} \sim c_2$). By matching eq. (6.9) to eq. (6.8), and assuming that W is not affected by the buffer thickness, we obtain

$$c_1 \approx -40 \log(e) \operatorname{Im}(r_{b,h}) \sin(\theta_{f,b}) / W \tag{6.10a}$$

and

$$c_2 \approx -2 \log(e) k_0 \sqrt{n_{eff,0}^2 - n_b^2}\ . \tag{6.10b}$$

Using analytical expressions (6.7)-(6.10), we can study the effect of the high-index medium to either fundamental or higher order modes, TE-polarized or TM-polarized modes of the buffered leaky structures.

6.3. Results and discussions

Here, we will study various aspects of the effect of a high-index medium in the proximity of a planar waveguide. We will use the FEM leaky mode solver reported in the previous chapter to compute rigorously the complex-valued leaky mode indices and use the approximate analytical expressions obtained through the perturbation method to interpret and gain some insight into the observed phenomenon. The FEM scheme being used in this work is the 2nd-order scheme. For the perturbation method, we use the transfer matrix method [11-12] to calculate the effective index of the unperturbed structure, the reflection coefficients, the phase-shift due to reflections, and the GHS. This study is carried out by taking a 5-layer leaky structure, which is made on a silicon substrate with a SiO_2 buffer layer made through thermal oxidation on its surface, and successively a Si_3N_4 core and SiO_2 cladding layer grown on top of it through PE-CVD, and air as the outermost cladding. The results presented here can also be generalized to understand other structures as well, such as the high-index-overlaid waveguide and the optical MEMS movement sensor.

The refractive indices of the Si, SiO_2 by oxidation, Si_3N_4, SiO_2 by PE-CVD, and air cladding are 3.476, 1.45, 1.98, 1.464, and 1, respectively at λ=1.55μm. Unless otherwise stated, the thickness of the buffer layer is varied from 1 to 8 μm, while the Si_3N_4 core is 0.14 μm, and SiO_2 cladding is 1 μm. The mode profiles of this structure for buffer layer thickness of only 1 μm are shown in Fig. 6.3, which shows a field that is weakly quasi-confined within the thin core layer, and leaks out into the high-index substrate. For this setting, the structure is effectively single-moded.

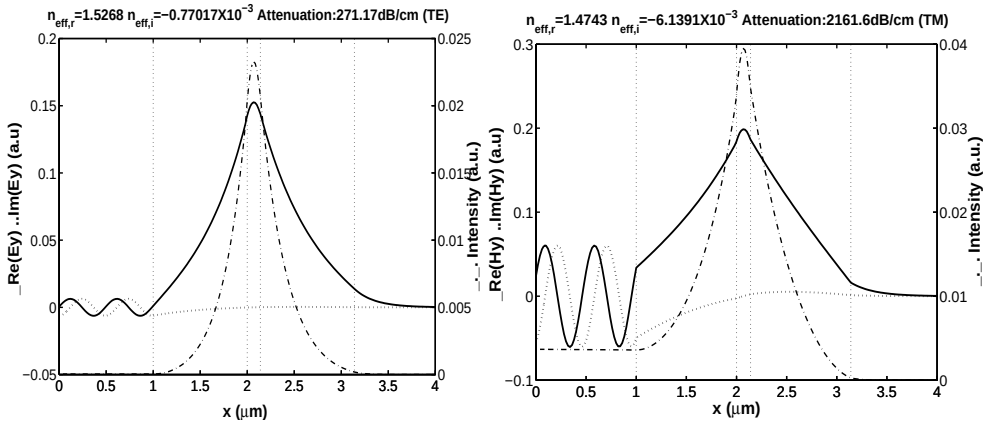

Figure 6.3. *Field and intensity profiles of the buffered leaky waveguide with buffer layer of 1μm: (a). TE and (b). TM modes.*

6.3.1. Effect of the buffer layer thickness

Fig. 6.4 shows the effect of thickening the buffer layer. As shown in Fig. 6.4a, if the thickness of the buffer layer is increased, the real part of the effective index will asymptotically approach the value of the effective index of the unperturbed structure, while the imaginary part will become smaller. Here, we observe that the existence of the high-index medium will decrease the $\mathrm{Re}\{n_{eff}\}$. Later on, we will show that it can also increase the $\mathrm{Re}\{n_{eff}\}$. Fig. 6.4b shows that the attenuation constant follows the two-parameter expression eq. (6.9) very well. The results of the perturbation method are also shown in Fig. 6.4. The curves of the perturbation method almost coincide with the finite element results, especially when the buffer layer is thick, i.e. when the perturbation is small. From our FEM simulation, we get c_1=12827.47 dB/cm and c_2= -1.7105 μm^{-1} for TE and c_1=17716.5 dB/cm and c_2= -1.0013 μm^{-1} for TM. Hence, given the maximum allowed loss, the minimum thickness of the buffer layer can be determined using eq. (6.9).

Figure 6.4b and eq. (6.10) also show that the attenuation of the TE-polarized mode is more sensitive to the buffer thickness than the attenuation of the TM mode due to the larger value of its unperturbed effective index, meaning that the loss of TE modes will decrease in a higher rate than TM if one increases the buffer thickness.

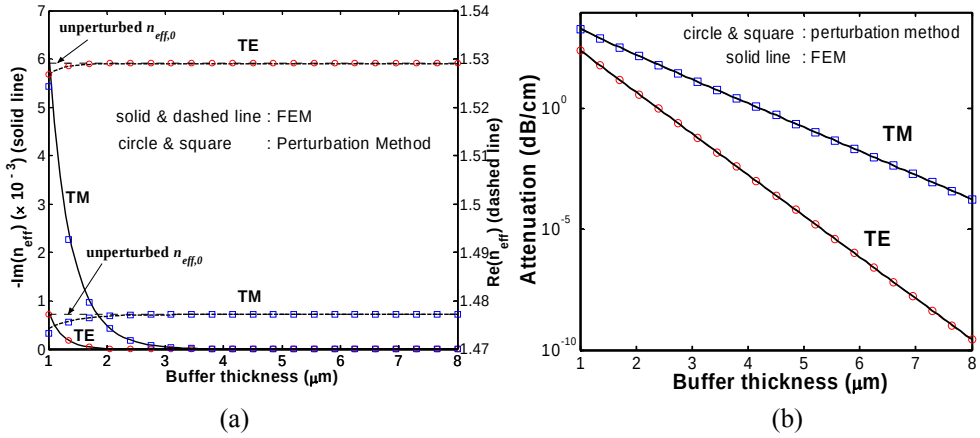

Figure 6.4. *The effect of the buffer thickness on (a). the effective indices and (b). the attenuation of a buffered leaky structure.*

6.3.2. Effect of the refractive index of the high-index medium

Figure 6.5 shows the effect of varying the refractive index of the high-index medium (n_h) on the real part of the effective index and the attenuation constant for a structure with buffer layer thickness of 1μm. For completeness, we vary n_h starting from the value of the buffer refractive index (n_b), although the term high-index medium is not suitable for this low refractive index value. As the buffer thickness is relatively small, the perturbation is relatively large, leading to noticeable difference between the rigorous results by the FEM and the approximate results by the perturbation method. However, we still can use the analytical expressions given by the perturbation method to study the behavior of the leaky waveguide. The figure clearly shows that the existence of the high index medium can lead to either an increase or a decrease of the real part of the effective index. Knowledge about this phenomenon may be important for tuning and sensing applications.

If n_h is just higher than n_b, the existence of the high-index medium will affect only to an increase of the real part of the effective index (see region located between points A to B for TE or A' to B' for TM). Hence, in this region, the structure is still a guided-wave structure. From eq. (6.7) it can be seen that the effect of changing n_h enters the expression for δn_{eff} through $r_{b,h}$. Here, we have neglected the effect of the high-index medium to the GHS, which is relatively small. Fig. 6.6 shows the evolution of $r_{b,h}$ for the corresponding modes in the complex plane as n_h being changed from n_b to ∞. From point A (A') to B (B'), the $r_{b,h}$ will have a real positive value as n_h is still lower than the unperturbed effective index ($n_{eff,0}$), leading to a real positive δn_{eff}.

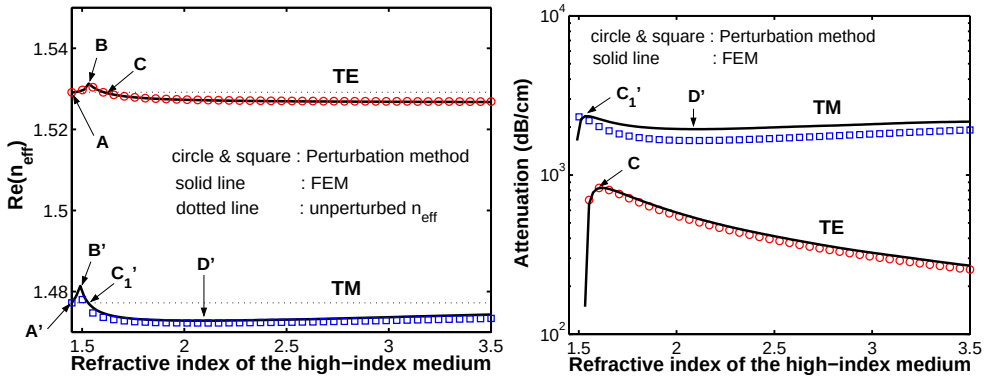

(a) (b)

Figure 6.5. *The effect of the refractive index of the high-index medium to (a). the real part of the mode effective index, and (b). the leakage loss.*

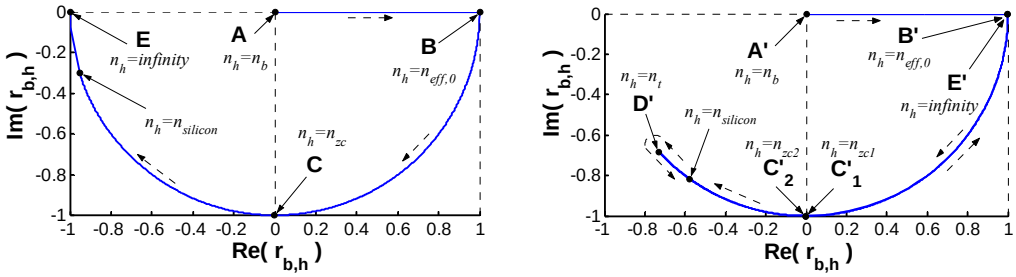

(a) (b)

Figure 6.6. *The evolution of $r_{b,h}$ in the complex plane as the refractive index of the high-index medium (n_h) changes from n_b to ∞ for (a) TE and (b) TM mode. The dashed arrows denote the direction of the trajectory that $r_{b,h}$ follows for positive change of n_h.*

Passing point B (B'), in the region where $n_h > n_{eff,0}$, the leakage loss is no longer zero, as $r_{b,h}$ becomes complex valued with a negative imaginary part. Until point C (C_1'), the $r_{b,h}$ is still located in the 4th quadrant of the complex plane, leading to a positive $\mathrm{Re}\{\delta n_{eff}\}$. At point C (C_1'), the attenuation arrives at its maxima while $\mathrm{Re}\{\delta n_{eff}\}$ arrives at its zero-crossing point. For an uncoated high-index medium, using the Fresnel reflection formula for a single interface to evaluate $r_{b,h}$, we obtain that this zero-crossing point is related to

$$n_h = n_{zc} = \left(2n_{eff,0}^2 - n_b^2\right)^{1/2} \tag{6.11a}$$

for TE, and

$$n_h = n_{zc1} = \left[\frac{n_b^4 - \sqrt{n_b^8 - 4\left(n_b^4 n_{eff,0}^4 - n_b^6 n_{eff,0}^2\right)}}{2\left(n_{eff,0}^2 - n_b^2\right)} \right]^{1/2} \tag{6.11b}$$

for TM. For TM, this is the first zero-crossing point, as later on we will see that this polarization has two zero-crossing points.

As the refractive index of the high-index medium is further increased such that the $r_{b,h}$ enters the 3rd quadrant of the complex plane, the existence of the high-index medium will decrease the real part of the effective index while the leakage loss will become smaller. For TE polarization, this happens monotonically until n_h goes to ∞ at point E. For TM, the behavior is different due to its unique Fresnel reflection properties. The decrease of the real part of n_{eff} and the leakage loss as we increase n_h will happen only until point D', thereafter these properties change their direction. We term this particular point as a turning point. For an uncoated high-index medium, by looking at the extrema of $r_{b,h}$, we find that this point is given by

$$n_h = n_t = \sqrt{2}\, n_{eff,0} \,. \tag{6.12}$$

After the turning point, the increase of n_h will increase the real part of n_{eff} toward $n_{eff,0}$ and increase the leakage loss toward another maxima. This behavior will happen until another zero-crossing point (C_2'), which for an uncoated high-index medium is associated to

$$n_h = n_{zc2} = \left[\frac{n_b^4 + \sqrt{n_b^8 - 4\left(n_b^4 n_{eff,0}^4 - n_b^6 n_{eff,0}^2\right)}}{2\left(n_{eff,0}^2 - n_b^2\right)} \right]^{1/2} \tag{6.13}$$

After this second zero-crossing point, the increase of n_h will monotonically increase the real part of the effective index above $n_{eff,0}$ and decrease the leakage loss. This behavior happens until n_h reaches ∞ at point E'. At point E (E'), the reflection coefficient is real for both polarization, meaning that as n_h reaches ∞, we will again have a lossless guided-wave structure. This surprising feature can also be checked by simply taking the limit of the Fresnel reflection formula for $n_h \to \infty$.

The dependence of the attenuation parameters (c_1 and c_2) on the refractive index of the high-index medium is depicted in Fig. 6.7. If the refractive index of the high-index medium is just larger than the effective index of the mode, the leakage loss starts to be non-zero. Although the attenuation constant varies according to the changes of the high-index medium refractive index, the sensitivity of the attenuation to the buffer thickness (c_2) is not itself sensitive to the changes of the refractive index of the high-index medium. Equations (6.9) and (6.10) show that the changes of the attenuation by changing the high-index medium refractive index, which are attributed to the changes of the imaginary part of the reflection coefficient $r_{b,h}$, only affect c_1, leaving c_2 to be unaffected.

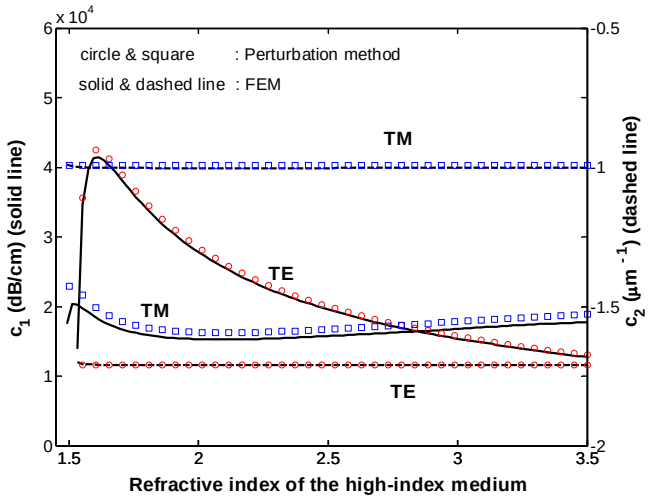

Figure 6.7. *The effect of the refractive index of the high-index medium to the attenuation parameters.*

6.3.3. Effect of the mode field quasi-confinement

Besides the thickness of the buffer layer, the isolation of the unperturbed structure from the high-index medium also depends on the degree of the quasi-confinement of the modal field. To investigate this, we take the same structure with a buffer layer thickness of only 1 μm and vary the thickness of the guiding layer. The results are shown in Fig. 6.8, where for guiding film that is sufficiently thick, the structure becomes multi-moded.

For a weakly-quasi-guiding condition, i.e. near to the cut-off of the modes, the perturbation due to the high-index substrate is quite pronounced as indicated by the large leakage losses and the noticeable difference between $\mathrm{Re}\{n_{eff}\}$ curves of the unperturbed structure (dotted line) and the leaky structure (solid line and circle/square) in Fig. 6.8a, and also between the FEM and the perturbation results in Fig. 6.8b. For a strongly-quasi-guiding condition, the losses are small, while the $\mathrm{Re}\{n_{eff}\}$ values of the unperturbed structure are very close to those of the leaky structure due to the relatively small perturbation. Hence, the unperturbed structure can be used to approximate the complete structure safely in most practical applications. Fig. 6.9 shows that as the modes become more quasi-confined within the guiding film, $|c_2|$ becomes larger, meaning that the attenuation becomes more sensitive to the buffer layer thickness, which is attributed to the higher value of the unperturbed effective indices as indicated by eq. (6.10b).

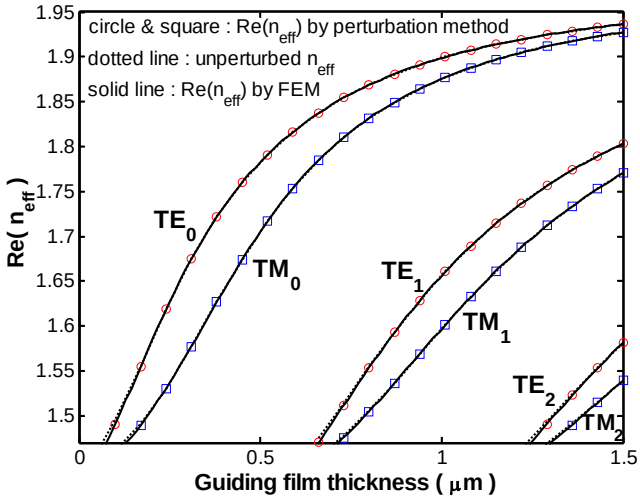

(a)

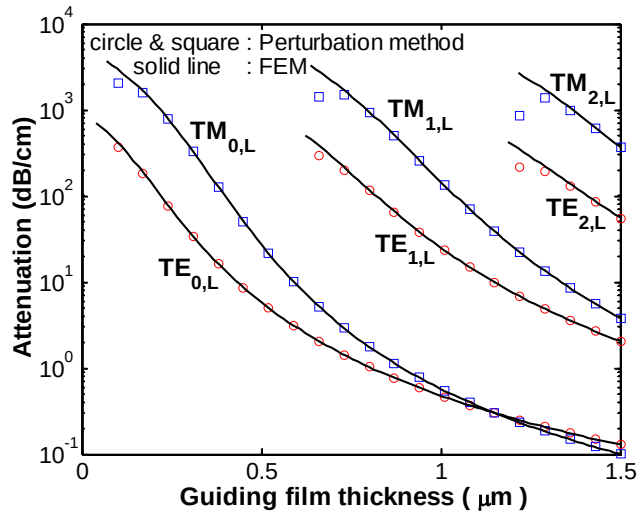

(b)

Figure 6.8. *(a). The dispersion curves of the leaky and the corresponding unperturbed lossless structure, and (b). the attenuation as function of core thickness.*

An interesting phenomenon can be seen in Fig. 6.8b. In the strongly-quasi-guiding but thin buffer layer setting, although the real part of the effective index of TM polarization is closer to the refractive index of the buffer layer than that of TE (which leads to a longer evanescent tail for TM compared to TE modes in the unperturbed structure; hence logically one would expect a larger attenuation for TM than for TE), this rigorous simulation shows that the attenuation of TM can be smaller than TE. This phenomenon becomes clear if we use eq. (6.9) and plot the buffer layer thickness for

which the attenuation of TE and TM modes of the same order have the same value, i.e. at the intersection of the two lines in Fig. 6.4b for each guiding film thickness. We term this particular buffer layer thickness as the characteristic buffer thickness $d_{b,char}$ and the corresponding attenuation value as the characteristic attenuation α_{char}. Fig. 6.10 shows that for the weakly-quasi-guiding condition, the characteristic buffer thickness has a non-physical negative buffer layer thickness value, but for the strongly-quasi-guiding condition it will have a positive value. For a buffer layer thickness smaller than this (positive) value, the attenuation of TM will be smaller than TE, regardless of the fact that the real part of the effective index of the TM mode is closer to the refractive index of the buffer layer than the effective index of the TE mode. For the weakly-quasi-guiding condition, the attenuation of TM is always larger than TE since it is impossible to have a buffer layer with negative thickness.

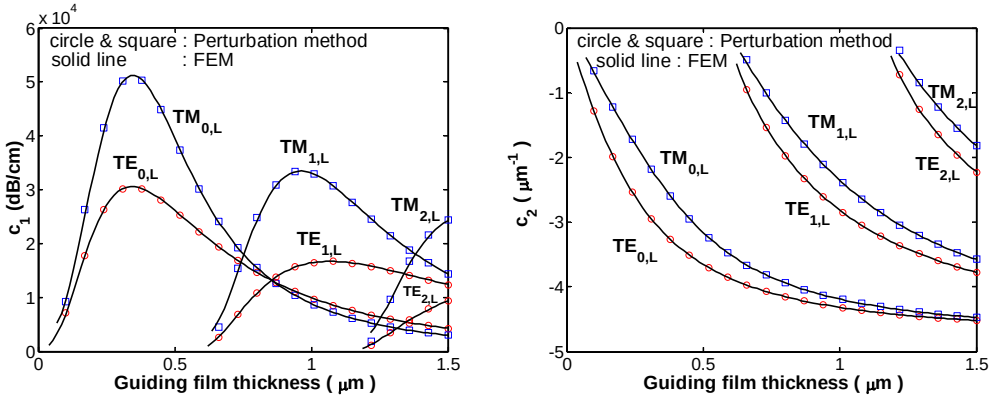

Figure 6.9. *The effect of the thickness of the core layer to the parameters of the attenuation: (a). c_1 and (b). c_2.*

6.4. Conclusions

The effects of a high-index medium in the proximity of planar waveguiding structures that makes up buffered leaky waveguides are studied using the FEM leaky mode solver and a perturbation method. The effect of the buffer layer thickness, the high-index-medium refractive index, and the quasi-confinement of the modal field are investigated. The study shows that the perturbation due to the high-index-medium does not always lead to an increase of the real part of the effective index, but can also decrease this quantity as well. Similarly, the leakage loss of TE-polarized mode is not always smaller than TM-polarized mode of the same order. The study also shows that if the refractive index of the high-index medium goes to infinity, a leaky-wave structure evolves into a lossless guided-wave structure.

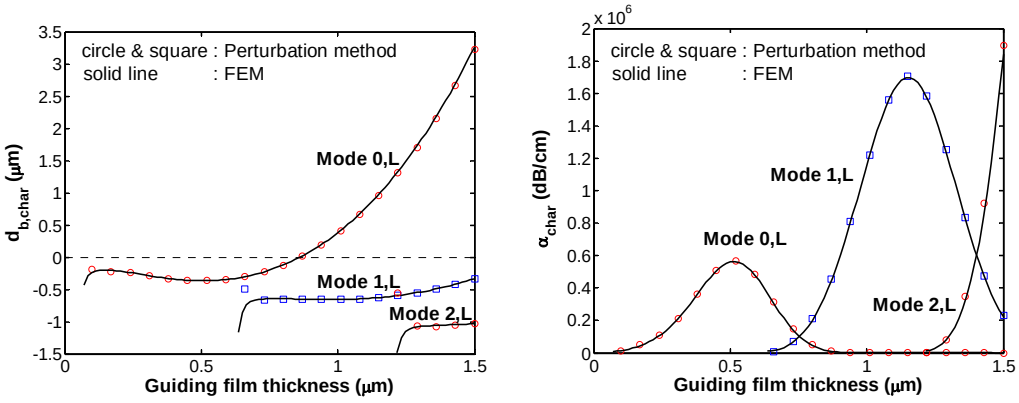

(a) (b)

Figure 6.10. *(a). The characteristic buffer thickness and (b). characteristic attenuation as function of the guiding film thickness.*

References

1. R.M. de Ridder *et al.*, "Silicon oxynitride planar waveguiding structures for application in optical communication," **J. Sel. Topics in Quantum Electron.**, Vol. 4, No. 6, pp. 930-937, 1998.
2. S. Ohke, T. Umeda, and Y. Cho, "TM-mode selective filter using leaky waveguide structure," **Elect. and Commun. In Japan Part 2**, Vol. 85, No. 8, pp. 9-15, 2002.
3. H.J.W.M. Hoekstra, J.C. van't Spijker, and H.M.M.K. Koerkamp, "Ray picture for prism-film coupling," **J. Opt. Soc. Am. A**, Vol. 10, No. 10, pp. 2226-2230, 1993.
4. G. Altena *et al.*, "A novel MOEMS device: detection of MEMS movements using free-standing Si_3N_4 suspended optical waveguides," **Proc. 8th Symposium IEEE LEOS Benelux Chapter**, Enschede, The Netherlands, pp. 25-28, 2003.
5. A.K. Ghatak, "Leaky modes in optical waveguides," **Opt. Quantum Electron.**, Vol. 17, pp. 311-321, 1985.
6. W.P. Huang *et al.*, "The perfectly matched layer boundary condition for modal analysis of optical waveguides: leaky mode calculation," **Photonics Technol. Lett.**, Vol. 8, No. 5, pp. 652-654, 1996.
7. C. Chen *et al.*, "Efficient and accurate numerical analysis of multilayer planar optical waveguides in lossy anisotropic media," **Optics Express**, Vol 7, No. 8, pp. 260-272, 2000.
8. J. Lu, S. He, and V.G. Romanov, "Study of the leakage loss in a silica-on-silicon slab waveguide," **Fiber and Integrated Optics**, Vol. 22, pp. 249-261, 2003.
9. H.P. Uranus, H.J.W.M. Hoekstra, and E. van Groesen, "Simple high-order Galerkin finite element scheme for the investigation of both guided and leaky modes in anisotropic planar waveguides," **Opt. Quantum Electron.**, Vol. 36, No. 1-3, pp. 239-257, 2004.

10. H.J.W.M. Hoekstra, "Theory for the effect of membrane/mirror on the modal field propagation," Internal Technical Report, IOMS group, Univ. Twente, 2003.

11. M. Born and E. Wolf, *Principles of Optics*, 6th Edition, Pergamon Press, Oxford, 1993.

12. H. Kogelnik, "Theory of optical waveguides," in *Guided-wave Optoelectronics*, T. Tamir, Ed., Springer Verlag, Berlin, 1990.

Chapter 7

Galerkin finite element scheme with transparent boundary conditions for a vectorial mode solver

A Galerkin finite element scheme furnished with 1st-order Bayliss-Gunzburger-Turkel-like boundary conditions is proposed to compute both the guided and leaky modes of anisotropic channel waveguides of non-magnetic materials with a diagonal permittivity tensor. The scheme is formulated using transverse components of the magnetic field for nodal-based quadratic triangular elements. Results for some structures will be presented. The effectiveness of the used boundary conditions will be illustrated using a step-index optical fiber with computational boundaries positioned near to the core, and the leaky modes computation of a rib ARROW. The computed results agree with their exact values (for optical fibers) and published results (for other structures). Using the scheme, the evolution of modes in a strip waveguide with anisotropic overlaid cladding and high-index substrate is observed.

This chapter is partly adapted from:
H.P. Uranus, H.J.W.M. Hoekstra, and E. van Groesen, "Galerkin finite element scheme with Bayliss-Gunzburger-Turkel-like boundary conditions for vectorial optical mode solver," **J. Nonlinear Opt. Phys. and Materials**, Vol. 13, No. 2, pp. 175-194, 2004.

Galerkin finite element scheme with transparent boundary conditions for a vectorial mode solver

7.1. Introduction

Mode solvers are indispensable tools in designing integrated optical waveguides. One of the widely used methods for optical mode solving is the finite element method (FEM), which offers versatility and flexibility. This method is well known for its ability to model waveguides with an arbitrary cross-section shape and anisotropic materials.

However, to model open structures, special treatment(s) on computational boundaries should be carried out in order to enable truncation of the finite element mesh. These boundary conditions (BCs) can be just the simple homogeneous Neumann boundary conditions (NBC) or Dirichlet boundary conditions (DBC) [1], discretizing the exterior domain using infinite elements [2], putting artificial absorbing materials, i.e. the so-called perfectly matched layers (PML) [3] near to the computational boundaries in addition to truncation of the mesh using the DBC, or the one based on treatment(s) of the fields at boundaries in such a way that they will pass the boundaries with minor reflection, i.e. the so-called transparent boundary conditions (TBC). The first two BCs can only be used to model guided modes, while the last two can model both guided and leaky modes. The PML-based BC is presently the most popular one. However, it enlarges the computational domain by the additional artificial absorbing materials and requires some "skill" on choosing the optimal material properties in order to let it work effectively. One of the TBC used for FEM optical mode solvers is the Sommerfeld-like TBC proposed by Hernandez-Figueroa *et al.* [4]. However, the accuracy of this BC is only $O(r^{-3/2})$ with r denoting the position of the computational boundary with respect to a chosen origin of the structure. Besides, iterations are required in order to obtain the modes.

In this chapter, we apply a Bayliss-Gunzburger-Turkel-like (BGT-like) [6] TBC for a FEM optical mode solver. The BC is embedded into a nodal-based Galerkin FEM scheme formulated using transverse components of the magnetic field for structures with diagonal permittivity tensor materials. The scheme is restricted to these materials for practical and simplicity reasons. This kind of materials is widely used and requires only a computational effort nearly similar to the isotropic one. The scheme is implemented for unstructured triangular mesh with quadratic basis functions. The

proposed boundary conditions are local, hence approximate, but preserve the matrix sparsity, with just one additional term in the boundary operator compared to the Sommerfeld-like TBC, while offering accuracy of $O(r^{-5/2})$, i.e. one order higher than the latter one. The shape of the computational boundaries can be arbitrary. The scheme can model both the guided and leaky modes. Although iterations are still required, only few iterations are normally needed for convergence depth of 10^{-10} in n_{eff}. For leaky modes computation, we propose an iteration strategy that uses the iterations as eigenvalue refinement mechanism using approximate results of some other simpler scheme as initial guesses. The scheme will be illustrated using some examples, i.e. optical fibers and a fused fiber coupler for guided mode computations, while a rib semiconductor-based ARROW and Si_3N_4 strip waveguide with DAST (4'-dimethylamino-*N*-methyl-4-stilbazolium tosylate) [23] overlaid cladding and Si substrate for leaky modes computations. The results show good agreement with the exact values (for optical fibers) and computational results of other methods (for other structures) as far as these have been published.

7.2. Description of the scheme

7.2.1. Finite element formulation

We consider optical waveguides with 2-D cross-section of arbitrary shape, composed of non-magnetic materials with a diagonal permittivity tensor of arbitrary index profiles. The vectorial wave equation for the magnetic fields of the waveguides can be written as

$$\nabla \times \bar{\bar{\varepsilon}}_r^{-1} \nabla \times \vec{H} = k_0^2 \vec{H} . \tag{7.1}$$

The structure is assumed to be invariant along *z*-axis. Using an ansatz of

$$\vec{H}(x,y,z,t) = \left[H_x, H_y, H_z \right]^T (x,y) \exp\left[j\left(\omega t - \beta z\right) \right], \tag{7.2}$$

with a propagation constant $\beta \equiv k_0 n_{eff}$ and Maxwell's equation

$$\nabla \bullet \vec{B} = 0 , \tag{7.3}$$

which implies also $\nabla \bullet \vec{H} = 0$ for non-magnetic material, we obtain from eq. (7.1) the vectorial wave equation that can be expressed in terms of only the transverse components of the magnetic fields as follows

$$\begin{bmatrix} \partial_y \left[\frac{1}{n_{zz}^2} \left(\partial_x H_y - \partial_y H_x \right) \right] \\ -\partial_x \left[\frac{1}{n_{zz}^2} \left(\partial_x H_y - \partial_y H_x \right) \right] \end{bmatrix} - \begin{bmatrix} \frac{1}{n_{yy}^2} \partial_x \left(\partial_x H_x + \partial_y H_y \right) \\ \frac{1}{n_{xx}^2} \partial_y \left(\partial_x H_x + \partial_y H_y \right) \end{bmatrix} + k_0^2 n_{eff}^2 \begin{bmatrix} \frac{1}{n_{yy}^2} H_x \\ \frac{1}{n_{xx}^2} H_y \end{bmatrix} = k_0^2 \begin{bmatrix} H_x \\ H_y \end{bmatrix}. \tag{7.4}$$

Following the Galerkin procedure, i.e. multiplying eq. (7.4) using weight function $\vec{w}_t = [w_x, w_y]^T$, and applying partial integration, we get the weak formulation of the problem as follows

$$\iint_{\Omega}\left\{\nabla_t\bullet\begin{bmatrix}-\frac{1}{n_{zz}^2}w_y\left(\partial_x H_y-\partial_y H_x\right)\\ \frac{1}{n_{zz}^2}w_x\left(\partial_x H_y-\partial_y H_x\right)\end{bmatrix}+\nabla_t\bullet\begin{bmatrix}-\frac{1}{n_{yy}^2}w_x\left(\partial_x H_x+\partial_y H_y\right)\\ -\frac{1}{n_{xx}^2}w_y\left(\partial_x H_x+\partial_y H_y\right)\end{bmatrix}\right.$$
$$+\frac{1}{n_{zz}^2}\left(\partial_x w_y-\partial_y w_x\right)\left(\partial_x H_y-\partial_y H_x\right)+\left[\partial_x\left(\frac{1}{n_{yy}^2}w_x\right)+\partial_y\left(\frac{1}{n_{xx}^2}w_y\right)\right]\left(\partial_x H_x+\partial_y H_y\right)$$
$$\left.+k_0^2 n_{eff}^2\left(\frac{1}{n_{yy}^2}w_x H_x+\frac{1}{n_{xx}^2}w_y H_y\right)-k_0^2\left(w_x H_x+w_y H_y\right)\right\}dx\,dy=0\,, \qquad (7.5)$$

with ∇_t denotes $\hat{x}\partial_x+\hat{y}\partial_y$ where the hat (^) symbol denotes the unit vector. Since the second and fourth terms in eq. (7.5) contain derivatives of discontinuous functions across interfaces, their discretization is not straightforward. By decomposing the discontinuous function as the sum of a continuous function and some value times Heaviside function, the discretization will produce additional terms at the second part of the right hand side (*rhs*) of following equations:

$$\iint_{\Omega}\nabla_t\bullet\begin{bmatrix}-\frac{1}{n_{yy}^2}w_x\left(\partial_x H_x+\partial_y H_y\right)\\ -\frac{1}{n_{xx}^2}w_y\left(\partial_x H_x+\partial_y H_y\right)\end{bmatrix}dxdy=\sum_{\substack{TriangularElement\\ e}}\left\{\iint_{\Omega_e}\nabla_t\bullet\begin{bmatrix}-\frac{1}{n_{yy}^2}w_x\left(\partial_x H_x+\partial_y H_y\right)\\ -\frac{1}{n_{xx}^2}w_y\left(\partial_x H_x+\partial_y H_y\right)\end{bmatrix}dxdy\right\}$$
$$-\sum_{\substack{InterfaceElement\\ e}}\left\{\int_{\Gamma_{\mathrm{int},e}}\Delta_x\left(\frac{1}{n_{yy}^2}\right)w_x\left(\partial_x H_x+\partial_y H_y\right)dy\right.$$
$$\left.+\int_{\Gamma_{\mathrm{int},e}}\Delta_y\left(\frac{1}{n_{xx}^2}\right)w_y\left(\partial_x H_x+\partial_y H_y\right)dx\right\} \qquad (7.6)$$

and

$$\iint_{\Omega}\left[\partial_x\left(\frac{1}{n_{yy}^2}w_x\right)+\partial_y\left(\frac{1}{n_{xx}^2}w_y\right)\right]\left(\partial_x H_x+\partial_y H_y\right)dxdy=$$
$$\sum_{\substack{TriangularElement\\ e}}\left\{\iint_{\Omega_e}\left[\partial_x\left(\frac{1}{n_{yy}^2}w_x\right)+\partial_y\left(\frac{1}{n_{xx}^2}w_y\right)\right]\left(\partial_x H_x+\partial_y H_y\right)dxdy\right\}$$
$$+\sum_{\substack{InterfaceElement\\ e}}\left\{\int_{\Gamma_{\mathrm{int},e}}\Delta_x\left(\frac{1}{n_{yy}^2}\right)w_x\left(\partial_x H_x+\partial_y H_y\right)dy\right.$$
$$\left.+\int_{\Gamma_{\mathrm{int},e}}\Delta_y\left(\frac{1}{n_{xx}^2}\right)w_y\left(\partial_x H_x+\partial_y H_y\right)dx\right\}, \qquad (7.7)$$

with

$$\Delta_x\left(\frac{1}{n_{yy}^2}\right)\equiv\left(\frac{1}{n_{yy}^2}\right)_{x=x_{\mathrm{int}+}}-\left(\frac{1}{n_{yy}^2}\right)_{x=x_{\mathrm{int}-}}, \qquad (7.8a)$$

$$\Delta_y\left(\frac{1}{n_{xx}^2}\right)\equiv\left(\frac{1}{n_{xx}^2}\right)_{y=y_{\mathrm{int}+}}-\left(\frac{1}{n_{xx}^2}\right)_{y=y_{\mathrm{int}-}}, \qquad (7.8b)$$

where *int*+ and *int*- subscripts in eq. (7.8) denote the right and left hand or the upper and lower sides of the interface, respectively. Since these additional terms (the two last

terms) of eqs. (7.6) and (7.7) have opposite sign, then they will cancel out each other. By discretizing the domain Ω into a finite number of triangular elements Ω_e, boundary line elements Γ_e (along the computational boundaries) and interface line elements $\Gamma_{int,e}$ (along the interfaces between different materials) and applying Green's theorem to the first terms of eq. (7.5) and *rhs* of eq. (7.6), we arrive at

$$\sum_{\substack{BoundaryElement\\ e}} \left\{ -\int_{\Gamma_e} \tfrac{1}{n_{zz}^2} w_y \left(\partial_x H_y - \partial_y H_x\right) dy - \int_{\Gamma_e} \tfrac{1}{n_{zz}^2} w_x \left(\partial_x H_y - \partial_y H_x\right) dx \right.$$
$$\left. -\int_{\Gamma_e} \tfrac{1}{n_{yy}^2} w_x \left(\partial_x H_x + \partial_y H_y\right) dy + \int_{\Gamma_e} \tfrac{1}{n_{xx}^2} w_y \left(\partial_x H_x + \partial_y H_y\right) dx \right\}$$
$$+ \sum_{\substack{InterfaceElement\\ e}} \left\{ -\int_{\Gamma_{\mathrm{int},e}} \tfrac{1}{n_{yy}^2} w_x \left(\partial_x H_x + \partial_y H_y\right) dy + \int_{\Gamma_{\mathrm{int},e}} \tfrac{1}{n_{xx}^2} w_y \left(\partial_x H_x + \partial_y H_y\right) dx \right\}$$
$$+ \sum_{\substack{TriangularElement\\ e}} \iint_{\Omega_e} \left\{ \tfrac{1}{n_{zz}^2} \left(\partial_x w_y - \partial_y w_x\right)\left(\partial_x H_y - \partial_y H_x\right) \right.$$
$$+ \left[\partial_x \left(\tfrac{1}{n_{yy}^2} w_x\right) + \partial_y \left(\tfrac{1}{n_{xx}^2} w_y\right) \right] \left(\partial_x H_x + \partial_y H_y\right)$$
$$\left. + k_0^2 n_{eff}^2 \left(\tfrac{1}{n_{yy}^2} w_x H_x + \tfrac{1}{n_{xx}^2} w_y H_y\right) - k_0^2 \left(w_x H_x + w_y H_y\right) \right\} dx\, dy = 0 . \quad (7.9)$$

Approximating the fields by interpolation of quadratic basis functions

$$H_\eta^{(\Gamma e)} = \sum_{i=1}^{3} N_{i,1D}^{(\Gamma e)} H_{\eta,i}^{(\Gamma e)} \qquad \text{for each boundary line element } \Gamma_e , \quad (7.10a)$$

$$H_\eta^{(\Gamma \mathrm{int},e)} = \sum_{i=1}^{3} N_{i,1D}^{(\Gamma \mathrm{int},e)} H_{\eta,i}^{(\Gamma \mathrm{int},e)} \qquad \text{for each interface line element } \Gamma_{int,e}, \quad (7.10b)$$

$$H_\eta^{(e)} = \sum_{i=1}^{6} N_{i,2D}^{(\Omega e)} H_{\eta,i}^{(\Omega e)} \qquad \text{for each triangular element } \Omega_e, \quad (7.10c)$$

where $\eta = x,y$; while $N_{i,1D}$ and $N_{i,2D}$ denoting the quadratic 1-D and 2-D basis functions, respectively with i denoting the local nodal points within the corresponding element; we can write the approximation to eq. (7.9) into a generalized eigenvalue equation as follows:

$$\left(\mathbf{M}_1 - n_{eff}^2 \mathbf{M}_2\right)\{H\} = \{0\}, \quad (7.11)$$

with column vector $\{H\}$ representing the approximate H_x and H_y fields at nodal points, while $\{0\}$ is a null vector. The matrices $\mathbf{M}_1$ and $\mathbf{M}_2$ are sparse and have the dimension of only $2N$ X $2N$, with N denoting the number of nodal points. Since the magnetic fields are continuous across material interfaces for non-magnetic materials, and also $\nabla \bullet \vec{B} = 0$ has been imposed into the formulation, no spurious mode will appear in this nodal based formulation [5].

7.2.2. Boundary conditions

7.2.2.1. Bayliss-Gunzburger-Turkel-like transparent boundary conditions

It is well known, that for scalar 2-D scattering problem, a family of differential operators

$$B_m\left(H\right)\Big|_\Gamma = O\left(1/r^{2m+1/2}\right), \tag{7.12}$$

with $B_m = \prod_{p=1}^{m}\left(\partial_r + jk_r + \frac{2p-3/2}{r}\right)$ can be imposed on field function at the computational boundaries Γ. In this operator, m denotes the order of the operator, r the distance of the boundary from a scatterer positioned at the origin, while k_r is the radial (or in our case transverse) wavenumber. This operation on fields at computational boundaries will exactly satisfy the first m-terms of the asymptotic radiation function expressed in a convergent series expansion of

$$H\left(r,\theta\right)\Big|_\Gamma = \sum_{p=0}^{\infty} H_p\left(\theta\right)\frac{\exp\left(-jk_r r\right)}{r^{p+1/2}}. \tag{7.13}$$

These boundary conditions are known as the Bayliss-Gunzburger-Turkel radiation boundary conditions (BGT RBC) [6].

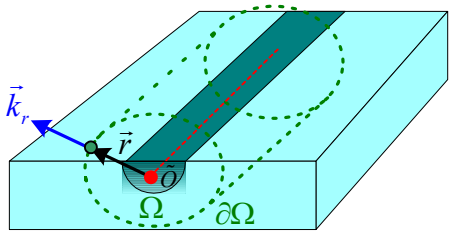

Figure 7.1. *Illustration of the concept of BGT-like TBC.*

Following the same way as Hernandez-Figueroa [4], we can think of the mode confinement within an optical channel waveguide as a sort of "line scatterer" from which the waves originate, as illustrated by Fig. 7.1. However, the radiative nature of the BGT RBC is not directly compatible with the guided modes of the waveguides, since in this kind of mode the field is not radiating out, but decays evanescently away from the core of the structure. In order to apply these boundary conditions for waveguiding problem, we need to treat k_r as a complex quantity. From eq. (7.13) it is clear that $\mathrm{Im}(k_r)<0$ represents decaying fields that suit the guided modes, while $\mathrm{Re}(k_r)>0$ corresponds to outward propagating fields which fit the leaky modes. Hence, by selecting the proper sign of the transverse wavenumber, using single scheme, both

guided and leaky modes can be modeled. For guided modes of structure with non-absorptive materials, the effective index will be real; hence consequently k_r will be purely imaginary.

In this work, we use "radiation" function in the vectorial form

$$\vec{H}(r,\theta)\Big|_{\Gamma} = \begin{bmatrix} H_x \\ H_y \end{bmatrix}\Bigg\|_{\Gamma} = \sum_{p=0}^{\infty} \frac{1}{r^{p+1/2}} \begin{bmatrix} H_{x,p}(\theta)\exp(-jk_{r,x}r) \\ H_{y,p}(\theta)\exp(-jk_{r,y}r) \end{bmatrix}, \tag{7.14}$$

with the 1st-order boundary operator

$$B_1\left(\begin{bmatrix} H_x \\ H_y \end{bmatrix}\right)\Bigg|_{\Gamma} = \left\{\left(\partial_r + \frac{1}{2r}\right)\begin{bmatrix} H_x \\ H_y \end{bmatrix} + j\begin{bmatrix} k_{r,x}H_x \\ k_{r,y}H_y \end{bmatrix}\right\}\Bigg|_{\Gamma} = O\left(r^{-5/2}\right) \tag{7.15}$$

and the transverse wavenumbers obtained by solving the wave equation (7.1) at the (assumed) elementwise homogeneous exterior domain are

$$k_{r,x} = k_0\sqrt{n_{xx}^2 - n_{eff}^2} \tag{7.16a}$$

and

$$k_{r,y} = k_0\sqrt{n_{yy}^2 - n_{eff}^2}\ . \tag{7.16b}$$

At this point, it is obvious that the proper sign of the transverse wavenumber discussed earlier corresponds to the proper sign of the square root within eq. (7.16). By neglecting the angular dependence of the fields, we get the approximate derivative operators as follows.

$$\partial_x H_x\big|_{\Gamma} = -\hat{r}\bullet\hat{x}\left(jk_{r,x} + \frac{1}{2r}\right)H_x\Big|_{\Gamma} + O\left(r^{-5/2}\right), \tag{7.17a}$$

$$\partial_y H_x\big|_{\Gamma} = -\hat{r}\bullet\hat{y}\left(jk_{r,x} + \frac{1}{2r}\right)H_x\Big|_{\Gamma} + O\left(r^{-5/2}\right), \tag{7.17b}$$

$$\partial_x H_y\big|_{\Gamma} = -\hat{r}\bullet\hat{x}\left(jk_{r,y} + \frac{1}{2r}\right)H_y\Big|_{\Gamma} + O\left(r^{-5/2}\right), \tag{7.17c}$$

$$\partial_y H_y\big|_{\Gamma} = -\hat{r}\bullet\hat{y}\left(jk_{r,y} + \frac{1}{2r}\right)H_y\Big|_{\Gamma} + O\left(r^{-5/2}\right). \tag{7.17d}$$

The approximate derivative operators given in eq. (7.17) can be used to evaluate the line integral along the computational boundaries in eq. (7.9). It is worth noting that the derivative terms within the boundary term in eq. (7.9) can also be expressed as a combination between normal and tangential derivatives with respect to (*w.r.t.*) the boundary line element, for which equivalently we can use approximate normal derivatives

$$\partial_n H_x\big|_{\Gamma} = -\hat{r}\bullet\hat{n}\left(jk_{r,x} + \frac{1}{2r}\right)H_x\Big|_{\Gamma} + O\left(r^{-5/2}\right), \tag{7.18a}$$

$$\partial_n H_y\big|_{\Gamma} = -\hat{r}\bullet\hat{n}\left(jk_{r,y} + \frac{1}{2r}\right)H_y\Big|_{\Gamma} + O\left(r^{-5/2}\right), \tag{7.18c}$$

as the Dirichlet to Neumann (DtN) map for handling the boundary terms, where $\hat{\partial}_n$ and $\hat{n}$ denote the normal derivative and unit normal vector *w.r.t.* the boundary line element, respectively. Although the vectorial radiation function eq. (7.14) is defined using polar coordinates, the shape of the computational boundary itself does not have to be circular, but can be any arbitrary regular shape, since each point at that boundary can be expressed in polar coordinates. Neglecting the $1/(2r)$ terms within eq. (7.17) or (7.18) will correspond to the Sommerfeld-like TBC as proposed by Hernandez-Figueroa *et al.* [4] which is only $O(r^{-3/2})$ accurate. Hence, the proposed 1st-order BGT-like TBC only need one extra term compared to the Sommerfeld-like TBC, but offers accuracy of one order higher in representing the derivatives of the fields at the computational boundaries. It is worth noting that this order of accuracy is *w.r.t.* single scatterer problem. Approximating the mode field (quasi-)confinement by single "scatterer" model itself will introduce additional inaccuracy, which is beyond the scope of this work.

7.2.2.2. Boundary conditions related to reflection symmetry

It is well known that the structural symmetry of a waveguide dictates the characteristics of the modal field solutions [7-8], which enables the use of only a sector of the structure to calculate a certain mode, and also enables the classification of modes and recognition of mode degeneracy. By exploiting the structural symmetry, the size of the computational domain can be reduced, which reduces both the memory and computational time cost of a numerical mode solver for the same level of accuracy. Besides, it enables one to get rid of difficulty in computing degenerate modes, since each of the degenerate modes is solved separately by using a different eigenvalue equation. The exploitation of symmetry has been widely used e.g. in numerical optical mode solvers [9-10] and photonic crystal computation [11].

In this section, we restrict ourselves to structures with reflection symmetry, since many optical waveguides possess this symmetry. This kind of structural symmetry enables the use of a simple perfect electric conductor (PEC) and/or a perfect magnetic conductor (PMC) at the symmetry plane as an exact truncation the computational domain. Although the exploitation of this type of symmetry has become common practice, their theoretical explanation is generally not given. This section is written as a brief introduction for the reader who is not familiar with the theory that leads to the use of PEC/PMC as exact boundary conditions for truncation of reflection symmetry structures at their symmetry plane.

To illustrate this, we consider a structure with C_{1v} symmetry as shown in Fig. 7.2.a, where $\varepsilon_r(x,y)=\varepsilon_r(-x,y)$ with structure symmetry plane located at $x=0$. Assume that $\varphi_k(x,y)$ is the k^{th}-order mode field profile of the structure. Due to the symmetry, if we

reflect the structure *w.r.t.* the symmetry plane, we will get the same structure again. This means that the same mode (i.e. the same field profile and the same propagation constant) is also the solution of the eigenvalue equation of the reflected structure. Since the eigenvector is scalable, we can write $\varphi_k(-x,y)=\alpha\varphi_k(x,y)$, with α a scaling constant. If we reflect the reflected structure once again, we will return to the original eigenvalue problem, but during the reflection we pick up another scaling factor. Hence, we can write $\varphi_k(x,y)= \alpha\varphi_k(-x,y)=\alpha^2\varphi_k(x,y)$. Therefore, α has the value of 1 or -1. If α=1, we will have $\varphi_k(-x,y)=\varphi_k(x,y)$, which is an even (symmetric) function across the structure symmetry plane. If α=-1, we will have $\varphi_k(-x,y)=-\varphi_k(x,y)$, which is an odd (anti-symmetric) function across the structure symmetry plane.

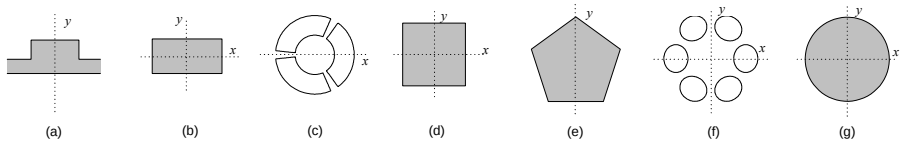

Figure 7.2. *Structures with reflection symmetry: (a). C_{1v}, (b). C_{2v}, (c). C_{3v}, (d). C_{4v}, (e). C_{5v}, (f). C_{6v}, and (g). $C_{\infty v}$. Dotted line denotes the possible truncation plane(s) by using PEC/PMC as boundary conditions.*

For a vector field, we should look at the parity of the modal field components. By using ansatz (7.2) for magnetic field and

$$\vec{E}(x,y,z,t)=\left[E_x,E_y,E_z\right]^T(x,y)\exp\left[j\left(\omega t-\beta z\right)\right] \tag{7.19}$$

for electric field, for structure made of non-magnetic material with diagonal permittivity tensor, Maxwell's eqs. (2.1)-(2.2) can be written as

$$\partial_y H_z + j\beta H_y = j\varepsilon_0 n_{xx}^2 \omega E_x\,, \tag{7.20a}$$

$$-j\beta H_x - \partial_x H_z = j\varepsilon_0 n_{yy}^2 \omega E_y\,, \tag{7.20b}$$

$$\partial_x H_y - \partial_y H_x = j\varepsilon_0 n_{zz}^2 \omega E_z\,, \tag{7.20c}$$

and

$$\partial_y E_z + j\beta E_y = -j\mu_0 \omega H_x\,, \tag{7.21a}$$

$$-j\beta E_x - \partial_x E_z = -j\mu_0 \omega H_y\,, \tag{7.21b}$$

$$\partial_x E_y - \partial_y E_x = -j\mu_0 \omega H_z\,, \tag{7.21c}$$

respectively. By keeping in mind that the normal derivative of an even (odd) function is an odd (even) function, inspecting eqs. (7.20)-(7.21) for a structure as in Fig. 7.2.a leads to 2 groups of field components with opposite parity, i.e. $\{E_y, E_z, H_x\}$ and $\{E_x, H_y, H_z\}$. It means that if E_y is an odd (even) function *w.r.t.* y-axis, E_z and H_x will also be odd (even) functions, while E_x, H_y, and H_z will be even (odd) functions. Following a similar procedure, we can also find a similar subdivision of modal field components for structures with y=0 as their reflection symmetry plane. This field parity is tabulated in Table 7.1. A similar discussion on parity of modal field components was also given by

Lohmeyer [12] and Hsueh *et al.* [13]. Note that Hsueh *et al.* used the wave equation instead of Maxwell's equations, and reported parity of modal field only for part of the field components which are enough for their numerical method.

Table 7.1. *Possible symmetry parity of the fields in structure with reflection symmetry.*

Structure symmetry	Group with the same field symmetry	Possible field symmetry *w.r.t.* structure symmetry plane	
$\varepsilon_r(x,y)=\varepsilon_r(-x,y)$	$\{E_y, E_z, H_x\}$	Symmetric (even function)	Anti-symmetric (odd function)
	$\{E_x, H_y, H_z\}$	Anti-symmetric (odd function)	Symmetric (even function)
$\varepsilon_r(x,y)=\varepsilon_r(x,-y)$	$\{E_y, H_x, H_z\}$	Symmetric (even function)	Anti-symmetric (odd function)
	$\{E_x, E_z, H_y\}$	Anti-symmetric (odd function)	Symmetric (even function)

Since the structure is continuous across the structural symmetry plane, the field and their normal derivative across that plane should also be continuous. For an even function, these continuity conditions lead to $\partial_n\varphi=0$, where ∂_n denotes normal derivative *w.r.t.* the structure symmetry plane, while for an odd function, they lead to $\varphi=0$ at the symmetry plane. Inspecting Table 7.1 by using these conditions leads to modal field solutions with either

$$H_t = 0, \tag{7.22a}$$
$$E_n = 0, \tag{7.22b}$$
$$\partial_n H_n = 0, \tag{7.22c}$$
$$\partial_n E_t = 0, \tag{7.22d}$$

or

$$H_n = 0, \tag{7.23a}$$
$$E_t = 0, \tag{7.23b}$$
$$\partial_n H_t = 0, \tag{7.23c}$$
$$\partial_n E_n = 0, \tag{7.23d}$$

at the symmetry plane, with n and t denoting normal and tangential *w.r.t.* structure symmetry plane, respectively. Conditions (7.22) and (7.23) are fulfilled by a PMC and a PEC put at the structure symmetry plane, respectively. The first-two equations in (7.22) and (7.23) are directly fulfilled by the definition of PMC and PEC themselves, respectively, while the fulfillment of the last-two equations can be verified by using Maxwell's equations. This means that the structure can be solved by using only a sector of the structure, i.e. firstly using PEC to truncate the structure at the symmetry plane and use that truncated structure to represent the full structure, and finally repeat the computation by using PMC.

For structures with C_{mv} symmetry with $m>1$, we can also use the same boundary conditions to truncate the structure by applying the truncation successively. Firstly, inspect whether the structure can be divided into 2 parts with reflection symmetry. If possible, then inspect whether the new (truncated) structure can be further divided into 2 parts. In our work, the minimum truncated structure is a quarter of the full structure, which is applicable for even number m, including $m=\infty$. This quarter structure is needed to capture the degenerate modes [7-8, 15]. For odd number m, the truncated structure is only a half of the full structure. The dotted line in Fig. 7.2 indicates the possible position of the truncation plane(s) for various structures. Comparing this scheme to the table of minimum sector provided by McIsaac [7] which is based on a full group theoretical treatment, the sector size that we take is the largest of the minimum sectors required to calculate all possible modes. However, we understand that this is not the most efficient sector size for some structures. Recently, by exploiting the rotational symmetry of the structure, Fini [14] proposed the use of only $2\pi/6$ radiant azimuthal sector for the computation of modes in a structure with C_{6v} symmetry, but the boundary conditions employed at the truncation plane are not the simple PEC/PMC anymore.

7.3. Computational results

To illustrate the functionality of the scheme, we take samples supporting both guided and leaky modes. For the guided mode cases, we choose both isotropic and anisotropic step-index optical fibers, for which exact solutions are available; and a simplified fused fiber coupler. Using the isotropic optical fiber, we will demonstrate the effectiveness of the proposed BGT-like boundary conditions and compare the results to the homogeneous DBC and Sommerfeld-like TBC. For leaky modes computations we take the informal benchmark case [3-4,20-22], i.e. the leaky rib anti-resonant reflecting optical waveguide (ARROW) made of compound semiconductor. Additionally, we also demonstrate the use of the scheme to study the evolution of leaky and guided modes of Si_3N_4 strip waveguide with an anisotropic overlay made of a DAST crystal and a Si substrate.

7.3.1. Optical fiber

Firstly, we consider a multimode isotropic step-index fiber with refractive indices of 1.47 and 1.46 for core and cladding, respectively. The core radius is 7.5 μm and the vacuum wavelength is 1.55 μm. The effective indices of the modes calculated using the proposed scheme by means of a full structure using computational domain of a circle with radius of r_b=15 μm together with the exact values are presented in Table 7.2. The exact values are calculated using the exact dispersion equation available in the

textbook [16]. Since the structure has $C_{\infty v}$ symmetry, it is possible to take advantage of the symmetry where only a quarter structure is required and use PEC/PMC at the structure symmetry plane. Here, we take the 4th quadrant substructure, apply the PEC/PMC at the computational boundaries coinciding with the structure reflection planes and the 1st-order BGT-like TBC at other boundary. The computational results by using a quarter of the structure are also presented in the table. The table shows that the results of present scheme using meshes presented in Fig. 7.3 agree to their exact values, both for those using full and just a quarter of the structure as the computational domain. The table shows that besides TE and TM modes, other modes are pairs of 2-fold degenerate modes, which can be accessed separately using different reflection-symmetry boundary conditions. It is also interesting to note that HE_{31} modes here are a degenerate pair, while in Chapter 8, we will see that they are non-degenerate pair for photonic crystal fiber (PCF) with C_{6v} symmetry. In Chapter 8, we will further discuss the mode degeneracy and demonstrate a simple procedure to evaluate the degeneracy and non-degeneracy of modes. The same procedure can be used to prove that the HE_{31} modes are degenerate here, but non-degenerate in the PCF with C_{6v} symmetry.

Table 7.2. *The calculated results for the isotropic step index fiber*

Mode	n_{eff}			Boundary conditions at vertical/horizontal symmetry plane for quarter structure located at the 4th quadrant
	Exact values	Present scheme		
		Full Structure (r_b=15μm, 5206 triangular elements)	Quarter structure (r_b=15μm, 1264 triangular elements)	
HE_{11}	1.46851198	1.46851146	1.46851142	PEC/PMC or PMC/PEC
TE_{01}	1.46627934	1.46627806	1.46627798	PEC/PEC
HE_{21}	1.46627071	1.46626949	1.46626942	PEC/PEC or PMC/PMC
TM_{01}	1.46626814	1.46626687	1.46626680	PMC/PMC
EH_{11}	1.46343274	1.46343020	1.46343008	PEC/PMC or PMC/PEC
HE_{31}	1.46342243	1.46342102	1.46342091	PEC/PMC or PMC/PEC
HE_{12}	1.46258582	1.46258371	1.46258361	PEC/PMC or PMC/PEC
EH_{21}	1.46017795	1.46016811	1.46016798	PEC/PEC or PMC/PMC

In order to illustrate the effectiveness of the proposed boundary conditions, we calculate the HE_{11} and HE_{12} modes of the same structure with various size of computational domain, and check the relative error in the calculated effective indices defined as

$$Err \equiv \frac{\left| n_{eff}^{calc} - n_{eff}^{exact} \right|}{n_{eff}^{exact}}, \tag{7.24}$$

where n_{eff}^{calc} and n_{eff}^{exact} denote the calculated and exact value of the effective index, respectively. The results, together with those of the same computations but using homogeneous DBC and Sommerfeld-like TBC are presented in Fig. 7.4. The figure shows the superiority of the proposed boundary conditions compared to the DBC and Sommerfeld-like TBC. Even when the outer boundary is located very near to the fiber core, i.e. at r_b=7.7μm; the 1st-order BGT-like TBC still gives relatively small error. For

high-order mode like HE_{12}, the scheme with DBC fails to find the mode using this rather small computational domain, because for this mode the field at the computational boundary is not negligible anymore.

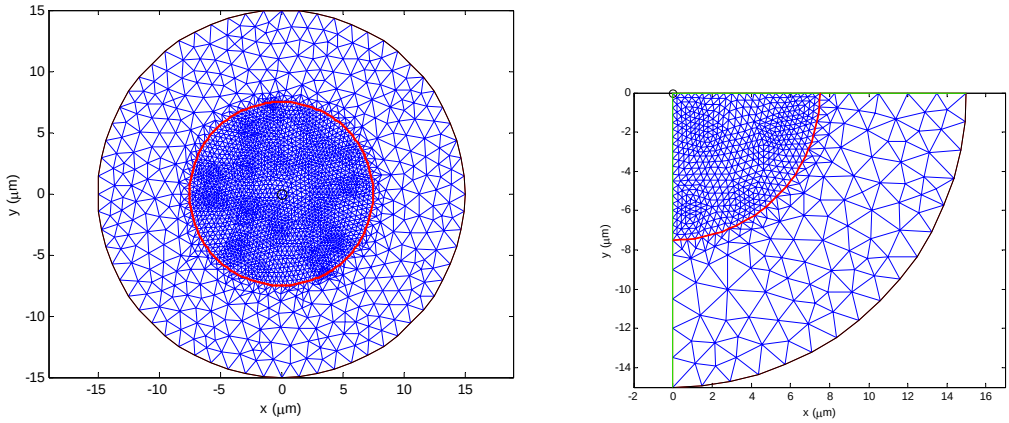

(a) (b)

Figure 7.3. *Meshes used in the computation of the isotropic step-index fiber using (a). full and (b). a quarter of the structure as the computational domain.*

Next, we consider a fiber with both core and cladding made of uniaxial crystals, for which exact solutions are also available [17]. The fiber consists of pure $LiNbO_3$ as the core and 5% MgO-doped $LiNbO_3$ as the cladding. Assume that the principle axes of the crystal coincide with the Cartesian-coordinate axes, with the crystal *c*-axis aligned in the direction of *z*-axis; hence $n_{xx}=n_{yy}=n_o$ and $n_{zz}=n_e$, with n_o and n_e denoting the ordinary and extraordinary refractive index of the crystals, respectively. For a vacuum wavelength of 0.633μm, the refractive indices of the $LiNbO_3$ are n_o=2.2866 and n_e=2.2028, while for 5% MgO-doped $LiNbO_3$ are n_o=2.2815 and n_e=2.1926 [17]. The radius of the core is 4μm, and a computational domain of a circle with radius of 5μm has been used with 7112 triangular elements. The computed first-few modes along with their exact values and the results of vectorial finite difference beam propagation method (VFD BPM) of Golant *et al*. [18] are given in Table 7.3. The exact values are obtained using dispersion equation given by Dai and Jen [17]. The table shows that the computed results using this rather small computational domain agree to the exact values and the results of other method.

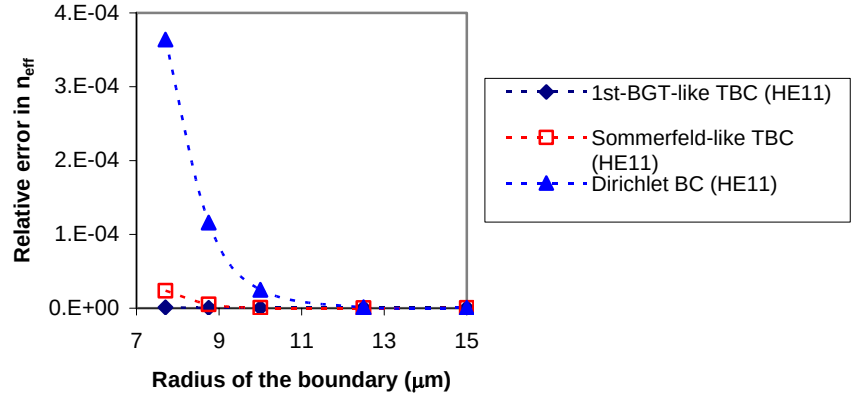

(a)

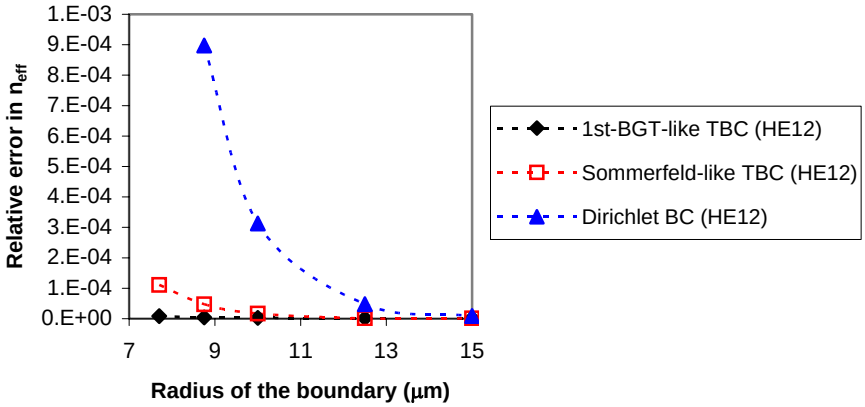

(b)

Figure 7.4. *The relative error of effective indices for various size of computational domain for the 1st-order BGT-like TBC, Sommerfeld-like TBC, and homogeneous DBC: (a). for low-order (HE_{11}) and (b). high-order (HE_{12}) modes of the isotropic optical fiber sample.*

Table 7.3. *Computed and exact effective indices of first-few modes for fiber with both core and cladding made of uniaxial crystals.*

Mode	n_{eff}		
	Exact	Present Scheme	VFD BPM (Golant *et al.*) [18]
HE_{11}	2.285993	2.285992	2.285991
TE_{01}	2.285121	2.285117	2.285121
HE_{21}	2.285073	2.285077	2.285061
TM_{01}	2.285024	2.285018	-

7.3.2. Fused fiber coupler

Next, we take a simplified fused fiber coupler with a dumbbell-shaped structure and mesh definition as shown in Fig. 7.5. We have chosen the same structural parameters as Yang and Chang [19] and Chiang *et al.*[10], i.e. the core index n_{core}=1.45, the cladding index n_{clad}=1, operating wavelength λ=1.523μm, aspect ratio $2d/(2r_{core})$=1.8, and normalized frequency $V \equiv k_0 r_{core}\left(n_{core}^2 - n_{clad}^2\right)^{1/2}$=50. Taking advantage of the symmetry of the structure, we only need to consider a quarter of the structure. We put the outer computational boundary at r_b=r_{core}+3μm. The results for a few low order modes are presented in Table 7.4 together with the results of Yang and Chang using surface integral equation method (SIEM) and Chiang *et al.* using vectorial finite difference method (VFDM) with curved-interface corrections. Since the modes are almost linearly polarized due to the breaking of the circular symmetry of the fiber, we decided to label the modes as quasi-TE (q-TE) and quasi-TM (q-TM) modes, instead of using the hybrid mode notation commonly used for optical fiber. The results show agreement in the normalized propagation constants $b \equiv \left(n_{eff}^2 - n_{clad}^2\right)/\left(n_{core}^2 - n_{clad}^2\right)$ with other two methods up to 5 digits. Please note that there are some notational errors in the results presented in the paper of Chiang *et al.* (private communication with the author), i.e. the results presented in Table I of their paper should be in the dimensionless normalized propagation constants, instead of propagation constants with unit of μm^{-1}. The mode profiles shown in Fig. 7.6 are obtained by rendering the mode profiles of the quarter structure.

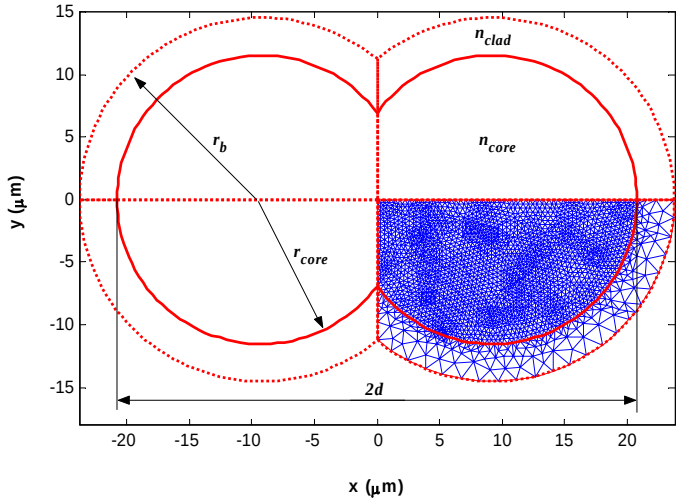

Figure 7.5. *The mesh definition and the computational domain of the simplified fused fiber coupler. Only a quarter of the structure is used in the computation.*

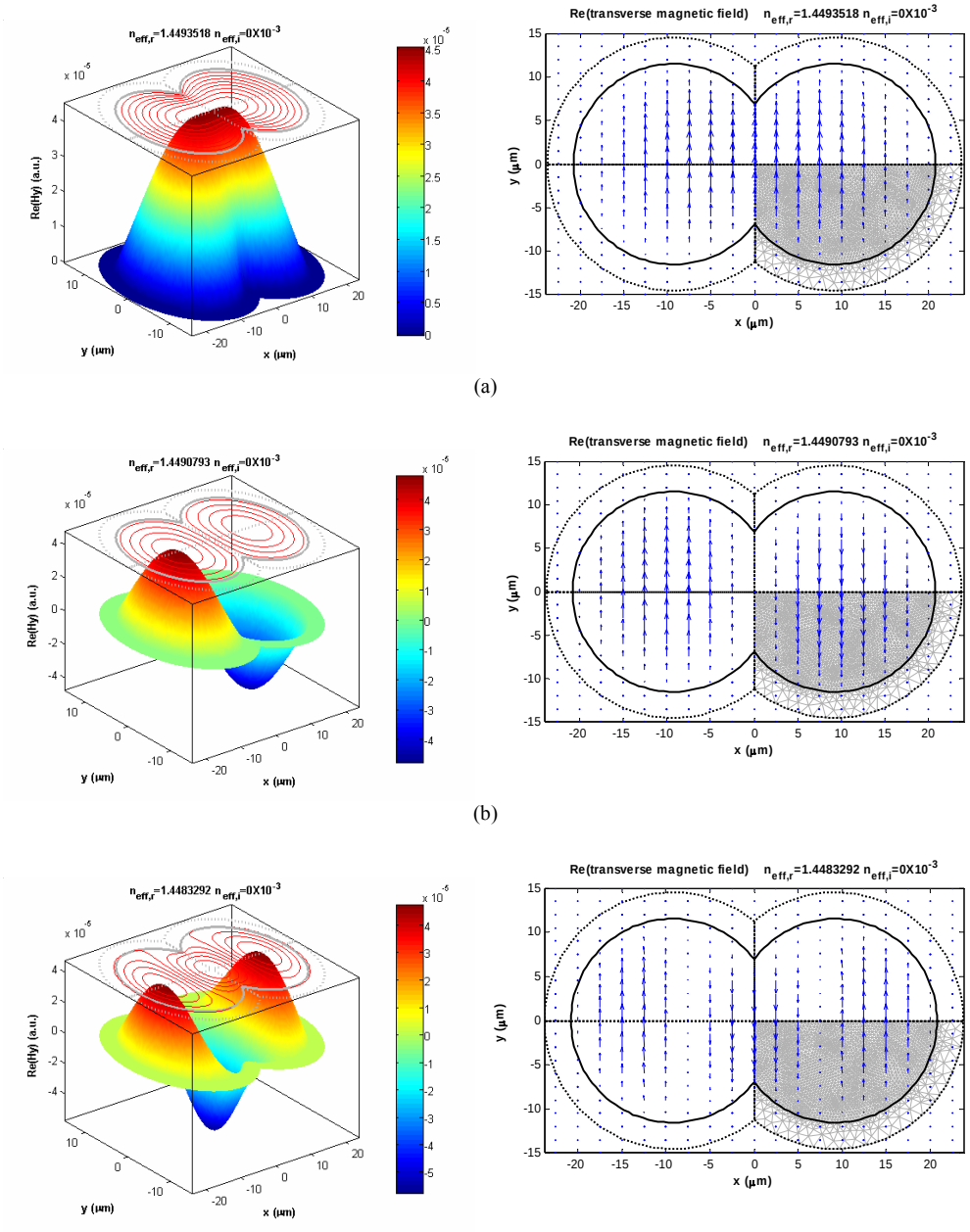

Figure 7.6. *Mode profile (left column) and transverse field vector (right column) of (a). q-TE$_{00}$ (b). q-TE$_{10}$, and (c). q-TE$_{20}$ modes of the fused fiber coupler sample.*

Table 7.4. *The calculated results for the fused fiber coupler sample. Only a few modes are shown.*

Mode	Present Scheme (quarter structure, 4941 triangular element)		SIEM (Yang & Chang)	VFDM (Chiang *et al.*) (quarter structure, 437 × 297 grid points)
	n_{eff}	*b*	*b*	*b*
q-TE_{00}	1.449351793	0.998295347	0.998298295	0.998298803
q-TE_{10}	1.449079314	0.997579010	0.997581191	0.997581862
q-TE_{20}	1.448329236	0.995607778		
q-TM_{00}	1.449347926	0.998285180	0.998287649	0.998287976
q-TM_{10}	1.449077169	0.997573371	0.997574799	0.997575478
q-TM_{20}	1.448332859	0.995617296		

7.3.3 Rib ARROW

As the first example of leaky modes computation, we take a rib ARROW made by a double-heterostructure of III-V compound semiconductor. The structure and the mesh definition of the waveguide are depicted in Fig. 7.7. The refractive index of the GaAs, 5% AlGaAs, 20% AlGaAs, and air are 3.59, 3.555, 3.452, and 1, respectively. The thicknesses t_1 to t_5 are 1μm, 1.1μm, 0.4μm, 1.6μm, and 0.95μm, respectively. The width of the rib is w=2.6μm. The operating wavelength is λ=1.064μm. The high index substrate causes the waveguide to be leaky. This structure has been modeled by a number of authors using various methods or schemes; i.e. spectral index method (Berry *et al*. [20]), FEM with Sommerfeld-like TBC (Hernandez-Figueroa *et al*. [4]), semivectorial imaginary distance (ID) BPM with PML (Tsuji & Koshiba [21]), FEM with anisotropic PML (Selleri *et al*. [3]), and vectorial ID BPM with PML (Obayya *et al*. [22]). In Table 7.5 and 7.6 we present our results together with the published results for even modes. Our computations were carried out using half of the structure with the computational boundaries located at 1μm below the substrate-lower-2nd-cladding interface, 0.25μm above the top of the rib, and 2.6μm to the right of the symmetry line. From the table, we can say that our results qualitatively agree with other's, especially with the results of Selleri *et al*., which use anisotropic PML with high-order edge elements FEM; and also to the results of Berry *et al*. Beside the q-TE modes, we also present the results for q-TM polarization, which are not shown in the paper of others. Figure 7.8 shows the mode profile of the real part of the dominant field of a few modes. For modes with large enough loss, the wave-like tail that indicates leakage into the high-index substrate becomes more noticeable. Here and everywhere in this thesis, the phase of the complex-valued modal field has been adjusted to make the real part be dominant. The phase factor has been determined based on the phase at nodal point where the dominant field component (either H_x or H_y) takes its largest magnitude. Hence, the not displayed imaginary part of the field is almost negligible.

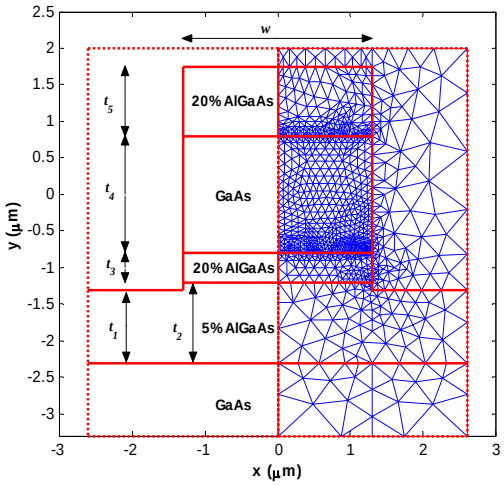

Figure 7.7. *The structure, computational window, and mesh definition of the rib ARROW.*

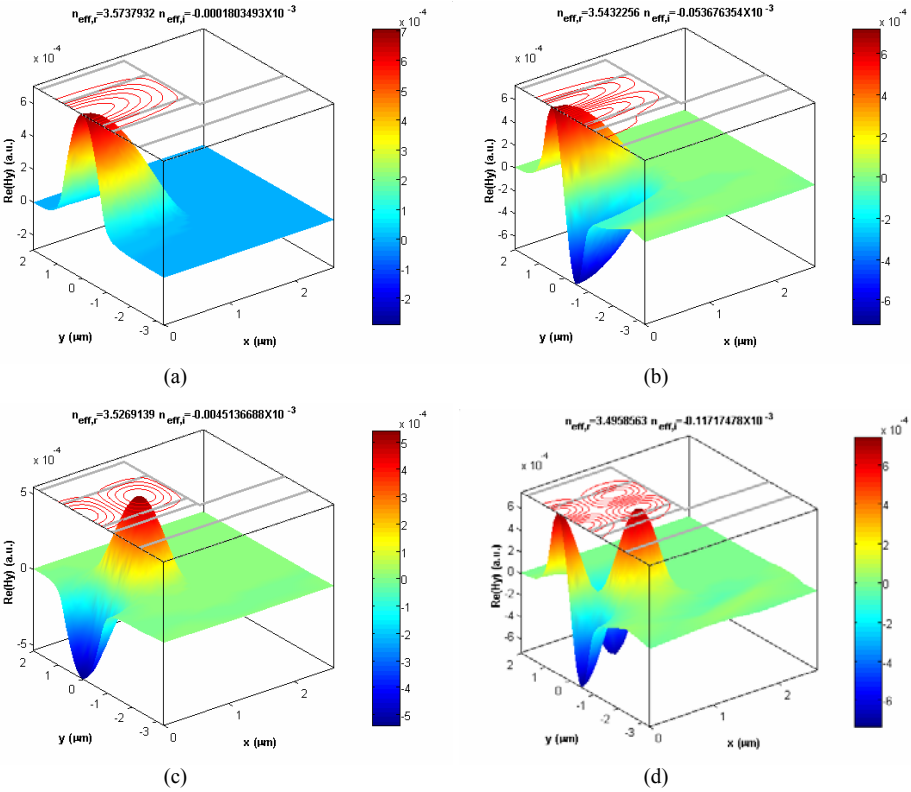

Figure 7.8. *Mode profiles of the real part of dominant magnetic field component for leaky (a). q-TE_{00}, (b). q-TE_{01}, (c). q-TE_{20}, and (d). q-TE_{21} of the rib ARROW.*

Table 7.5. *The real part of the calculated effective indices of the rib ARROW.*

Mode	Re(n_{eff})					
	Present scheme (half structure, 1889 triangles)	Hernandez-Figueroa *et al*.	Tsuji & Koshiba	Berry *et al*.	Selleri *et al*. (half structure, 1996 triangles)	Obayya *et al*.
q-TE_{00}	3.573793	3.574125	3.574131	3.573800	3.573795	3.573733
q-TE_{01}	3.543226	3.543505	3.543530	3.5432314	3.543225	3.543067
q-TE_{20}	3.526914	3.529994	3.529949		3.526932	
q-TE_{21}	3.495856	3.498680	3.495891		3.495866	
q-TE_{02}	3.494239			3.4942785	3.494256	3.493831
q-TM_{00}	3.573849					
q-TM_{01}	3.542647					
q-TM_{20}	3.529636					
q-TM_{21}	3.498008					
q-TM_{02}	3.493295					

Table 7.6. *The imaginary part of the calculated effective indices of the rib ARROW.*

Mode	-Im(n_{eff})					
	Present scheme (half structure 1889 triangles)	Hernandez-Figueroa *et al*.	Tsuji & Koshiba	Berry *et al*.	Selleri *et al*. (half structure, 1996 triangles)	Obayya *et al*.
q-TE_{00}	1.8035E-7	1.7649E-7	1.6976E-7	1.6968E-7	1.7120E-7	1.692E-7
q-TE_{01}	5.3676E-5	5.5352E-5	5.4823E-5	5.4810E-5	5.5691E-5	5.739E-5
q-TE_{20}	4.5137 E-6	1.4923E-6	1.6915E-6		6.7865E-6	
q-TE_{21}	1.1717E-4	1.2272E-4	1.2316E-4		1.1539E-4	
q-TE_{02}	8.5828E-4			8.8414E-4	8.8313E-4	9.179E-4
q-TM_{00}	1.7283E-7					
q-TM_{01}	5.8220E-5					
q-TM_{20}	1.3413E-6					
q-TM_{21}	1.1549E-4					
q-TM_{02}	9.1754E-4					

7.3.4. Buffered leaky Si_3N_4 strip waveguide with DAST overlaid cladding and Si substrate: the modes evolution

In this section, we consider a Si_3N_4 strip waveguide made on Si substrate with SiO_2 buffer layer. A DAST crystal [23], which is a highly anisotropic biaxial material, is overlaid on top of the strip with an air gap in between. In order to show the effect of the DAST cladding and the Si substrate separately, we consider two different structures as shown in Fig. 7.9. Both of these structures are in most cases in this section, the buffered leaky waveguides. We assume that the principal axes of the DAST coincide with the Cartesian coordinate system of the waveguide with the axis associated with the highest refractive index aligned to the *z*-direction. The refractive indices of the DAST are $n_{clad,xx}$=1.602, $n_{clad,yy}$=1.575, and $n_{clad,zz}$=2.132, while the refractive index of the Si_3N_4, SiO_2, Si, and air are n_{core}=1.99, n_b=1.45, n_s=3.5, and n_1=1, respectively for a vacuum wavelength of 1.55μm. The size of the core is h=0.3μm and w=2μm, while the gap thickness (g) and buffer thickness (b) will be varied.

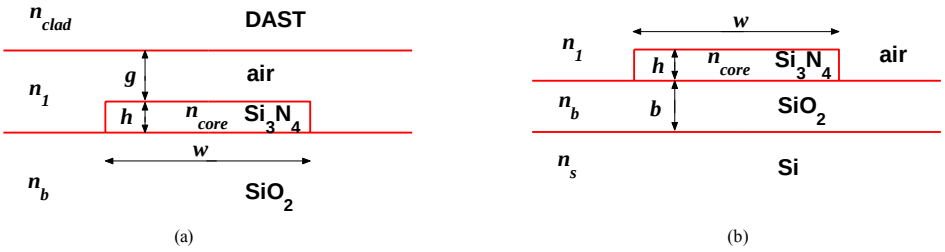

Figure 7.9. *Structure of a Si_3N_4 strip waveguide with: (a). DAST overlaid cladding and (b). Si substrate.*

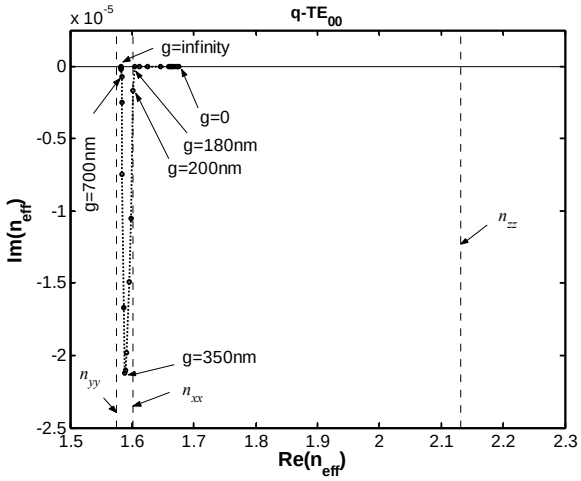

Figure 7.10. *The evolution of effective index of q-TE_{00} mode in the complex plane as one varies the size of the air gap of a DAST overlaid Si_3N_4 strip waveguide. The refractive indices of the DAST are shown for reference. Circular shapes denote the calculated results, while dotted line connects them to aid vision.*

Without the DAST cladding and Si substrate, the structure supports two guided modes, i.e. q-TE_{00} and q-TE_{10}. This setting is denoted by $g=\infty$ and $b=\infty$ throughout this section. Fig. 7.10 shows the evolution of the calculated effective index of q-TE_{00} mode in the complex plane as one varies g of structure shown in Fig. 7.9a. The existence of the DAST cladding increases the real part of n_{eff} since the refractive index of DAST has not crossed the zero crossing point yet (see explanation in section 6.3.2). By solving vectorial wave equation for uniform structure consisting of DAST only using the method given in Section 1.3.3 of the book of Chew [24], we found that for the above given orientation of DAST, the effective index (i.e. $\hat{z}\cdot\vec{k}/k_0$) of the

DAST is bounded by $n_{clad,xx}$. Therefore $n_{clad,xx}$ will determine the onset of the leaky modes. As long as n_{eff} is larger than $n_{clad,xx}$ the mode is still guided mode (see calculation results until g around 180nm). If one further enlarges the gap thickness such that $\mathrm{Re}\{n_{eff}\}$ becomes smaller than $n_{clad,xx}$, the mode becomes leaky. Fig. 7.10 shows two effects that dictate the properties of the leaky mode. The first one is: as the gap size enlarges, the $\mathrm{Re}\{n_{eff}\}$ moves further below $n_{clad,xx}$, resulting in a larger leakage loss value. The second one is: as the gap size increases, the effect of the DAST cladding decreases, meaning that the mode evolves toward the lossless guided mode of the structure without DAST cladding, leading to a decrease of the leakage loss. These two effects that influence the leakage loss in opposing direction, lead to a maximum leakage loss at gap thickness around 350nm. Fig. 7.11 shows the mode profiles of q-TE_{00} at g=0 (lossless) and 350 nm (attenuation=7.45dB/cm).

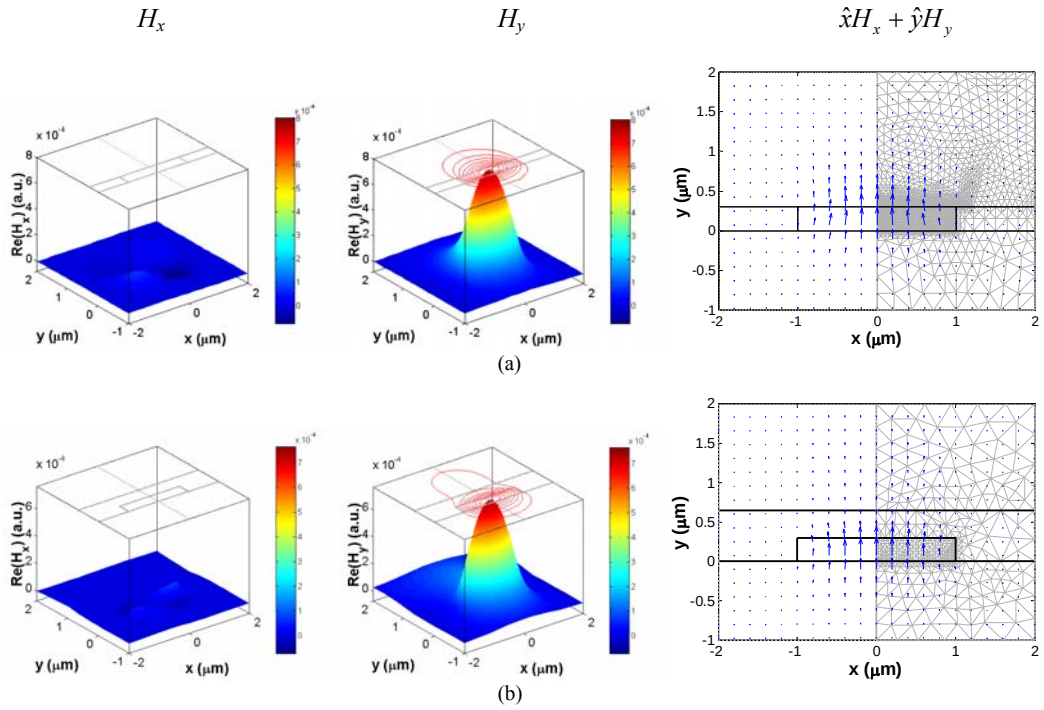

Figure 7.11. *Mode profiles of q-TE_{00} at (a). g=0, and (b) g=350nm.*

More complicated phenomena are observed for q-TM_{00}, q-TE_{10}, and q-TE_{11} modes. Fig. 7.12 shows the evolution of these modes in the complex plane as one varies g. The points with circular, square, diamond, and triangular shapes denote the computational results, while dotted lines are used to connect points, which show similar features in their transverse field vector plots.

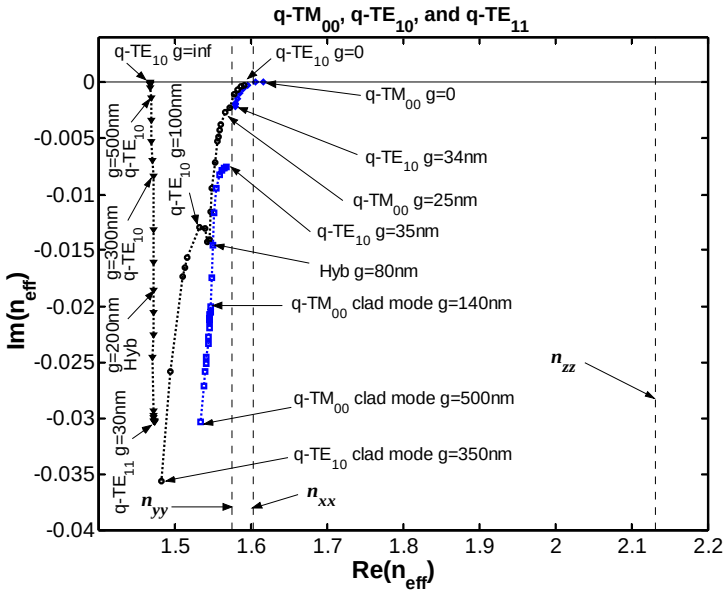

(a)

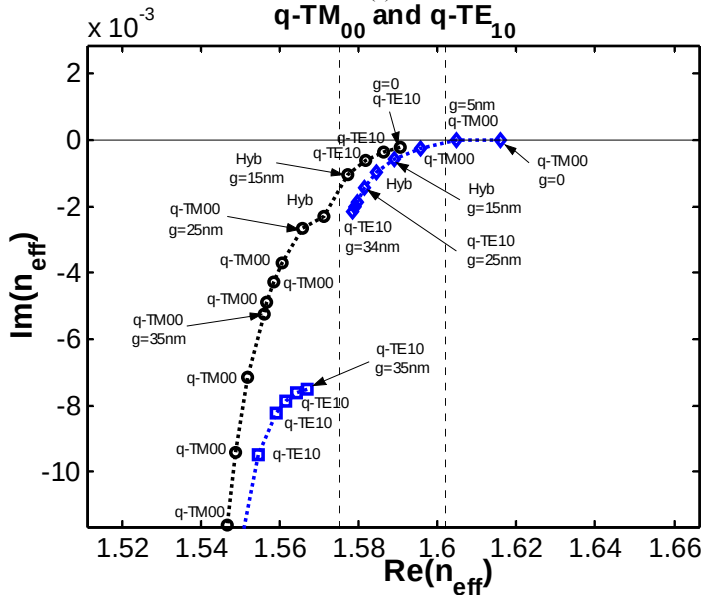

(b)

Figure 7.12. *(a). The evolution of effective indices of q-TM_{00}, q-TE_{10}, and q-TE_{11} modes in the complex plane as one varies the size of the air gap (g) of a DAST overlaid Si_3N_4 strip waveguide, and (b). a zoomed plot of part of figure (a). "Hyb" denotes mode with hybrid field profile.*

The q-TM_{00} mode, which is not observed for structure without DAST cladding, is observed to be guided mode for g=0. We believe that for structure without DAST cladding, this mode is a very leaky cladding (or more precisely buffer) mode with its main field component residing in the SiO_2 buffer. Since the introduction of DAST cladding will lift the $\mathrm{Re}\{n_{eff}\}$ up, this mode will become guided mode if this value becomes larger than $n_{clad,xx}$. If one enlarges the gap size, the $\mathrm{Re}(n_{eff})$ becomes smaller. Once it becomes smaller than $n_{clad,xx}$, the mode will become a leaky mode. During varying of g, this mode (q-TM_{00}) will change its modal field profiles back and forth into q-TE_{10} (see points denoted by diamond shapes in Fig. 7.12) as shown by Fig. 7.13, where the term hybrid has been used to denote a mode with profile which is a combination of two linearly polarized modes. This mixing phenomenon can be understood as these two modes have the same field symmetries, i.e. symmetric H_x and anti-symmetric H_y across the vertical symmetry axis.

At g=0, we also observe the existence of leaky q-TE_{10} mode, with $\mathrm{Re}(n_{eff})$ which is lower than $n_{clad,xx}$, and attenuation 75.7 dB/cm. By changing g, the mode profile of this mode also changes back and forth into q-TM_{00} (see points denoted by circular shapes in Fig. 7.12) as shown by Fig. 7.14.

At g=35nm we also observe q-TE_{10} mode, which evolves into q-TM_{00} cladding mode as one enlarges g (see points denoted by square shapes in Fig. 7.12), as shown by Fig. 7.15.

An interesting phenomenon shown by Fig. 7.12a is that q-TM_{00} and q-TE_{10} of small g will evolve into the highly leaky q-TM_{00} cladding mode and q-TE_{10} cladding mode as one enlarges g. On the other hand, the highly leaky q-TE_{11} core-cladding mode will evolve into q-TE_{10} core mode as one enlarges g (see points denoted by triangular shapes in Fig. 7.12) as shown by Fig. 7.16. The latter figure shows that as one enlarges g, the humps located at the DAST cladding will become weaker and weaker until the mode profile evolves into q-TE_{10} core mode.

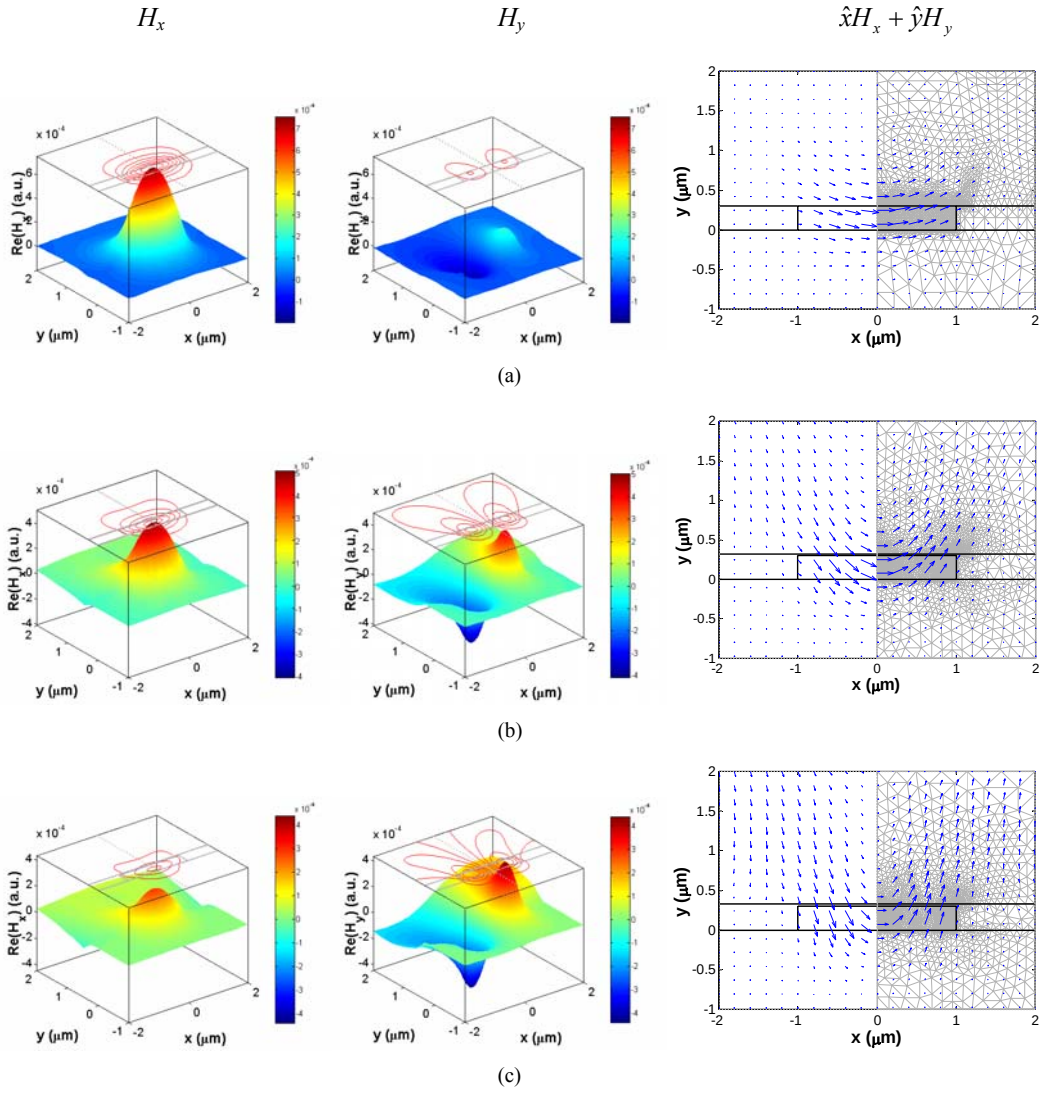

Figure 7.13. *Mode profiles at points denoted by diamond shapes in Fig. 7.12: (a) q-TM_{00} mode at g=0, (b) hybrid mode at g=15nm, and (c). q-TE_{10} mode at g=25nm. The figure shows the evolution of modes from q-TM_{00} in figure (a) into q-TE_{10} in figure (c) as one changes the gap size.*

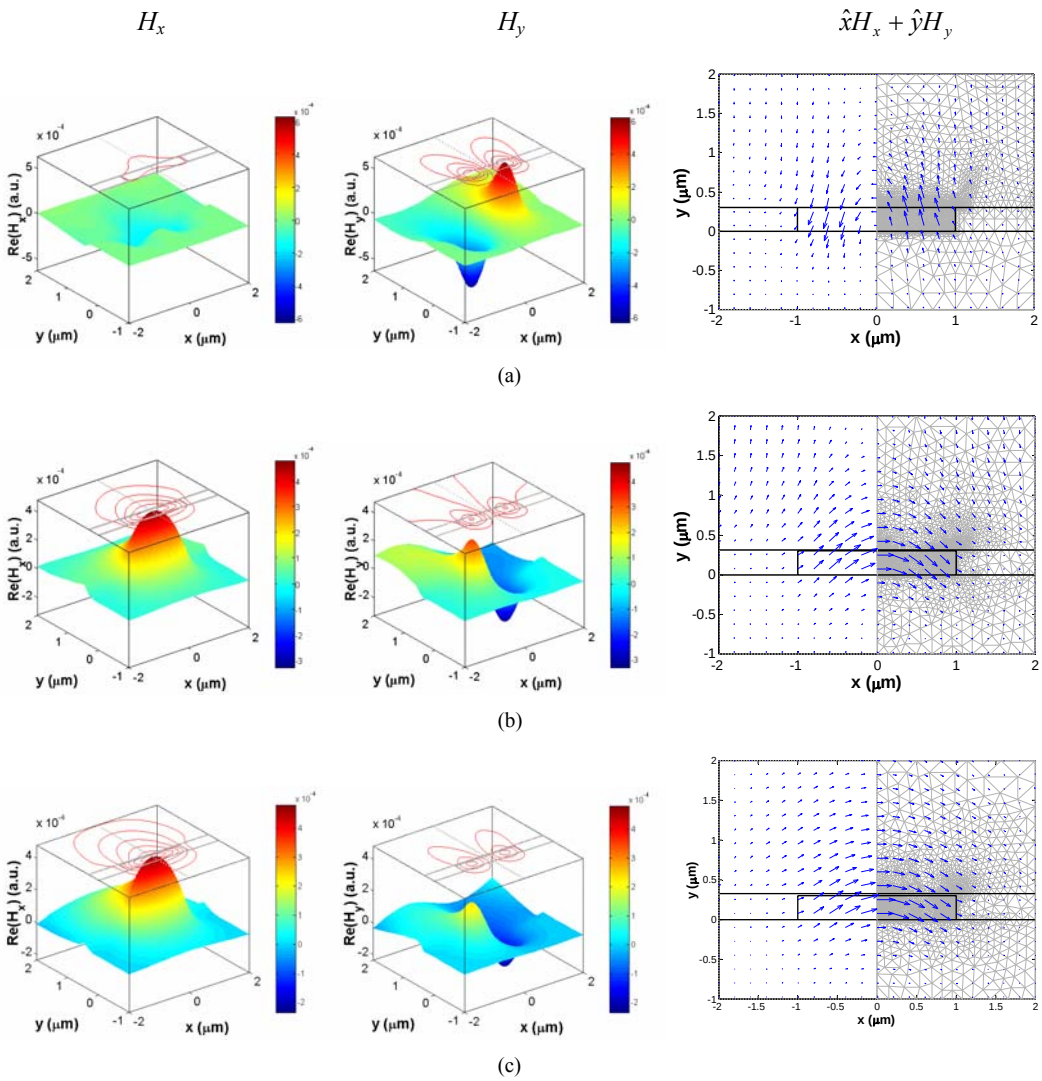

Figure 7.14. *Mode profiles at points denoted by circular shapes in Fig. 7.12: (a) q-TE_{10} mode at g=0, (b) hybrid mode at g=15nm, and (c). q-TM_{00} mode at g=25nm. The figure shows the evolution of modes from q-TE_{10} in figure (a) into q-TM_{00} in figure (c) as one changes the gap size.*

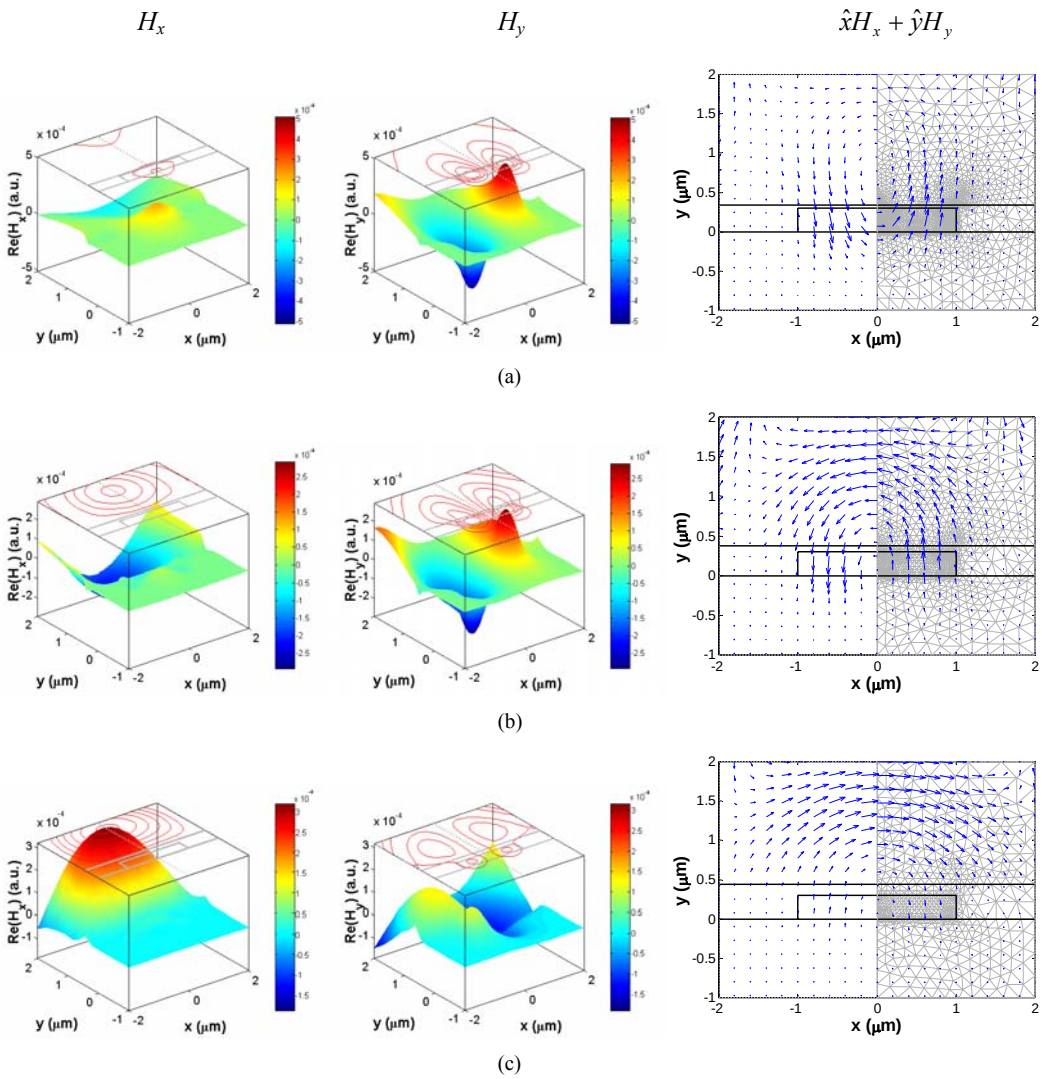

Figure 7.15. *Mode profiles at points denoted by square shapes in Fig. 7.12: (a) q-TE_{10} core mode at g=35nm, (b) core-cladding hybrid mode at g=80nm, and (c). q-TM_{00} cladding mode at g=140nm. The figure shows the evolution of modes from q-TE_{10} core mode in figure (a) into q-TM_{00} cladding mode in figure (c) as one changes the gap size.*

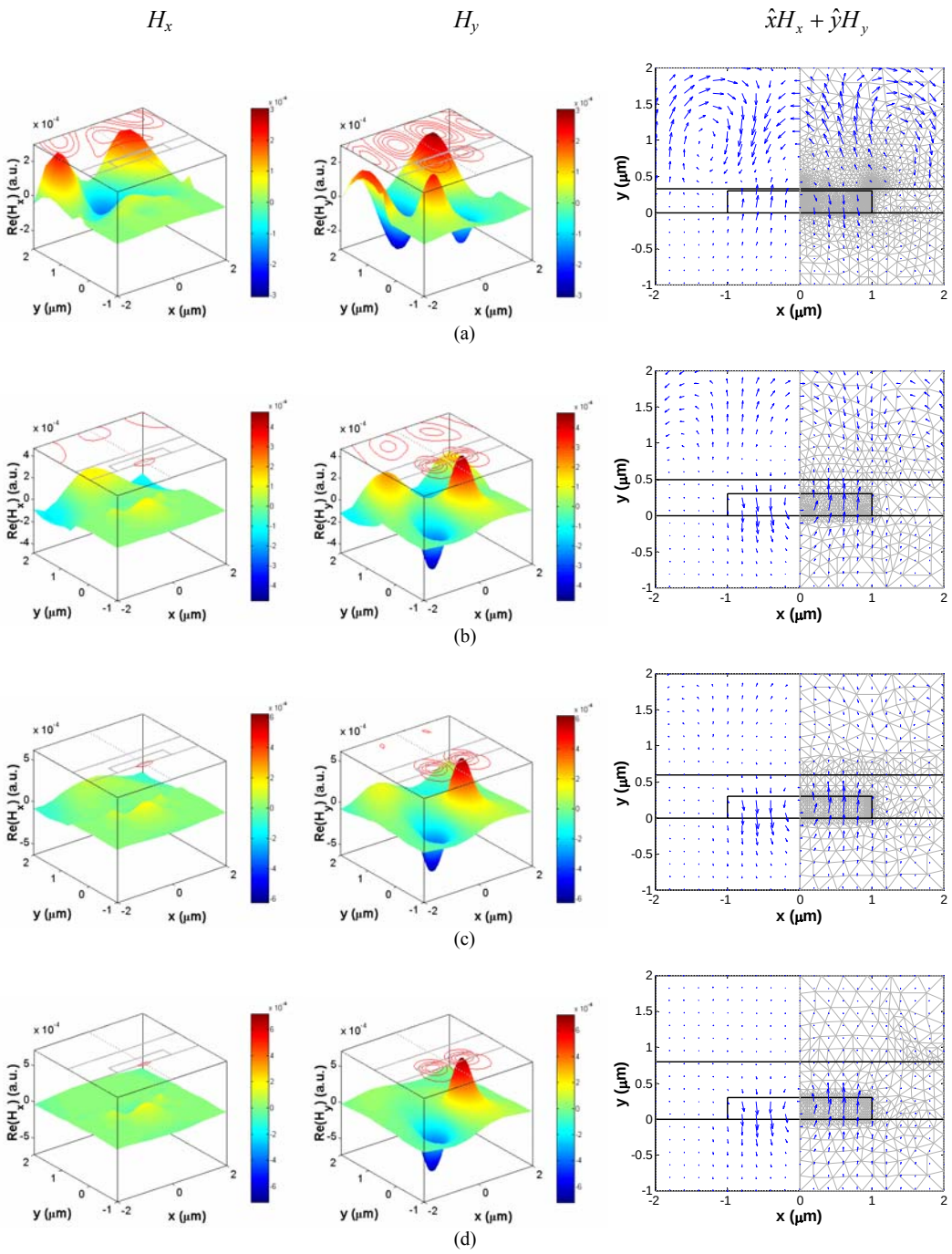

Figure 7.16. *Mode profiles at points denoted by triangular shapes in Fig. 7.12: (a) q-TE_{11} core-cladding mode at g=30nm, (b) hybrid mode at g=200nm, (c). q-TE_{10} core mode at g=300nm, and (d). q-TE_{10} core mode at g=500nm. The figure shows the evolution of modes from q-TE_{11} core-cladding mode in figure (a) into q-TE_{10} core mode in figure (d) as one changes the gap size.*

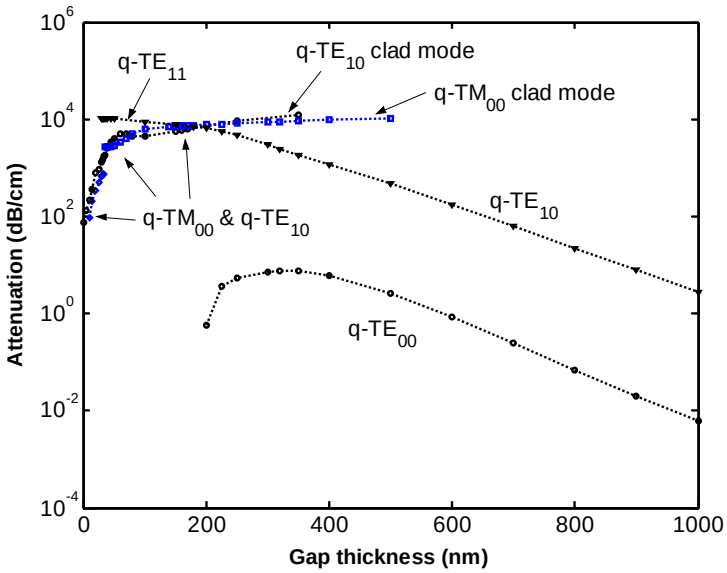

Figure 7.17. *Attenuation as function of gap thickness for the DAST overlaid Si_3N_4 strip waveguide.*

Figure 7.17 shows the attenuation of previously discussed modes as function of the gap thickness. For large gap thickness, the attenuation curves follow the two-parameter formula (6.9) nicely.

The effect of the DAST cladding can be concluded as follows. Without DAST cladding, the structure only supports guided q-TE_{00} and q-TE_{10} modes, while other modes are highly leaky cladding (or more precisely buffer) modes. By introducing DAST cladding, for g up to 5nm, a guided q-TM_{00} mode exists, while q-TE_{00} mode remains guided and q-TE_{10} becomes effectively suppressed by its large leakage loss. By further enlarging g, the q-TM_{00} mode becomes quite leaky. Hence, the structure becomes effectively single moded and single polarization (practically support q-TE_{00} mode only) until g=180nm, thereafter the attenuation of q-TE_{00} mode can be tuned by g. For sufficiently large g, q-TE_{10} mode will show up again by decreasing leakage loss following increasing g. The latter mode evolves from the q-TE_{11} core-cladding mode, which is originally very leaky. Note that the q-TE_{10} mode of large g does not correspond to q-TE_{10} mode of small g (see Fig. 7.12).

The effect of the silicon substrate (see structure of Fig. 7.9b) is much simpler. Fig. 7.18 shows the evolution of n_{eff} of q-TE_{00} and q-TE_{10} modes in the complex plane and their associated leakage loss as one varies buffer thickness b. Since the refractive index of Si is large enough, such that it is larger than zero crossing point (see explanation in Section 6.3.2), the $\mathrm{Re}\{n_{eff}\}$ of structure with Si substrate is lower than

n_{eff} of structure without the substrate ($b=\infty$). The leakage loss follows the two-parameter formula eq. (6.9) nicely, except at the highly lossy region, where eq. (6.9) is no longer applicable. Fluctuations at the highly lossy region indicate error induced by the boundary conditions. Fig. 7.19 shows the mode profiles of leaky q-TE_{00} and q-TE_{10} modes for several sampled calculation points, which shows the wave-like tail in the Si substrate region which is more pronounced for leakier structure.

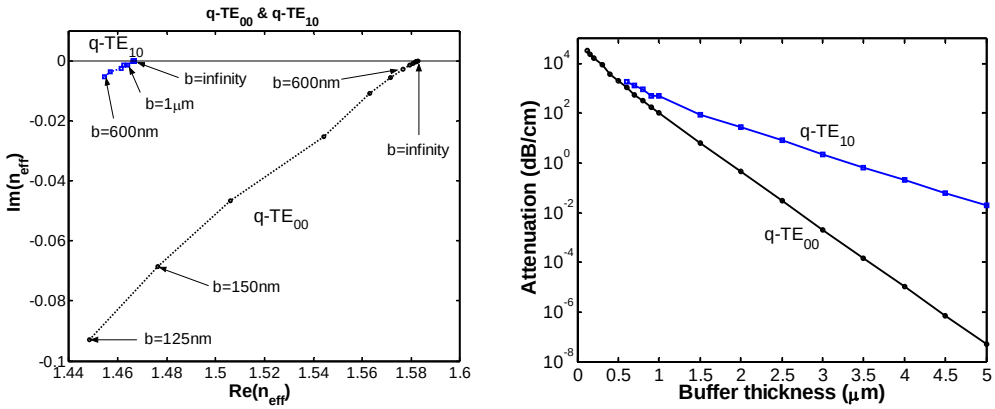

(a) (b)

Figure 7.18. *(a). Evolution of effective indices in the complex plane and (b). the associated attenuation constant as one varies the buffer thickness in a Si_3N_4 strip waveguide made on Si substrate with SiO_2 buffer layer.*

7.4. Issues related to implementation

Since k_r in eq. (7.16) is function of n_{eff}, some entries within matrix $\mathbf{M}_1$ which correspond to the computational boundaries will be function of n_{eff} as well. Hence, the eigenvalue equation will become non-linear. In this chapter, we linearize the eigenvalue equation through a simple iteration scheme, by using n_{eff} of the previous iteration to evaluate entries in $\mathbf{M}_1$, hence within each iteration the eigenvalue problem can be solved using linear eigenvalue solver. Within each iteration, the sign of the square root in eq. (7.16) should be correctly chosen based on arguments given in Section 7.2.2.1. In this work, we have used the implicitly restarted Arnoldi method available through the ARPACK package [25] used by Matlab as the eigenvalue solver. The shift-and-invert algorithm [26] used by Matlab, which enables searching of several complex eigenvalues nearby the shift (i.e. our initial and intermediate guesses), made it suitable for this simple iteration scheme. All results presented in this and following chapters have been obtained for convergence depth of 10^{-10} in n_{eff}, i.e. $|n_{eff,k}-n_{eff,k-1}|\leq 10^{-10}$ with k denoting the final iteration number.

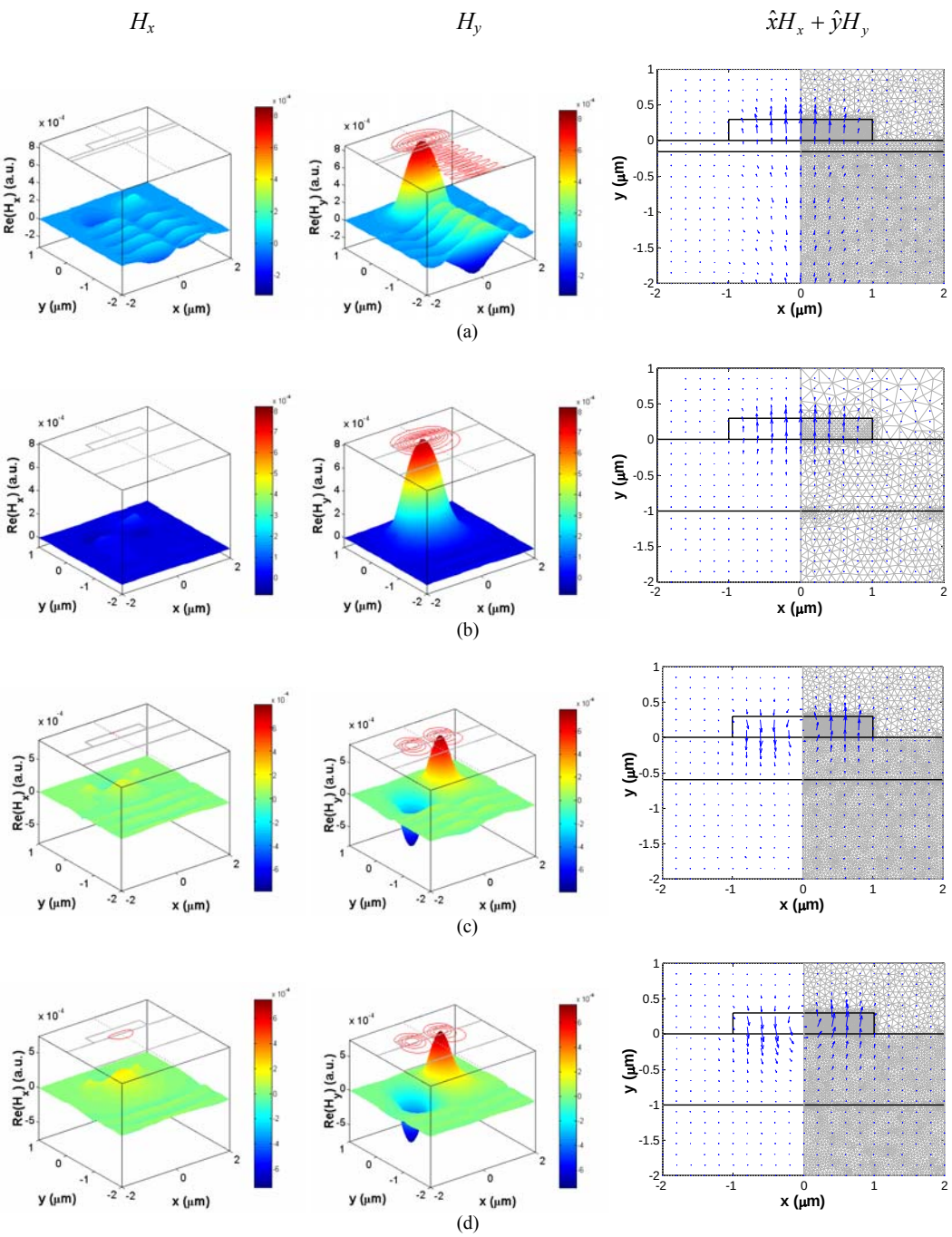

Figure 7.19. *Mode profile of q-TE_{00} mode at (a). b=150nm and (b). b=1μm, and mode profile of q-TE_{10} mode at (c). b=600nm and (d). b=1μm for the Si_3N_4 strip waveguide on Si substrate with SiO_2 buffer layer.*

It is well known that the efficiency and stability of an iteration process depends strongly on the initial guess. In the work presented in this and also following chapters, we implemented several iteration strategies. The first iteration strategy is for guided modes, where the eigenvalue next to the previously converged result is used as the initial guess for finding the next eigenvalue (see Fig. 7.20: the $n_{eff,0}$ in Fig. 7.20b is the eigenvalue next to $n_{eff,3}$ in Fig. 7.20a, which are obtained when iterating for HE_{11} mode). The second iteration strategy is for leaky modes, where we use the eigenvalues, obtained by enforcing the DBC, as the initial guesses (see Fig. 7.20: the real-valued $n_{eff,0}$ in Fig. 7.20c and 7.20d is obtained by using DBC instead of TBC). This can be justified as we realize that modes of interest in optical waveguides are those of small leakage loss and localized or quasi-localized one and the real eigenvalues and their associated eigenvectors with zero-field-value at boundaries obtained through the DBC can be regarded as the rough approximations to the complex eigenvalues to be searched. Hence, this iteration strategy can be regarded as using the iteration as an eigenvalue refinement mechanism, i.e. refining those approximate eigenvalues obtained through the simpler DBC scheme. The matrices for the DBC itself can be extracted from the matrices generated for the 1st-order BGT-like TBC with minor changes. Of course for specific structures, other simpler and more efficient approximate method (e.g. effective index method) can also be used to generate the initial guesses. This iteration strategy might not work well for highly-leaky modes (i.e. modes with large $|\mathrm{Im}\{n_{eff}\}|$) and modes which are not really quasi-confined within the waveguide (e.g. cladding resonance modes), since both the real-valued initial guess and zero-field-value at computational boundaries as assumed for DBC is not a good approximation for this kind of modes anymore. However, these highly-leaky modes are not interesting for most applications. Besides these two iteration strategies, there is also an option to have iteration based on user-supplied initial guesses, in case the user can get approximate n_{eff} by other simpler method or when the DBC can not give good initial guesses. Fig. 7.20 shows the convergence process of the iteration for step-index fiber case (guided mode, 1st iteration strategy) and rib ARROW case (leaky mode, 2nd iteration strategy).

In order to efficiently search for only those modes of interest, we limit the n_{eff} search within user-defined upper and lower bounds. In addition, the code of the implemented mode solver includes an algorithm to detect and skip diverging iterations, which might result from bad initial guess. In order to prevent searching for uninteresting highly-leaky modes, we also implement a leakage loss filter, which skips iterations that converge to modes with leakage loss beyond a user-defined leakage loss threshold value.

Other issue related to the implementation is the generation of the finite element meshes. In this implementation, we use mesh generator available in the Matlab

partial differential equation toolbox, which provides unstructured triangular mesh suitable for nodal-based FEM with linear basis functions. In order to implement nodal-based FEM with quadratic basis functions as presented in this chapter, we need additional nodal points in the middle of every side of the triangular elements (see Fig. 2.4 in Chapter 2). These points can be easily generated by using the vertex nodal points supplied by the mesh generator. In addition, it is possible to refine meshes located at specific regions of the structure, within which the field is expected to be more significant or has higher gradient.

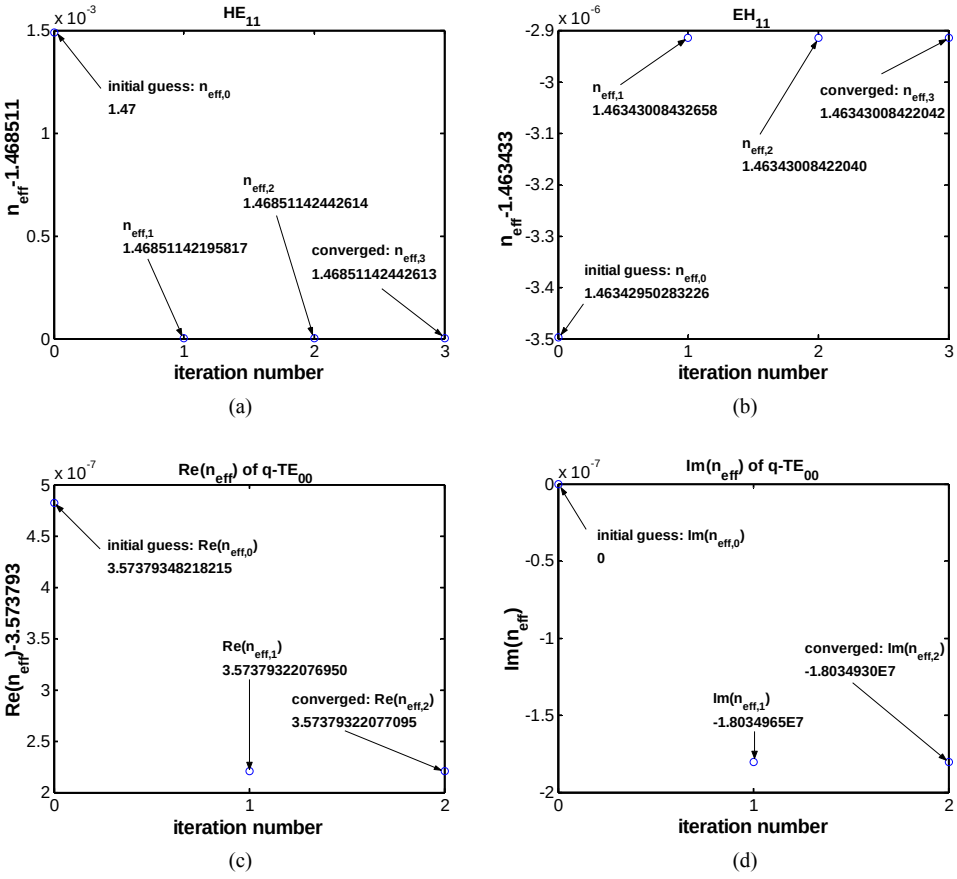

Figure 7.20. *Convergence process of the iteration for (a). the HE_{11} mode and (b). the EH_{11} mode of the step index fiber case, and (c). the real and (d) the imaginary part of n_{eff} of the q-TE_{00} mode of the rib ARROW case.*

7.5. Conclusion

A nodal-based finite element method furnished with 1st-order BGT-like TBC is reported for vectorial mode solving of optical waveguides with 2-D cross-section. The

scheme works for both guided and leaky mode computations. The scheme, which was implemented using the quadratic triangular basis functions, was demonstrated for computations of modes of optical fibers, fused fiber coupler, and leaky rib waveguide. The results show good agreement with the exact values (for optical fibers) and published results (for other structures). Using an isotropic step-index optical fiber, the superiority of the proposed boundary conditions compared to the simple homogeneous DBC and Sommerfeld-like TBC, was also demonstrated. Using the scheme, the evolution of modes of a buffered leaky strip waveguide with anisotropic overlaid cladding and high-index substrate as one varies the position of the cladding/substrate, was observed.

References

1. S. Selleri and J. Petracek, "Modal analysis of rib waveguide through finite element and mode matching methods," **Opt. Quantum Electron.**, Vol. 33, No. 4-5, pp. 373-386, 2001.
2. B.M.A. Rahman and J.B. Davies, "Finite-element analysis of optical and microwave waveguide problems," **Trans. Microwave Theory and Tech.**, Vol. MTT-32, No. 1, pp. 20-28, 1984.
3. S. Selleri *et al.*, "Complex FEM modal solver of optical waveguides with PML boundary conditions," **Opt. Quantum Electron.**, Vol. 33, No. 4-5, pp. 359-371, 2001.
4. H.E. Hernandez-Figueroa *et al.*, "Vectorial finite element modeling of 2D leaky waveguides," **Trans. Magnetics**, Vol. 31, No. 3, pp. 1710-1713, 1995.
5. B.M. Dillon and J.P. Webb, "A comparison of formulations for the vector finite element analysis of waveguides," **Trans. Microwave Theory and Tech.**, Vol. 42, No. 2, pp. 308-316, 1994.
6. A. Bayliss, M. Gunzburger, and E. Turkel, "Boundary conditions for the numerical solution of elliptic equations in exterior regions," **SIAM J. Appl. Math.**, Vol. 42, No. 2, pp. 430-451, 1982.
7. P.R. McIsaac, "Symmetry-induced modal characteristics of uniform waveguides – I: summary of results," **Trans. Microwave Theory and Tech.**, Vol. MTT-23, No. 5, pp. 421-429, 1975.
8. P.R. McIsaac, "Symmetry-induced modal characteristics of uniform waveguides – II: theory," **Trans. Microwave Theory and Tech.**, Vol. MTT-23, No. 5, pp. 429-433, 1975.
9. M. Koshiba, K. Hayata, and M. Suzuki, "Improved finite-element formulation in terms of the magnetic field vector for dielectric waveguides," **Trans. Microwave Theory and Tech.**, Vol. MTT-33, No. 3, pp. 227-233, 1985.
10. Y.C. Chiang, Y.P. Chiou, and H.C. Chang, "Improved full-vectorial finite-difference mode solver for optical waveguides with step-index profiles," **J. Lightwave Technol.**, Vol. 20, No. 8, pp. 1609-1618, 2002.

11. J.D. Joannopoulos, R.D. Meade, and J.N. Winn, *Photonic crystals: molding the flow of light*, Princeton Univ. Press, New Jersey, 1995.

12. M. Lohmeyer, *Guided waves in rectangular integrated magnetooptic devices*, Section 1.1.3, Ph.D. dissertation, Univ. Osnabruck, 1999.

13. Y.L. Hsueh *et al.*, "Opposite-parity orthonormal function expansion for efficient full-vectorial modeling of holey optical fibers," **Optics Lett.**, Vol. 28, No. 14, pp. 1188-1190, 2003.

14. J.M. Fini, "Improved symmetry analysis of many-moded microstructure optical fibers," **J. Opt. Soc. Am. B**, Vol. 21, No. 8, pp. 1431-1436, 2004.

15. R. Guobin, W. Zhi, L. Shuqin, and J. Shuisheng, "Mode classification and degeneracy in photonic crystal fibers," **Optics Express**, Vol. 11, No. 11, pp. 1310-1321, 2003.

16. A. W. Snyder and J.D. Love, *Optical Waveguide Theory*, Chapman and Hall, New York, 1983.

17. J.D. Dai and C.K. Jen, "Analysis of cladded uniaxial single-crystal fibers," **J. Opt. Soc. Amer. A.**, Vol. 8, No. 12, pp. 2021-2025, 1991.

18. E.I. Golant *et al.*, "New mode solver for anisotropic fibers with crystalline jackets," **Proc. SPIE**, Vol. 4769, pp. 162-173, 2002.

19. S.W. Yang and H.C. Chang, "Numerical modeling of weakly fused fiber-optic polarization beam splitters – Part I: Accurate calculation of coupling coefficients and form birefringence," **J. Lightwave Technol.**, Vol. 16, No. 4, pp. 685-690, 1998.

20. G.M. Berry *et al.*, "Analysis of multilayer semiconductor rib waveguides with high refractive index substrate," **Electron. Lett.**, Vol. 29, No. 22, pp. 1941-1942, 1993.

21. Y. Tsuji and M. Koshiba, "Guided-mode and leaky-mode analysis by imaginary distance beam propagation method based on finite element scheme," **J. Lightwave Technol.**, Vol. 18, No. 4, pp. 618-623, 2000.

22. S.S.A. Obayya *et al.*, "Full vectorial finite-element-based imaginary distance beam propagation solution of complex modes in optical waveguides," **J. Lightwave Technol.**, Vol. 20, No. 6, pp. 1054-1060, 2002.

23. F. Pan et al., "Electro-optic properties of the organic salt 4-N, N-dimethylamino-4'-N'-methyl-stilbazolium tosylate," **Appl. Phys. Lett.**, Vol. 69, No. 1, pp. 13-15, 1996.

24. W.C. Chew, *Waves and fields in inhomogeneous media*, Section 1.3.3, IEEE Press, New York, 1995.

25. http://www.caam.rice.edu/software/ARPACK/

26. J. Mielewski and M. Mrozowski, "Application of the Arnoldi method in FEM analysis of waveguides," **Microwave Theory and Tech.**, Vol. 8, No. 1, pp.7-9, 1998.

Chapter 8

Rigorous modeling of photonic crystal fibers

The finite-element-based vectorial optical mode solver reported in previous chapter is used to rigorously analyze photonic crystal fibers (PCFs). Both the real and imaginary part of the modal indices can be computed in a relatively small computational domain. Results for PCFs with either circular or non-circular microstructured holes, solid- or air-core will be presented, including the air-core silica-air Bragg fiber. The results of the solid-core structures are in good agreement with the results of other methods, while the results of the air-core silica-air Bragg fiber agree to the experimental results. Using the mode solver, a commercial endlessly single-mode PCF were investigated.

This chapter is partly adapted from:
H.P. Uranus and H.J.W.M. Hoekstra, "Modelling of microstructured waveguides using a finite-element-based vectorial mode solver with transparent boundary conditions," **Optics Express**, Vol. 12, No. 12, pp. 2795-2809, 2004.
H.P. Uranus, H.J.W.M. Hoekstra, and E. van Groesen, "Modes of an endlessly single-mode photonic crystal fiber: a finite element investigation," **Proc. of The 9th Annual Symp. IEEE/LEOS Benelux**, pp. 311-314, IEEE & Univ. Ghent, Dec. 2-3, 2004, Ghent, Belgium.

Rigorous modeling of photonic crystal fibers

8.1. Introduction

Since the introduction of the photonic crystal fiber (PCF) [1], various waveguiding structures that utilize the arrangement of microstructured holes [2] or thin layers [3] have been realized. Due to the finite number of holes or layers in the cladding, the structures are usually leaky. In this class of structures, both the real and imaginary parts of the modal indices are essential parameters. The real part of the modal indices determines among others, the dispersion properties [4, 5], while the imaginary part determines the confinement loss [6]. The confinement loss is an important parameter to discriminate one mode from the others; hence, one can have structures with wide effectively-single-mode operation wavelength range [7] or non-polarization-degenerate effectively-single-mode operation [8-10]. Therefore, the ability to calculate both the real and imaginary part of the modal indices is important.

The large variety of possible hole shapes and arrangements demand the use of numerical methods that can handle arbitrary cross-sectional shapes to analyze this kind of structures. Besides, the existence of interfaces with high index-contrast between the host material and air holes requires a vectorial method to accurately model the structure. Among others; plane-wave expansion method [11], supercell lattice method [12], multipole method [13], Fourier decomposition method [14], beam propagation method (BPM) [15, 16], and also mode solver based on finite difference method (FDM) [17, 18], and finite element method (FEM) [19-21] have been used to model the PCFs. Some of these methods can calculate only the real part of the mode effective indices.

With the multipole method one can calculate both the real and imaginary part of the modal indices, but it is restricted to circular holes. The Fourier decomposition method with adjustable boundary conditions (FDM-ABC) is suitable for calculation of both the real and imaginary part of the modal indices of structure with either circular or non-circular holes arranged in a circularly oriented setting and homogeneous exterior domain. The BPM with perfectly matched layers (PMLs) is able to calculate both the real and imaginary part of the modal indices of structures with arbitrary cross-section, but might be rather intricate for multimode calculation. FDM and FEM mode solvers employing PML [18, 22-23] can be used to calculate both the real and imaginary part of the modal indices of structure with arbitrary cross-section shape, but the PML itself occupies extra memory space and requires some skill to determine the optimal parameters to work effectively.

In this chapter, we discuss results of applying the vectorial optical mode solver based on Galerkin finite element method, which is furnished with a 1st-order Bayliss-Gunzburger-Turkel-like (BGT-like) transparent boundary conditions (TBC) as described in previous chapter, to rigorously model various kinds of PCFs. Thanks to the boundary conditions, the structure can be analyzed in a relatively small computational domain for its complex-valued modal indices and field profiles. The structures being considered include those with either solid material or air as the core; thin solid layers, circular or non-circular microstructured holes arranged around the core. In addition, arguments leading to a simple procedure was used to explain the degeneracy and non-degeneracy of modes of the structure. Using the mode solver, we also evaluated a commercial endlessly single mode PCF (ESM-PCF) for its single-modeness.

8.2. Solid-core photonic crystal fibers

8.2.1. Photonic crystal fiber with circular microstructured holes

As the first sample of PCF with solid core, we choose a structure with 6 circular holes arranged in a hexagonal setting as shown in Fig. 8.1a. Later on, we also consider similar structures, but with more rings of holes up to the one shown in Fig. 8.1b and found that they exhibit almost similar properties, except the confinement loss. Hence, we will concentrate the computation mainly on the 6-hole structure and consider structure with larger number of holes only if necessary.

In order to enable comparison of our results with the results of other methods, we take the structure shown in Fig. 8.1a and choose the same structure parameters as in the references [13, 14]. The diameter of the holes is d=5μm with a pitch length of Λ=6.75μm. The refractive index of the background material is n_{bg}=1.45, while the refractive index of the holes is n_{hole}=1. The vacuum wavelength used in the calculation is 1.45μm. Taking advantage of the symmetry of the structure; we only use a quarter circle with a radius of r_b=10μm as the computational domain with the curved boundary located just slightly after the hole. The 1st-order BGT-like TBC is applied to the curved boundary while symmetry boundary conditions, which consist of a perfect electric conductor (PEC) and/or a perfect magnetic conductor (PMC), are applied at the two boundaries coinciding with the structure symmetry planes. The computational domain is discretized into 1648 triangular elements.

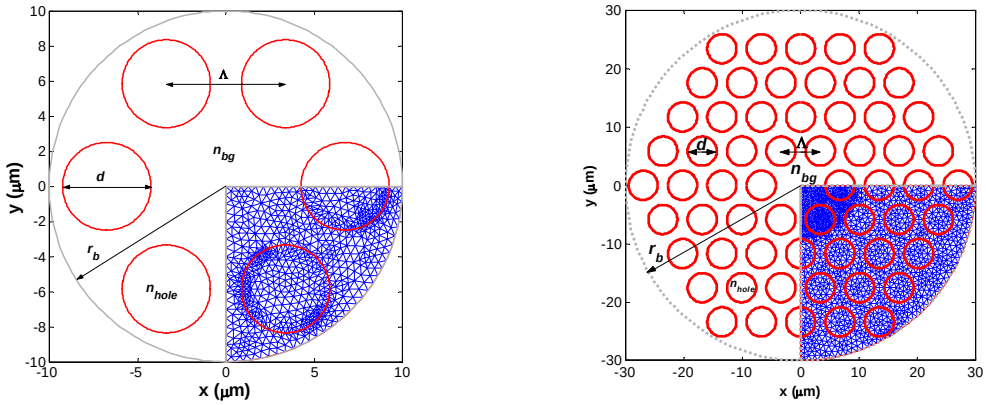

Figure 8.1. *The PCF with (a). 6 circular holes and (b). 60 circular holes together with their computational domain and triangulation.*

Table 8.1. *Computational results of the PCF with 6 circular holes and their comparison with those of other methods.*

Mode	Present FEM Scheme (1648 triangular elements)			Multipole Method (5 multipole moments) (White *et al.*)		Vector FDM-ABC (70 azimuthal, 54 radial terms) (Issa & Poladian)	
	Re(n_{eff})	-Im(n_{eff})	Att. (dB/cm)	Re(n_{eff})	-Im(n_{eff})	Re(n_{eff})	-Im(n_{eff})
HE_{11}^{a} -like	1.4453935	4.11E-8	0.0155	1.4453953	3.15E-8	1.4453954	3.07E-8
HE_{11}^{b} -like	1.4453931	4.13E-8	0.0155				
TE_{01} -like	1.4385760	3.97E-7	0.1493	1.4385858	4.99E-7	1.4385890	5.43E-7
HE_{21}^{a} -like	1.4384419	7.13E-7	0.2684	1.4384458	9.93E-7	1.4384442	9.62E-7
HE_{21}^{b} -like	1.4384376	7.11E-7	0.2674				
TM_{01} -like	1.4383622	1.03E-6	0.3865	1.4383667	1.37E-6	1.4383643	1.38E-6
HE_{31}^{b} -like	1.4303848	2.25E-5	8.4687	1.430175	2.22E-5		
EH_{11}^{a} -like	1.4299517	1.67E-5	6.2762	1.4299694	1.58E-5		
EH_{11}^{b} -like	1.4299459	1.68E-5	6.3246				
HE_{31}^{a} -like	1.4292608	9.17E-6	3.4507	1.4292553	9.34E-6		

Table 8.1 shows our computed results for the first ten modes and the results of other methods. The mode labeling in the table makes use of the similarity of the mode profiles to those of ordinary step-index fiber with additional superscripts *a* and *b* denoting the results obtained using PMC and PEC at the horizontal symmetry plane, respectively. The table shows that our results using rather modest mesh size and small computational domain are in good agreement with the results of the multipole method [13] and the vector FDM-ABC [14]. The agreement in the real part of the effective indices is better than that of the imaginary part. By varying the mesh size and the

computational boundary position, we see indication that the absolute error of the Im(n_{eff}) is a few orders better than that of the Re(n_{eff}), meaning that the error terms contain larger real component than imaginary component. We guess this is caused by the fact that the boundary term (to which the leaky mode computation ability is attributed) occupies only small fraction of the non-zero entries within the FEM matrices. However, due to their very small values, it is very hard to get high relative accuracy (small relative error) for the Im(n_{eff}). Since only modest mesh size and relatively small computational window were used in the results shown in Table 1, the convergence test indicates that in general only the order (for some modes also the first digit of the same order) of the computed Im(n_{eff}) is significant, while for the Re(n_{eff}), at least 4 decimal digits for the high order modes and 5 decimal digits for the low order modes are significant.

Fig. 8.2 shows the real part of the transverse magnetic fields vector of the modes, i.e. $\hat{x}\,\mathrm{Re}(H_x) + \hat{y}\,\mathrm{Re}(H_y)$. The transverse fields of modes labeled with the same subscript but different superscript (and also *TE*- and *TM*-like modes), i.e. those shown at the left and right column in Fig. 8.2, are perpendicular to each other at every point in the structure cross-section. Therefore, they can be regarded as pairs. From the computed results (see Table 8.1, and also later on Fig. 8.4 and 8.5), group theoretical arguments [13, 24], and the arguments to be presented in Section 8.4, we can see that HE_{11}^{a}- and HE_{11}^{b}-like, HE_{21}^{a}- and HE_{21}^{b}-like, EH_{11}^{a}- and EH_{11}^{b}-like modes are degenerate pairs, while HE_{31}^{a}- and HE_{31}^{b}-like, and also TE_{01}- and TM_{01}-like modes are non-degenerate pairs. Fig. 8.3 shows similarity of the longitudinal component of the time-averaged Poynting vector of vectorial modes which correspond to the same *LP* modes of standard optical fiber scalar analysis.

The table also shows that using different symmetry boundary conditions at the two symmetry planes, the computed effective indices of the degenerate modes agree to each other up to 5 decimal digits in Re(n_{eff}). The small numerical birefringence comes from the fact that the mesh used in the discretization has broken the structure symmetry; the effect of which will show up in the discrepancies of the discretization error of the computed degenerate modes. By reducing the discretization error, e.g. using a finer mesh, one can expect smaller numerical birefringence [25].

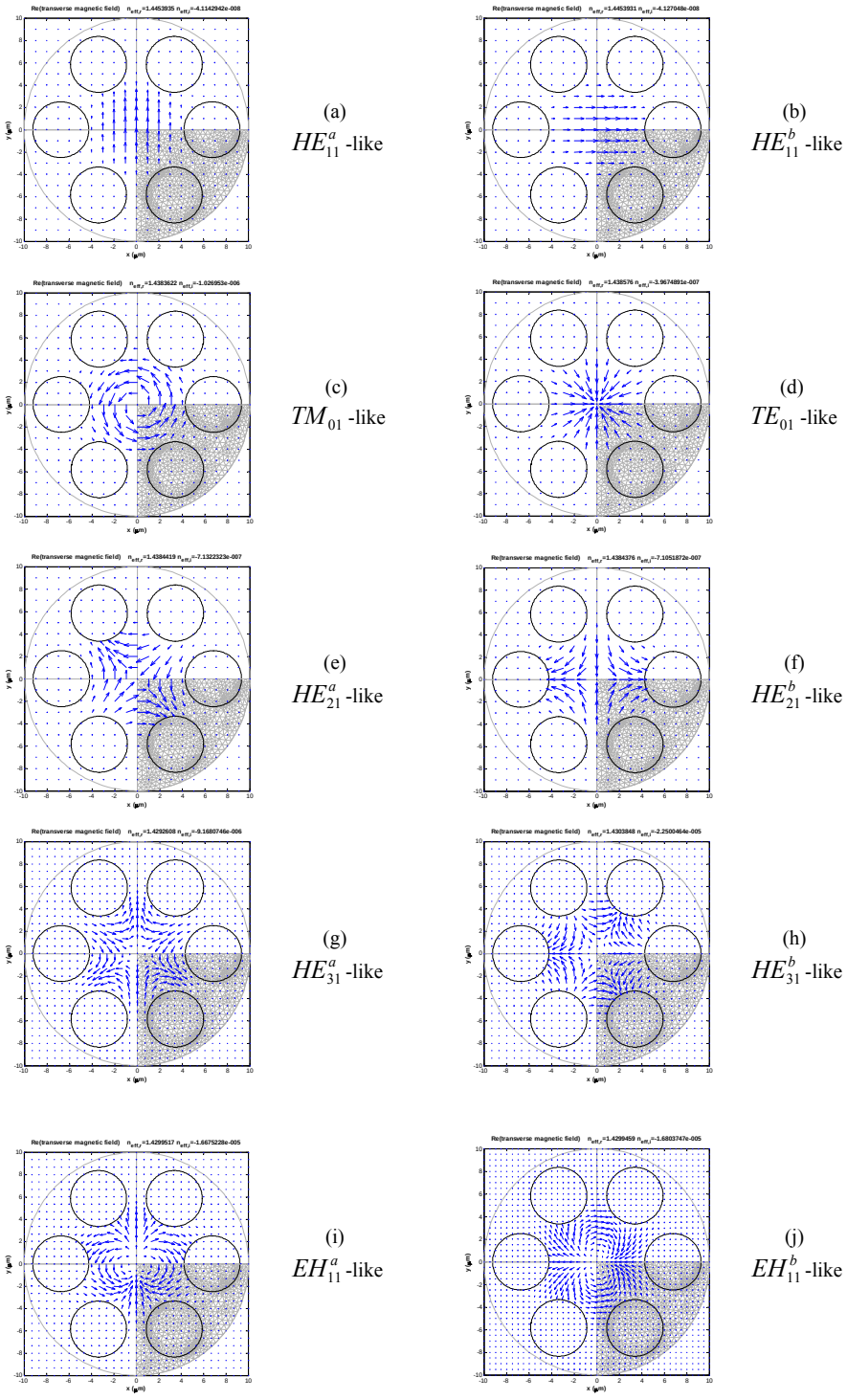

(a) HE_{11}^{a} -like

(b) HE_{11}^{b} -like

(c) TM_{01} -like

(d) TE_{01} -like

(e) HE_{21}^{a} -like

(f) HE_{21}^{b} -like

(g) HE_{31}^{a} -like

(h) HE_{31}^{b} -like

(i) EH_{11}^{a} -like

(j) EH_{11}^{b} -like

Figure 8.2. *Transverse magnetic field vector plot of modes of the 6-hole PCF.*

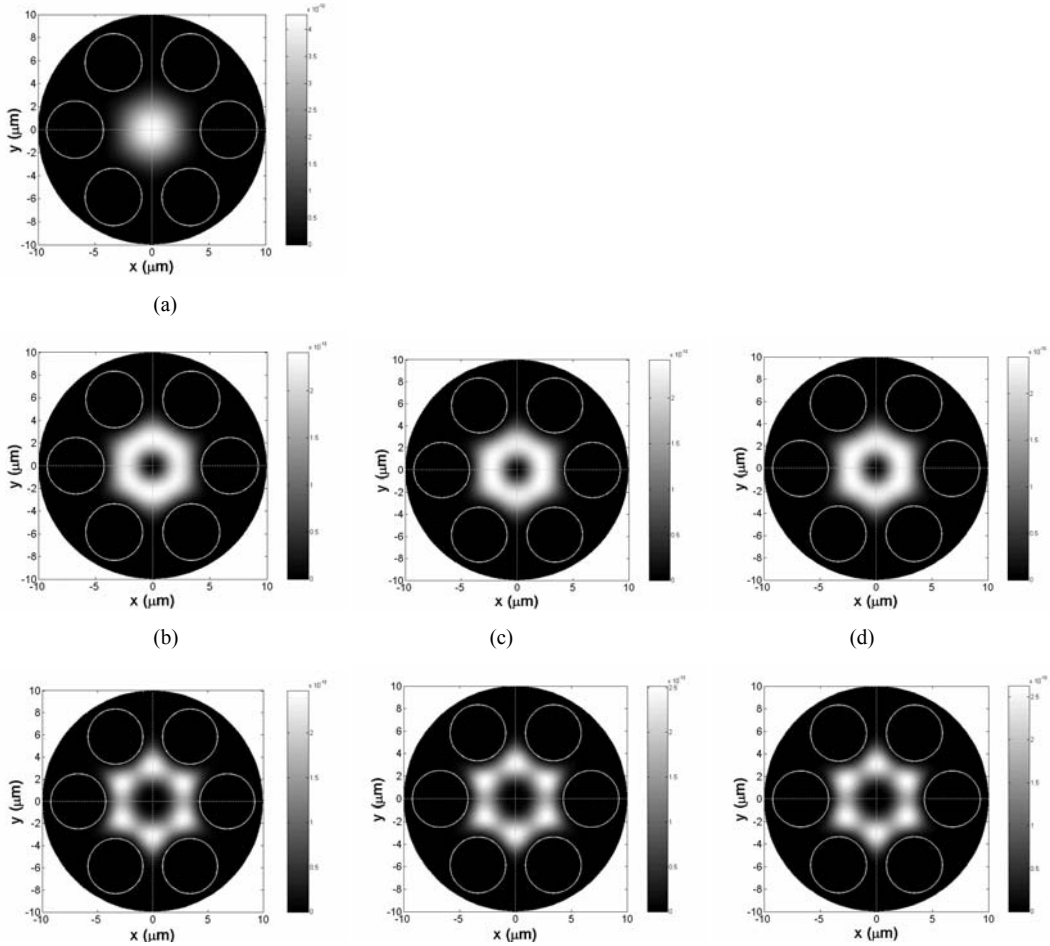

Figure 8.3. *Longitudinal component of the time-averaged Poynting vector of (a). HE_{11} -, (b). TE_{01} -, (c). HE_{21} -, (d). TM_{01} -, (e). HE_{31}^{b} -, (f). EH_{11} -, (g). HE_{31}^{a} -like modes of the 6-hole PCF. Figures in the 1st, 2nd, and 3rd row correspond to the LP_{01}, LP_{11}, and LP_{21} modes of scalar model, respectively.*

We also take a similar structure (the same geometrical parameter, but different refractive index) and perform a spectral-scan characterization. We assume that pure silica has been used as the host material and take the more realistic value of the refractive index from its Sellmeier's equation [26] for each wavelength, i.e.

$$n^2 = 1 + \frac{0.6961663\lambda^2}{\lambda^2 - (0.0684043)^2} + \frac{0.4079426\lambda^2}{\lambda^2 - (0.1162414)^2} + \frac{0.8974794\lambda^2}{\lambda^2 - (9.896161)^2} \qquad (8.1)$$

with λ is wavelength in μm. In this way, the material dispersion effect is rigorously taken into account here and also in all other wavelength-dependent plots in this

chapter. For the air holes, we take a constant value of refractive index of 1. Fig. 8.4 shows the real part of the effective indices and the corresponding dispersion parameter as function of wavelength. The dispersion parameter is calculated using [4]

$$Dispersion = -\frac{\lambda}{c}\frac{\partial^2}{\partial\lambda^2}\left[\mathrm{Re}\left(n_{eff}\right)\right] \tag{8.2}$$

The derivation of this formula will be given in Appendix 2. The curves show three groups of modes, which correspond to the first-three *LP* modes. By using the present vectorial solver, it is possible to distinguish modes within the same group. The different between the curves of modes associated with the same group is more pronounced for longer wavelengths, where the dimension of the structure becomes more comparable to the wavelength. The divergence between curves for HE_{31}^{a}- and HE_{31}^{b}-like modes also confirms their non-degeneracy as discussed earlier. The figure also shows that the HE_{11}-like mode has zero-dispersion wavelength at shorter wavelength than the ordinary fiber.

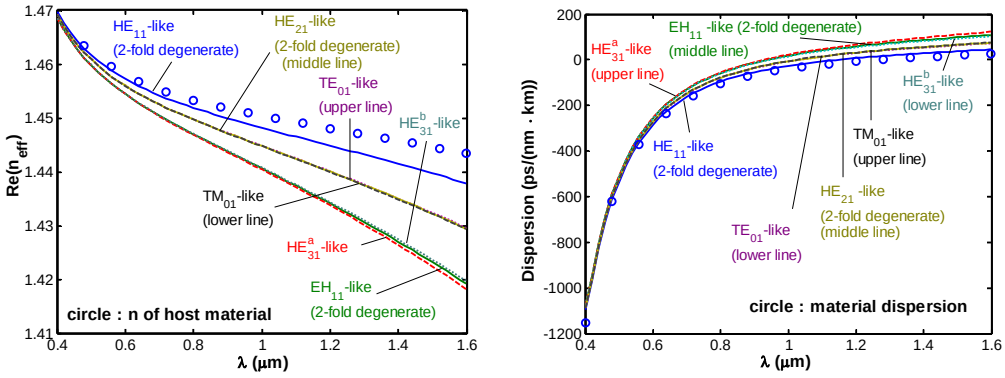

(a) (b)

Figure 8.4. *(a) The real part of the mode effective indices and (b) the dispersion parameter of the structure with 6 circular holes.*

Fig. 8.5a shows the confinement loss as a function of wavelength. The difference between modes within the same groups is even more pronounced here. Since loss is one of the important parameters of the PCF, these results emphasize that the vectorial method is necessary for such structure, especially in the long wavelength regime (and also at large d/Λ ratio [28], which determines the local air filling fraction in the ring of holes). As the wavelength increases, the modes become less quasi-confined; consequently, the confinement loss also increases. As the HE_{11}-like mode is the one with lowest loss, the structure will be effectively single-moded after a certain propagation distance. In Section 8.5 we will further discuss PCF that is specially designed to exhibit this property. Fig. 8.5b shows the effect of adding more rings of

holes around the central core, with the holes in the cladding arranged in a triangular-lattice-like setting. In this case; 2-ring, 3-ring, and 4-ring structures will have 18, 36, and 60 holes (see Fig. 8.1b) in the cladding, respectively. We found that adding rings of holes will reduce the confinement loss, but will not change the dispersion parameter very much. Some small fluctuations in the curve of the structure with 60 holes in the short wavelength region are due to the very small value of the loss, which is beyond the machine accuracy of the computing platform.

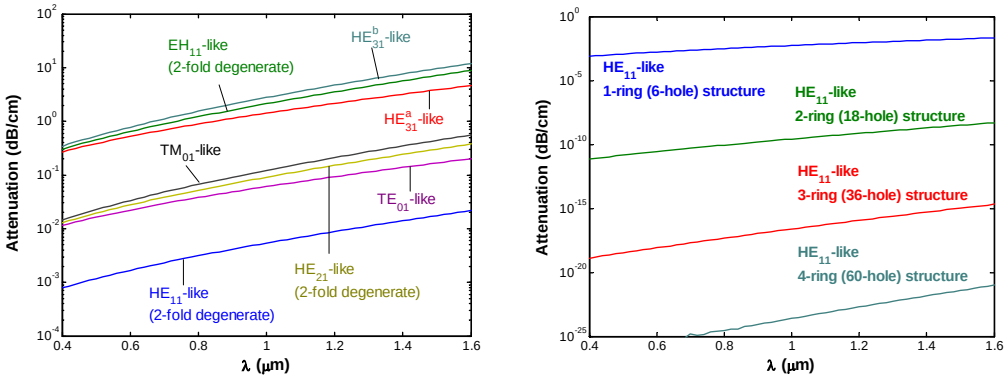

Figure 8.5. *The confinement loss of the structure with circular holes. (a) Confinement loss of the first-ten modes of the 1-ring (6-hole) structure. (b) The effect of adding more rings of holes in the cladding.*

8.2.2. Photonic crystal fiber with annular-sector shaped holes

Next, we consider a structure with 3 annular-sector shaped holes as shown in Fig. 8.6. The host material is pure silica with a refractive index of 1.44402362 at a wavelength of 1.55μm, while the refractive index of the holes is 1. The annular-sector shaped holes have an inner radius r_1=1μm and outer radius r_2=2μm and angular width of 108°. We take a half-circle with radius r_b=2.5μm as our computational domain with the 1st-order BGT-like TBC at the curved boundary, and either PEC or PMC at the boundary located at the structure symmetry plane. The computational domain is discretized into 1937 triangular elements as shown in Fig. 8.6. The results of the first-six modes of this structure are given in Table 8.2 with comparison to the results obtained using the vector FDM-ABC [14]. The vector FDM-ABC used in this calculation is slightly different than the one discussed in [14]. Here, it employs Fourier decomposition only in the azimuthal direction, while in the radial direction it uses a finite difference discretization. Due to the vectorial character of the modes, the scalar method [27] is simply not good enough, hence it will not be considered in the comparison. The table shows good agreement between results of our FEM scheme and the vector FDM-ABC. As in previous example, the HE_{11}^{a}- and HE_{11}^{b}-like, and also HE_{21}^{a}- and HE_{21}^{b}-like

modes are degenerate pairs, while TE_{01}- and TM_{01}-like modes are non-degenerate pairs. The vector plots of the real part of the transverse magnetic fields of these modes are given in Fig. 8.7. The real part of the effective indices and the dispersion parameter of this structure are depicted in Fig. 8.8, while the imaginary part of the effective indices and the confinement loss are shown in Fig. 8.9. Again, to obtain these spectral plots, we used the Sellmeier's equation (8.1) of pure silica at each wavelength. Fig. 8.8a shows that at around 1.483μm, the real part of n_{eff} of HE_{21}- and TM_{01}-like modes cross over, which indicates their rather dissimilar dispersion properties as shown in Fig. 8.8b. Since this structure has much smaller core size and larger (local) air filling fraction than the previous sample, the effect of the air holes is stronger, hence the zero-dispersion wavelength of the HE_{11}-like mode is located at a shorter wavelength (see arguments given in [5]). Besides, the vectorial character is also more pronounced as indicated by more divergent curves of TE_{01}-, TM_{01}-, and HE_{21}-like modes (which are associated to LP_{11} mode of scalar analysis), both in their real and imaginary part of the effective indices.

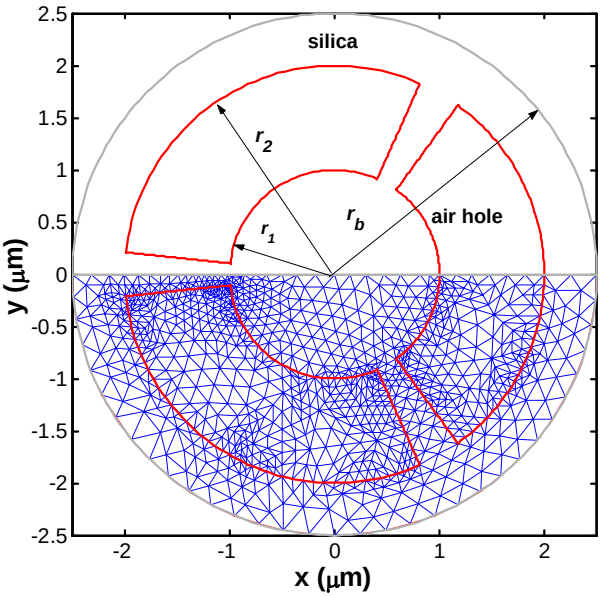

Figure 8.6. *Structure with 3 annular-sector shaped holes.*

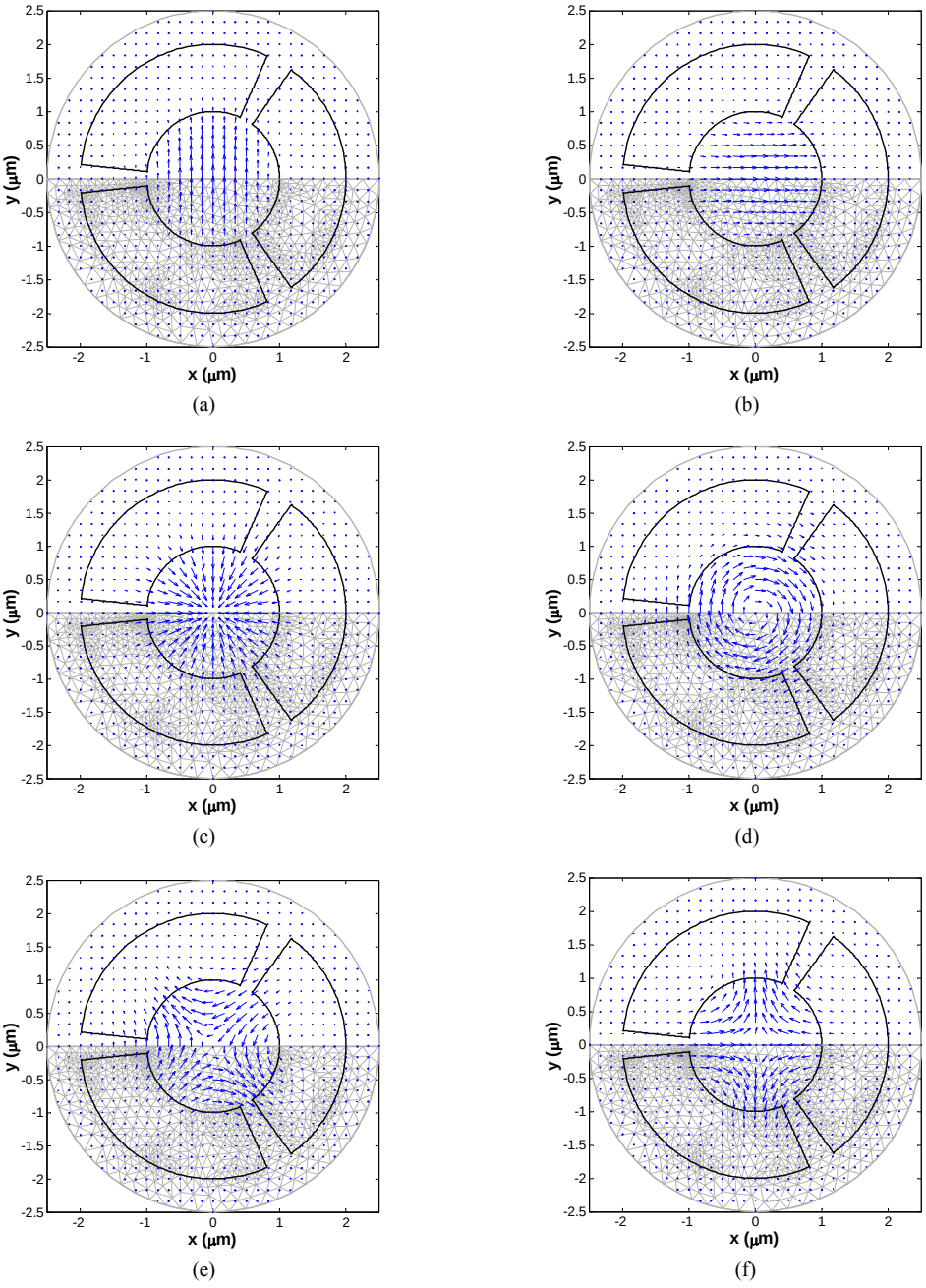

Figure 8.7. *The real part of the transverse magnetic fields of the first-six modes of the structure with 3 annular-sector shaped holes. (a) HE_{11}^{a} -, (b) HE_{11}^{b} -, (c) TE_{01} -, (d) TM_{01} -, (e) HE_{21}^{a} -, and (f) HE_{21}^{b} -like modes.*

Table 8.2. *Calculated mode effective indices of the structure with 3 annular-sector shaped holes.*

Mode	Present FEM scheme (1937 triangular elements)			Vector FDM-ABC (800 radial, 180 angular resolution) (Issa & Poladian)	
	Re(n_{eff})	-Im(n_{eff})	Attenuation (dB/cm)	Re(n_{eff})	-Im(n_{eff})
HE_{11}^{a} -like	1.35580	4.95E-5	17.44	1.35584	5E-5
HE_{11}^{b} -like	1.35581	4.96E-5	17.45		
TE_{01} -like	1.23950	5.67E-4	199.81	1.23957	5.09E-4
TM_{01} -like	1.21655	1.96E-3	690.11	1.21652	1.96E-3
HE_{21}^{a} -like	1.21480	1.11E-3	390.09	1.21476	1.25E-3
HE_{21}^{b} -like	1.21479	1.11E-3	390.52		

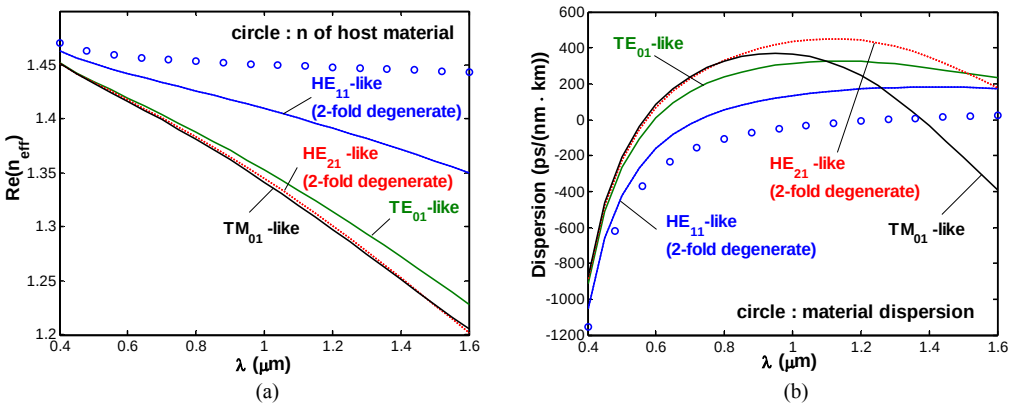

Figure 8.8. *(a) The real part of the effective indices and (b) the dispersion parameter of the modes of structure with 3 annular-sector shaped holes.*

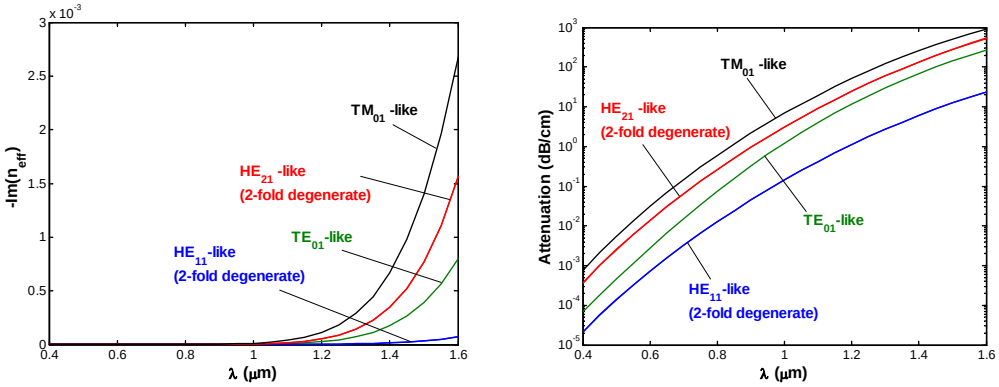

Figure 8.9. *(a) The imaginary part of the effective indices and (b) the confinement loss of the modes of structure with 3 annular-sector shaped holes.*

8.2.3. Hole-assisted multi-ring fiber

So far, we have studied PCFs that work in the leaky mode regime. In this section, we will consider fibers, which operate in the guided mode regime, but employ microstructured holes to tune their properties. These fibers are known as the hole-assisted fiber [29]. We will show that microstructured holes could be used to tune both the number of guided modes and the dispersion properties of such fiber.

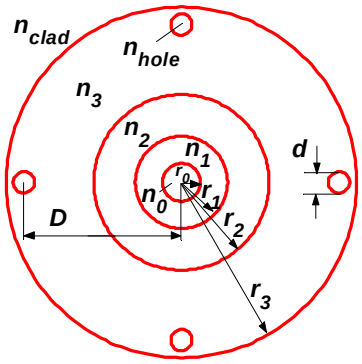

Figure 8.10. *The hole-assisted multi-ring fiber.*

Here, we consider a multi-ring fiber [30] with depressed core and tuned by four holes located in its outer ring as shown in Fig. 8.10. The refractive index of the outermost cladding n_{clad} is taken from the Sellmeier's equation (8.1), while the refractive indices of the rings follow from $n_i=(1+\Delta_i)n_{clad}$, with Δ_0, Δ_1, Δ_2, and Δ_3 are

-0.1%, 0.45%, -0.33%, and 0.1%, respectively, and the refractive index of the holes are n_{hole}=1. The size of the rings r_0, r_1, r_2, and r_3 are 0.41r_1, 3.9μm, 1.9r_1, and 3.8r_1, respectively. The diameter (d) and position (D=s[r_2+r_3]/2, where s is a measure of the hole position offset from the center of the outer ring) of the holes as well as light wavelength are to be varied. This structure is similar to the one discussed by Yan *et al.* [31], but here we have lowered the refractive index of one of the rings in order to obtain single mode properties as well as low dispersion parameter (D), and hence low group velocity dispersion (GVD) in the telecom 3rd wavelength window. Our computation showed that although low GVD can be achieved for the fundamental mode of the structure proposed by Yan *et al.* (where Δ_1=0.48% has been used), but their fiber is not single-moded in the expected wavelength range.

Fig. 8.11 shows the mode indices and their associated dispersion parameter for the multi-ring fiber without air holes. This structure is multi-moded within the wavelength range of interest. Fig. 8.12a shows the effect of introducing the four air holes to the dispersion parameter of the fundamental mode of the fiber. Enlarging the diameter of the air holes will lift the dispersion curve up, while moving the holes away from the core will flatten the curve. Fig. 8.12b shows the dispersion parameter of the guided modes of the fiber for d=2.2μm and s=1. For this setting, the fiber is single-moded and has a dispersion parameter of less than 4 ps/(nm·km) in the telecom 3rd wavelength window. A smaller dispersion parameter can be obtained by holes with d=1.8μm and s=1, but for the latter setting, the fiber is not single-moded anymore in the S-band. The introduction of air holes will reduce the average refractive index of the outer ring; therefore will reduce the number of guided modes as well. The fact that this fiber works in the guided mode regime and the possibility to engineer its dispersion and modal properties by the arrangement of the air holes might be interesting for some applications.

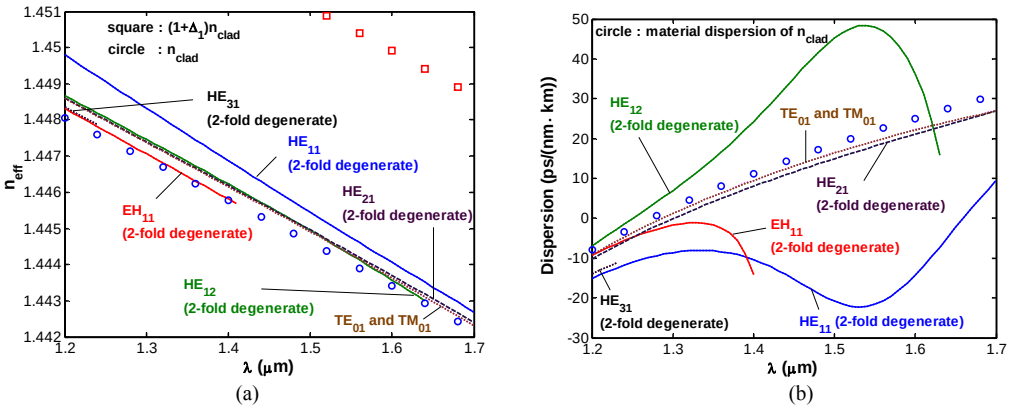

Figure 8.11. *The mode effective indices and their associated dispersion parameter for the multi-ring fiber without the microstructured air holes.*

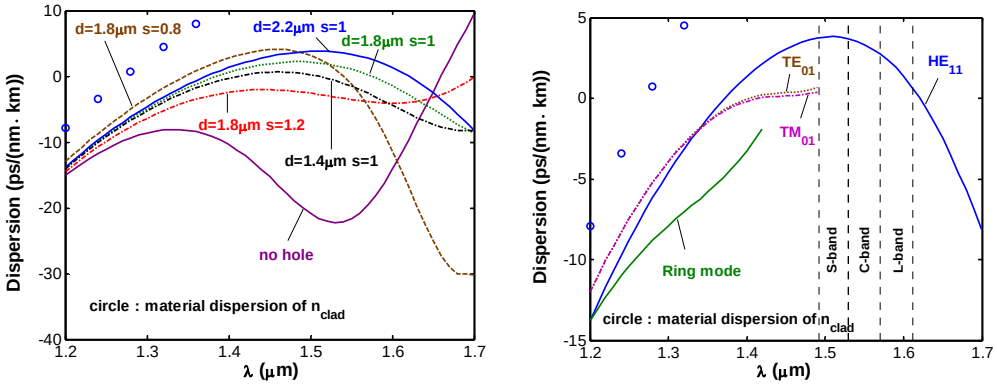

(a) (b)

Figure 8.12. *Dispersion parameter of (a). the fundamental (HE_{11}) mode tuned by various hole diameter and position and (b). the guided modes for holes with d=2.2μm and s=1 of the hole-assisted multi-ring fiber.*

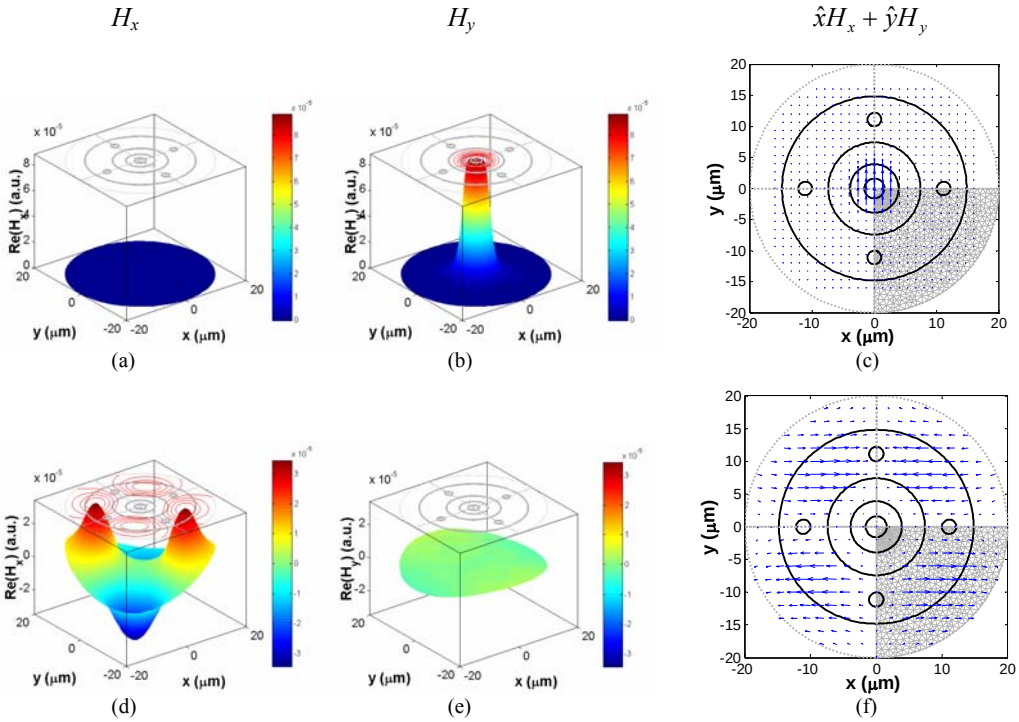

Figure 8.13. *Mode profile of (a).-(c). the fundamental (HE_{11}) and (d).-(f). the "ring" mode of structure with air holes with d=2.2μm and s=1 at λ=1.2μm.*

We also notice that by introducing the air holes, a mode with a modal field shape never reported for ordinary fibers appears. We label this 2-fold degenerate mode as "ring" mode since its field is confined within the outer ring as shown by Fig. 8.13d-f. The mode profile of this mode looks like q-TM_{11} while its degenerate pair looks like q-TE_{11} of a waveguide with square core. This is not surprising as the introduction of the air holes changes the symmetry of the structure from $C_{\infty v}$ into C_{4v}.

8.3. Air-core photonic bandgap fiber with rings of annular-sector shaped holes

Next, we consider an air-silica Bragg fiber structure recently demonstrated experimentally by Vienne *et al*. [33], which is an air-core structure with 3 rings of annular-sector shaped holes around it. We use the model depicted in Fig. 8.14, which parameters are taken from the fabricated structure but slightly simplified for computational efficiency. The radius of the air core is r_{core}=10μm. We assume that the holes are of annular-sector shaped with uniform thickness of $t_{annular}$=2.3μm. The corners of the holes are rounded with circles tangent to the side of the annular-sector shaped holes with radius of $r_{corner}=t_{annular}/4$. The thin rings of the host material located in-between two neighboring rings of holes have a thickness of t_{ring}=0.2μm. These thin rings of solid material are supported by thin bridges with a mid position thickness of t_{bridge}=45nm. For computational efficiency, we assume that the number of holes are 24, 34, and 44 in the first, second, and third rings of holes, respectively, which are slightly different than the fabricated one that has 24, 35, and 46 holes at the corresponding rings. By this simplification, we have changed the symmetry of the structure into C_{2v}, which enables the use of a computational window of a quarter structure. We use computational window with radius r_b=19μm, with the curved boundary located not too far from the outermost ring of holes. The 1st-order BGT-like TBC is applied at this curved boundary, while the PEC and/or PMC are used at the boundaries coinciding with the structure symmetry planes. The computational domain is discretized into 17638 triangular elements. This large number of elements is induced by the very thin bridges located between two adjacent holes in the same ring. In the calculation, we used the wavelength of 1.06μm, which corresponds to the laser used in the experiments to measure the modal near field intensity pattern. The refractive index of the silica as the host material is taken from the Sellmeier's equation (8.1), while the refractive index of air is 1.

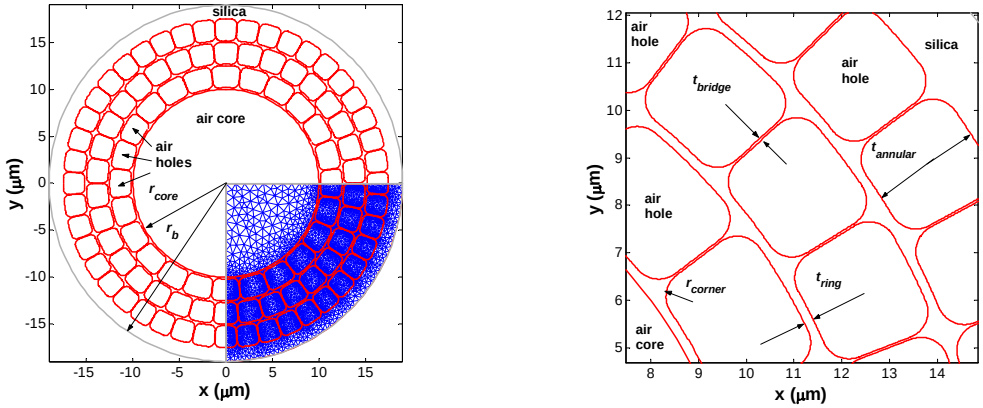

(a) (b)

Figure 8.14. *The model of the air-silica Bragg fiber with 3 rings of annular-sector shaped holes in the cladding.*

The results of the first-six modes are given in Table 8.3, which shows that the TE_{01}-like mode exhibits the lowest confinement loss; a property that is typical for Bragg fibers [8, 9]. This is as expected by the designer(s) of this structure, since the structure is a Bragg fiber if we simply neglect the existence of the thin bridges. The value of the calculated confinement loss of the dominant TE_{01}-like mode agrees very well to the measured results in the experiment [33] which is 0.015 dB/cm at λ=1.04μm. It should be noted that since our model has only 2-fold rotational symmetry, all the modes are non-degenerate (see explanation to be given in Section 8.4). Fig. 8.15 shows that the modal fields are very well quasi-confined within the air-core due to the quasi-bandgap effect of the finite alternating solid-air rings in the cladding. Fig. 8.16 shows the mode profiles of the HE_{11}- and TE_{01}-like modes, while their longitudinal component of time averaged Poynting vectors are given in Fig. 8.17. The latter figure visually agrees to the measured nearfield intensity pattern given in the paper of Vienne *et al.* [33].

Table 8.3. *The computational results of the first-six modes of the air-silica Bragg fiber.*

Mode	Present FEM scheme (17638 triangular elements)		
	Re(n_{eff})	-Im(n_{eff})	Attenuation (dB/cm)
HE_{11}^{a}-like	0.99915	2.43E-6	1.25
HE_{11}^{b}-like	0.99915	8.52E-7	0.44
TE_{01}-like	0.99791	2.96E-8	0.015
HE_{21}^{b}-like	0.99785	2.78E-7	0.14
HE_{21}^{a}-like	0.99785	4.52E-7	0.23
TM_{01}-like	0.99776	8.24E-8	0.042

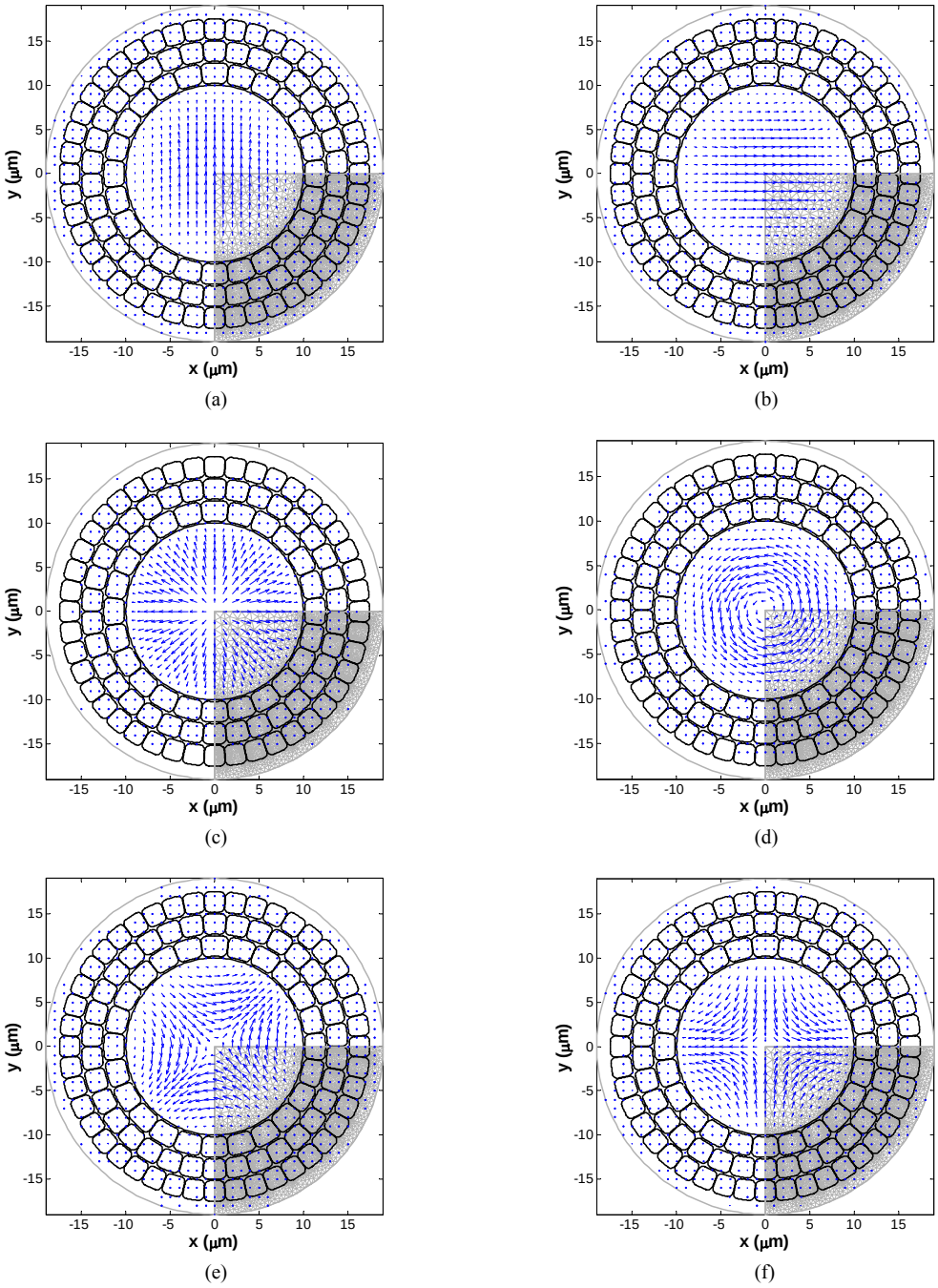

Figure 8.15. *The real part of the transverse magnetic fields of the modes of the air-silica Bragg fiber: (a) HE_{11}^{a}-, (b) HE_{11}^{b}-, (c) TE_{01}-, (d) TM_{01}-, (e) HE_{21}^{a}-, and (f) HE_{21}^{b}-like modes.*

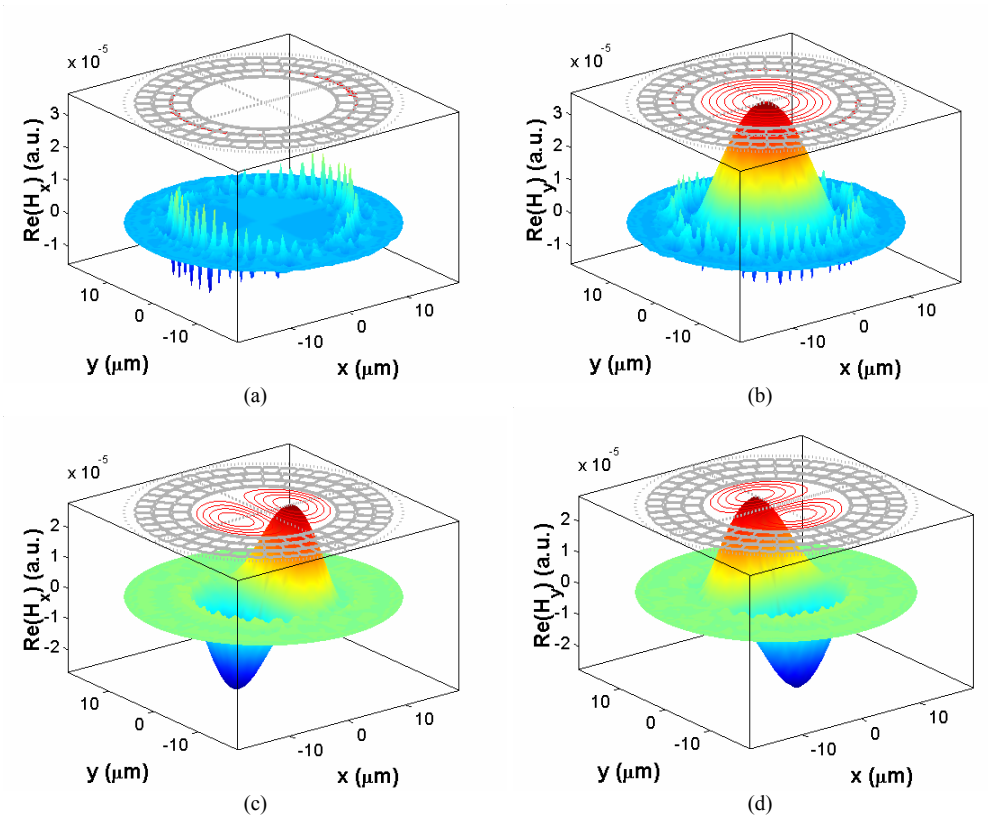

Figure 8.16. *The real part of the field profiles of (a) & (b) the HE_{11}^{a} -like and (c) & (d) the TE_{01} -like modes of the air-silica Bragg fiber.*

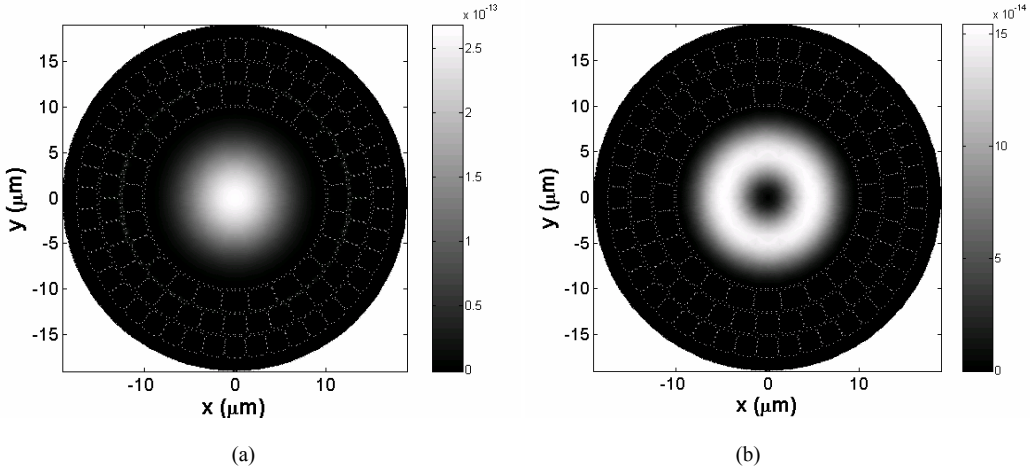

Figure 8.17. *The longitudinal component of the time averaged Poynting vector of (a) the HE_{11}^{a} - and (b) the TE_{01} -like modes of the air-silica Bragg fiber.*

The profile of the HE_{11}-like mode shows the existence of bright resonance spots at the cladding layers that were also observed in the nearfield patterns measured in the experiments of Vienne *et al*. These spots indicate the onset of anti-crossing with the cladding resonance mode. Such modes are also observed in the solid-core PCF with small air holes (see Section 8.5). For air-core PBF, since the effective indices of interest are below 1, the transverse wavenumber $k_t = k_0\sqrt{n_{\text{Solid}}^2 - n_{\text{eff}}^2}$ is rather large, which enables resonances to take place even in thin solid material. This is why recent design of air-core PBFs which exhibit low loss [35], employs very thin solid material to form the 2-D photonic crystal of the cladding, i.e. to suppress the possibility to have anti-crossing with such cladding resonance modes. Fig. 8.18 shows modal fields of such a mode. Besides this mode, we also observed the existence of cladding resonance modes with main field component residing at the solid material near to the core. Such modes are often referred to as surface modes in the literature [34].

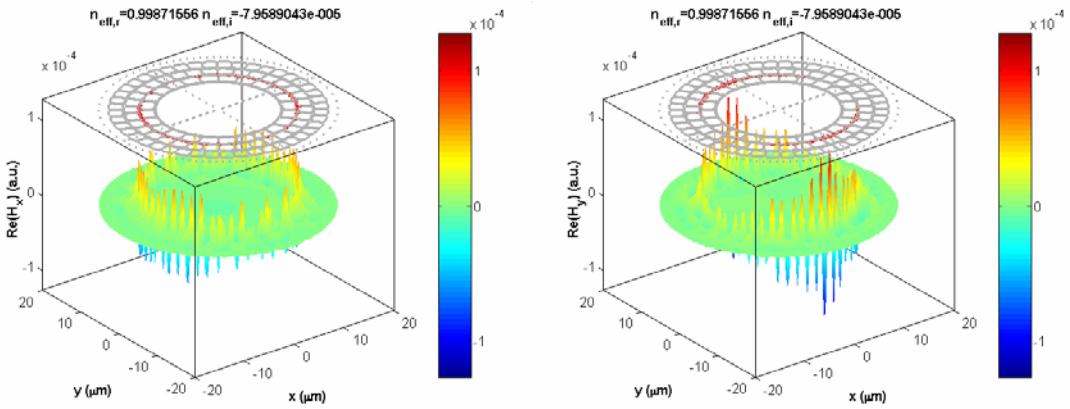

(a) (b)

Figure 8.18. *The real part of (a). H_x and (b). H_y of a cladding resonance mode with Re(n_{eff}) nearby HE_{11}-like modes.*

The employment of silica enables the use of tools/techniques inherited from ordinary optical fiber technology, like the use of connector, splicing with other fibers, tapering, etc. Hence, this air-silica Bragg fiber might be an interesting alternative to conventional air-core Bragg fibers [8].

8.4. Structure symmetry and mode degeneracy in photonic crystal fibers

Mode degeneracy in PCF has attracted several theoretical and computational investigations [13, 24-25, 36-37]. Based on their numerical results, Ferrando *et al.* [36] explicitly said that the two HE_{11}-like modes (e.g. HE_{11}^a - and HE_{11}^b-like in Fig. 8.2) of a

PCF with six-fold symmetry have slightly different propagation constants, meaning that they are only nearly degenerate, hence they are non-degenerate modes. Steel *et al.* [37] using group theoretical arguments as given by McIsaac [38], field rotation and inner product, and multipole method, proved that these modes are degenerate. Koshiba and Saitoh [25] used a mesh refinement in the FEM mode solver to numerically prove that these modes are degenerate. The mode degeneracy and non-degeneracy of this type of PCFs are later on tabulated in several papers [13, 24]. However, it is not easy to understand the arguments on mode degeneracy and their relation to structure symmetry given in these papers. Simple procedure is required such that one can easily evaluate the mode degeneracy of any structure (not only the 6-fold symmetry structure) just by visual inspection on the modal field profile, without any requirement to know group theory or carrying out extra computations. Here, we present arguments that lead to a simple procedure to recognize the degeneracy/non-degeneracy of computed modes based on their field profiles. In the light of this simple procedure, the degeneracy/non-degeneracy of modes discussed in Section 8.2-8.3 and in the previous chapter, can be understood easily.

The result of a symmetry operation (i.e. operation like rotation and reflection, which when acting on a structure, will leave the structure unchanged) on a modal field can be expressed as a linear combination of modal fields of all degenerate modes, including the original mode itself, i.e.

$$\mathbb{S}\vec{\Psi}_k = \sum_{i=1}^{p} a_i \vec{\Psi}_i \tag{8.3}$$

where $\mathbb{S}$ is such symmetry operation, $\left\{\vec{\Psi}_1..\vec{\Psi}_p\right\}$ are degenerate modes with $\vec{\Psi}_k \in \left\{\vec{\Psi}_1..\vec{\Psi}_p\right\}$, p>1 for degenerate modes and p=1 for non-degenerate mode. Eq. (8.3) comes from the fact that $\mathbb{S}$ has to commute with the eigenvalue operator of the problem. From eq. (8.3), it follows that if the result of all possible symmetry operations on a modal field can not be reconstructed by just scaling of the original modal field itself, then the mode should be degenerate. It also means that for 2-fold degenerate modes, we can reconstruct one modal field with the linear combination of two intermediate modal fields obtained by different symmetry operations on the other modal field of the degenerate pair, provided that these two intermediate modal fields are not linearly dependent. Note that this consequence holds also in the case that one of these symmetry operations is just the identity operation. Hence, by just looking at the possibility to reconstruct one modal field from fields derived from its pair (see e.g. Fig. 8.2), one can recognize the degeneracy/non-degeneracy of modes. This procedure is simple, and can be carried out quickly just by visual inspection. Note that accidental degeneracy is beyond the discussion given above.

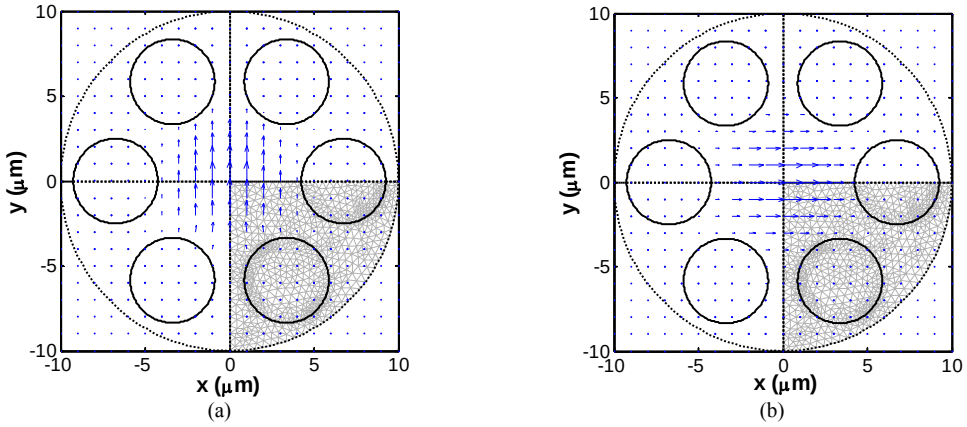

Figure 8.19. *(a).* $\vec{\Psi}_1$ *and (b).* $\vec{\Psi}_2$ *which are* $\hat{x}H_x + \hat{y}H_y$ *of* HE_{11}^a*- and* HE_{11}^b*-like modes of the 6-hole PCF, respectively.*

To illustrate the procedure, we will take the PCF as shown in Fig. 8.1a and show the degeneracy of its HE_{11}-like modes by showing that HE_{11}^b-like modal field can be reconstructed by linear combination of two modal fields obtained by different rotational symmetry operations on HE_{11}^a-like modal fields. Assume that $\vec{\Psi}_1$ (as shown by Fig. 8.19a) is the modal field of HE_{11}^a-like mode of the structure. Since the structure has six-fold rotational symmetry, rotation of the modal field by $2\pi m/6$ radiant with integer m, is a symmetry operation. Assume that $\vec{\Psi}_{1,(2\pi/6)}$ and $\vec{\Psi}_{1,2(2\pi/6)}$ as shown in Fig. 8.20 are the rotated $\vec{\Psi}_1$ with rotation of $2\pi/6$ radiant (i.e. m=1) and $2(2\pi/6)$ radiant (i.e. m=2) clockwise, respectively. Fig. 8.21 shows $\vec{\Psi}_3 = \left(\vec{\Psi}_{1,(2\pi/6)} + \vec{\Psi}_{1,2(2\pi/6)}\right)$ which is obtained by linear combination of $\vec{\Psi}_{1,(2\pi/6)}$ and $\vec{\Psi}_{1,2(2\pi/6)}$ with scaling constant a and b equal to 1. Visual inspection of Fig. 8.21 and 8.19b (where $\vec{\Psi}_2$ is the modal field of the HE_{11}^b-like mode) shows that $\vec{\Psi}_2$ and $\vec{\Psi}_3$ are linearly dependent, meaning that we can reconstruct $\vec{\Psi}_2$ by linear combination of $\vec{\Psi}_{1,(2\pi/6)}$ and $\vec{\Psi}_{1,2(2\pi/6)}$. Hence, we can understand that HE_{11}^a- and HE_{11}^b-like modes are degenerate.

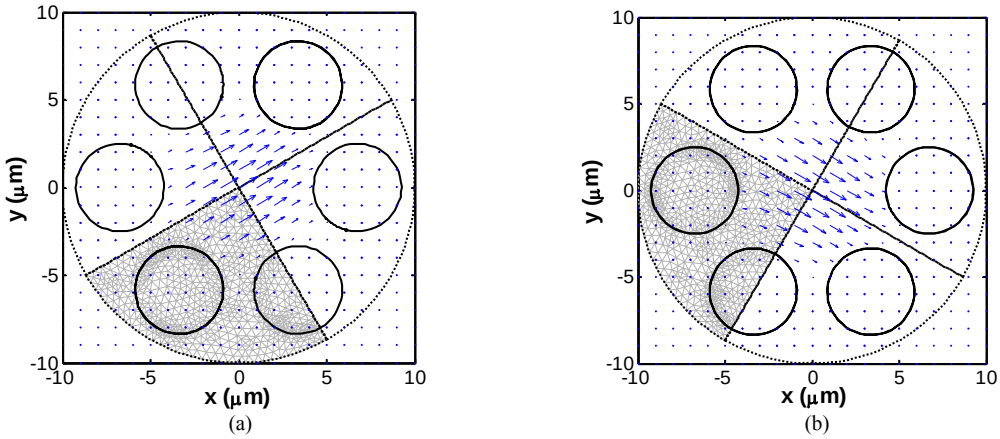

Figure 8.20. *(a).* $\vec{\Psi}_{1,(2\pi/6)}$ *and (b).* $\vec{\Psi}_{1,2(2\pi/6)}$*, which are* $\hat{x}H_x + \hat{y}H_y$ *of the rotated* $\vec{\Psi}_1$ *with rotation angle of (2π/6) and 2(2π/6) radiant clockwise, respectively.*

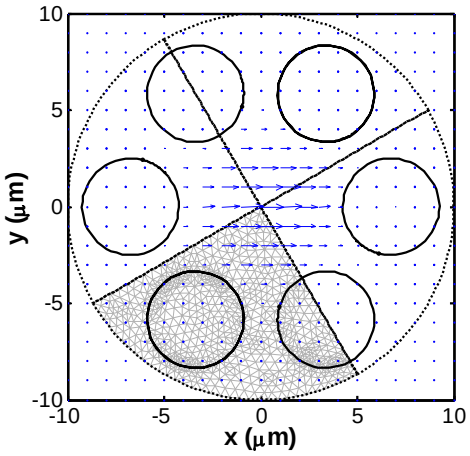

Figure 8.21. $\vec{\Psi}_3 = \left(\vec{\Psi}_{1,(2\pi/6)} + \vec{\Psi}_{1,2(2\pi/6)}\right)$ *obtained by linear combination of* $\vec{\Psi}_{1,(2\pi/6)}$ *and* $\vec{\Psi}_{1,2(2\pi/6)}$.

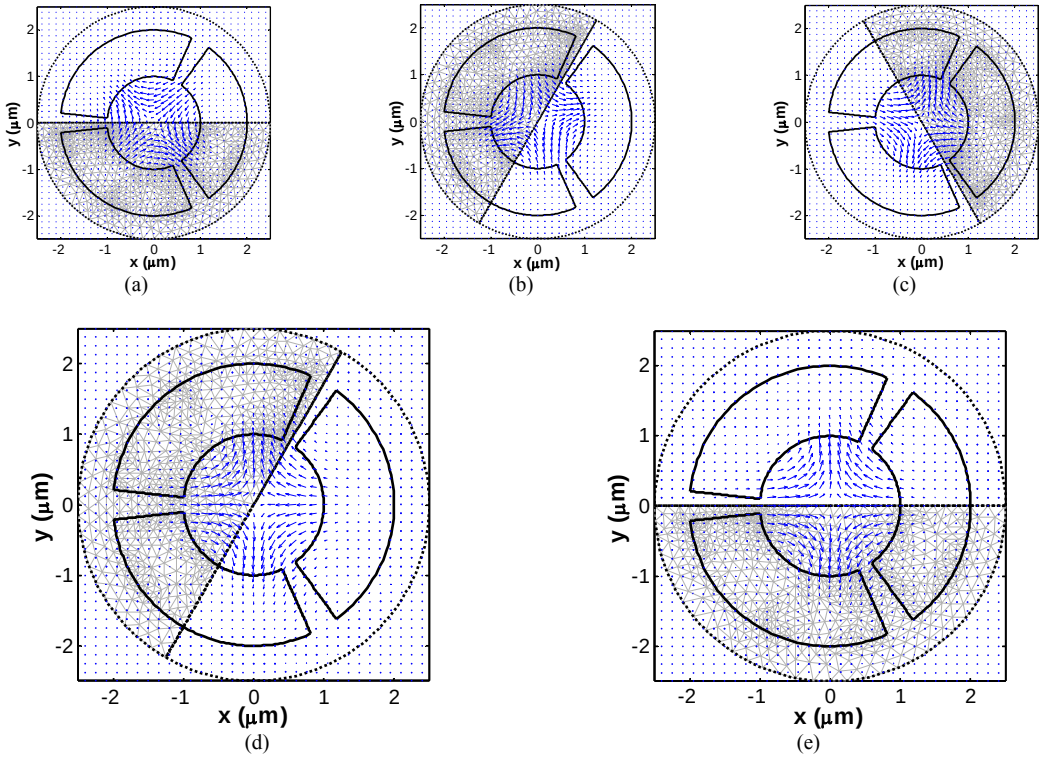

Figure 8.22. *(a).* $\vec{\Psi}_1$ *(corresponding to* HE_{21}^a*-like mode), (b).* $\vec{\Psi}_{1,(2\pi/3)}$*, (c).* $\vec{\Psi}_{1,2(2\pi/3)}$*, (d).* $\vec{\Psi}_3 = \left(-\vec{\Psi}_{1,(2\pi/3)} + \vec{\Psi}_{1,2(2\pi/3)}\right)$ *and (e).* $\vec{\Psi}_2$ *(corresponding to* HE_{21}^b*-like mode) of the PCF with 3 annular-sector shaped holes.*

The same procedure can be generalized to other (higher-order) modes and other structures as well. Fig. 8.22 shows how that applied to show the degeneracy of HE_{21}^a- and HE_{21}^b-like modes of the PCF with 3 annular-sector shaped holes discussed in Section 8.2.2. Similarly, the non-degeneracy of HE_{31}^a-like (Fig. 8.2g) and HE_{31}^b-like (Fig. 8.2h) modes of PCF with six-fold symmetry can be understood as there is no way to reconstruct field shown in Fig. 8.2h by linear combination of symmetry-operated versions of field shown in Fig. 8.2g, or vice versa. Note that this situation does not happen in ordinary fiber case (see Section 7.3.1 in the previous chapter). Since the fiber has $C_{\infty v}$ symmetry, rotation by any angle is symmetry operation. By just rotating the field of HE_{31}^a, we can reconstruct the field of HE_{31}^b modes, and vice versa, hence these modes are degenerate in ordinary optical fiber.

8.5. Modes of an endlessly single mode photonic crystal fiber

One of the attractive properties of the PCFs is their possibility to be single-moded over a wide wavelength range, surpassing the ordinary single-mode fibers which become multi-moded for wavelength below their single-mode cut-off wavelength. PCFs, which are specially designed with this property are called endlessly single-mode (ESM-) PCFs [7]. A simple model used to study the PCF is effective index model, where the high index core surrounded by the lower effective index of the cladding due to the presence of the periodic holes, guides light by a so-called modified total internal reflection mechanism [2]. In the case of cladding with small air-filling-fraction, one will get a low index-contrast equivalent waveguide, which is required for single-mode operation. At shorter wavelengths, the effective index of the cladding will get closer to the refractive index of the silica. This dispersive property will somehow compensate the decrease of the wavelength and keep the single-mode behavior over a wide wavelength range.

However, the practical PCFs have a limited size of the holey cladding, embedded within a large area of uniform outer cladding, leading to a structure with inherent confinement losses. With the growing of interests in investigating both the dispersion and the confinement losses of the PCFs, a leaky-wave model has been proposed as a more rigorous model for the PCFs [6]. Among the large number of leaky modes, the single-modeness of an ESM-PCF is attributed to the loss discrimination between the dominant mode and other modes. Several papers have been published on the criterion of the endlessly single-modeness of the ESM-PCF. Such criteria can be based on the sensitivity of the imaginary part of the mode indices of the higher-order modes to the changes of the structural parameters [39], or the confinement of the field within the core area [40]. These criteria lead to a relatively small cladding air filling fraction as a requisite for the ESM operation. As small air filling fraction will lead to a high confinement loss, the design of a commercial ESM-PCF will apparently face a trade-off between the endlessly single-modeness and the confinement loss. In this section, we will compute the modes of a commercial ESM-PCF and study its single-modeness. We will use the loss discrimination as the single-modeness criterion. As the confinement losses are a function of the fiber length, the latter quantity will play an important role in the single-modeness of the ESM-PCF.

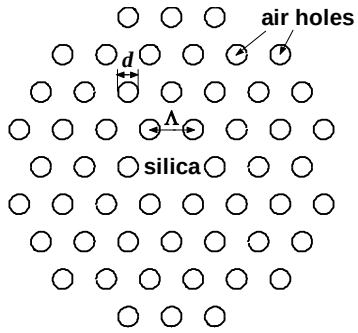

Figure 8.23. *The structure of ESM-12-01.*

We consider the ESM-12-01 fiber made by BlazePhotonics [41] as our sample. This commercial PCF is claimed to be endlessly single-mode and suitable for short wavelength applications by the factory. The structure of the fiber is depicted in Fig. 8.23, with d=3.68μm and Λ=8μm. For our computations, the refractive index of the undoped silica as the host material has been taken from the Sellmeier's equation (8.1), while the refractive index of the air holes is assumed to be unity within the wavelength region of interest.

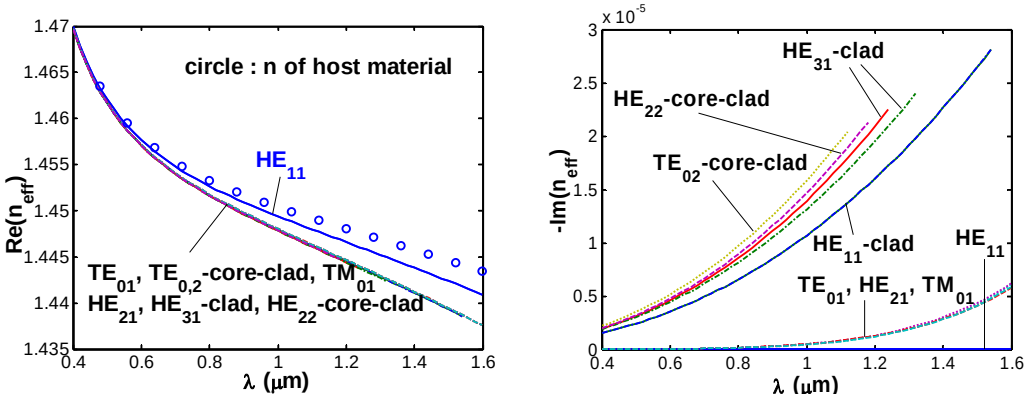

(a) (b)

Figure 8.24. *The calculated (a). real and (b). imaginary parts of the effective indices of the first-few modes of the ESM-PCF. In (b), the curve for HE_{11}-like mode almost coincides with the horizontal axis.*

The first-few modes of the considered PCF with attenuation constant of smaller than 10 dB/cm were calculated using the FEM mode solver reported in the previous chapter, for wavelength spanning from 0.4μm to 1.6μm. Within this calculation, the material loss is not taken into account. The real and imaginary parts of

the mode effective indices are shown in Fig. 8.24, while the dispersion parameters and the attenuation constants are depicted in Fig. 8.25.

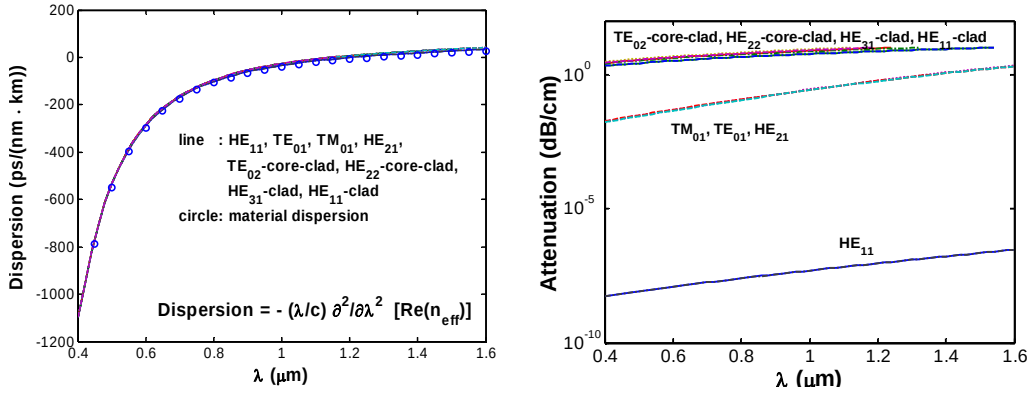

(a) (b)

Figure 8.25. *The calculated (a). dispersion parameter and (b). attenuation constant of first-few modes of the ESM-PCF. The curves in (a) almost coincide, indicating the weak waveguide dispersion.*

Fig. 8.24a shows that the real part of the effective index of the fundamental HE_{11}-like mode is well separated from other modes, indicating the single-mode behavior, which is stronger for longer wavelengths. Fig. 8.25a shows that the dispersion properties of those modes are dominated by the material dispersion of the bulk silica as the air holes effect is weak due to the small d/Λ ratio. However, looking at the loss properties of the modes (Fig. 8.24b and 8.25b), we notice the existence of 3 groups of modes. The first group contains only the fundamental HE_{11}-like mode which has very low loss. The second one consists of the higher order core modes associated with LP_{11}-like scalar mode, i.e. TE_{01}-, TM_{01}-, and HE_{21}-like modes. Since the d/Λ is small, the equivalent waveguide is a low-index-contrast one, hence the vectorial character of the modes is less pronounced as indicated by the very similar loss properties of these 3 modes. The last group of modes has an unusual field distribution. These are the cladding-resonance and the core-cladding-resonance modes as depicted in Fig. 8.26. Their existence can be understood by viewing the holey section of the cladding (including the core) as a defect in the uniform cladding background, hence forming a resonance center. For PCFs with large d/Λ, the complex-valued n_{eff} of these resonance modes are far apart from that of the modes of interest, hence seldom observed both computationally and experimentally. Since they are less quasi-confined than the core modes, they are leakier.

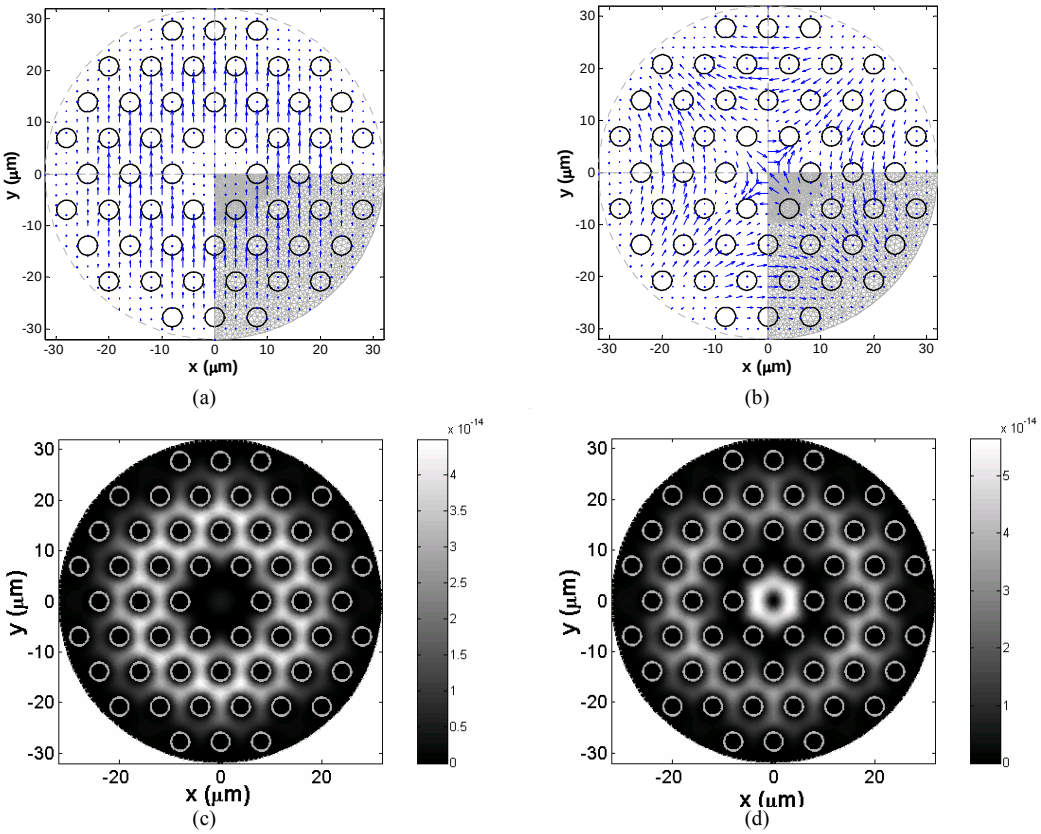

Figure 8.26. *The transverse component of the magnetic field of (a). the HE_{11}-like cladding-resonance and (b). the HE_{22}-like core-cladding-resonance modes and (c) & (d) the longitudinal component of their time-averaged Poynting vectors as calculated at λ=1μm.*

The single-modeness of the ESM-PCF can be evaluated by comparing the difference in confinement losses between the dominant mode and the nearest higher order modes. We define a quantity called multi-mode rejection ratio (MMRR) as a measure of the single-modeness as follows.

$$MMRR = 10\log\left(P_0/P_1\right) = \left(\alpha_1 - \alpha_0\right)L \tag{8.4}$$

with P_0 and P_1 denoting the power of the dominant fundamental and the nearest higher-order mode (which are assumed to be equally excited), while α_0, α_1, and L denoting the attenuation constant of the dominant mode, the nearest higher-order mode, and the length of the fiber, respectively. By putting 20dB as the minimum MMRR (meaning that the power of the fundamental mode is at least 100 times larger than the nearest higher order mode) as the single-modeness criterion, we get the minimum length of the fiber for single mode operation are 11.97m, 3.86m, and 0.78m for wavelength of 0.4μm, 0.6328μm, and 1μm, respectively, as shown in Fig. 8.27. Allowing the power

of the fundamental mode to be just at least 10 times the nearest higher order mode, the minimum length is just half of those of the previous criterion. Hence, although this fiber geometry does not fulfill the ESM criterion of Mortensen *et al*. [40], it still can be regarded as ESM-PCF for long fiber-length applications. While, for short fiber-length applications (e.g. if one thinks of gas/liquid sensing applications), especially for short wavelength region, the endlessly single-modeness should be considered with some precaution. Although the attenuation of the fundamental mode is 6 orders lower (in dB scale) than the nearest higher order modes, the low attenuation of these higher order modes can make them to be quite significant for these particular applications. This suggests the requirement of ESM-PCF which is specially designed for short fiber-length applications. As these applications can tolerate higher attenuation, the use of smaller d/Λ and less rings of air holes can be incorporated. Otherwise, some manner to strip off higher order modes might be required.

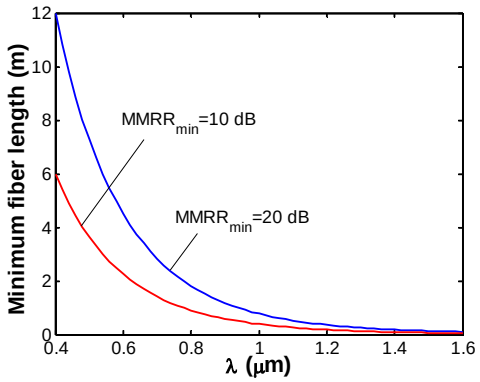

Figure 8.27. *Minimum fiber length for single-mode operation by the loss discrimination criterion for minimum MMRR of 10 and 20 dB.*

8.6. Conclusion

A finite-element-based vectorial optical mode solver furnished with a 1st-order BGT-like TBC reported in the previous chapter was applied to study the PCF. The boundary conditions allow the calculation of both the real and imaginary part of the modal indices in a relatively small computational domain. Both solid- and air-core structures with either circular or non-circular holes were rigorously analyzed. The computed results agree with the results obtained using other methods or experiments. The modes of a commercial ESM-PCF were investigated using a finite-element-based vectorial mode solver. Based on the loss discrimination, the single-modeness of the PCF were verified, which suggests that ESM-PCF for short and long fiber-length applications should be designed differently.

Acknowledgements

We greatly acknowledge the help of N.A. Issa from Univ. Sidney for providing his FDM-ABC results.

References

1. J.C. Knight, T.A. Birks, P.S.J. Russell, and D.M. Atkin, "All-silica single-mode optical fiber with photonic crystal cladding," **Optics Lett.**, Vol. 21, No. 19, pp. 1547-1549, 1996.
2. P. Russell, "Photonic Crystal Fibers," **Science**, Vol. 299, No. 5605, pp. 358-362, 2003.
3. Y. Fink *et al.*, "Guiding optical light in air using an all-dielectric structure," **J. Lightwave Technol.**, Vol. 17, No. 11, pp. 2039-2041, 1999.
4. A. Ferrando, E. Silvestre, J.J. Miret, and P. Andres, "Nearly zero ultraflattened dispersion in photonic crystal fibers," **Optics Lett.**, Vol. 25, No. 11, pp. 790-792, 2000.
5. J.C. Knight *et al.*, "Anomalous dispersion in photonic crystal fiber," **Photonics Technol. Lett.**, Vol. 12, No. 7, pp. 807-809, 2000.
6. T.P. White *et al.*, "Confinement losses in microstructured optical fibers," **Optics Lett.**, Vol. 26, No. 21, pp. 1660-1662, 2001.
7. T.A. Birks, J.C. Knight, and P.S.J. Russell, "Endlessly single-mode photonic crystal fiber," **Optics Lett.**, Vol. 22, No. 13, pp. 961-963, 1997.
8. S.G. Johnson *et al.*, "Low-loss asymptotically single-mode propagation in large-core OmniGuide fibers," **Optics Express**, Vol. 9, No. 13, pp. 748-779, 2001.
9. I.M. Basset and A. Argyros, "Elimination of polarization degeneracy in round waveguides," **Optics Express**, Vol. 10, No. 23, pp. 1342-1346, 2002.
10. A. Argyros, N. Issa, I. Basset, and M. van Eijkelenborg, "Microstructured optical fiber for single-polarization air guidance," **Optics Lett.**, Vol. 29, No. 1, pp. 20-22, 2004.
11. A. Ferrando *et al.*, "Full-vector analysis of a realistic photonic crystal fiber," **Optics Lett.**, Vol. 24, No. 5, pp. 276-278, 1999.
12. W. Zhi, R. Guobin, L. Shuqin, and J. Shuisheng, "Supercell lattice method for photonic crystal fibers," **Optics Express**, Vol. 11, No. 9, pp. 980-991, 2003.
13. T.P. White *et al.*, "Multipole method for microstructured optical fibers. I. Formulation," **J. Opt. Soc. Am. B**, Vol. 19, No. 10, pp. 2322-2330, 2002.
14. N.A. Issa and L. Poladian, "Vector wave expansion method for leaky modes of microstructured optical fibers," **J. Lightwave Technol.**, Vol. 21, No. 4, pp. 1005-1012, 2003.
15. F. Fogli *et al.*, "Full vectorial BPM modeling of index-guiding photonic crystal fibers and couplers," **Optics Express**, Vol. 10, No. 1, pp. 54-59, 2002.

16. K. Saitoh and M. Koshiba, "Full-vectorial imaginary-distance beam propagation method based on a finite element scheme: application to photonic crystal fibers," **J. Quantum Electron.**, Vol. 38, No. 7, pp. 927-933, 2002.

17. C.P. Yu and H.C. Chang, "Applications of the finite difference mode solution method to photonic crystal structures," **Opt. Quantum Electron.**, Vol. 36, No. 1-3, pp. 145-163, 2004.

18. C.P. Yu and H.C. Chang, "Yee-mesh-based finite difference eigenmode solver with PML absorbing boundary conditions for optical waveguides and photonic crystal fibers," **Optics Express**, Vol. 12, No. 25, pp. 6165-6177, 2004.

19. F. Brechet, J. Marcou, D. Pagnoux, and P. Roy, "Complete analysis of the characteristics of propagation into photonic crystal fibers by finite element method," **Optical Fiber Technol.**, Vol. 6, No. 2, pp. 181-191, 2000.

20. A. Cucinotta, S. Selleri, L. Vincetti, and M. Zoboli, "Holey fiber analysis through the finite element method," **Photonics Tech. Lett.**, Vol. 14, No. 11, pp. 1530-1532, 2002.

21. M. Koshiba, "Full-vector analysis of photonic crystal fibers using the finite element method," **IEICE Trans. Electron.**, Vol. E85-C, No. 4, pp. 881-888, 2002.

22. D. Ferrarini *et al.*, "Leakage properties of photonic crystal fibers," **Optics Express**, Vol. 10, pp. 1314-1319, 2002.

23. K. Saitoh and M. Koshiba, "Leakage loss and group velocity dispersion in air-core photonic bandgap fibers," **Optics Express**, Vol. 11, No. 23, pp. 3100-3109, 2003.

24. R. Guobin, W. Zhi, L. Shuqin, and J. Shuisheng, "Mode classification and degeneracy in photonic crystal fibers," **Optics Express**, Vol. 11, No. 11, pp. 1310-1321, 2003.

25. M. Koshiba and K. Saitoh, "Numerical verification of degeneracy in hexagonal photonic crystal fibers," **Photonics Technol. Lett.**, Vol. 13, No. 12, pp. 1313-1315, 2001.

26. I.H. Malitson, "Interspecimen comparison of the refractive index of fused silica," **J. Opt. Soc. Am.**, Vol. 55, pp. 1205-1209, 1965.

27. L. Poladian, N.A. Issa, and T.M. Monro, "Fourier decomposition algorithm for leaky modes of fibres with arbitrary geometry," **Optics Express**, Vol. 10, No. 10, pp. 449-454, 2002.

28. T.M. Monro D.J. Richardson, N.G.R. Broderick, and P.J. Bennett, "Modeling large air fraction holey optical fibers," **J. Lightwave Technol.**, Vol. 18, No. 1, pp. 50-56, 2000.

29. T. Hasegawa *et al.*, "Hole-assisted lightguide fiber for large anomalous dispersion and low optical loss," **Optics Express**, Vol. 9, No. 13, pp. 681-686, 2001.

30. K. Thyagarajan *et al.*, "A novel design of a dispersion compensating fiber," **Photonics Technol. Lett.**, Vol. 8, No. 11, pp. 1510-1512, 1996.

31. M.Yan, P. Shum, and C. Lu, "Hole-assisted multiring fiber with low dispersion around 1550nm," **Photonics Technol. Lett.**, Vol. 16, No. 1, pp. 123-125, 2004.

32. M. Born and E. Wolf, *Principles of Optics*, 6th Edition, Pergamon Press, Oxford, 1993.

33. G. Vienne *et al.*, "First demonstration of air-silica Bragg fiber," Post Deadline Paper PDP25, **Optical Fiber Conference 2004**, Los Angeles, 22-27 Feb. 2004.

34. K. Saitoh, N.A. Mortensen, and M. Koshiba, "Air-core photonic band-gap fibers: the impact of surface modes," **Optics Express**, Vol. 12, No. 3, pp. 394-400, 2004.

35. B.J. Mangan *et al.*, "Low loss (1.7 dB/km) hollow core photonic bandgap fiber," Post Deadline paper PDP24, **Optical Fiber Conference 2004**, Los Angeles, 22-27 Feb. 2004.

36. A. Ferrando *et al.*, "Vector description of higher-order modes in photonic crystal fibers," J. Opt. Soc. Am. A., Vol. 17, No. 7, pp. 1333-1340, 2000.

37. M.J. Steel et al., "Symmetry and degeneracy in microstructured optical fibers," **Optics Lett.**, Vol. 26, No. 8, pp. 488-490, 2001.

38. P.R. McIsaac, "Symmetry-induced modal characteristics of uniform waveguides – I: summary of results," **Trans. Microwave Theory and Tech.**, Vol. MTT-23, No. 5, pp. 421-429, 1975.

39. B.T. Kuhlmey, R.C. McPhedran, and C.M. de Sterke, "Modal cutoff in microstructured optical fibers," **Optics Lett.**, Vol. 27, No. 19, pp. 1684-1686, 2002.

40. N.A. Mortensen *et al.*, "Modal cutoff and the V parameter in photonic crystal fibers," **Optics Lett.**, Vol. 28, No. 20, pp. 1879-1881, 2003.

41. http://www.blazephotonics.com/pdf/ESM%20-%2012%20-%2001.pdf

Chapter 9

Toward low-loss hollow-core integrated optical waveguides: the material composition aspects

The role of cladding bilayer material compositions to obtain low-loss hollow-core integrated optical waveguides was studied. Using the simple Fresnel reflection formula, the optimal material composition was determined. The results show that bilayer with higher index-contrast does not always lead to a lower loss for linearly polarized modes. Based on that knowledge, structures that exhibit very low leakage loss for quasi-TE_{00} mode are proposed and designed using Si-compatible materials. An iterative procedure using a semivectorial effective index method leaky mode solver has been employed in optimizing the bilayer thicknesses.

This chapter is adapted from:
H.P. Uranus, H.J.W.M. Hoekstra, and E. van Groesen, "Considerations on material composition for low-loss hollow-core integrated optical waveguides," (to be submitted for publication).

Toward low-loss hollow-core integrated optical waveguides: the material composition aspects

9.1. Introduction

Recently, hollow-core integrated optical waveguides have attracted the interest of many researchers [1-5]. This kind of structures allows quasi-confinement of light into the hollow-core, hence offers properties like low absorption, low dispersion, low thermal sensitivity, and a high damage threshold. Besides, it allows intense interaction between light and gas or liquid filled into the core on one hand and prospective for integration of various components (not only photonic components, but also micro-fluidic and MEMS components) in a chip scale on the other hand. Hence, it is interesting for applications like sensing, spectroscopy, light-driven biological/chemical processes, or non-linear optics of gas/liquids, as well as telecommunication.

Low leakage loss can easily be obtained in hollow-core waveguides made in slab structures with 1-D confinement [1] and in structures with circular core cross-section for 2-D confinement [6]. This is due to the existence of modes, which maintain the consistency of their polarization and orientation of transverse wavevector at reflector layers stack in such structures, hence eases the optimization of such layers, especially for TE polarization where the reflection is relatively high. Here, consistency means the orientation of such quantities relative to the interface are the same at every layer. These are not the case for integrated optical waveguides, which usually have rectangular cross-sectional shapes. Many experimental work on hollow-core integrated optical waveguides with a 2-D core cross-section have been reported [1-5]. However, most of the reported structures exhibit rather high losses ranging from few dB/cm [4, 5] up to few tens of dB/cm [1, 3], hence they are applicable only for limited number of functionalities. Part of the losses comes from the fabrication imperfection like deviation of the thicknesses of the cladding layers from the design, the existence of unexpected air gap, or scattering due to surface roughness. The other part of the losses indeed comes from the leakage loss of the leaky-wave structure as a consequence of the low-index core. While the first source of losses is determined by the precision of the fabrication technologies, the latter source of losses remain a fundamental issue, which could be improved by better understanding of the theory. Besides, the knowledge on architectures and material compositions, which could enable low leakage loss might suggest the direction of the fabrication technology and material research, and omit many unnecessary trial and error experiments.

In this chapter, we consider integrated optical structures with air forming the rectangular core, a cladding composed of a finite number of periods of bilayer with alternating high/low refractive index materials, and a high index background. We report study on the relevance of the material composition of such layers to the performance of the waveguides using the simple Fresnel reflection formulae. Based on that, we propose material compositions and structures that give low leakage loss. We used the finite element method (FEM) leaky mode solver discussed in Chapter 7 to verify several structures, which were designed based on the knowledge about well performing material compositions. We show structures, which to the best of our knowledge, exhibit leakage loss down to 40 times (on a dB scale) lower than the so-far reported lowest loss hollow-core integrated optical waveguide in the literature.

9.2. The material composition considerations

Besides the anti-resonant condition set by the correct choice of thicknesses of the bilayer and the architecture of the structure, the reflection at interfaces between core/cladding and between cladding layers are of importance to achieve low leakage loss. Since microstructuring for integrated optical waveguides mostly results in a rectangular-like cross-sectional shape, the modes of such structures will be nearly linearly polarized in most cases, except in structures with nearly square cross-sectional shape, where hybrid polarizations could exist. Due to the rectangular shape, it is hard to maintain consistency of the polarization and the orientation of the transverse wavevector at interfaces between cladding and core layers in such structures. For a q-TE mode in a structure with rectangular cross-sectional shape, the light will have TE-like behavior at the horizontal interface, but TM-like behavior at the vertical interface of the layer stack. Hence, it is instructive to look at the reflection of these two polarizations at a planar interface between two materials. Using the Fresnel reflection formulae for light going from material 1 to 2, the reflection of light corresponding to a mode of the waveguide can be written in a simple picture as

$$r_{TE} = \frac{k_{n,1} - k_{n,2}}{k_{n,1} + k_{n,2}} = \frac{\sqrt{n_1^2 - n_{eff}^2} - \sqrt{n_2^2 - n_{eff}^2}}{\sqrt{n_1^2 - n_{eff}^2} + \sqrt{n_2^2 - n_{eff}^2}} \tag{9.1}$$

for TE polarization, and

$$r_{TM} = \frac{n_2^2 k_{n,1} - n_1^2 k_{n,2}}{n_2^2 k_{n,1} + n_1^2 k_{n,2}} = \frac{n_2^2\sqrt{n_1^2 - n_{eff}^2} - n_1^2\sqrt{n_2^2 - n_{eff}^2}}{n_2^2\sqrt{n_1^2 - n_{eff}^2} + n_1^2\sqrt{n_2^2 - n_{eff}^2}} \tag{9.2}$$

for TM polarization, where n_1, n_2, $k_{n,1}$, $k_{n,2}$, and n_{eff} denote the refractive index of material 1 and 2, normal component of wavevector at material 1 and 2, and effective index of the mode, respectively.

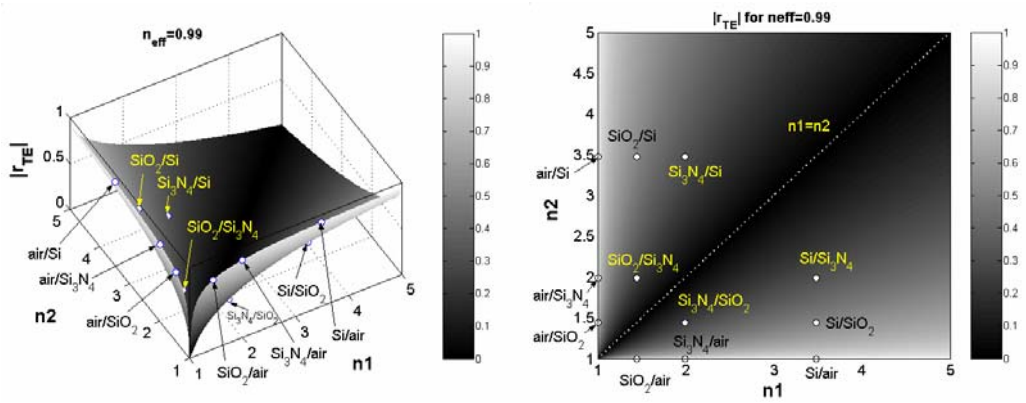

(a) (b)

Figure 9.1. *The absolute value of the reflection coefficient for TE polarization of light associated with n_{eff}=0.99 hitting planar interface between two materials with refractive index ranging from 1 to 5.*

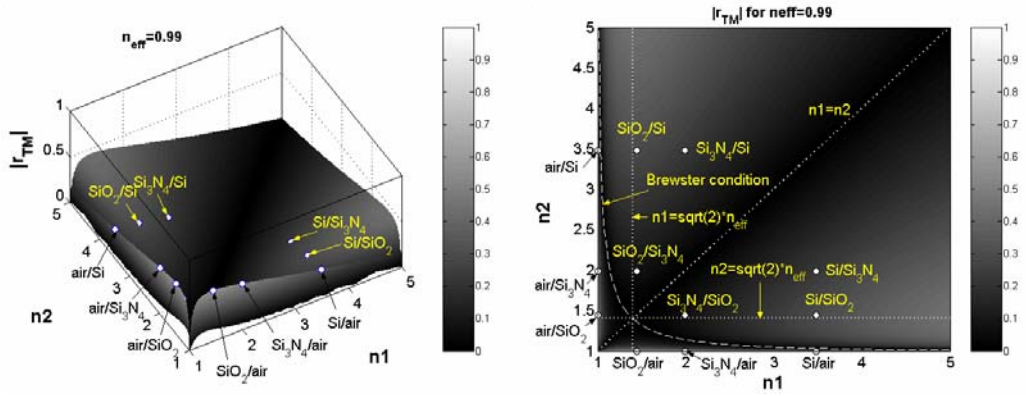

(a) (b)

Figure 9.2. *The absolute value of the reflection coefficient for TM polarization of light associated with n_{eff}=0.99 hitting planar interface between two materials with refractive index ranging from 1 to 5.*

By taking n_{eff}=0.99, which is close to a typical value for the fundamental mode of a hollow-core integrated optical waveguide, we plotted the absolute value of reflection coefficient for n_1 and n_2 ranging from 1 to 5 in Fig. 9.1 and 9.2. Since presently Si seems to be the most interesting substrate to realize such structures due to the availability of the fabrication technologies and the overlap with other disciplines (like micro-electronics, MEMS, and microfluidic), we also highlight some points related to combination of commonly used Si-compatible materials, including air. Fig. 9.1 clearly shows that high reflection coefficient for TE polarization can be achieved by using air at one side and material with as high as possible refractive index at the

other side. Hence, bilayers made up of materials with higher index-contrast are more preferable for this polarization. However, this rule is not valid for TM polarization as shown by Fig. 9.2. The dashed line in this figure denotes the Brewster condition which leads to zero reflection for TM, while the vertical and horizontal dotted lines denote $\partial r_{TM} / \partial n_1 = 0$ and $\partial r_{TM} / \partial n_2 = 0$ conditions, respectively, i.e. the location of the extrema of the curves. Using eq. (9.2), it can be shown that these two lines are corresponding to $n_1 = \sqrt{2} n_{eff}$ and $n_2 = \sqrt{2} n_{eff}$, respectively, which is around 1.4 for n_{eff}=0.99. Note that, this value is relatively close to the refractive index of pure SiO_2 (1.444 at 1.55μm), leading to almost similar reflection curves as shown in Fig. 9.3a. Since the maxima of TM reflection is located at these lines, material with a refractive index as close as possible to $\sqrt{2} n_{eff}$ is preferable to form one part of the bilayer. Considering commonly used Si-compatible materials as shown in Table 9.1, we suggest that air-Si interface is preferable to obtain high TE reflection, while air-SiO_2 is preferable for TM. Considering only all-solid silicon-compatible material composition of bilayer, SiO_2/Si is more beneficial than Si_3N_4/Si or SiO_2/Si_3N_4 for both polarizations. Therefore, to obtain a low loss q-TE mode, Si-air (if the fabrication technology permits) or Si/SiO_2 (if all-solid bilayer has to be used) are preferable for the top and bottom stack of bilayers, while SiO_2/air (if the fabrication technology permits) or Si/SiO_2 (if all-solid bilayer has to be used) for the left and right stack of bilayers. Note that consistent with this argument, the relatively well performing hollow-core integrated optical waveguides with only few dB/cm measured loss [4, 5] reported in the literature, were fabricated using Si/SiO_2 bilayers. It is also worth noting that since air is used as the core, besides the number of bilayer periods, the selection of which material of the bilayer that has direct contact with the core is also relevant for reducing the leakage loss, especially for bilayer with TM-like polarization, where the reflection coefficient is relatively limited. The table also suggests that air/Si bilayer gives the largest discrimination between the reflection coefficient of the two polarizations, hence if the fabrication technology permits, it could be used to obtain low loss (and highly single-moded) for fiber-HE_{21}-like mode, since this mode will have TE-like behavior at both vertical and horizontal core/cladding interfaces. Note that this mode (which is not linearly polarized) is supported by structures with a square cross-sectional shape. However, a vectorial 2-D mode solver, which can address this mode directly, is required to optimize the thicknesses of the bilayer for such mode.

Table 9.1. *The reflection coefficient for various composition of bilayer using Si-compatible materials for light associated with mode with n_{eff}=0.99. The refractive indices are taken from the typical value for λ=1.55μm.*

n_1/n_2		r_{TE}	r_{TM}	$\lvert r_{TE}\rvert$-$\lvert r_{TM}\rvert$
Air/SiO_2	1/1.444	-0.76336	-0.56272	0.20064
Air/Si_3N_4	1/1.99	-0.84891	-0.51102	0.33789
Air/Si	1/3.48	-0.91886	-0.32269	0.59618
SiO_2/Si_3N_4	1.444/1.99	-0.24305	0.072578	0.17047
SiO_2/Si	1.444/3.48	-0.52081	0.29329	0.22751
Si_3N_4/Si	1.99/3.48	-0.31801	0.22552	0.092498

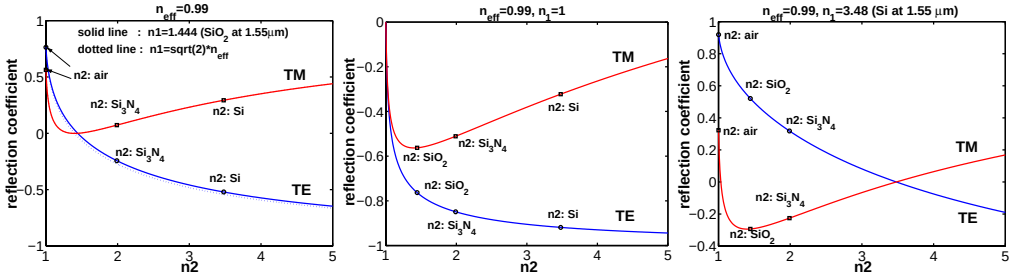

(a) (b) (c)

Figure 9.3. *The reflection coefficient for various n_2 with n_1 fixed at (a). 1.444 and $\sqrt{2}n_{eff}$, (b). 1, and (c). 3.48 for n_{eff}=0.99.*

9.3. ARROW design

By taking into account the material considerations as discussed previously, we propose several low-loss hollow-core integrated optical waveguides. In order to have a good fiber to chip coupling, we consider structures with a square hollow-core of 10μm×10μm size. To ease the fabrication, we consider all-solid top and down bilayers, while allowing the use of air for the left and right bilayers. In order to have low leakage loss for q-TE_{00} mode, we used Si/SiO_2 bilayers (which give moderate TE-like reflection) for top and bottom claddings, and SiO_2/air bilayers (which give high TM-like reflection) for left and right claddings. Si and SiO_2 are the outermost media in vertical and horizontal direction, respectively. One of such structures is shown in Fig. 9.4. We believe that some of such structures (with sufficiently thick vertical walls) could be fabricated with the present technology. The thicknesses of the bilayers have been optimized using an iterative method similar to the one proposed by Kubica [7], but in our case, we have used a semivectorial effective index method (EIM) leaky

mode solver to calculate the leaky q-TE_{00} mode of the structure with 2-D cross-section, and determine the optimized thickness of the anti-resonant layers within each iteration step using

$$d_{i,k} = \frac{\left[2M + 1 + \frac{\left(\phi_{1,i} + \phi_{2,i}\right) \bmod \left(2\pi\right)}{\pi}\right]\lambda}{4\,\mathrm{Re}\left(\sqrt{n_i^2 - n_{eff,k}^2}\right)} \tag{9.3}$$

where $d_{i,k}$ and $n_{eff,k}$, n_i, M, $\phi_{1,i}$ and $\phi_{2,i}$, and λ are the optimized thickness of layer i and calculated effective index at iteration step k, refractive index of layer i, anti-resonant order (M=0,1,…), phase shifts at both interfaces of layer i, and wavelength, respectively. In eq. (9.3) A mod B denotes the remainder after integer division of A over B. The incorporation of phase shifts $\phi_{1,i}$ and $\phi_{2,i}$ is important if their sum is not a multiple of 2π. This could be the case for the layer closest to the core [4], if that layer is composed of SiO_2 for TE-like polarization or Si for TM-like polarization for Si/SiO_2 bilayer as can be verified using Fig. 9.3. In this case, the optimal thickness of this layer is different from similar layer of other bilayers, and the optimal thickness for TE-like is different from TM-like polarization. Note that this fact can be used to get reasonably performing structure with moderate loss for linearly polarized modes [4] or polarization independent devices [1]. Since this phase shift issue is not the case in our structure (which is to be optimized for q-TE_{00} mode) due to the choice of materials, we will end up with the same thickness for the bilayer closest to the core and the other similar bilayers. Note that the top and bottom layer closest to the core, which will be optimized for the anti-resonant condition (hence high reflection) for TE-like polarization, at the same time will be situated at the resonant condition (hence low reflection) for TM-like polarization due to these phase shifts. This fact will help to suppress the q-TM modes.

In order to handle leaky mode in the EIM we have used our 1-D FEM leaky mode solver, which has been discussed in Chapter 5. Note that we have used the approximately calculated mode of 2-D cross-sectional structure leading to a reasonable estimate to n_{eff}, while other authors used only 1-D cross-section structure to determine the optimized layer thickness. Since the EIM is relatively efficient, the optimization process only takes few seconds to converge to $\sum_i \left|d_{i,k} - d_{i,k-1}\right| < 10^{-6}$ nm on an ordinary Pentium-4 desktop computer. Table 9.2 shows the thicknesses of the anti-resonant layers (which has been rounded to nm) and the Re(n_{eff}) of q-TE_{00} mode (according to EIM) of the final iteration round. The attenuation according to EIM is around 0.04dB/cm. Within this optimization, λ=1.55μm has been used, and the refractive index of Si and SiO_2 are taken from their Sellmeier's equation [8], while the refractive index of air is 1.

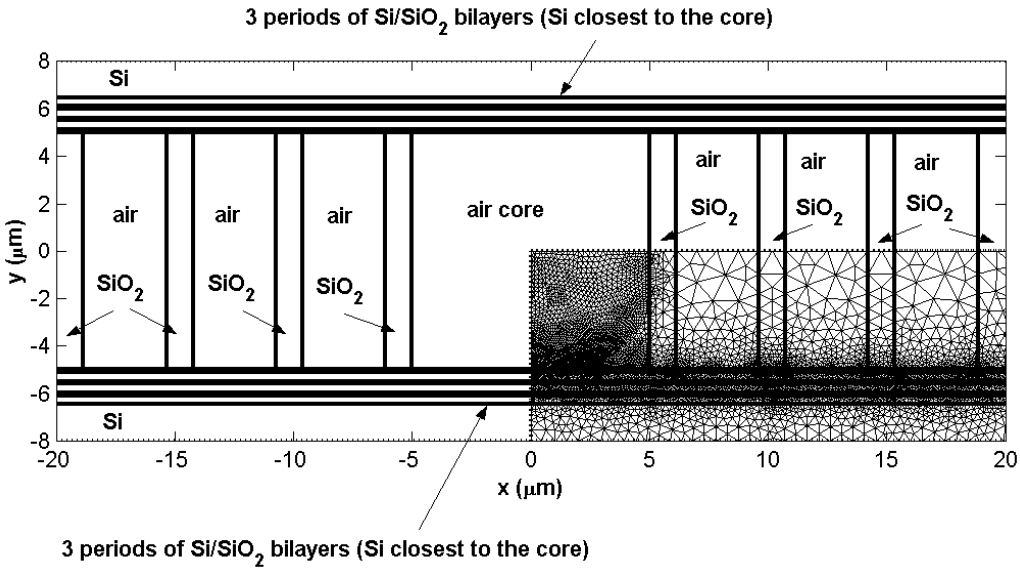

Figure 9.4. *The proposed low leakage loss hollow-core integrated optical structure and the FEM mesh used to verify the design.*

Table 9.2. *The optimized thickness of the anti-resonant bilayers for the proposed structures.*

Structure	Re(n_{eff}) of q-TE_{00} by EIM	Top-bottom bilayers	Left-right bilayers
Waveguide 1	0.993923	3 periods of Si/SiO_2 with M=0 (Si closest to the core) d_{Si}=116nm, d_{SiO2}=370nm	3 periods of SiO_2/air with M=0 d_{SiO2}=370nm, d_{air}=3520nm
Waveguide 2	0.993875	3 periods of Si/SiO_2 with M=0 (Si closest to the core) d_{Si}=116nm, d_{SiO2}=370nm	3 periods of SiO_2/air with M=1 for SiO_2 and M=0 for air d_{SiO2}=1110nm, d_{air}=3506nm
Waveguide 3	0.993779	3 periods of Si/SiO_2 with M=0 (Si closest to the core) d_{Si}=116nm, d_{SiO2}=370nm	3 periods of SiO_2/air with M=2 for SiO_2 and M=0 for air d_{SiO2}=1849nm, d_{air}=3479nm

To verify the proposed structures, we used our FEM vectorial leaky mode solver to compute the modes of the structure. We found that there are 3 dominant modes in such structures, i.e. q-TE_{00}, q-TE_{10}, and q-TE_{01}. Table 9.3 shows the computed effective index of these modes, while Fig. 9.5 shows the real part of the dominant component of the magnetic field of modes of waveguide 1. Since the structures are optimized for q-TE_{00} mode, this mode will have a very low leakage loss as expected. The q-TE_{00} mode of the structure with M=0 in all anti-resonant layers has the lowest loss, which to the best of our knowledge is 40 times (on a dB scale) lower than the loss of the lowest-loss hollow-core integrated optical waveguides reported in the literature. The loss of structure with higher anti-resonant order is higher. This can be understood from eq. (9.3), where the error in estimating the optimal layer thickness is higher for higher M. Waveguide 1 seems to be difficult to be realized, while we believe that waveguide 2 and 3, which have a slightly higher leakage loss, can be realized using present fabrication technology. We understand that our calculated loss still not includes losses due to fabrication imperfections. However, we believe that these results, which show the possibility to get theoretically low loss hollow-core integrated optical waveguides, will seed optimism and will be helpful for the selection of proper materials in these research topics.

Table 9.3. *The computed dominant modes of the proposed structures.*

Structure	q-TE_{00}		q-TE_{10}		q-TE_{01}	
	Re(n_{eff})	Att. (dB/cm)	Re(n_{eff})	Att. (dB/cm)	Re(n_{eff})	Att (dB/cm)
Waveguide 1	0.993924	0.039	0.985419	1.94	0.984815	0.14
Waveguide 2	0.993902	0.08	0.985347	2.01	0.984791	0.24
Waveguide 3	0.993851	0.09	0.985203	2.22	0.984755	14.55

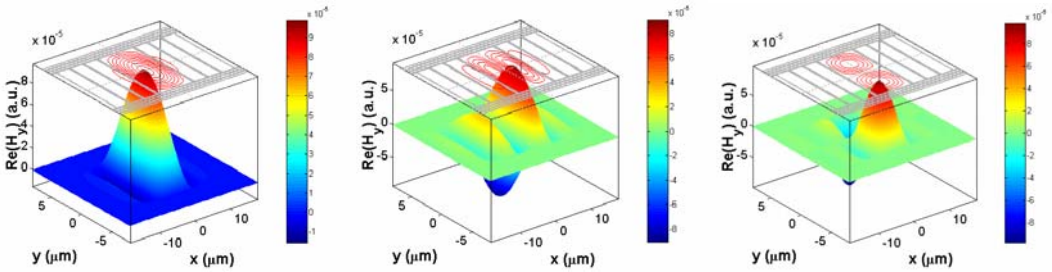

(a) (b) (c)

Figure 9.5. *The real part of the dominant component of the magnetic field for q-TE_{00}, q-TE_{10}, and q-TE_{01} modes of waveguide 1.*

9.4. Conclusions

The role of material composition of the cladding anti-resonant bilayers to achieve low leakage loss for hollow-core integrated optical waveguides was studied. The simple Fresnel reflection formulae for a planar interface between 2 materials have been used to determine the optimal material composition for linearly polarized modes. Based on that knowledge, low-loss hollow-core structures composed of Si-compatible materials were proposed. Iterative procedure was employed using the semivectorial EIM leaky mode solver for optimizing the thicknesses of the anti-resonant bilayers. The optimized structures were verified using the FEM vectorial leaky mode solver.

References

1. T. Miura, F. Koyama, and A. Matsutani, "Modeling and fabrication of hollow optical waveguide for photonic integrated circuits," **Jpn. J. Appl. Phys.**, Vol. 41, No. 7B, pp. 4785-4789, 2002.
2. S. Campopiano *et al.*, "Microfluidic sensor based on integrated optical hollow waveguides," **Opt. Lett.**, Vol. 29, No. 16, pp. 1894-1896, 2004.
3. D. Yin *et al.*, "Integrated ARROW waveguides with hollow cores," **Opt. Express**, Vol. 12, No. 12, pp. 2710-2715, 2004.
4. G.R. Hadley, J.G. Fleming, and S. Lin, "Bragg fiber design for linear polarization," **Opt. Lett.**, Vol. 29, pp. 809-811, 2004.
5. S. Lo, M. Wang, and C. Chen, "Semiconductor hollow optical waveguides formed by omni-directional reflectors," **Opt. Express**, Vol. 12, No. 26, pp. 6589-6593, 2004.
6. S. Johnson *et al.*, "Low-loss asymptotically single-mode propagation in large-core OmniGuide fibers," **Opt. Express**, Vol. 9, No. 13, pp. 748-779, 2001.
7. J.M. Kubica, "A rigorous design method for antiresonant reflecting optical waveguides," **Photon. Technol. Lett.**, Vol. 6, No. 12, pp. 1460-1462, 1994.
8. D.E. Gray (ed), *AIP Handbook*, 3rd ed, McGraw-Hill, New York, 1972.

Summary and Outlook

A large varieties of optical waveguiding structures are used in practice. Conventional guided-wave planar and channel waveguides still play an important role in many applications. However, new structures employing different mechanisms of controlling the propagation of light are emerging. Such structures do not only improve the existing applications, but also open up many new application areas. Interesting properties like widely engineerable group velocity dispersion, single modeness down to short wavelength region with large core, high birefringence but low temperature sensitivity, can be attained by such structures. Moreover, structures that are able to efficiently guide light in a low-index medium, like air or liquid core, which are of importance for some applications, are now available. These advanced structures are becoming hot topics of research. Modeling tools play an important role in the study and development of these structures.

Summary

This thesis reports a series of techniques we have developed for the modal analysis of a large number of optical waveguiding structures, ranging from guided-mode structures with 1-D cross-sections, up to leaky-mode structures with complicated 2-D cross-sections. In general, we considered structures, which are composed of linear, lossless, non-magnetic, anisotropic materials with a diagonal permittivity tensor of either constant or variable index profiles. Numerical schemes and boundary conditions occupy the main part of this thesis. Additionally, for some cases, we also considered analytical techniques, which give more insight and efficiency, but are in general less rigorous for the considered problem. Applying the developed modeling tools to study specific structures is another essential part of this thesis.

We modeled *guided-wave structures with 1-D cross-section* both with the finite difference method (FDM) and the finite element method (FEM). For the FDM, we developed a discretization scheme that takes into account both the smooth index gradient and the sharp index discontinuity at interfaces between different graded-index anisotropic materials. This scheme is suitable for the analysis of planar structures composed of anisotropic materials with complicated index profiles, like titanium-indiffused proton-exchanged $LiNbO_3$ waveguides. For the FEM, we employed the

variational method with transparent boundary conditions (TBCs) using decaying basis functions adopted from the WKB method for the exterior domain, while ordinary 1st-order polynomial basis functions are employed in the interior domain. Using Richardson-like extrapolation, we extended the scheme into a 4th-order accurate one for the discretization of the interior domain, while still using the simple 1st-order polynomial basis functions. We also combined the scheme with the semivectorial (SV-) effective index method (EIM) to analyze indiffused channel waveguides, made by using uniaxial crystals.

For *leaky-wave structures with 1-D cross-section*, we developed a high-order Galerkin FEM scheme furnished with Sommerfeld-like TBCs to calculate the complex-valued mode index and field profiles. Again, using the Richardson-like extrapolation, we present schemes up to 6th-order of accuracy in the computed effective index by only applying the simple 1st-order basis functions. The same scheme can also deal with guided-wave structures as well. Using this scheme, we studied the properties of ARROW structures. Together with a perturbation method, we also applied the scheme to study buffered-leaky waveguides (in the presence of a high-index outermost medium) and pointed out some interesting properties of such structures, e.g. evolution from guided- to leaky- and then back to guided-wave structures again as one varies the refractive index of the 'high-index' medium.

For *leaky- and guided-wave structures with 2-D cross-section*, we developed a vectorial mode solver based on a nodal-based Galerkin FEM with quadratic triangular basis functions. The scheme is furnished with 1st-order Bayliss-Gunzburger-Turkel-like TBCs, which can handle both guided and leaky modes using a relatively small computational domain. Various structures were modeled, including Si_3N_4 strip waveguides with a bulk DAST (4'-dimethylamino-*N*-methyl-4-stilbazolium tosylate) overlaid on top of it, where we noticed the evolution of modes (from q-TM_{00} to q-TE_{10}, and back to q-TM_{00} again, from q-TE_{11} to q-TE_{10}, from guided to leaky and back to guided again) as one varies the gap thickness. By exploiting the capability of the mode solver to handle structures with complicated cross-section geometry, high index-contrast, and complex-valued effective index, we also applied the solver to rigorously study various types of photonic crystal fibers (PCFs), including those with circular or non-circular holes in the cladding, solid or air as the core.

Apart from the developments of the numerical schemes, we would like to highlight some important results of our research that might add to the knowledge of optical waveguiding. The findings on the 'strange' behavior of modes in the buffered-leaky waveguides with respect to the refractive index of the 'high-index' material (Section 6.3.2) and the buffer/gap position (Section 7.3.4) are noteworthy. To the best of our knowledge, these properties have never been reported before; although the

utilization of these knowledge for new applications would need further research. We anticipate that these features might be useful for sensing applications. The discussions on the material composition aspects of anti-resonant bilayer (Chapter 9), although quite simple, are fundamental, and might contribute to knowledge for realization of low-loss hollow-core integrated optical waveguides.

Outlook

Next, we present our view on the need and possible extensions of the mode solver developed in this research and on the emerging field of hollow-core integrated optics.

To our opinion, the developed vectorial mode solver for structure with 2-D cross-sections is very promising and hence requires special attention for future development. The first area of improvement could be the efficiency, since during our work, we did not pay special attention to the optimization of the code, neither for memory nor for time efficiency. New developments, such as the more and more complicated advanced photonic structures proposed by researchers (see e.g. Section 1.3) require such optimization. In particular, this is because of some of these structures employ very thin nanometer-scale features with complicated shapes (see e.g. Fig. 1.3 and 1.4) combined with large core. The occurrence of the very thin features requires a very fine mesh, which in turn will blow up the size of the FEM matrices. We found that for such cases, the computation is rather resource demanding. Even though we have reduced the computational load as much as possible, i.e. we exploited the structure symmetry, which enables us to use only part of the structure in the computations, employed a scheme with only 2 vector components for the vectorial formulation, and reduced the computational domain with the help of the TBCs; the computation of such structures is still a heavy job. Along with the emergence of more complicated structures, there is another reason for revisions. All of our codes were implemented using (interpreter-based) Matlab and executed on an ordinary personal computer. To our opinion, implementing the vectorial mode solver using a more efficient and a more portable (so that it can be run on other platform like a Linux-cluster supercomputer as well) programming language along with the optimization of the algorithm and data structure could be important. But, this might need some efforts since the solver requires supporting tools like a mesh generator and eigenvalue solver, which are very accessible in Matlab. We understand that libraries of similar tools are available in other platforms as well, but efforts might be required to adapt the code to the new interfaces and data structures.

Another area of adaptation of the numerical schemes is to extend it to handle structures with special material properties. In the present code, as described in this thesis, structures are restricted to certain material properties, such as linear, lossless,

non-magnetic, and anisotropic with diagonal permittivity tensor. The extension of the vectorial mode solver to handle other materials will be interesting to be able to tackle a wider range of applications. For instance, we believe that migrating to edge-element FEM is important for tackling certain materials, as this FEM scheme can handle interface conditions transparently, which is important for inclusion of magnetic materials or implementation of an E-field formulation. Anticipating on the emergence of increasingly complicated structure cross-section shapes, the implementation of isoparametric triangular elements might also be interesting.

Finally, we present our view about hollow-core integrated optics. This is one type of structures on which we have spent quite some time and ended up with those reported in Chapter 9. We have strong confidence that this structure is very promising as it allows the intense interaction between light and matter filled into the core of the structure at one hand, and allows integration of various components (not only photonic components, but also micro-fluidic and MEMS components) in a chip scale at the other hand. Hence, it is prospective for applications like sensing, spectroscopy, light-driven biological/chemical process, or non-linear optics of gas/liquid. Both the study and fabrication of this kind of structures are challenging and are not well developed yet. We have found a strategy to reduce the leakage loss and designed structures of hollow-core integrated optics that exhibit confinement loss down to 40 times lower (on a dB scale) than what have ever been reported, to the best of our knowledge, at the moment of the writing of this thesis. However, further research is required to understand this particular structure better, e.g. regarding how to enhance its single-modeness while keeping its low-loss property and convenient mode field size for easy fiber to chip coupling. Besides, development of good optimization tools is important to determine the best structure parameters, which could be realize by the available fabrication technology. This could be another prospective future topic of research.

List of publications

Scientific journals

1. H.P. Uranus, H.J.W.M. Hoekstra, and E. van Groesen, "Analysis of integrated optical waveguides," **J. Indonesian Mathematics Soc.**, Vol. 8, No. 4, pp. 49-62, 2002. ISSN 0854-1380.
2. H.P. Uranus, H.J.W.M. Hoekstra, and E. van Groesen, "Finite difference scheme for planar waveguides with arbitrary index profiles and its implementation for anisotropic waveguides with diagonal permittivity tensor," **Opt. and Quantum Elect.**, Vol. 35, pp. 407-427, Mar-Apr. 2003. ISSN 0306-8919.
3. H.P. Uranus, H.J.W.M. Hoekstra, and E. van Groesen, "Fourth-order variational mode solving for anisotropic planar structures," **J. Nonlinear Opt. Phys. and Materials**, Vol. 12, No. 2, pp. 247-261, 2003. ISSN 0218-8635.
4. H.P. Uranus, H.J.W.M. Hoekstra, and E. van Groesen, "Simple High-order Galerkin Finite Element Scheme for the Investigation of Both Guided and Leaky Modes in Anisotropic Planar Waveguides," **Opt. and Quantum Elect.**, Vol. 36, pp. 239-257, Jan-Peb. 2004. ISSN 0306-8919.
5. H.P. Uranus, H.J.W.M. Hoekstra, and E. van Groesen, "Galerkin finite element scheme with Bayliss-Gunzburger-Turkel-like boundary conditions for vectorial optical mode solver," **J. Nonlinear Opt. Phys. and Materials**, Vol. 13, No. 2, pp. 175-194, June 2004. ISSN 0218-8635.
6. H.P. Uranus and H.J.W.M. Hoekstra, "Modelling of microstructured waveguides using a finite-element-based vectorial mode solver with transparent boundary conditions," **Optics Express**, Vol. 12, No. 12, pp. 2795-2809, 14 June 2004. ISSN 1094-4087.
7. H.P. Uranus, H.J.W.M. Hoekstra, and E. van Groesen, "Numerical investigations of quasi-guiding light in the lower refractive index core layer(s)," **J. Indonesian Mathematics Soc.** (accepted 2005).
8. H.P. Uranus, H.J.W.M. Hoekstra, and E. van Groesen, "Finite element and perturbative study of buffered leaky planar waveguides," (submitted to **Optics Commun.**).

9. H.P. Uranus, H.J.W.M. Hoekstra, and E. van Groesen, “Considerations on material composition for low-loss hollow-core integrated optical waveguides,” (to be submitted for publication).

Conferences

1. H.P. Uranus, H.J.W.M. Hoekstra, and E. van Groesen, “Finite difference scheme for planar waveguides with arbitrary index profiles and its implementation for anisotropic waveguides with diagonal permittivity tensor,” **10th Int. Workshop on Optical Waveguide Theory and Numerical Modelling**, Nottingham, UK, 5-6 April 2002.
2. H.P. Uranus, H.J.W.M. Hoekstra, and E. van Groesen, “Analysis of integrated optical waveguides,” **1st Indonesian Appl. Math. Soc. in the Netherlands (IAMS-N) Seminar**, Enschede, The Netherlands, May 23-24, 2002.
3. H.P. Uranus, H.J.W.M. Hoekstra, and E. van Groesen, “Fourth-order variational mode solving for anisotropic planar structures,” **Int. Symp. On Modern Optics**, Bandung, Indonesia, 3-5 July 2002.
4. H.P. Uranus, H.J.W.M. Hoekstra, and E. van Groesen, “Numerical schemes for modal analysis of optical waveguides with diagonal permittivity,” **The AIO Workshop on Photonic Media**, Ameland, The Netherlands, Sept. 22-27, 2002, (poster).
5. H.P. Uranus, H.J.W.M. Hoekstra, and E. van Groesen, “Galerkin finite element scheme with Bayliss-Gunzburger-Turkel-like boundary conditions for vectorial optical mode solver,” **Conf. Booklet of Int. Symposium in Modern Opt. and Its Applications 2003**, ITB, Bandung, Indonesia, pp. 49, 25-29 August 2003.
6. H.P. Uranus, H.J.W.M. Hoekstra, and E. van Groesen, “Numerical investigations of quasi-guiding light in the lower refractive index core layer(s),” **Seminar Booklet of the 2nd Indonesian Applied Math. Soc. in the Netherlands (IAMS-N) Seminar**, Enschede, The Netherlands, 20 Sept. 2003.
7. H.P. Uranus, H.J.W.M. Hoekstra, and E. van Groesen, "Simple High-order Galerkin Finite Element Scheme for the Investigation of Both Guided and Leaky Modes in Anisotropic Planar Waveguides," **Proc. of 11th Int. Workshop on Optical Waveguide Theory and Numerical Modelling**, Prague, Czech Republic, pp. 106, Apr. 4-5, 2003. ISBN 80-01-02720-1.
8. H.P. Uranus, H.J.W.M. Hoekstra, and E. van Groesen, “Modelling of microstructured waveguides using a finite-element-based vectorial mode solver with transparent boundary conditions,” **Proc. The 12th Int. Workshop on Optical**

waveguide Theory and Numerical Modelling, Univ. Ghent, Ghent, Belgium, pp. 42, 22-23 March 2004. ISBN 90-76-54603-7.

9. H.P. Uranus, H.J.W.M. Hoekstra, and E. van Groesen, "Modes of an endlessly single-mode photonic crystal fiber: a finite element investigation," **Proc. The 9th Annual Symposium IEEE/LEOS Benelux**, Univ. Ghent, Ghent, Belgium, pp. 311-314, 2-3 Dec. 2004. ISBN 9076546061.

For complete list of publications, including those not related to this project, please check http://www.math.utwente.nl/~uranushp/publist.htm.

Appendix 1

Why 1st-order accuracy at interfaces still gives 2nd-order overall accuracy: a perturbative explanation.

This appendix is aimed to explain the statement given in section 3.3.3 of Chapter 3, that a finite difference (FD) scheme with 2nd-order discretization error at most of the grid points but 1st-order error at (few) grid points adjacent to interfaces, will still give a 2nd-order global accuracy in the calculated effective index for a sufficiently large number of total grid points.

After the FD discretization, we will get a matrix eigenvalue equation of the form

$$\left(\mathbf{A}_{\text{num}} - \beta_{\text{num}}^2 \mathbf{I}\right)\{\varphi_{\text{num}}\} = 0 . \tag{A1.1}$$

This matrix eigenvalue equation should be satisfied by any eigenvalue. For the k^{th}-order mode, we get

$$\left(\mathbf{A}_{\text{num}} - \beta_{\text{num,k}}^2 \mathbf{I}\right)\{\varphi_{\text{num,k}}\} = 0 . \tag{A1.2}$$

Assume that we can get the quasi-exact solutions (solutions that are very accurate, e.g. the result of higher order scheme) from

$$\left(\mathbf{A}_{\text{ex}} - \beta_{\text{ex}}^2 \mathbf{I}\right)\{\varphi_{\text{ex}}\} = 0 \tag{A1.3}$$

with $\mathbf{A}_{\text{ex}}$ denotes the matrix of the quasi-exact discretization.

Suppose that the FD discretization will give a truncation error of $O(\Delta x^2)$ at most grid points, but $O(\Delta x)$ at certain (few) fixed number of grid points next to interfaces. Using 1st-order perturbation analysis, we regard the quasi-exact system as the unperturbed system, and the numerical system as the perturbed system. By looking at the k^{th}-order mode solution, we will get

$$\mathbf{A}_{\text{num}} = \mathbf{A}_{\text{ex}} + \delta\mathbf{A}_1 + \delta\mathbf{A}_2 \tag{A1.4}$$

$$\beta_{\text{num,k}}^2 = \beta_{\text{ex,k}}^2 + \delta\beta_{\text{k}}^2 \tag{A1.5}$$

$$\{\varphi_{\text{num,k}}\} = \sum_{\text{m}} a_{\text{m}} \{\varphi_{\text{ex,m}}\} \tag{A1.6}$$

where $\delta\mathbf{A}_1$ corresponds to discretization error of grids located around interfaces which is first-order, and $\delta\mathbf{A}_2$ corresponds to discretization error of other grid points which is second-order. Hence, we can write

$$\delta\mathbf{A}_1 = \Delta x \mathbf{D}_1 \tag{A1.7a}$$

$$\delta \mathbf{A}_2 = \Delta x^2 \mathbf{D}_2 \tag{A1.7b}$$

It should be noted, that for the same structure, $\delta\mathbf{A}_1$ and $\mathbf{D}_1$ have fix number of non-zero entries regardless on how fine the discretization is, because these non-zero entries related to discretization of grid points adjacent to interfaces which are fixed. In eq. (A1.6) we have expanded the k^{th}-order modal field of numerical solution into a linear combination of the quasi-exact eigenvector (modal field). Substituting eqs. (A1.4)-(A1.6) into (A1.2) leads to

$$\left(\mathbf{A}_{\text{ex}} + \delta\mathbf{A}_1 + \delta\mathbf{A}_2\right)\sum_{\text{m}} a_{\text{m}} \left\{\varphi_{\text{ex,m}}\right\} - \left(\beta_{\text{ex,k}}^2 + \delta\beta_{\text{k}}^2\right)\sum_{\text{m}} a_{\text{m}} \left\{\varphi_{\text{ex,m}}\right\} = 0 \tag{A1.8}$$

Taking the inner product of eq. (A1.8) with respect to the quasi-exact eigenvector of the k^{th}-order mode and make use of the orthogonality among modes of the quasi-exact solution leads to

$$\begin{aligned} & a_{\text{k}} \left\langle \left(\mathbf{A}_{\text{ex}} - \beta_{\text{ex,k}}^2\right)\left\{\varphi_{\text{ex,k}}\right\}, \left\{\varphi_{\text{ex,k}}\right\} \right\rangle \\ & \quad + a_{\text{k}} \left[\left\langle \left(\delta\mathbf{A}_1 + \delta\mathbf{A}_2\right)\left\{\varphi_{\text{ex,k}}\right\}, \left\{\varphi_{\text{ex,k}}\right\} \right\rangle - \delta\beta_{\text{k}}^2 \left\langle \left\{\varphi_{\text{ex,k}}\right\}, \left\{\varphi_{\text{ex,k}}\right\} \right\rangle \right] = 0 \,. \end{aligned} \tag{A1.9}$$

Since the k^{th}-order mode of the quasi-exact solution should satisfy eq. (A1.3), the first term in eq. (A1.9) vanishes. Since the numerical eigenvector should be close to the quasi-exact eigenvector of the same order of mode, it follows that $a_{\text{k}} \neq 0$. Therefore, we will get

$$\delta\beta_{\text{k}}^2 = \frac{\left\langle \delta\mathbf{A}_1 \left\{\varphi_{\text{ex,k}}\right\}, \left\{\varphi_{\text{ex,k}}\right\} \right\rangle + \left\langle \delta\mathbf{A}_2 \left\{\varphi_{\text{ex,k}}\right\}, \left\{\varphi_{\text{ex,k}}\right\} \right\rangle}{\left\langle \left\{\varphi_{\text{ex,k}}\right\}, \left\{\varphi_{\text{ex,k}}\right\} \right\rangle} \tag{A1.10}$$

which can be written as

$$\delta\beta_{\text{k}}^2 = \frac{\Delta x \left\langle \mathbf{D}_1 \left\{\varphi_{\text{ex,k}}\right\}, \left\{\varphi_{\text{ex,k}}\right\} \right\rangle + \Delta x^2 \left\langle \mathbf{D}_2 \left\{\varphi_{\text{ex,k}}\right\}, \left\{\varphi_{\text{ex,k}}\right\} \right\rangle}{\left\langle \left\{\varphi_{\text{ex,k}}\right\}, \left\{\varphi_{\text{ex,k}}\right\} \right\rangle} \tag{A1.11}$$

Hence, the order of error will depends on both $\Delta x \left\langle \mathbf{D}_1 \left\{\varphi_{\text{ex,k}}\right\}, \left\{\varphi_{\text{ex,k}}\right\} \right\rangle$ and $\Delta x^2 \left\langle \mathbf{D}_2 \left\{\varphi_{\text{ex,k}}\right\}, \left\{\varphi_{\text{ex,k}}\right\} \right\rangle$. We can rewrite eq. (A1.11) as

$$\delta\beta_{\text{k}}^2 = \Delta x\, c_1\left(N\right) + \Delta x^2 c_2 \tag{A1.12}$$

with

$$c_1\left(N\right) = \frac{\left\langle \mathbf{D}_1 \left\{\varphi_{\text{ex,k}}\right\}, \left\{\varphi_{\text{ex,k}}\right\} \right\rangle}{\left\langle \left\{\varphi_{\text{ex,k}}\right\}, \left\{\varphi_{\text{ex,k}}\right\} \right\rangle} \tag{A1.13a}$$

$$c_2 = \frac{\left\langle \mathbf{D}_2 \left\{\varphi_{\text{ex,k}}\right\}, \left\{\varphi_{\text{ex,k}}\right\} \right\rangle}{\left\langle \left\{\varphi_{\text{ex,k}}\right\}, \left\{\varphi_{\text{ex,k}}\right\} \right\rangle}, \tag{A1.13b}$$

where N denotes the number of grid points (i.e. the number of entries in vector $\left\{\varphi_{\text{ex,k}}\right\}$). If the number of grid points increases, c_1 will decrease because $\left\langle \mathbf{D}_1 \left\{\varphi_{\text{ex,k}}\right\}, \left\{\varphi_{\text{ex,k}}\right\} \right\rangle$ remains almost the same value (because the number of non-zero entries in $\mathbf{D}_1$ will remain the same and the value of the corresponding entries will almost be the same as the grid relative position to the interface only fluctuates slightly

as the number of grid points being increased), while $\left\langle \{\varphi_{\mathrm{ex,k}}\}, \{\varphi_{\mathrm{ex,k}}\} \right\rangle$ increases as the size of the column vector increases, if we discretize the same field. As a consequence, for sufficiently large N, it follows

$$c_1(N) \sim \frac{1}{N} \sim \Delta x \tag{A1.14a}$$

$$c_1(N) \approx \Delta x\, c_3 . \tag{A1.14b}$$

In contrary, c_2 is not much affected by the number of grid points because the increase in $\left\langle \mathbf{D}_2 \{\varphi_{\mathrm{ex,k}}\}, \{\varphi_{\mathrm{ex,k}}\} \right\rangle$ as the number of grid points increase will be compensated by the increase in $\left\langle \{\varphi_{\mathrm{ex,k}}\}, \{\varphi_{\mathrm{ex,k}}\} \right\rangle$ (that is why if the discretization error is uniformly 2nd-order, hence $\delta\beta_{\mathrm{k}}^2$ is also 2nd-order for the case where the interface discretization error is already 2nd order, as generally understood). Hence, by incorporating eq. (A1.14), the first term in eq. (A1.12) is proportional to Δx^2 for sufficiently large number of total grid points. Therefore, we can write

$$\delta\beta_{\mathrm{k}}^2 \equiv \beta_{\mathrm{num,k}}^2 - \beta_{\mathrm{ex,k}}^2 \approx \Delta x^2 c_3 + \Delta x^2 c_2 = O\left(\Delta x^2\right) \tag{A1.15}$$

which proves that the error of β^2 is second-order. This behavior is confirmed by the computational results (see e.g. Fig. 3.3.b).

The order of error of $\beta_{\mathrm{num,k}}$ will be the same as the order of error of $\beta_{\mathrm{num,k}}^2$ as we may write $\delta\beta_{\mathrm{k}}^2 = 2\beta_{\mathrm{k}}\delta\beta_{\mathrm{k}}$, where δ denotes small variation. More precisely, we may also use Taylor's expansion as follows. By assuming $\delta\beta_{\mathrm{k}}^2 = O\left(\Delta x^2\right)$, we will get

$$\beta_{\mathrm{num,k}} = \sqrt{\beta_{\mathrm{ex,k}}^2 + O\left(\Delta x^2\right)} = \beta_{\mathrm{ex,k}}\sqrt{1 + O\left(\Delta x^2\right)} \tag{A1.16}$$

which can written as

$$\beta_{\mathrm{num,k}} = \beta_{\mathrm{ex,k}}\left[1 + \tfrac{1}{2}O\left(\Delta x^2\right) - \tfrac{1}{8}O\left(\Delta x^4\right) + ...\right] = \beta_{\mathrm{ex,k}} + O\left(\Delta x^2\right) \tag{A1.17}$$

The proof and explanation given above can be generalized to any order of error, i.e. the effect of $O(\Delta x^{\mathrm{p}})$ error in FD discretization of a fix finite number of grid points, while the rest grid points has $O(\Delta x^{\mathrm{p+1}})$ error, is $O(\Delta x^{\mathrm{p+1}})$ error in the computed eigenvalue.

Appendix 2

The dispersion parameter

In Chapter 8, we present curves of the dispersion parameter D as function of wavelength. Although the derivation of this parameter can be found in standard textbook on fiber optic [1], we put a brief derivation here just as a reference for reader who is not familiar with this term.

As a measure of how much an optical pulse will broaden as it travels in an optical waveguide with wavelength-dependent properties, dispersion parameter D is defined as

$$D = \frac{\partial \tau_g}{\partial \lambda} \tag{A3.1}$$

where the group delay is

$$\tau_g = \frac{1}{v_g} = \frac{\partial}{\partial \omega}\mathrm{Re}(\beta) \tag{A3.2}$$

with v_g is the group velocity. Here, we treat the longitudinal component of the wavevector β as a complex quantity for compatibility with leaky modes being considered in Chapter 8, where only the real part contributes to the phase of the field. By substituting

$$\mathrm{Re}(\beta) = k_0\,\mathrm{Re}(n_{\mathrm{eff}}) = (\omega/c)\,\mathrm{Re}(n_{\mathrm{eff}}) \tag{A3.3}$$

into eqs. (A3.2), where n_{eff} is the wavelength-dependent effective index of the mode, and using

$$\lambda = \frac{2\pi c}{\omega}, \tag{A3.4}$$

eq. (A3.1) can be written as

$$D = -\frac{\lambda}{c}\frac{\partial^2}{\partial \lambda^2}\mathrm{Re}(n_{eff}). \tag{A3.5}$$

The latter equation is the formula that we used in Chapter 8 of this thesis, and also used by other authors [2, 3]. Note that in the literature, one can also find other ways to express the dispersion parameter, e.g.

$$D = -\frac{\omega^2}{2\pi c}\frac{\partial^2}{\partial \omega^2}\mathrm{Re}(\beta) \tag{A3.6}$$

as used by Johnson *et al.* [4], and

$$D = -\frac{2\pi c}{\lambda^2}\frac{\partial^2}{\partial\omega^2}\mathrm{Re}(\beta) \qquad \text{(A3.7)}$$

as used by Zhang *et al.* [5]. By using eqs. (A3.3)-(A3.4), it can be shown that eqs. (A3.6) and (A3.7) are identical to (A3.5). The relation of the dispersion parameter *D* to the group velocity dispersion (*GVD*)

$$GVD = \frac{\partial^2}{\partial\omega^2}\mathrm{Re}(\beta) \qquad \text{(A3.8)}$$

can be clearly seen from eqs. (A3.6) and (A3.7). Note that very often the term *GVD* is confusingly used to denote *D* [4, 5].

References

1. G.P. Agrawal, *Fiber-optic communication systems*, Section 2.3.1., 3rd ed., John Wiley and Sons Inc., New York, 2002.
2. A. Ferrando, E. Silvestre, J.J. Miret, and P. Andres, "Nearly zero ultraflattened dispersion in photonic crystal fibers," **Optics Lett.**, Vol. 25, No. 11, pp. 790-792, 2000.
3. K. Saitoh *et al.*, "Chromatic dispersion control in photonic crystal fibers: application to ultra-flattened dispersion," **Optics Express**, Vol. 11, No. 8, pp. 843-852, 2003.
4. S.G. Johnson *et al.*, "Low-loss asymptotically single-mode propagation in large-core OmniGuide fibers," **Optics Express**, Vol. 9, No. 13, pp. 748-779, 2001.
5. R. Zhang et al., "Group velocity dispersion of tapered fibers immersed in different liquids," **Optics Express**, Vol. 12, No. 8, pp. 1700-1707, 2004.